

Applied Condition Monitoring

Tahar Fakhfakh

Fakher Chaari

Lasaad Walha

Moez Abdennadher

Mohamed Slim Abbas

Mohamed Haddar *Editors*

# Advances in Acoustics and Vibration

Proceedings of the International  
Conference on Acoustics and Vibration  
(ICAV2016), March 21–23, Hammamet,  
Tunisia

 Springer

# **Applied Condition Monitoring**

Volume 5

## **Series editors**

Mohamed Haddar, National School of Engineers of Sfax, Tunisia

Walter Bartelmus, Wrocław University of Technology, Poland

Fakher Chaari, National School of Engineers of Sfax, Tunisia  
e-mail: fakher.chaari@gmail.com

Radoslaw Zimroz, Wrocław University of Technology, Poland

### *About this Series*

The book series Applied Condition Monitoring publishes the latest research and developments in the field of condition monitoring, with a special focus on industrial applications. It covers both theoretical and experimental approaches, as well as a range of monitoring conditioning techniques and new trends and challenges in the field. Topics of interest include, but are not limited to: vibration measurement and analysis; infrared thermography; oil analysis and tribology; acoustic emissions and ultrasonics; and motor current analysis. Books published in the series deal with root cause analysis, failure and degradation scenarios, proactive and predictive techniques, and many other aspects related to condition monitoring. Applications concern different industrial sectors: automotive engineering, power engineering, civil engineering, geoenvironmental engineering, bioengineering, etc. The series publishes monographs, edited books, and selected conference proceedings, as well as textbooks for advanced students.

More information about this series at <http://www.springer.com/series/13418>

Tahar Fakhfakh · Fakhher Chaari  
Lasaad Walha · Moez Abdennadher  
Mohamed Slim Abbas · Mohamed Haddar  
Editors

# Advances in Acoustics and Vibration

Proceedings of the International Conference  
on Acoustics and Vibration (ICAV2016),  
March 21–23, Hammamet, Tunisia

*Editors*

Tahar Fakhfakh  
National School of Engineers of Sfax  
Sfax  
Tunisia

Moez Abdennadher  
Preparatory Engineering Institute of Sfax  
Sfax  
Tunisia

Fakher Chaari  
National School of Engineers of Sfax  
Sfax  
Tunisia

Mohamed Slim Abbes  
National School of Engineers of Sfax  
Sfax  
Tunisia

Lasaad Walha  
National School of Engineers of Sfax  
Sfax  
Tunisia

Mohamed Haddar  
National School of Engineers of Sfax  
Sfax  
Tunisia

ISSN 2363-698X  
Applied Condition Monitoring  
ISBN 978-3-319-41458-4  
DOI 10.1007/978-3-319-41459-1

ISSN 2363-6998 (electronic)  
ISBN 978-3-319-41459-1 (eBook)

Library of Congress Control Number: 2016944485

© Springer International Publishing Switzerland 2017

This work is subject to copyright. All rights are reserved by the Publisher, whether the whole or part of the material is concerned, specifically the rights of translation, reprinting, reuse of illustrations, recitation, broadcasting, reproduction on microfilms or in any other physical way, and transmission or information storage and retrieval, electronic adaptation, computer software, or by similar or dissimilar methodology now known or hereafter developed.

The use of general descriptive names, registered names, trademarks, service marks, etc. in this publication does not imply, even in the absence of a specific statement, that such names are exempt from the relevant protective laws and regulations and therefore free for general use.

The publisher, the authors and the editors are safe to assume that the advice and information in this book are believed to be true and accurate at the date of publication. Neither the publisher nor the authors or the editors give a warranty, express or implied, with respect to the material contained herein or for any errors or omissions that may have been made.

Printed on acid-free paper

This Springer imprint is published by Springer Nature  
The registered company is Springer International Publishing AG Switzerland

# Preface

The first International Conference on Acoustics and Vibration ICAV2016 was held in Hammamet, Tunisia, from March 21 to March 23, 2016. This book contains a compilation of 30 papers presented during this conference. ICAV2016 is the first conference of the Tunisian Association of Industrial Acoustics and Vibration (ATAVI). One of the main objectives of this association is to promote communication and collaboration between international and local communities involved in the fields of acoustics and vibration through the organization of conferences and seminars to promote science-based research and encourage meetings between professionals and researchers in the fields of interest. ICAV2016 was an excellent opportunity to gather about 100 researchers who discussed in plenary sessions and parallel sessions all aspects related to the topics of the conference which are summarized as following:

- Structural Acoustics and Vibration
- Industrial and Environmental Acoustics
- Fault Diagnosis and Prognosis
- Fluid-Structure Interaction
- Noise Source Identification
- Vibration Field Measurements and Force Identification
- Vibration and acoustics of Mechatronic systems

All the chapters included in this book were rigorously reviewed by referees. We would like to express our gratitude to all persons who contributed to the success of

ICAV2016: organizing committee, scientific committee, and all participants coming from Tunisia, Algeria, France, Saudi Arabia, and China. Thanks to Springer for supporting the first edition of ICAV2016.

Sfax, Tunisia  
March 2016

Tahar Fakhfakh  
Fakher Chaari  
Lasaad Walha  
Moez Abdennadher  
Mohamed Slim Abbas  
Mohamed Haddar

# Contents

<b>Fault Diagnosis in Gas Turbine Based on Neural Networks: Vibrations Speed Application</b> . . . . .	1
Mohamed Ben Rahmoune, Ahmed Hafaifa and Mouloud Guemana	
<b>Early Detection of Gear Faults in Variable Load and Local Defect Size Using Ensemble Empirical Mode Decomposition (EEMD)</b> . . . . .	13
H. Mahgoun, Fakher Chaari, A. Felkaoui and Mohamed Haddar	
<b>Design of Shunted Piezoelectric Patches Using Topology Optimization for Noise and Vibration Attenuation</b> . . . . .	23
Walid Larbi, Jean-François Deü and Luciano Pereira da Silva	
<b>Prediction of Sound Radiation from Submerged Cylindrical Shell Structure with an Interpolation Method for the Measured Surface Velocity</b> . . . . .	35
Yilin Zhang, Haijun Wu and Weikang Jiang	
<b>Identification of Small Objects with Near-Field Data in Quasi-Backscattering Configurations</b> . . . . .	43
Housseem Haddar and Mohamed Lakhel	
<b>Characterization of Sandwich Beams with Shear Damage by Linear Vibration Method</b> . . . . .	55
I. Ben Ammar, C. Karra, A. El Mahi, R. El Guerjouma and Mohamed Haddar	
<b>Parameter Identification of a Sandwich Beam Using Numerical-Based Inhomogeneous Wave Correlation Method</b> . . . . .	65
R. Ajili, O. Bareille, M.-L. Bouazizi, M.-N. Ichchou and N. Bouhaddi	
<b>Time Domain Stability Analysis for Machining Processes</b> . . . . .	77
Asia Maamar, Belhassen Chedli Bouzgarrou, Vincent Gagnol and Raouf Fathallah	



<b>Modeling and Control for Lateral Rail Vehicle Dynamic Vibration with Comfort Evaluation . . . . .</b>	89
Mortadha Graa, Mohamed Nejlaoui, Ajmi Houidi, Zouhaier Affi and Lotfi Romdhane	
<b>Vibration Detection in Gas Turbine Rotor Using Artificial Neural Network Combined with Continuous Wavelet . . . . .</b>	101
Benrabeh Djaidir, Ahmed Hafaifa and Abdallaha Kouzou	
<b>A Finite Element Model for Elastic-Viscoelastic-Elastic Composite Structures . . . . .</b>	115
Zhicheng Huang, Zhaoye Qin and Fulei Chu	
<b>Application of the Operational Modal Analysis Using the Independent Component Analysis for a Quarter Car Vehicle Model . . . . .</b>	125
Dorra Ben Hassen, Mariem Miladi, Mohamed Slim Abbes, S. Caglar Baslamisli, Fakher Chaari and Mohamed Haddar	
<b>Feature Extraction Using S-Transform and 2DNMF for Diesel Engine Faults Classification . . . . .</b>	135
Ezzeddine Ftoutou and Mnaouar Chouchane	
<b>Experimental Study of Combined Gear and Bearing Faults by Sound Perception . . . . .</b>	145
Younes Ramdane, Ouelaa Nouredine, Hamzaoui Nacer and Djebala Abderrazek	
<b>Modal Analysis of Spur Gearbox with an Elastic Coupling . . . . .</b>	153
Atef Hmida, Ahmed Hammami, Fakher Chaari, Mohamed Taoufik Khabou and Mohamed Haddar	
<b>Planet Load Sharing Behavior During Run Up . . . . .</b>	165
Ahmed Hammami, Alfonso Fernandez Del Rincon, Fakher Chaari, Fernando Viadero Rueda and Mohamed Haddar	
<b>Multi-objective Design Optimization of the NBTTL Mechanism . . . . .</b>	175
B. Najlawi, M. Nejlaoui, Z. Affi and L. Romdhane	
<b>Appropriation Effects in the Estimation of Modal Damping . . . . .</b>	185
Mohamed Krifa, Noureddine Bouhaddi and Scott Cogan	
<b>Simulation of Resonance Phenomenon in Pipelines Caused by Water Hammer . . . . .</b>	195
Noura Bettaieb and Ezzeddine Haj Taieb	
<b>Sensitivity of GFRP Composite Integrity to Machining-Induced Heat: A Numerical Approach . . . . .</b>	205
Ali Mkaddem, Muhammad Zain-ul-Abdein, Salah Mezlini, Abdullah S. Bin Mahfouz and Abdessalem Jarraya	

**A Comparative Assessment of In-Operation Modal Analysis and Frequency Domain Decomposition Algorithm Using Simulated Data** . . . . . 215  
 Maher Abdelghani, Morteza Ghalishooyan and Ahmad Shoostari

**Experimental Investigation for Forced Vibration of Honeycomb Sandwich Beams** . . . . . 223  
 Souhir Zghal and Rachid Nasri

**Theoretical and Experimental Analysis of the Vibrational Behavior of a Polyester Composite Material**. . . . . 235  
 Idris Chenini, Charfeddine Mrad and Rachid Nasri

**Robust Multi-objective Collaborative Optimization of Complex Structures** . . . . . 247  
 H. Chagraoui, M. Soula and M. Guedri

**Investigations on the Validity of the Poisson Assumption in Reliability Based Optimization of TMD Parameters** . . . . . 259  
 E. Mrabet, M. Guedri, M. Soula, M. Ichchou and S. Ghanmi

**FE Modeling of Wear Mechanisms in UD-GFRP Composites Using Single-Indenter Scratch Test: A Micromechanical Approach**. . . . . 269  
 S. Mzali, F. Elwasli, A. Mkaddem and S. Mezlini

**Dynamic Analysis of the Perforation of Aluminum Alloy at Low Velocity Impact** . . . . . 281  
 S. Koubaa, J. Mars, M. Wali and F. Dammak

**Non-linear Dynamics Analysis of Multilayer Composite Shells with Enhanced Solid-Shell Elements**. . . . . 291  
 A. Hajlaoui, E. Triki, A. Frikha and F. Dammak

**An Effective Method for the Identification of Support Features in Multi-supported Systems**. . . . . 301  
 A. Baklouti, J. Antunes, V. Debut, T. Fakhkakh and Mohamed Haddar

**Dynamic Analysis of a Wedge Disc Brake According to the Variations of Friction Coefficient** . . . . . 313  
 K.R.M. Mahmoud

**Index** . . . . . 327

# Fault Diagnosis in Gas Turbine Based on Neural Networks: Vibrations Speed Application

Mohamed Ben Rahmoune, Ahmed Hafaifa and Mouloud Guemana

**Abstract** The diagnosis of faults and failures in industrial systems is becoming increasingly essential. This work proposes the development of a fault diagnostics system based on artificial intelligence technique, using neural networks applied to a GE MS3002 gas turbine. This technique with its generalization and memory skills provides an effective diagnostic tool for the examined system.

**Keywords** Diagnosis of defects · Neural networks · Modeling · Generation of residues · Gas turbine · Vibration

## 1 Introduction

The dream of creating an intelligence system is presented for a long time in the human imagination. Several applications in this direction have been conducted by scientists with the use of neural networks as a decision support tool (Hafaifa et al. 2011a, b, c, 2013, 2014b, c, 2015a, b; Chen and Lee 2002; Tsai and Chang 1995; Halimi et al. 2014a, b; Eshati et al. 2013; Temurtas 2009; Galindo et al. 2013; McGhee et al. 1997; Kim et al. 2011; Leger et al. 1998; Owen 2012; Nikpey et al. 2014). The creation of neural systems requires a thorough knowledge of several technical aspects (Sanaye and Tahani 2010; Wahba and Nawar 2013; Wu et al. 2011; Yang et al. 2000; Kim et al. 2010; Zhang et al. 1994). In the diagnosis of

---

M. Ben Rahmoune · A. Hafaifa (✉)  
Applied Automation and Industrial Diagnostics Laboratory,  
University of Djelfa, 17000 Djelfa, DZ, Algeria  
e-mail: hafaifa.ahmed.dz@ieee.org

M. Ben Rahmoune  
e-mail: B.rahmoune@univ-djelfa.dz

M. Guemana  
Faculty of Science and Technology, University of Médéa,  
26000 Médéa, DZ, Algeria  
e-mail: Guemana\_M@univ-medea.dz

faults and failures of industrial systems, this area is becoming more and more complex. Artificial neural networks, are now a well understood and managed data processing technique that allows the engineer to extract, in many situations, the most relevant information of the data it has: control processes, prediction properties, modeling, pattern recognition.

It is from the assumption that intelligent behavior emerges from the structure and behavior of brain basics, the artificial neural networks have developed. Each artificial neuron is a functional unit. He receives a variable number of inputs from upstream neuron. Each one of these entries is associated with a weight  $\omega$  representative of the strength of the connection. Each functional unit has a single output, which branches to supply follows, a variable number of downstream neuron (Eshati et al. 2013). In this context there are several applications of neural networks for fault diagnosis and in particular, for the diagnosis of faults of several industrial applications.

In this work, vibration measurements parameters are used for the development of a vibration monitoring system based on neural networks system. These parameters can be the displacement, velocity and acceleration; in time or frequency domain. These quantities are useful in the prediction of fatigue failure of a particular component of the machine and are important in the analysis, thereby reducing vibration of the examined gas turbine. This work proposes the development of a fault diagnostic system based on artificial intelligence technique, using neural networks applied to a typical GE MS3002 gas turbine. This technique with its generalization and memory skills provides an effective diagnostic tool for examining system.

## 2 Diagnosis Based on Neural Network

By analogy with the biological neuron, artificial neuron behavior, shown in Fig. 1, is modeled by two phases (Er et al. 2010):

- A summation operator, which develops the potential  $a$ . This operator performs a weighted sum of the inputs. Is subtracted from both the sum of the activation threshold  $\theta_i$ .

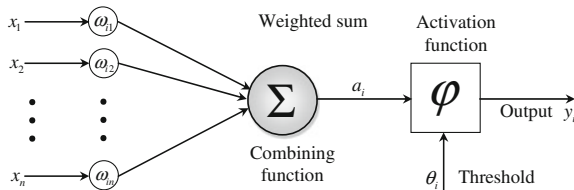


**Fig. 1** Nonlinear model of an artificial neuron

- A nonlinear operator which calculates the value of the activation. This operator is called the transfer function.

$\theta_i$  is the threshold of the neuron  $i$  which represents the limit at which the neuron will activate. And  $x_j$  is the neuron input (output of the upstream neuron  $j$ ), the value of the synaptic weight connecting neuron  $j$  led to the neuron  $i$ :

- A positive weight indicates an excitatory effect of the transmitter neuron  $j$  to the receiver neuron  $i$ ,
- A negative weight represents an inhibitory effect.

The combination function returns the scalar product between the input vector and the vector of the synaptic weights. In other words, it calculates the weighted sum of the inputs of the following expression:

$$a_i = \sum_{j=1}^n w_{ij}x_j \quad (1)$$

From this value, a transfer function (or activation function, or thresholding function)  $\varphi$  calculates the value of the neuron state. This will be sent to downstream neurons, using the flowing equation:

$$y_i = \varphi(a_i - \theta_i) \quad (2)$$

Neurons which are most frequently used are those for which the function  $\varphi$  is a nonlinear function (typically a hyperbolic tangent) linear combinations entries. The large amount of existing connectionist models, first led researchers to classify them according to their different properties to better understand the advantages and disadvantages of choosing one model over another. Indeed, there are several established neural network models based on attributes adopted, such as (Galindo et al. 2013):

- The nature of the individual cells that make up the (binary continuous or continuous),
- The architecture and the number of network controllers,
- The nature of the connections,
- The learning method,
- The classification performance of the storage mechanisms.

The network with radial function, shown in Fig. 2, has the same structures as the multi-perceptive, but the activation function is a Gaussian type function. This network, because of its architecture, most often uses the error correction learning rule and rule by competitive learning. He may have a learning which combines together the supervised learning and unsupervised learning. This network gets comparable or superior to those of the Multilayer Perception. Moreover, their faster and easier learning are the tools of choice for many types of applications, including classification and function approximation. However, this network has not so great

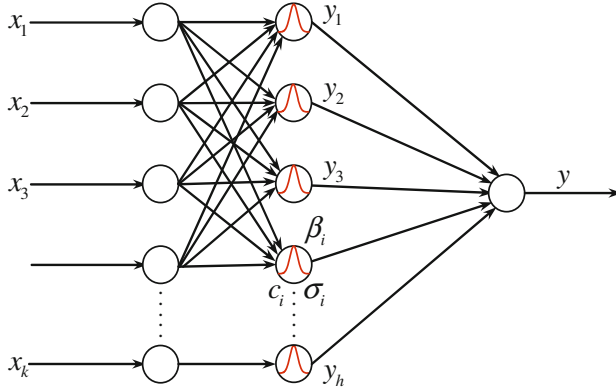


**Fig. 2** Network with radial function

research that the multilayer perceptive (Er et al. 2010). The most commonly activation function used is a Gaussian function is defined by:

$$y_i(x) = \exp\left(\frac{-\|x - c_i\|^2}{\sigma_i^2}\right) \quad (3)$$

where  $c_i$  and  $\sigma_i$  are respectively the center and radius of the Gaussian function. The output of the network is as follows:

$$y = \sum_i^h \beta_i y_i. \quad (4)$$

## 2.1 Neural Networks Learning

We can consider neural networks as a black box containing the information it needs to learn and remember. But at the start when choosing our network, the black box is empty and contains no information and no knowledge of his subject, so learning is needed. The instruction that is to undergo the neural network is a learning which is a phase of the development of a neural network in which the system behavior is modified to achieve the desired behavior. The learning is the main feature of neural networks. It is to adapt its various parameters (weight) from an iterative algorithm adjustment or adaptation enabling it to take into consideration all data (examples) that are provided on their entry and adjust its settings to find the balance to support any instance or data appearing at its input from its environment (Hafaifa et al. 2014a; Halimi et al. 2014a). There are two types of learning: supervised learning and unsupervised learning. Learning algorithms performed better when provided

with multiple and varied examples; and the network can assimilate all knowledge. There is different learning rules among which can be distinguished (Halimi et al. 2014a), the rule Widrow-Hoff, Hebb rule, and reverse propagation.

### 2.1.1 Back Propagation Algorithm

The back propagation algorithm is applied in two steps, the first is the spread forward during which the excitement  $X_p$  is applied to the input layer and propagates forward in the network to compute the output  $O_p$ , and error  $(d_p - O_p)$  from the  $d_p$  desired output. During the second phase—backward propagation—this error propagates backward to calculate the error for each neuron, and make appropriate changes in the weight of the network (Kim et al. 2011; Leger et al. 1998; Owen 2012; Nikpey et al. 2014; Er et al. 2010; Gobatto et al. 2011; Simani and Patton 2008; Sanaye and Tahani 2010). The algorithm is given as follows:

#### A. Forward propagation

1. Initialize the weights  $W_{ij}$  and bias neurons to small random values,
2. Applying the input vector  $X$  and the desired response vector  $d$ ,
3. Calculate the inputs of the internal layers using the flowing formula:

$$a_{pj}^h = w_{ij}^h X_{pj} + \theta_j^h \quad (5)$$

4. Calculate the outputs of the internal layers using the flowing formula:

$$I_{pj} = f\left(a_{pj}^n\right) \quad (6)$$

5. Calculate the output neurons entries using the flowing formula:

$$O_{pk}^0 = \sum_{i=1}^n w_{ki}^0 I_{pi} + \theta_k^0 \quad (7)$$

6. Calculate the network outputs using the flowing formula:

$$O_{pk}^0 = f\left(a_{pk}^0\right) \quad (8)$$

#### B. Back Ward propagation

7. Calculate the error term for the output layer

$$\delta_{pk} = (d_{pk} - O_{pk}) \dot{f}\left(a_{pk}^0\right) \quad (9)$$

8. Adjust the weight of the output layer

$$w_{kj}^0(t+1) = w_{kj}^0(t) + \eta \delta_{pk}^0 I_{pj} \quad (10)$$

9. Calculate the terms of the error for hidden layers

$$\delta_{pj}^h = f'(a_{pk}^h) \cdot \sum_k \delta_{pk}^0 w_{kj}^0 \quad (11)$$

10. Edit the weights of hidden layers

$$w_{ij}^h(t+1) = w_{ij}^h(t) + \eta \delta_{pj}^h X_{pj} \quad (12)$$

11. Repeat for each training vector

12. Calculate the error

$$E = \frac{1}{2} \sum_k (d_{pk} - O_{pk})^2 \quad (13)$$

Until the error has not reached the threshold, repeat steps 2–11.

Note that  $w_{ij}$  is the connection weights between neuron  $i$  and the neuron  $j$ ,  $a_{pj}^h$  is the input of the neuron  $j$ ,  $a_{pk}^0$  is the total input of the neuron  $k$ ,  $\theta_j^h$  is the fictitious weight of neuron  $j$  and  $f$  is the sigmoid activation function, given by the following equation:

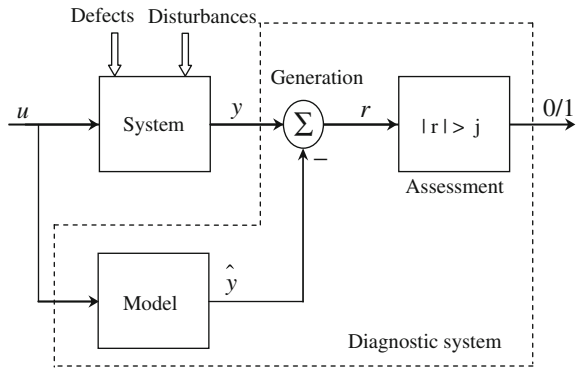
$$f(a) = \frac{1}{1 + e^{-a}}. \quad (14)$$

## 2.2 Generating Residues

The diagnostic procedure based on the most commonly used models, especially in industrial applications in real time, is that based on the residue approach. This diagnostic procedure is usually performed in two consecutive steps: the generation and evaluation of residues. Often used as a fault indicator, a residual  $r$  is a signal varying over time and produced a fundamental component in diagnostic systems using waste called tailings generator. This generator is based on a model of the system being monitored (analytical redundancy) and its known input  $u$  to produce an estimate  $\hat{y}$  which is then compared with the output of the system are measured,



**Fig. 3** General structure of a model-based diagnostic



shown in Fig. 3. The difference between the measured output and thus determines instantly estimate the amplitude of the residual.

Normally, the residue is designed so that its amplitude is zero (or low in the case of a real application in the presence of noise and with an uncertain model of the system) in the absence of defects, and it significantly differs to zero when a fault is present.

Residues generation is a crucial issue for diagnostics. Indeed, the structure of the generated residue number system depend robustness of the localization.

The approaches using a mathematical model of the process to generate residues, can be classified into three groups: the approach of the parameter estimation, the parity space approach and the approach based on observers (Hafaifa et al. 2011a).

### 2.2.1 Evaluation of Residues

We saw different approaches to the generation of waste, the next step in their evaluation. The residue assessment phase is to determine whether the system monitors is in a state of normal operation or not, is the detection step. If an anomaly is detected, it is to determine which element of the system is faulty; it is the location step. The derivatives of this modeling techniques are varied but not always effective. Indeed, the physical processes are often complex dynamic systems with strong nonlinearities in their operation. Simplifications are needed to formulate a workable model. Thus, the linearization techniques around an operating or reduction of order point are all methods degrading the performance of the mathematical model. Similarly, other problems remain with some measurable model parameters or time-varying. Another approach is the modeling of neuronal processes. The goal is to design a neural model for the generation of residues.

The general concept of the generation of waste remains the same as for the analytical models. By analogy with the theory of observers, neuronal models generate neuronal observers. It involves comparing the outputs of the process to their estimated. But in this case the estimates are calculated by a neural model. The vector of residuals  $r(t)$  is calculated by the difference between the actuator output vector  $y(t)$  and the output vector of the neural model.

$$r(t) = y(t) - \hat{y}(t). \quad (15)$$

### 3 Application Results

Robustness tests of the proposed approach in this work have allowed us to confirm the ability efficacies of this approach for the diagnosis of the examined gas turbine. Supervised learning from a database on the history of the gas turbine is considered well suited, as shown in Figs. 4 and 5.

The results we obtained indicate diagnostic confidence, and especially that falling generalization level returns to the transitions between normal and abnormal operation of the machine. Because we chose the sigmoid function which ensures continuity. Figure 6 shows the residual variation of the speed of rotation of the turbine examined.

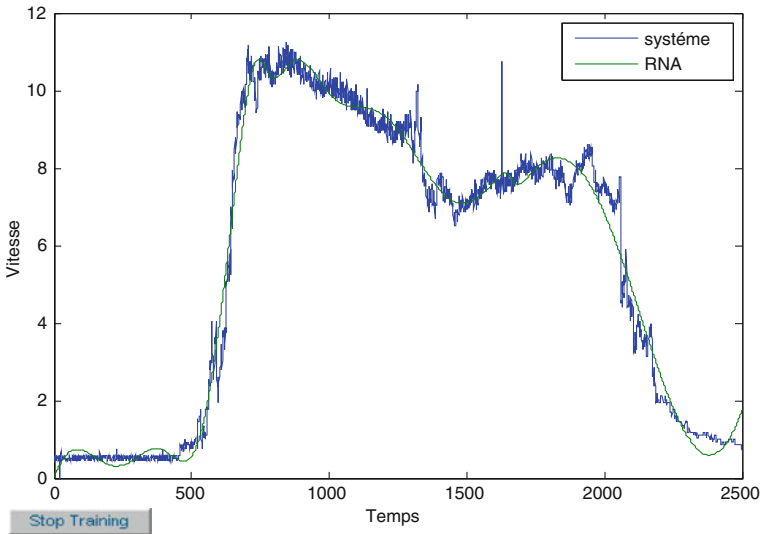


Fig. 4 Supervised learning from a database on the examined gas turbine test 1

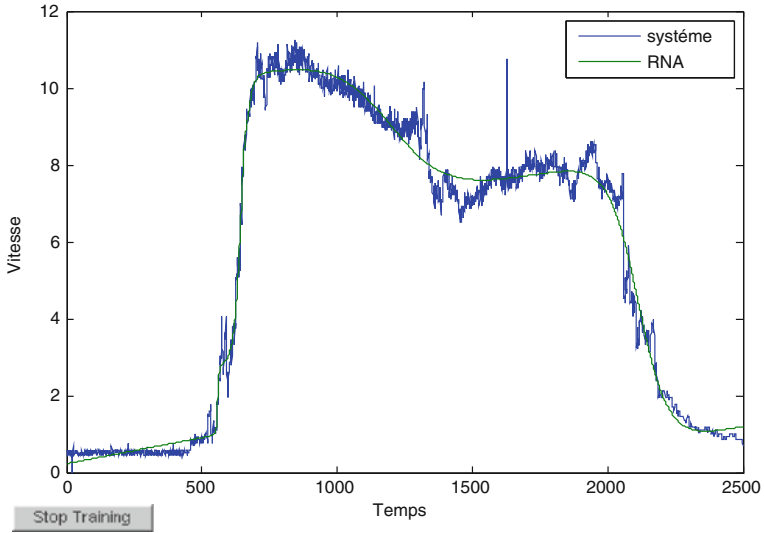


Fig. 5 Supervised learning from a database on the examined gas turbine test 2

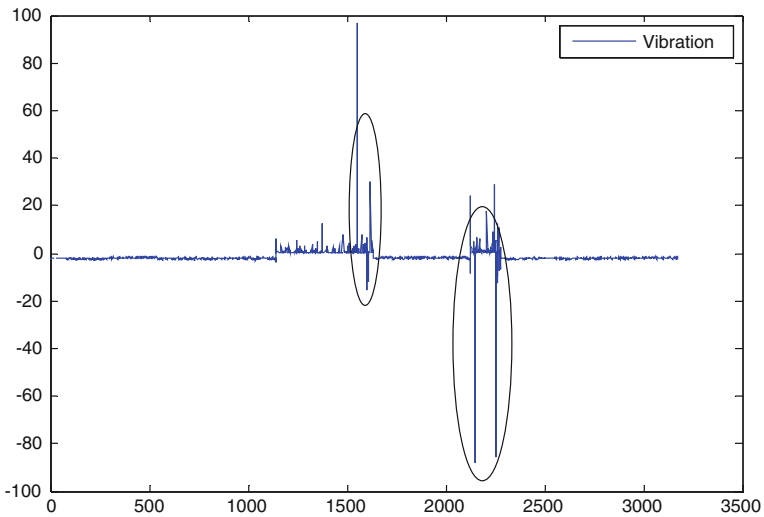


Fig. 6 Residual variation of the speed of rotation of the examined gas turbine

## 4 Conclusion

The study of neural network models, we were able to identify the main features that differentiate them from conventional techniques used in solving problems in several areas such as: artificial intelligence, signal processing, recognition of forms. By this

method, we gave a neural model that simulates the operation of our system examined. The results are very effective per se for the detection or localization. Can confirm that models based on neural networks are very good approximations. This advantage is mainly due to the simplicity of the residues analyzed to generate neural network system.

## References

- Chen YM, Lee ML (2002) Neural networks-based scheme for system failure detection and diagnosis. *Math Comput Simul* 58(2):101–109
- Er O, Yumusak N, Temurtas F (2010) Chest diseases diagnosis using artificial neural networks. *Expert Syst Appl* 37(12):7648–7655
- Eshati S, Abu A, Laskaridis P, Khan F (2013) Influence of water–air ratio on the heat transfer and creep life of a high pressure gas turbine blade. *Appl Therm Eng* 60(1–2):335–347
- Galindo J, Fajardo P, Navarro R, García-Cuevas LM (2013) Characterization of a radial turbocharger turbine in pulsating flow by means of CFD and its application to engine modeling. *Appl Energy* 103:116–127
- Gobbato P, Masi M, Toffolo A, Lazzaretto A (2011) Numerical simulation of a hydrogen fuelled gas turbine combustor. *Int J Hydrogen Energy* 36(13):7993–8002
- Hafaifa A, Daoudi A, Guemana M (2011a) SCADA for Surge Control: Using a SCADA network to handle surge control in gas suppression systems in pipelines. *ISA Trans Control Global Process Autom Technol J* 24(3):69–71
- Hafaifa A, Daoudi A, Laroussi K (2011b) Application of fuzzy diagnosis in fault detection and isolation to the compression system protection. *Control Intell Syst* 39(3):151–158 (ACTA Press)
- Hafaifa A, Laouad F, Laroussi K (2011c) A numerical structural approach to surge detection and isolation in compression systems using fuzzy logic controller. *Int J Control Autom Syst (IJCAS)* 9(1):69–79
- Hafaifa A, Djeddi AZ, Daoudi A (2013) Fault detection and isolation in industrial control valve based on artificial neural networks diagnosis. *J Control Eng Appl Inform (CEAI)* 15(3):61–69
- Hafaifa A, Belhadeif R, Guemana M (2014a) Modelling of surge phenomena in a centrifugal compressor: experimental analysis for control. *Syst Sci Control Eng Open Access J* 2(1):632–641 (Taylor & Francis)
- Hafaifa A, Belhadeif R, Boumehraz M (2014b) Reliability modelling based on incomplete data: oil pump application. *Manag Syst Prod Eng J* 3(15):140–144
- Hafaifa A, Guemana M, Daoudi A (2014c) Fault detection and isolation in industrial systems based on spectral analysis diagnosis. *Intell Control Autom* 4(1):36–41
- Hafaifa A, Guemana M, Belhadeif R (2015a) Fuzzy modeling and control of centrifugal compressor used in gas pipelines systems. *Multiphys Model Simul Syst Design Monit Appl Cond Monit* 2:379–389
- Hafaifa A, Guemana M, Daoudi A (2015b) Vibration supervision in gas turbine based on parity space approach to increasing efficiency. *J Vib Control* 21:1622–1632
- Halimi D, Hafaifa A, Bouali E, Guemana M (2014a) Use modeling as part of a compressor maintenance program. *Gas Process* 55–59 (Sept/Oct)
- Halimi D, Hafaifa A, Bouali E (2014b) Maintenance actions planning in industrial centrifugal compressor based on failure analysis. *Q J Maint Reliab* 16(1):17–21
- Kim YS, Lee JJ, Kim TS, Sohn JL, Joo YJ (2010) Performance analysis of a syngas-fed gas turbine considering the operating limitations of its components. *Appl Energy* 87(5):1602–1611
- Kim KH, Ko H-J, Perez-Blanco H (2011) Analytical modeling of wet compression of gas turbine systems. *Appl Therm Eng* 31(5):834–840

- Leger RP, Garland WJ, Poehlman WFS (1998) Fault detection and diagnosis using statistical control charts and artificial neural networks. *Artif Intell Eng* 12(1–2):35–47
- McGhee J, Henderson IA, Baird A (1997) Neural networks applied for the identification and fault diagnosis of process valves and actuators. *Measurement* 20(4):267–275
- Nikpey H, Assadi M, Breuhaus P, Mørkved PT (2014) Experimental evaluation and ANN modeling of a recuperative micro gas turbine burning mixtures of natural gas and biogas. *Appl Energy* 117:30–41
- Owen JM (2012) Theoretical modelling of hot gas ingestion through turbine rim seals. *Propuls Power Res* 1(1):1–11
- Sanaye S, Tahani M (2010) Analysis of gas turbine operating parameters with inlet fogging and wet compression processes. *Appl Therm Eng* 30(2–3):234–244
- Simani S, Patton RJ (2008) Fault diagnosis of an industrial gas turbine prototype using a system identification approach. *Control Eng Pract* 16(7):769–786
- Temurtas F (2009) A comparative study on thyroid disease diagnosis using neural networks. *Expert Syst Appl* 36(1):944–949
- Tsai C-S, Chang C-T (1995) Dynamic process diagnosis via integrated neural networks. *Comput Chem Eng* 19(1):747–752
- Wahba EM, Nawar H (2013) Multiphase flow modeling and optimization for online wash systems of gas turbines. *Appl Math Model* 37(14–15):7549–7560
- Wu X-J, Huang Q, Zhu X-J (2011) Thermal modeling of a solid oxide fuel cell and micro gas turbine hybrid power system based on modified LS-SVM. *Int J Hydrogen Energy* 36(1):885–892
- Yang SH, Chen BH, Wang XZ (2000) Neural network based fault diagnosis using unmeasurable inputs. *Eng Appl Artif Intell* 13(3):345–356
- Zhang J, Morris AJ, Montague GA (1994) Fault diagnosis of a cstr using fuzzy neural networks. *Annu Rev Autom Program* 19:153–158

# Early Detection of Gear Faults in Variable Load and Local Defect Size Using Ensemble Empirical Mode Decomposition (EEMD)

H. Mahgoun, Fakher Chaari, A. Felkaoui and Mohamed Haddar

**Abstract** In stationary condition, when a local gear fault occurs, both amplitude and phase of the tooth meshing vibration are modulated. If the rotating speed of the shaft is invariable, the gear-fault-induced modulation phenomenon manifest as frequency sidebands equally spaced around the meshing frequency and its harmonics in vibration spectra. However, under variable load and rotating speed of the shaft, the meshing frequency and its harmonics and the sidebands vary with time and hence the vibration signal becomes non-stationary. Using Fourier transform doesn't allow detecting the variation of the rotating machine and its harmonics which reflect the gear fault. In this study, we propose to use the ensemble empirical decomposition (EEMD) to decompose signals generated by the variation of load and the size of the defect. This method is particularly suitable for processing non stationary signals. By using EEMD the signal can be decomposed into a number of IMFs which are mono component, we use also the spectrum and spectrogram of each IMF to show and calculate the frequency defect.

**Keywords** Fault detection · Vibration · Ensemble empirical mode decomposition (EEMD) · Gear · Rotating machines

## 1 Introduction

Gears are widely used in rotating machinery to transmit power. Gear defects are inevitable and considered as one of the major sources of noise and vibration (McFadden 1986) giving rise to abnormal operation and failure of the transmission.

---

H. Mahgoun (✉) · A. Felkaoui  
Laboratoire de Mécanique de précision Appliquée, Université Ferhat Abbas Sétif 1,  
Sétif, Algeria  
e-mail: mahafida006@yahoo.fr

F. Chaari · M. Haddar  
Laboratoire de Mécanique, Modélisation et Production (LA2MP), Ecole Nationale  
d'ingénieurs de Sfax, Sfax, Tunisia

Vibration analysis is considered as one of the main tools to diagnose gear faults since vibration signals can carry valuable information about the health status of machines (McFadden 1986).

A local gear defect causes both amplitude and phase modulations of the tooth meshing vibration signals (Capdessus 1992). For constant rotational speed, the modulation phenomenon can be characterized in vibration spectra by sidebands equally spaced around the meshing frequency and its harmonics. However, under variable rotating speeds, meshing frequency and its harmonic and sidebands are time varying leading to non-stationary signals (Wu et al. 2012).

The use of the conventional fault diagnosis methods such as the Fourier analysis and the Hilbert transform do not provide valuable results. Methods based on the decomposition of vibration signal into bands are more suitable in these situations.

Until now, many methods were applied to detect the fault at an early stage, among these methods traditional ones including statistical analysis based on the signal itself such as (root mean square, crest factor kurtosis, and so on) and the frequency domain analyses based essentially on the Fourier transform. Therefore, the Fourier analysis gives good results if the vibration signal is stationary and linear and it is inapt to analyze the non stationary signal, which may lead to false information about the mechanical faults (Cohen 1989). To solve this problem new methods have been introduced. The time-frequency analysis methods such as Wigner Ville decomposition (WVD) (Forrester 1989), short Fourier transform (STFT) (Staszewski 1997) and wavelet transform (WT) (Wang and Mcfadden 1997) seem to be the suitable tool to identify the frequency content and to provide information about its variability. These methods are classified into linear time frequency representation such as STFT and wavelet transform, and bilinear methods such as Wigner Ville distributions. The STFT is appropriate only to analyzing signals with slow variation (Mallat 1998) and it is inefficient for non stationary signals. The WT was widely applied because it's a multiresolution analyses (Mallat 1998), able to detect transient features to extract impulses and denoising. Nevertheless, the wavelet analysis is also a linear transform using functions named wavelets as window function like the STFT. The window changes its width by using a dilatation parameter. Then, at high frequency we have high time resolution and a low frequency resolution. While, at low frequencies we have low time resolution and high frequency resolution. Then, we can't have a good resolution for all time-scale map due to the Heisenberg uncertainty principle (Staszewski 1997). In addition, this method gives a time-scale representation which is difficult to interpret as a time-frequency representation; we must have a relation between the scale and the frequency to understand the obtained results and to identify the fault frequencies. Another limitation of the WT is how to select the mother wavelet used in the analyses of the signal, since different wavelets have different time frequency structures, also, how to calculate the range scale used in the WT is another deficiency of the transform (Liu et al. 2005). Many researchers demonstrated that the use of the WT introduce border distortion and energy leakage.

In mechanical application, Yang et al. (2011) confirm that this method is highly dependent on the rotational speed and pre-knowledge of the machine. To overcome

the deficiencies of these methods empirical mode decomposition (EMD) was proposed by Huang et al. (1998) for nonlinear and non-stationary signals and was applied in fault diagnosis of rotating machinery (Liu et al. 2005; Mahgoun et al. 2010). It does not use a priori determined basis functions and can iteratively decompose a complex signal into a finite number of zero mean oscillations named intrinsic mode functions (IMFs). Each resulting elementary component (IMF) can represent the local characteristic of the signal. However, one of the problems of EMD is mode mixing as a result of intermittency (Huang et al. 2003; Rilling and Flandrin 2008). Mode mixing occurs when different frequencies that should appear separately in different IMFs are presented in one IMF. This problem gives a vague physical significance of the IMF. EMD is unable to separate different frequencies in separate IMFs. Also, the IMFs are not orthogonal each other, which produce end effects. To solve the problem of mode mixing the ensemble empirical mode decomposition EEMD method was proposed by Wu and Huang (2009) by adding several realizations of Gaussian white noise to the signal, and then using the EMD to decompose the noisy signal, multiple IMFs can be obtained and the added noise is canceled by averaging the IMFs. The ensemble empirical mode decomposition (EEMD) proposed by Huang et al. to analyze nonlinear and non-stationary signals. The method was largely applied in fault diagnosis of rotating machinery (Wu et al. 2009; Mahgoun et al. 2012) because it does not use a priori determined basis functions and can iteratively decompose a complex signal into a finite number of intrinsic mode functions (IMFs). Each resulting elementary component IMF can represent the local characteristic of the signal. But all these papers used the EEMD to analyze signals collected from test bench which work under stationary conditions, where the speed of the shaft is constant or slowly variable. The ensemble empirical decomposition (EEMD) can be used for processing non stationary signals.

In this work we analyze vibration signals given by a dynamic modeling of a gear transmission in the case of non stationary load and speed with a variation in the defect size. The spectrum of each IMF is also used to detect the fault frequency.

The structure of the paper is as follows: Sect. 2 introduces the basic of EMD and EEMD. In Sect. 3, the method EEMD and the spectrum are applied for early faults gearbox detection. In Sect. 4, a conclusion of this paper is given.

## 2 EMD and EEMD Algorithms

The EMD consists to decompose iteratively a complex signal into a finite number of intrinsic mode functions (IMFs) which verify the two following conditions:

- (a) The number of extrema and the number of zeros of an IMF must be equal or differ at most by one.
- (b) An IMF must be symmetric with respect to local zero mean.



For a given signal  $x(t)$  the EMD algorithm used in this study is given in literatures (Huang et al. 1998; Mahgoun et al. 2012).

To alleviate the mode mixing effect of EMD, the EEMD was used. The EEMD decomposition algorithm of the original signal  $x(t)$  used in this work is summarized in the following steps (Wu and Huang 2009):

1. Add a white noise  $n(t)$  with given amplitude  $\beta_k$  to the original signal  $x(t)$  to generate a new signal:

$$x_k(t) = x(t) + \beta_k n(t) \quad (1)$$

2. Use the EMD to decompose the generated signals  $x_k(t)$  into  $N$  IMFs  $IMF_{nk}(t), n = 1, \dots, N$ , where the  $n$ th IMF of the  $k$ th trial is  $IMF_{nk}(t)$ .
3. Repeat steps (1) and (2)  $K$  times with different white noise series each time to obtain an ensemble of IMFs:  $IMF_{nk}(t), k = 1, \dots, K$ .
4. Determine the ensemble mean of the  $K$  trials for each IMF as the final result:

$$IMF_n(t) = \lim_{K \rightarrow \infty} \frac{1}{K} \sum_{k=1}^K IMF_{nk}(t), \quad n = 1, \dots, N \quad (2)$$

### 3 Application

In this section we will put in evidence the efficiency of EEMD method through simulations performed starting from a dynamic model of bevel gear transmission which is subjected time varying operating conditions (speed and load). Previous analysis of simulated vibration signals from gear models using Wigner Ville (Chaari et al. 2013) or spectrogram (Chaari et al. 2013; Bartelmus et al. 2009) was not able to provide clear information about the presence of local defect at an early stage. This is mainly caused by the fact that impacts induced by this localized defect are masked by the part of the signal with simultaneous amplitude and frequency modulation induced by speed and load variation.

Let's consider a bevel gear transmission model driven by a squirrel cage electric motor and having the characteristics given in Mahgoun et al. (2016). The transmission is loaded with a torque having sawtooth shape with frequency  $f_L = 5$  Hz as presented in Fig. 1a.

The variation of load leads to a fluctuation in the rotational speed (Fig. 1b) and consequently to variation of the mesh frequency. The mean value of the motor rotational speed is  $n_r = 1320$  rpm which corresponds to a mean mesh frequency  $f_{gm} = 308$  Hz. A crack on one pinion tooth is considered leading to defect frequency of 22 Hz and a period of 0.045 s.

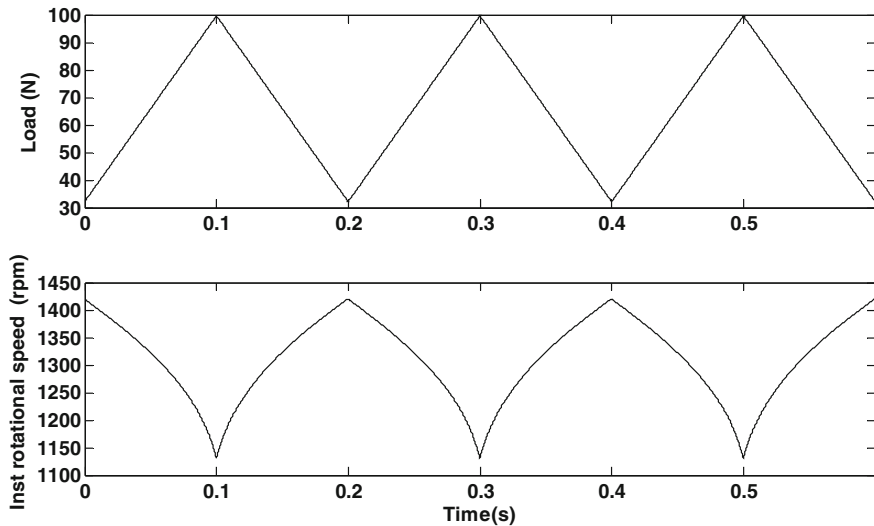


**Fig. 1** a Evolution of the applied load, b evolution of the instantaneous rotational speed

The sampling frequency is 30,800 Hz for all signals. A crack is simulated by a decrease in the gear mesh stiffness function when the defected tooth meshes. In this work we propose to study acceleration signals on pinion bearing for different loads (constant load, load fluctuation of 10 % and load fluctuation of 50 %). We have considered also different severities of crack defect as following:

- (a) *Healthy gear*
- (b) *gear with an incipient defect (1 % loss in mesh stiffness)*
- (c) *gear with a medium defect (5 % loss in mesh stiffness)*
- (d) *gear with an important defect (10 % loss in mesh stiffness).*

So, we will have twelve signals that are decomposed by using the EEMD method.

The acceleration signals for healthy gear and faulty gear for early and advanced stage for a fluctuation of load 50 % are given in Fig. 2.

From literature the spectrum of a gear transmission running under constant loading conditions is dominated only by the gear mesh frequency and its harmonics with eventual sidebands induced by the presence of defects (Capdessus et al. 1992). For non-stationary conditions, family of sidebands will be noticed around the mesh frequency  $f_{gm}$  and its harmonics induced by the non uniformity of the gear mesh period (Fig. 3) and this can be thought to be a frequency modulation of the gear mesh stiffness.

The zoom around the mesh frequency for the defect cases (Fig. 3b–d) shows many asymmetric sidebands around this frequency, which indicate a frequency modulation.

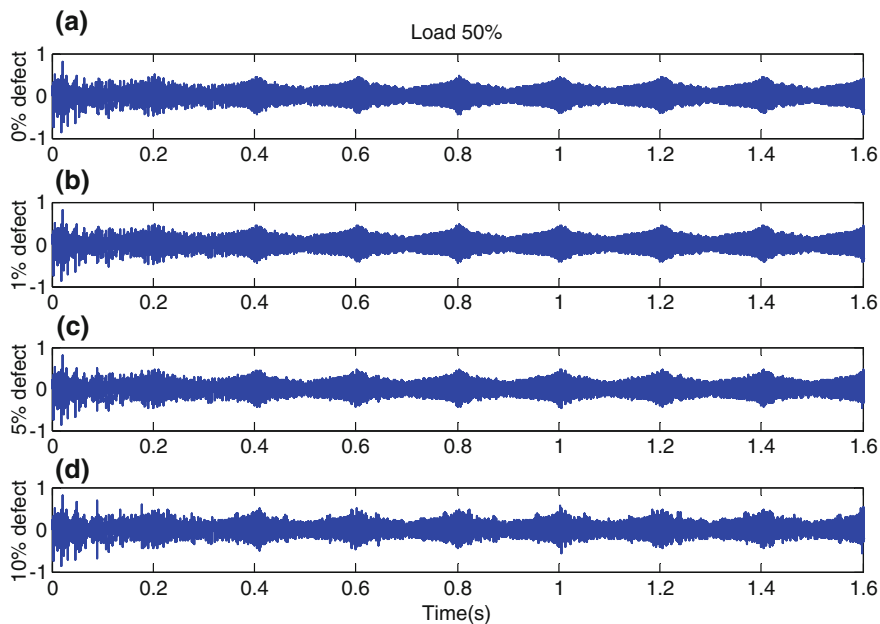


Fig. 2 Acceleration signals for 50 % of load a healthy gear, b–d faulty gear

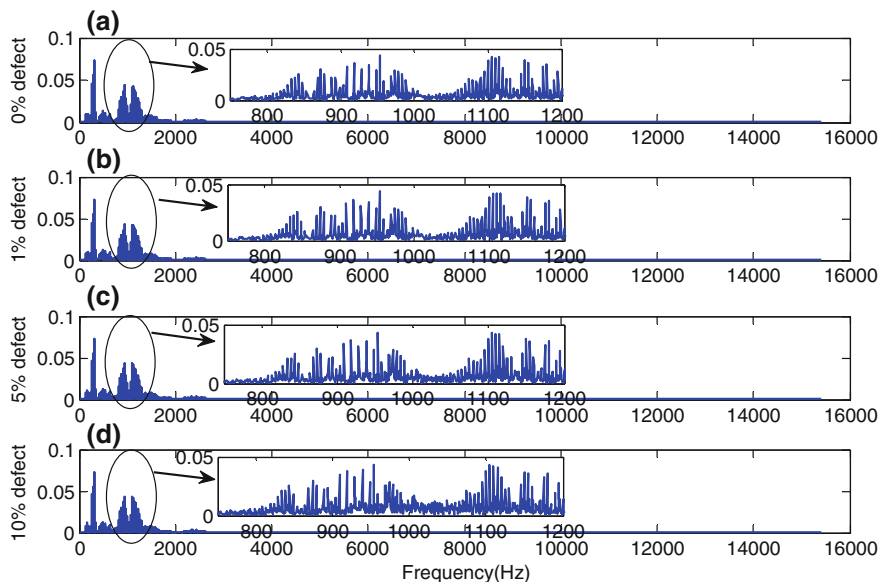


Fig. 3 Spectrum of the signals for 50 % of load a healthy gear, b–d faulty gear

From the presented zoomed spectrum (Fig. 3a) for healthy case, we can observe also presence of sidebands which may cause confusion with the defected case when diagnosing the transmission.

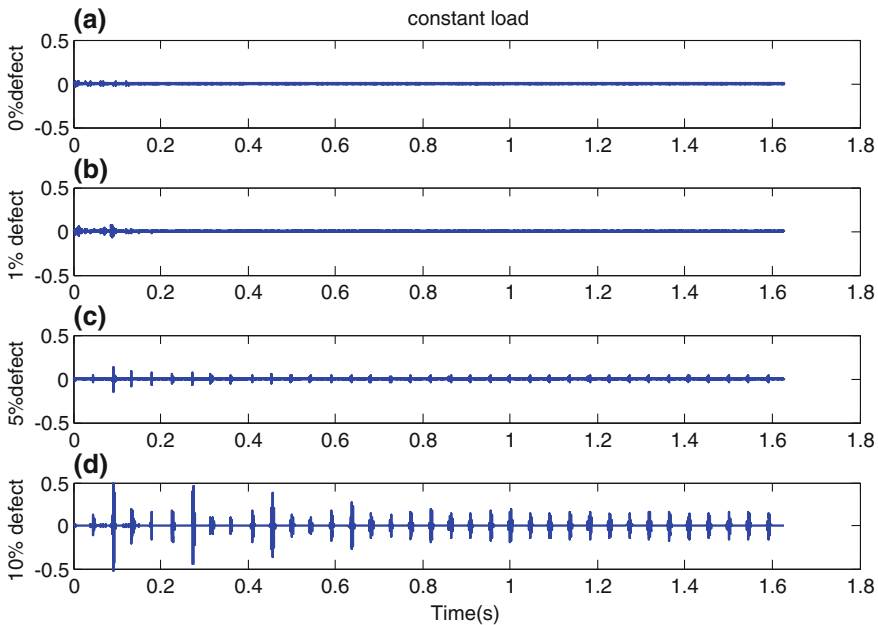
In order to overcome this difficulty, we propose to use EEMD to analyze such signals. The objective is to look at the efficiency of this method and its limits especially in the presence of an excessive load variation.

Figure 4 presents the first IMF of four signals in the case of a constant load. From this figure we can clearly observe for the case of faulty gear the position of impacts starting from 5 % of severity.

Figure 5 presents the first IMF of four studied signals in the case of a load fluctuation of 10 %. From this figure we can observe the impulses due to the defect if the severity is greater than 5 %.

Figure 6 presents the first IMF of four studied signals in the case of a load fluctuation is 50 %. From this figure we can observe the position of the variation of the load which can hide the impulses due to the defect and precisely at early stage (1 and 5 % defect). It is possible to observe the impulses due to defect if the severity is greater than 5 %. The period between two impulses is 0.045 s which is equivalent to the frequency defect.

The spectrogram of this IMF gives an idea on the variation of the load (Figs. 7 and 8) and gives also information of the position of the maximum load. It shows clearly the position of the impulses due to the fault. The periodicity of the defect can be clearly observed for 5 % of defect better than 1 % of defect.



**Fig. 4** IMF1 of signal regular load **a** healthy gear, **b-d** faulty gear

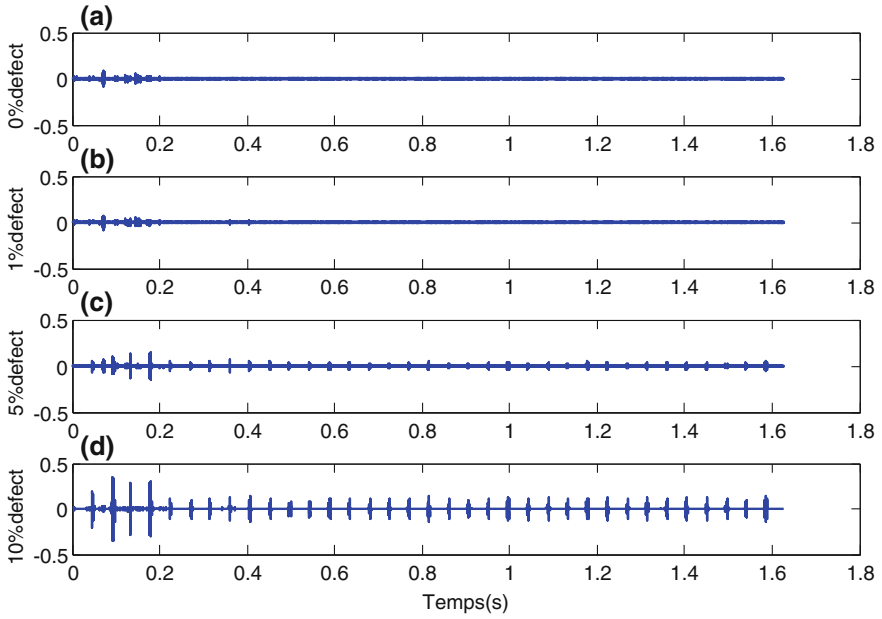


Fig. 5 IMF1 of signal for 10 % of load a healthy gear, b–d faulty gear

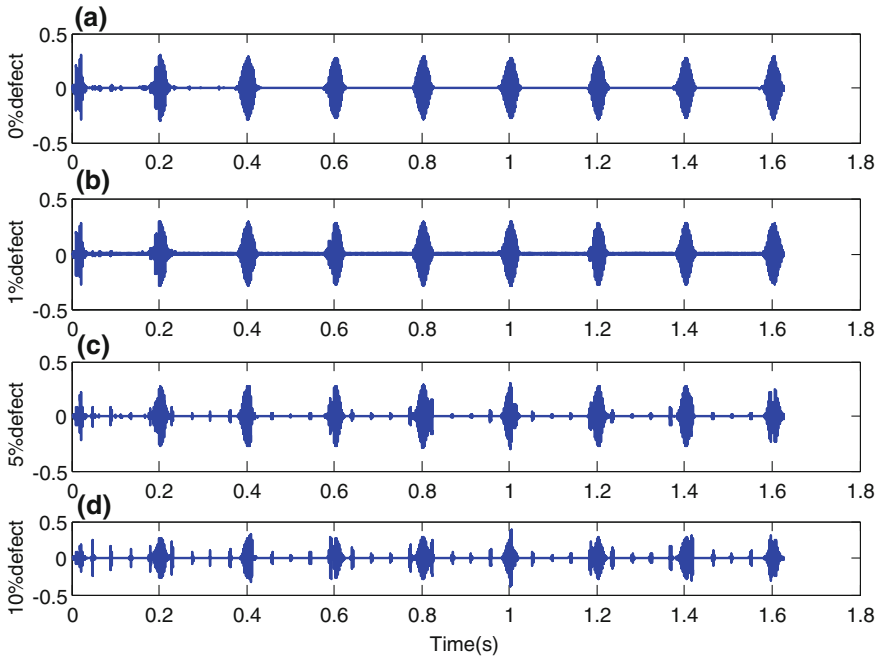
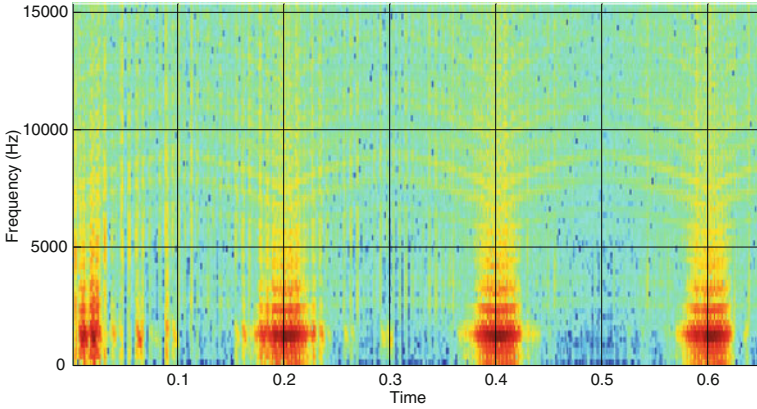
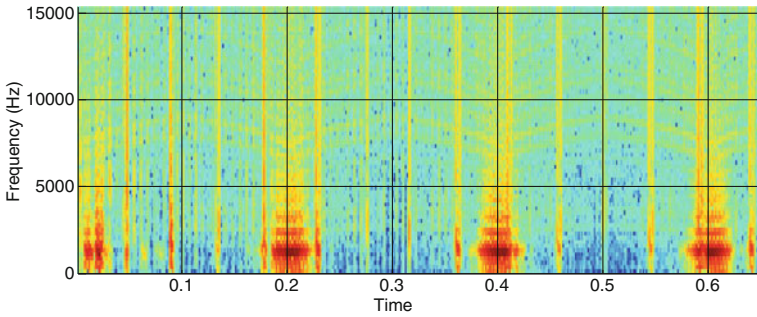


Fig. 6 IMF1 of signal for 50 % of load a healthy gear, b–d faulty gear



**Fig. 7** Spectrogram of the first IMF for 1 % of defect and 50 % of load



**Fig. 8** Spectrogram of the first IMF for 5 % of defect and 50 % of load

## 4 Conclusion

In this study we have used the EEMD method to analyze non-stationary signals that give information about the variable conditions such as variable speed and load. The EEMD method achieves good modes separation. To detect the fault masked by simultaneous variation of load and presence of defect, EEMD showed successful separation of the different modes that correspond to the variation of load and the effect of fault. We have also used the spectrogram to detect the period of the impulses due to the fault, and we have observed that the huge load (50 %) cover information if the defect is less than 5 % in severity.

## References

- Bartelmus W, Zimroz R (2009) Vibration condition monitoring of planetary gearbox under varying external load. *Mech Syst Signal Process* 23(1):246–257
- Capdessus C, Sidahmed M (1992) Analyse des vibrations d'un engrenage cepstre, corrélation, spectre, traitement du signal, vol 8, no 5, pp 365–371
- Chaari F, Abbas MS, Rueda FV, del Rincon AF, Haddar M (2013) Analysis of planetary gear transmission in non-stationary operations. *Front Mech Eng* 8(1):88–94
- Cohen L (1989) Time–frequency distributions a review. *Proc IEEE* 77(7):941–981
- Forrester BD (1989) Use of Wigner Ville distribution in helicopter transmission fault detection. In *Proceedings of the Australian, symposium on signal processing and applications, ASSPA89, Adelaide, Australia, 17–19 April 1989*, pp 77–82
- Huang NE, Shen Z, Long SR (1998) The empirical mode decomposition and the Hilbert spectrum for nonlinear and non-stationary time series analysis. *Proc R Soc Lond Ser* 454:903–995
- Huang NE, Wu ML, Long SR (2003) A confidence limit for the empirical mode decomposition and Hilbert spectral analysis. *Proc R Soc Lond* 459:2317–2345
- Liu B, Riemenschneider S, Xub Y (2005) Gearbox fault diagnosis using empirical mode decomposition and Hilbert spectrum. *Mech Syst Signal Process* 17(9):1–17
- Mahgoun H, Bekka R-E, Felkaoui A (2010) Application of ensemble empirical mode Decomposition (EEMD) method for detection of localized faults in gear, *IMPACT2010, Djerba 22–24 March 2010*
- Mahgoun H, Bekka RE, Felkaoui A (2012) Gearbox fault diagnosis using ensemble empirical mode decomposition (EEMD) and residual signal. *Mech Ind* 13(01):33–44
- Mahgoun H, Chaari F, Felkaoui A (2016) Detection of gear faults in variable rotating speed using variational mode decomposition (VMD). *Mech Ind* 17:207
- Mallat SG (1998) *A wavelet tour of signal processing*. Academic, San Diego
- McFadden PD (1986) Detecting fatigue cracks in gears by amplitude and phase demodulation of the meshing vibration. *Trans ASME J Vib Acoust Stress Reabil design* 108:165–170
- Rilling G, Flandrin P (2008) One or two frequencies? The empirical mode decomposition answers. *IEEE Trans Signal Process* 56(1):85–95
- Staszewski WJ (1997) Local tooth fault detection in gear boxes using a moving window procedure. *Mech Syst Signal Process* 11(3):331–350
- Wang WJ, Mcfadden PD (1997) Application of orthogonal wavelet to early gear damage detection. *Mech Syst Signal Process* 9(5):497–507
- Wu TY, Chung YL (2009) Misalignment diagnosis of rotating machinery through vibration analysis via hybrid EEMD and EMD approach. *Smart Mater Struct* 18(9)
- Wu Z, Huang NE (2009) Ensemble empirical mode decomposition: a noise-assisted data analysis method. *Adv Adap Data Anal* 1(1):1–41 (world scientific publishing company)
- Wu TY, Chen JC, Wang CC (2012) Characterization of gear faults in variable rotating speed using Hilbert-Huang transform and instantaneous dimensionless frequency normalization. *Mech Syst Signal Process* 30(1):103–122
- Yang W, Court R, Tavner PJ, Crabtree CJ (2011) Bivariate empirical mode decomposition and its contribution to wind turbine condition monitoring. *J Sound Vib* 330(15):3766–3782

# Design of Shunted Piezoelectric Patches Using Topology Optimization for Noise and Vibration Attenuation

Walid Larbi, Jean-François Deü and Luciano Pereira da Silva

**Abstract** Passive structural vibration reduction and noise attenuation by means of shunted piezoelectric patches is addressed in this paper. In this technology, an elastic structure is equipped piezoelectric patches that are connected to passive shunt circuits. The piezoelectric patches convert a fraction of the mechanical energy of the vibrating structure into electrical energy, which is then dissipated via the shunt circuits. The optimization in terms of damping efficiency, of the full electromechanical system composed by a host elastic structure with bonded piezoelectric patches connected to shunt circuits, is under study in this work. The concept of topology optimization, based on the Solid Isotropic Material with Penalization method (SIMP), is employed to optimize the geometry of piezoelectric patches as well as their placement on the host elastic structure. The proposed optimization procedure consists of distributing the piezoelectric material in such a way as to maximize the modal electro-mechanical coupling factor (MEMCF) of the mechanical vibration mode to which the shunt is tuned.

**Keywords** Piezoelectric patches · Shunt · Topology optimization · Vibration reduction

## 1 Introduction

Passive structural vibration reduction and noise attenuation by means of shunted piezoelectric patches is addressed in this paper. In this technology, an elastic structure is equipped with one or several piezoelectric patches that are connected to passive shunt circuits. The piezoelectric patches convert a fraction of the mechanical energy of the vibrating structure into electrical energy, which is then dissipated via the shunt circuits. The optimization in terms of damping efficiency, of

---

W. Larbi (✉) · J.-F. Deü · L. Pereira da Silva  
Structural Mechanics and Coupled System Laboratory, Conservatoire National des Arts et Métiers, Paris, France  
e-mail: walid.larbi@cnam.fr



the full electromechanical system composed by a host elastic structure with bonded piezoelectric patches connected to a shunt circuit, is under study in this work. An original finite element formulation (Thomas et al. 2009), adapted to any elastic structures with surface-mounted thin piezoelectric patches, is proposed to solve the electromechanical problem. Then, the so-called modal electromechanical coupling factors (MEMCF) can be defined, each one being associated to one piezoelectric patch and one eigenmode of the structure (Trindade and Benjeddou 2009; Thomas et al. 2012). The optimization of the electromechanical system relies on the fact that the tuning as well as the performances of the shunt connected to the piezoelectric patches depends only on two parameters: the MEMCF and the structural damping. Since the latter is in most practical cases a problem data, the only parameter that has to be considered is the MEMCF. Optimization of the geometry and placement of piezoelectric patches on a host elastic structure has received large attention in the last decades. A recent literature review (Belloli and Ermanni 2007) shows that active control applications are mainly considered. A few studies address the application of piezoelectric shunt optimization. Moreover, most of them keep fixed shape piezoelectric patches (rectangular, for example) and only their size or positions are optimized. This imposes a constrained optimization problem which limits the optimality of the solution. The concept of topology optimization (Bendsøe and Sigmund 2003), based on the Solid Isotropic Material with Penalization method (SIMP method), is employed in the present work in order to overcome this limitation and to find an optimal distribution of the piezoelectric material over a host elastic structure to provide damping efficiency for a resonant shunted system. An optimization algorithm, based on the work of Silva and Kikuchi (1999), is developed with the MEMCF as objective function. Numerical examples are proposed to validate and analyze the optimization strategy.

## 2 Electromechanical Model

### 2.1 *Finite Element Formulation*

We consider the vibration of an elastic structure with  $P$  piezoelectric patches. The elastic structure is subjected to a prescribed displacement  $u_i^d$  on a part and to a prescribed surface force density  $t_i^d$  on the complementary part of its external boundary. The piezoelectric patches have its upper and lower surfaces covered with a very thin electrode and they are polarized in their transverse direction (i.e. the direction normal to the electrodes). By using a set of practical assumptions, detailed in Thomas et al. (2009), we can obtain an original variational formulation and then an efficient finite element formulation of the above electromechanical spectral problem:

$$-\omega^2 \begin{bmatrix} \mathbf{M}_{uu} & \mathbf{0} \\ \mathbf{0} & \mathbf{0} \end{bmatrix} \begin{Bmatrix} \mathbf{U} \\ \mathbf{V} \end{Bmatrix} + \begin{bmatrix} \mathbf{K}_{uu} & \mathbf{K}_{uv} \\ -\mathbf{K}_{uv}^T & \mathbf{K}_{vv} \end{bmatrix} \begin{Bmatrix} \mathbf{U} \\ \mathbf{V} \end{Bmatrix} = \begin{Bmatrix} \mathbf{F} \\ \mathbf{Q} \end{Bmatrix} \quad (1)$$

where  $\{\mathbf{U}\}$  is the column vector of nodal values of mechanical displacement, of length  $N$  ( $N$  is the number of mechanical degrees of freedom),  $[\mathbf{M}_{uu}]$  and  $[\mathbf{K}_{uu}]$  are the mass and stiffness matrices of the system (elastic structure with piezoelectric patches), of size  $N \times N$ , and  $\{\mathbf{F}\}$  is the column vector of mechanical force, of length  $N$ . Moreover,  $\{\mathbf{Q}\} = [Q^{(1)} \dots Q^{(P)}]^T$  and  $\{\mathbf{V}\} = [V^{(1)} \dots V^{(P)}]^T$  are the column vectors of electric charges (contained in the upper electrode) and potential differences in each patch,  $[\mathbf{K}_{uv}]$  is the electromechanical coupling matrix, of size  $N \times P$  and  $[\mathbf{K}_{vv}] = \text{diag}([C^{(1)} \dots C^{(P)}])$  is diagonal matrix filled with the  $P$  capacitances of the piezoelectric patches where  $C^{(p)} = \epsilon_{33} S^{(p)} / h^{(p)}$  with  $\epsilon_{33} = \epsilon_{ik} n_i n_k$  being the piezoelectric permittivity in the direction normal to the electrodes and  $S^{(p)}$  is the area of the patch electrodes surfaces.

The above discretized formulation equation is adapted to any elastic structures with surface mounted thin piezoelectric patches. Its originality is that the system electrical state is fully described by only a couple of variables per piezoelectric patch, namely (i) the electric charge contained in the electrodes and (ii) the voltage between the electrodes. One of the advantages of using the global charge/voltage variables is that they are intrinsically adapted to include any external electrical circuit into the problem and to simulate the effect of shunt damping techniques. The additional relation for the case of a resonant shunt composed of a resistor  $R_e$  and an inductor  $L_e$  in series, connected to the  $p$ th patch, writes  $V^{(p)} + \omega^2 L_e Q^{(p)} - j\omega R_e Q^{(p)} = 0$ . By introducing this relation in Eq. (1) and considering a mechanical viscous damping in the system, we finally obtain the general finite element formulation of the electromechanical spectral problem when the piezoelectric patches are shunted:

$$-\omega^2 \begin{bmatrix} \mathbf{M}_{uu} & \mathbf{0} \\ \mathbf{0} & \mathbf{L}_e \end{bmatrix} \begin{Bmatrix} \mathbf{U} \\ \mathbf{Q} \end{Bmatrix} + j\omega \begin{bmatrix} \mathbf{C}_{uu} & \mathbf{0} \\ \mathbf{0} & \mathbf{R}_e \end{bmatrix} \begin{Bmatrix} \mathbf{U} \\ \mathbf{Q} \end{Bmatrix} + \begin{bmatrix} \mathbf{K}_{uu} + \mathbf{K}_{uv} \mathbf{K}_{vv}^{-1} \mathbf{K}_{uv}^T & \mathbf{K}_{uv} \mathbf{K}_{vv}^{-1} \\ \mathbf{K}_{vv}^{-1} \mathbf{K}_{uv}^T & \mathbf{K}_{vv}^{-1} \end{bmatrix} \begin{Bmatrix} \mathbf{U} \\ \mathbf{Q} \end{Bmatrix} = \begin{Bmatrix} \mathbf{F} \\ \mathbf{0} \end{Bmatrix} \quad (2)$$

where  $[\mathbf{C}_{uu}]$  is the mechanical damping matrix,  $[\mathbf{R}_e]$  and  $[\mathbf{L}_e]$  are the diagonal matrices filled with the electrical resistances  $R_e$  and the electrical inductances  $L_e$  of the shunt circuits and  $j = \sqrt{-1}$ . Note that since  $[\mathbf{K}_{vv}]$  is diagonal the evaluation of  $[\mathbf{K}_{vv}^{-1}]$  is straightforward.

Moreover, depending on whether the patches are short-circuited ( $\{\mathbf{V}\} = \{\mathbf{0}\}$ ) or in open-circuit ( $\{\mathbf{Q}\} = \{\mathbf{0}\}$ ), the homogeneous spectral problem associated to the discretized formulation of Eq. (2) takes the following forms:

$$([\mathbf{K}_{uu}] - \omega^2[\mathbf{M}_{uu}])\{\mathbf{U}\} = \{\mathbf{0}\} \quad \text{short-circuit (SC),} \quad (3)$$

$$([\mathbf{K}_{uu} + \mathbf{K}_{uv}\mathbf{K}_{vv}^{-1}\mathbf{K}_{uv}^T] - \omega^2[\mathbf{M}_{uu}])\{\mathbf{U}\} = \{\mathbf{0}\} \quad \text{open-circuit (OC).} \quad (4)$$

## 2.2 Reduced-Order Model and Coupling Factors

The shunted electromechanical problem given by Eq. (2) can be reduced by projecting the mechanical displacement into the first  $\bar{N}$  short-circuit eigenmodes  $\{\Phi_i\}$ , such as  $\{\mathbf{U}(\omega)\} = \sum_{i=1}^{\bar{N}} \{\Phi_i\} \varphi_i(\omega)$ ,  $\bar{N} \ll N$ . As a result, the reduced problem consists in solving the following system:

$$\begin{cases} (-\omega^2 + 2j\omega\xi_i\omega_i + \omega_i^2)\varphi_i + \sum_{p=1}^P \sum_{n=1}^{\bar{N}} \frac{\chi_i^{(p)}\chi_n^{(p)}}{C^{(p)}} \varphi_n + \sum_{p=1}^P \frac{\chi_i^{(p)}}{C^{(p)}} Q^{(p)} = F_i \quad \forall i \\ (-\omega^2 L_e^{(p)} + j\omega R_e^{(p)} + \frac{1}{C^{(p)}}) Q^{(p)} + \sum_{n=1}^{\bar{N}} \frac{\chi_n^{(p)}}{C^{(p)}} \varphi_n = 0 \quad \forall p \end{cases} \quad (5)$$

where  $F_i = \{\Phi_i\}^T \{\mathbf{F}\}$ ,  $\omega_i$  and  $\xi_i$  are the modal force, SC natural frequency and modal damping coefficient of the  $i$ th mode, and  $\chi_i^{(p)}$  is the modal coupling coefficient associated to the  $i$ th mode and the  $p$ th patch, which is defined by  $(\chi_i^{(1)} \chi_i^{(2)} \dots \chi_i^{(P)}) = \{\Phi_i\}^T [\mathbf{K}_{uv}]$ ,  $\forall i \in \{1 \dots \bar{N}\}$ . These modal coupling coefficients are related to the modal electromechanical coupling factors (MEMCF), denoted  $k_i^{(p)}$ , which characterize, for each mode  $i$ , energy exchange between the mechanical structure and the piezoelectric patch  $p$  (Thomas et al. 2009):

$$k_i^{(p)} = \frac{\chi_i^{(p)}}{\sqrt{C^{(p)}}\omega_i} \quad (6)$$

Those factors ( $k_i^{(p)}$ ) are found very close to the classical effective electromechanical coupling factor (EEMCF) defined in IEEE (Thomas et al. 2009). Moreover, the optimal electric parameters are classically obtained as closed-formed expressions which depend only on (i) the natural frequency in short circuit of the considered vibration mode as well as its modal coupling factor and (ii) the equivalent electrical blocked capacity of the patches (Thomas et al. 2009).

### 3 Topology Optimization Based on SIMP Method

#### 3.1 Piezoelectric Material Model

The SIMP method combines the finite element method with an optimization algorithm to find the optimal material distribution inside a given domain (Bendsøe and Sigmund 2003). This method introduces the so-called pseudo-density  $0 < x_{\min} \leq x \leq 1$  for each of the  $\tilde{N}$  finite elements of the optimization domain, yielding the optimization design vector  $\{\mathbf{x}\} = [x_1 x_2 \cdots x_{\tilde{N}}]^T$ . For  $x = 1$  the material is present, while for  $x = x_{\min}$  the material is absent (the value  $x = 0$  is usually excluded in order to avoid the stiffness and mass matrix become singular). Although  $x$  has a physical interpretation only for these two extremes values, its continuous change between zero and unity during the optimization avoids numerical instabilities caused by multiple local minima of the discrete design space (Bendsøe and Sigmund 2003; Silva and Kikuchi 1999).

By using the standard SIMP interpolation form  $x^p$ , the local tensor properties and mass density in each element  $n$  can be expressed as:

$$c_{ijkl}^{(n)} = x_n^{p_c} c_{ijkl}^0, \quad e_{ijk}^{(n)} = x_n^{p_e} e_{ijk}^0, \quad \epsilon_{ijk}^{(n)} = x_n^{p_\epsilon} \epsilon_{ijk}^0, \quad \rho^{(n)} = x_n^{p_\rho} \rho^0 \quad (7)$$

where  $c_{ijkl}^0$ ,  $e_{ijk}^0$ ,  $\epsilon_{ijk}^0$  and  $\rho^0$  are the stiffness tensor, piezoelectric tensor, dielectric tensor and mass density of the piezoelectric material. To prevent intermediate values for  $x$ , the penalization factors  $p_c$ ,  $p_e$ ,  $p_\epsilon$  and  $p_\rho$  are employed in Eq. (7), which penalize intermediate densities and pushes  $x$  to the limiting values zero and unity. But one also has to restrict the total amount of design material  $\int \{\mathbf{X}\} d\Omega$  and, a complexity constraint, such as a filter, should be considered to avoid potential mesh dependency and checkerboard problems (Bendsøe and Sigmund 2003). For the piezoelectric shunt problem, it is shown in Pereira da Silva et al. (2015) that the combination of penalty exponents  $p_\rho = p_\epsilon = p_c = 1$  and  $p_e = 2$  yields excellent results with a very small grayness. This combination is therefore considered in the present work.

Considering the new material properties of Eq. (7), the local finite element stiffness and mass matrices of the piezoelectric patches become:

$$\begin{aligned} \left[ \tilde{\mathbf{K}}_{uu}^e \right]_n &= x_n^{p_c} \left[ \mathbf{K}_{uu}^e \right]_n, & \left[ \tilde{\mathbf{K}}_{uv}^e \right]_n &= x_n^{p_e} \left[ \mathbf{K}_{uv}^e \right]_n, \\ \left[ \tilde{\mathbf{K}}_{vv}^e \right]_n &= x_n^{p_\epsilon} \left[ \mathbf{K}_{vv}^e \right]_n, & \left[ \tilde{\mathbf{M}}_{uu}^e \right]_n &= x_n^{p_\rho} \left[ \mathbf{M}_{uu}^e \right]_n \end{aligned} \quad (8)$$

The finite element formulation of Eq. (1) is now written as:

$$-\omega^2 \begin{bmatrix} \mathbf{M}_{uu}^s + \widetilde{\mathbf{M}}_{uu} & \mathbf{0} \\ \mathbf{0} & \mathbf{0} \end{bmatrix} \begin{Bmatrix} \mathbf{U} \\ \mathbf{V} \end{Bmatrix} + \begin{bmatrix} \mathbf{K}_{uu}^s + \widetilde{\mathbf{K}}_{uu} & \widetilde{\mathbf{K}}_{uv} \\ -\widetilde{\mathbf{K}}_{uv}^T & \widetilde{\mathbf{K}}_{vv} \end{bmatrix} \begin{Bmatrix} \mathbf{U} \\ \mathbf{V} \end{Bmatrix} = \begin{Bmatrix} \mathbf{F} \\ \mathbf{Q} \end{Bmatrix} \quad (9)$$

where  $[\mathbf{K}_{uu}^s]$  and  $[\mathbf{M}_{uu}^s]$  are the global stiffness and masse matrices of the host elastic structure and,  $[\widetilde{\mathbf{K}}_{uu}]$  and  $[\widetilde{\mathbf{M}}_{uu}]$  are the modified global stiffness and masse matrices of the patches.

### 3.2 Optimization Problem

To improve the damping level for passive or semi-passive shunted piezoelectric devices, a key issue is the optimization of the whole system, in terms of location and geometry of the piezoelectric patches and electric circuit components choice. It was shown in Thomas et al. (2009, 2012) that the only parameters to maximize are the modal coupling factors (MEMCF). Since the optimal value of the electric circuit parameters are known as functions of the MEMCF and the system structural characteristics, they can be evaluated in a second step. Thus, the mechanical optimization consists in maximizing the MEMCF by optimizing the patches positions and geometries, i.e. finding the best design. Considering all these features, the optimization problem can be described as:

$$\text{maximize : } \mathcal{H}(\mathbf{x}) = \left( k_i^{(p)} \right)_{\{\mathbf{x}\}}^2, \quad \text{where } \{\mathbf{x}\} = [x_1 x_2 \dots x_N]^T$$

$$\text{subjected to: } ([\mathbf{K}_{uu}(\mathbf{x})] - \omega_i^2 [\mathbf{M}_{uu}(\mathbf{x})]) \{\Phi_i\} = \{\mathbf{0}\} \text{ (SC modal problem)}$$

$$0 < x_{\min} \leq x_n \leq 1$$

$$\widetilde{\Omega}(x_n) = \int \{\mathbf{x}\} d\Omega \leq \widetilde{\Omega}_{\max}$$

where  $\widetilde{\Omega}$  is the volume of the design domain and  $\widetilde{\Omega}_{\max}$  is the upper bounds restricting the material to be used in the piezoelectric layer.

### 3.3 Sensitivity Analysis

The present work uses sequential linear programming (SLP) to solve the optimization problem as done in Silva and Kikuchi (1999). It consists of sequential

solution of approximate linear subproblems that can be defined by writing a Taylor series expansion for the objective function around the current design point  $x_n$  in each iteration step. This requires knowledge of the sensitivities (gradients) of the objective function  $\mathcal{H}$  in relation to the design variables  $x_n$  (see Silva and Kikuchi 1999; Pereira da Silva et al. 2015 for more details).

### 4 Numerical Implementation

The algorithm employed in this study is shown in Fig. 1. In order to construct the electromechanical FE models and solve the problems, the finite element code Nastran is used in association with Matlab software (Pereira da Silva et al. 2015).

In the optimization procedure, suitable move limits are defined for the design variables between consecutive interactions. Thus, after each interaction, a new set of design variables  $x_n$  is obtained and updated in design domain. The procedure stops when the objective function converges. As a result, an optimum distribution of  $x_n$  is obtained. This distribution may contain intermediate values (grey zone) that represent no real material. These intermediate values need to be interpreted as zero (void) or one (real material).

To assess the quality of the final design, the amount of intermediate material (“grayness”) can be quantified by the measure (Bendsøe and Sigmund 2003):

$$M_{nd} = \frac{\sum_{n=1}^{\tilde{N}} 4x_n(1 - x_n)}{\tilde{N}} \times 100 \% \tag{10}$$

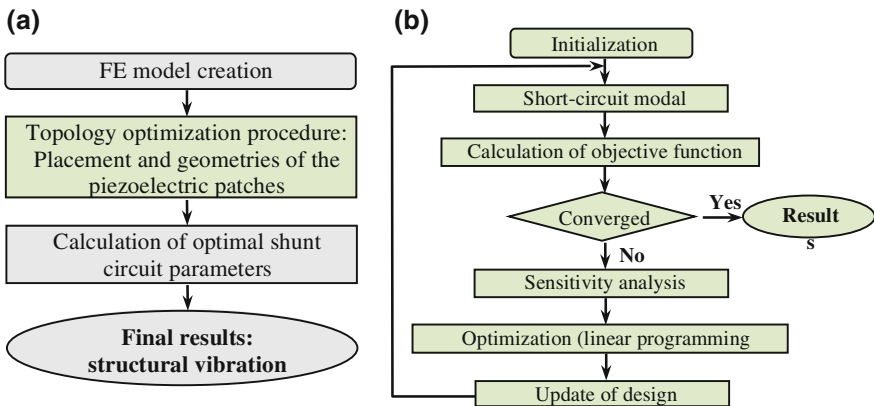


Fig. 1 a Main algorithm. b Optimization algorithm

A fully discrete design (all elements densities  $x_n = 1$ ) is represented by  $M_{nd} = 0\%$ , while a design totally grey (all elements densities  $x_n = 0.5$ ) yields  $M_{nd} = 100\%$ .

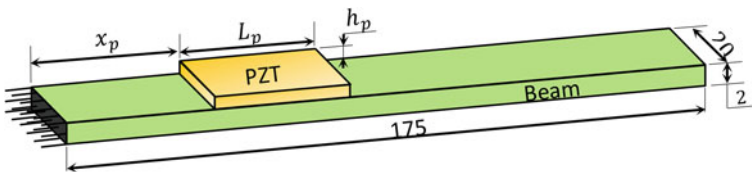
## 5 Examples

In the following, the proposed topology optimization approach is applied to find the better placement and geometry of piezoelectric patches in piezoelectric shunt problems. Moreover, linear quadrilateral shell elements (QUAD 4) and the first-order shear deformation laminate theory are considered to model the structures with surface mounted piezoelectric patches.

### 5.1 A Cantilever Beam with One Piezoelectric Patch



In this first example, the proposed optimization procedure is validated by comparison to an analytical solution given in Thomas et al. (2012). The system under study consists of a cantilever beam made of aluminum ( $\rho = 2700 \text{ kg/m}^3$ ,  $\gamma = 0.33$  and  $E = 74 \text{ GPa}$ ) and with one piezoelectric device, as sketched in Fig. 2. The piezoelectric device which is made of PIC-151 (see Thomas et al. 2009, 2012; Pereira da Silva et al. 2015 for the properties) is assumed to be perfectly bounded to the beam and has the same width.

For this system, Thomas et al. (2012) have been used an analytical solution to the optimization of the position ( $x_p$ ), thickness ( $h_p$ ) and length ( $L_p$ ) of the piezoelectric patch with a rectangular form. In the present work, the beam and piezoelectric layer are modeled with 70 QUAD 4 elements, as shown in Table 1. With only one element through the width and for a fixed thickness of the piezoelectric layer, the optimization problem consists to find the optimal length of a rectangular patch ( $L_p$ ) and its optimal position defined by its  $x$ -coordinate ( $x_p$ ). Moreover, the optimization procedure has been started with an initial value of  $x_n = 0.5$  for all elements and no volume restriction ( $\tilde{\Omega}_{\max}$ ) was considered.



**Fig. 2** A cantilever beam with one piezoelectric device (dimensions in mm)

**Table 1** Resulting topologies for the first bending mode

<b>First bending beam mode</b>	
Analytical solution	
	
Optimization procedure	
	
$M_{nd} = 2.69 \%$	

As shown in Table 1, the proposed optimization approach yields excellent results compared to the analytical solution with a very low grayness so that little postprocessing.

To conclude, this first example validates our optimization approach and shows its efficiency compared to analytical solution.

### 5.2 Sound Power Radiated from a Thin Plate

In this example, a free-clamped rectangular plate with two rectangular reinforcements perfectly bonded on its underside surface is considered, as shown in Fig. 3a. The plate and the reinforcements are made of 2 mm thick aluminum plates ( $E = 70 \text{ GPa}$ ,  $\gamma = 0.33$ ,  $\rho = 2700 \text{ kg/m}^3$ ). We refer the reader to Pereira da Silva et al. (2015) for a complete description of the problem.

In order to reduce the sound radiation of modes 1, 6 and 14 (most radiating modes as shown in Fig. 3b) and get a multi-modal damping of the structure, a shunt system with three piezoelectric devices, made of PIC151 (see Thomas et al. 2009,

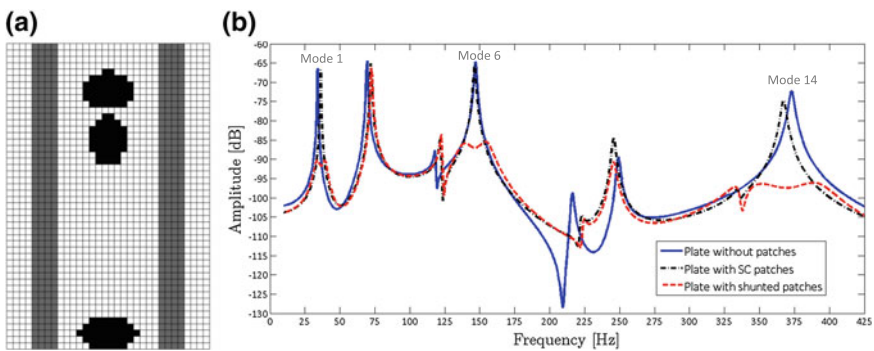


**Fig. 3** **a** Mesh and optimal configuration for the piezoelectric shunt system. **b** Plate FRF—attenuation of the sound radiation of modes 1, 6 and 14



2012; Pereira da Silva et al. 2015 for the properties) and with 0.5 mm of thickness, is used.

Three zones on the top surface of the plate were delimited to attach and design each piezoelectric device (Pereira da Silva et al. 2015). In addition, an upper bound  $\tilde{\Omega}_{\max} = 3 \text{ cm}^3$  on the volume is employed to limit the material used in each device. Thus, the value of  $x_n = 0.2$  for all elements in the three design domains is used as initial guess (all constraints satisfied).

The FRF are computed with a modal reduction approach using the first 40 SC eigenmodes. Mechanical damping was introduced through a modal damping coefficient  $\xi = 0.005$  for all eigenmodes in the selected reduced modal basis.

Figure 3a shows the best design obtained with the optimization procedure where the resulting MEMCFs are  $k_1^{(1)} = 19.9 \%$ ,  $k_6^{(2)} = 13.8 \%$  and  $k_{14}^{(3)} = 16.2 \%$ . Moreover, Fig. 3b presents the FRF of the system with and without shunt control. This figure illustrates again the performance of the shunt technique in vibration and sound radiation reduction of the select modes. These results also show that the optimization of the patches geometry causes better performance in terms of attenuation compared to arbitrary geometries and demonstrates the effectiveness of the proposed approach.

## 6 Conclusions

The present contribution was dedicated to the study of passive vibration damping by using piezoelectric patches and resonant shunt circuits. The concept of topology optimization was successfully applied in order to optimize the placement and geometry of piezoelectric patches. An optimization algorithm was employed and validated. Numerical examples demonstrate the effectiveness of the proposed approach for the design of piezoelectric devices in shunt damping problems. No checkerboard patterns were observed in the examples treated in the present work. Moreover, the topology optimization procedure is applied here to resonant shunts but it remains valid for resistive shunts or switch techniques since the mechanical and electrical optimizations are uncoupled.

## References

- Belloli A, Ermanni P (2007) Optimum placement of piezoelectric ceramic modules for vibration suppression of highly constrained structures. *Smart Mater Struct* 16:1662–1671
- Bendsøe MP, Sigmund O (2003) *Topology optimization—theory, methods and applications*. Springer, New York
- Pereira da Silva L, Larbi W, Deü J-F (2015) Topology optimization of shunted piezoelectric elements for structural vibration reduction. *J Intell Mater Syst Struct* 26(10):1219–1235

- Silva ECN, Kikuchi N (1999) Design of piezoelectric transducers using topology optimization. *Smart Mater Struct* 8:350–364
- Thomas O, Deü J-F, Ducarne J (2009) Vibrations of an elastic structure with shunted piezoelectric patches: efficient finite elements formulation and electromechanical couplings coefficients. *Int J Numer Meth Eng* 80:235–268
- Thomas O, Ducarne J, Deü J-F (2012) Placement and dimension optimization of shunted piezoelectric patches for vibration reduction. *J Sound Vib* 331:3286–3303
- Trindade MA, Benjeddou A (2009) Effective electromechanical coupling coefficients of piezoelectric adaptive structures: critical evaluation and optimization. *Mech Adv Mater Struct* 16:210–223

# Prediction of Sound Radiation from Submerged Cylindrical Shell Structure with an Interpolation Method for the Measured Surface Velocity

Yilin Zhang, Haijun Wu and Weikang Jiang

**Abstract** An interpolation method is proposed for the reestablishing of the surface velocity of cylindrical shell structures. The surface velocity is expressed by the Fourier series in the circumferential direction and the piecewise Lagrange functions in the axial direction. Numerical examples demonstrate that the interpolation method can get smooth continuous velocity distribution on the surface of the cylindrical shell structures, which is satisfactory for predicting the acoustic radiation based on few measured surface velocities. The accuracy and applicability of the interpolation method for the prediction of sound radiation are both numerically and experimentally validated.

**Keywords** Interpolation method · Sound radiation · Submerged cylindrical shell

## 1 Introduction

Cylinder structures are widely used in submerged engineering applications. Characteristics of the sound radiation of submerged vehicles can be simplified into the analyzing of single or double cylindrical shell structures. The analysis and prediction methods of the sound radiation of the cylindrical shell structures can be divided into two kinds: the numerical methods and the experimental methods (Wu et al. 2000; Guz and Kubenko 2002; Chen et al. 2014; Liu et al. 2014).

Due to the limitation of experiment equipment, usually the number of the measuring points cannot be very large in the on site experiment. Thus, interpolation

---

Y. Zhang · H. Wu · W. Jiang (✉)  
Institute of Vibration, Shock & Noise, Shanghai Jiao Tong University,  
Shanghai 200240, China  
e-mail: wkjiang@sjtu.edu.cn

Y. Zhang  
e-mail: drizztzhang@sjtu.edu.cn

H. Wu  
e-mail: haijun.wu@sjtu.edu.cn

method is usually used to prediction the vibration response on unmeasured points (Yang and Parvin 2003). Firstly, the model is discretized base on the position of measuring points, then the responses on other positions are obtained based on linear or high-order interpolation method within discrete element. This kind of interpolation only considers the velocity conditions of adjacent elements. The response on interpolation points cannot be accurately obtained. In this paper, based on the characteristic of the axial symmetry cylindrical shell, a semi-analytical global interpolation method is provided to obtained the layout of the velocity on the surface of the cylindrical shell.

For the analytical expression of the surface velocity of the cylindrical shell, it has been studied for years. It can be expanded by Fourier series or polynomial functions. But for complicate structures like submarine, the accurate expressions cannot be obtained analytically. Thus, the experimental method, as a supplement, is introduced here. For such structure, after choosing certain form of series of its surface velocity expression, according to the experimental results, the coefficient of each series can be identified, then the velocity at other positions can be got by interpolating.

In this paper, an interpolation method is provided to get the continual velocity layout on the surface of the structure from measured surface velocity. Base on the obtained continual velocity distribution, the sound radiation of the structure can be fast and precisely obtained through boundary element method. This interpolation method is also validated experimentally.

## 2 Interpolation Method for Surface Velocity on Structure

For an axial symmetric cylinder model, only half of its surface needs to be calculated because of its symmetry. The velocity function is expanded using Fourier cosine series in the circumferential direction and Lagrange polynomial  $g_m(x)$  along the axial direction. The expression of the surface velocity can be written as:

$$v(\theta, x) = \sum_{m=1}^M \sum_{n=0}^N a_n^m \cos(n\theta) g_m(x) \quad (1)$$

where  $0 \leq \theta \leq 2\pi$ ,  $0 \leq x \leq L$ ,  $L$  is the length of the cylindrical model;  $N$  is the number of the points used in the Fourier interpolation;  $M$  is the number of the points used in the Lagrange interpolation; the Lagrange interpolation is written as:

$$g_m(x) = \frac{(x - x_1) \cdots (x - x_{m-1})(x - x_{m+1}) \cdots (x - x_M)}{(x_m - x_1) \cdots (x_m - x_{m-1})(x_m - x_{m+1}) \cdots (x_m - x_M)} \quad (2)$$

Equation (2) is a polynomial function with order  $M - 1$ .

The expansion parameter  $a_n^m$  can be determined by the velocity  $v(\theta, x_m)$ , it has the following expression:

$$a_n^m = \mu_n \int_0^{2\pi} v(\theta, x_m) \cos(n\theta) d\theta \quad (3)$$

in which  $\mu_n = \begin{cases} 1/2\pi, n = 0 \\ 1/\pi, n \neq 0 \end{cases}$ .

Based on the Rahola Theorems 4.2 and 4.3 (Rahola 1996), and the analysis of Wu et al. (2010), when the number of integration points is larger than  $|m| + 1$ , it can be calculated by rectangle integration formula accurately:

$$a_n^m = \mu_n \Delta\theta \sum_{l=1}^N v(\theta_l, x_m) \cos(n\theta_l) \quad (4)$$

in which,  $\Delta\theta$  is the radian gap between two measuring points,  $v(\theta_l, x_m)$  is the surface velocity at measuring point  $(\theta_l, x_m)$ .

The expansion parameter  $a_n^m$  can be obtained from Eq. (4) based on the data of the velocity at the measuring points, the boundary condition at the other position  $(\theta, x)$  can be obtained from Eq. (1).

### 3 Sound Radiation Prediction from Cylindrical Shell

In the analysis of outer field sound radiation, the far-field radiation condition is satisfied, the boundary element method (BEM) can be used to calculate the radiated sound field. BEM is a numerical algorithm based on boundary integral equation:

$$c(x)p(x) = \int_S \left( G(x, y) \frac{\partial p(y)}{\partial n(y)} - \frac{\partial G(x, y)}{\partial n(y)} p(y) \right) dS(y) \quad (5)$$

$$G(\mathbf{x}, \mathbf{y}) = \frac{e^{ik_f \|\mathbf{x} - \mathbf{y}\|}}{4\pi \|\mathbf{x} - \mathbf{y}\|} \quad (6)$$

in which  $x, y$  are field point and source point on surface  $S$ ;  $G(x, y)$  is the free space Green's function.  $c(x)$  is a variable depending on the position of the field point  $x$ , here  $c(x) = 0$  in the domain interior,  $c(x) = 1$  at an exterior point and  $c(x) = 0.5$  on a smooth surface.

After the continual velocity layout being obtained by the interpolation method described in Sect. 2, by using BEM that based on Burton-Miller equation, the sound pressure on the structure surface can be calculated. Then the sound pressure on an arbitrary point can be predicted through Eq. (5).

### 3.1 Numerical Simulation

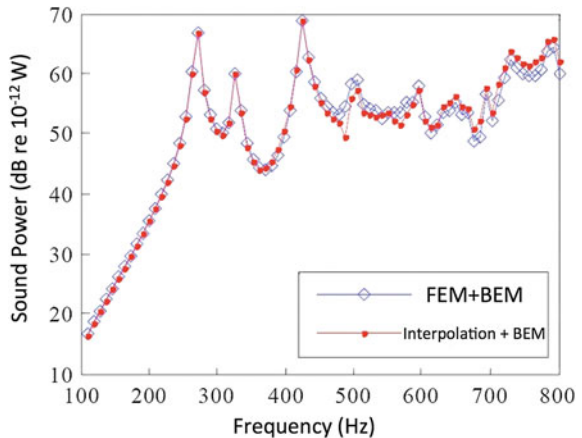
A discretized model of a ring-stiffened single cylindrical shell is modeled in ANSYS using 3-node shell elements (SHELL 63), with the length being 2 m, radius being 0.6 m and thickness being 0.005 m. Damping is included in the numerical model using a structural loss factor of 0.005. The flow media is estimated as water when calculating the sound radiation, with the density being  $1000 \text{ kg/m}^3$  and sonic being 1500 m/s.

The model is discretized into 160 elements along the circumferential direction and 72 elements along the axial direction. The model has 11,680 nodes and 11,520 rectangle elements. Six degrees on both ends of the cylindrical shell are constrained, a normal point force is applied on the shell surface. The radiated sound power of the cylindrical shell is then calculated by FE/BE methods numerically.

In order to validate the interpolation method numerically, 32 nodes along the longitude direction and 19 nodes along the circumferential direction are picked out from the discretized model of the cylindrical shell. By using the interpolation method described in Sect. 2, the velocity at other nodes on the shell surface is then obtained. The radiated sound power of the cylindrical shell is calculated by BEM.

The radiated sound power of the cylindrical shell is calculated for the entire frequency interval from 100 to 800 Hz in increments of 20 Hz and the spectrum are shown in Fig. 1, the errors between two methods are least then 2 dB, which shows a good agreement.

**Fig. 1** Sound power of the numerical simulation model



### 3.2 Experimental Verification

The radiated sound power of a double cylindrical shell is also experimentally measuring in an out-door underwater testing field. The object is a double cylindrical shell as shown in Fig. 2a and its three view drawing with dimensions in Fig. 2b. The thickness of the inner shell is 5 mm and the outer shell is 2 mm. The layout of the acceleration sensors is also shown in Fig. 2b. Only half of the model needs to be measured. 9 acceleration sensors are evenly arranged on half of the circumferential surface with the spacing being 0.23 m. 8 acceleration sensors are evenly arranged along the axial direction with the spacing being 0.2 m. There are 72 acceleration sensors in total.

The sound power radiation of the cylindrical shell is also measured experientially. The underwater testing field is in a lake with the water depth being 11 m, which can be seen as a free field for the sound radiation. 10 hydrophones are arranged along the axial direction outside the cylindrical shell, as shown in Fig. 3. The spacing between two hydrophones is 1 m. The distance between the hydrophone array and the axis of the cylindrical is 4.2 m. Only the circumferential radiated sound pressure is measured.

The model rotated every 30° during testing, an envelope cylindrical surface is formed to calculate the radiated sound power. The enveloping surface is divided into rectangle grids. The radiated sound power can be calculated from the following expression.

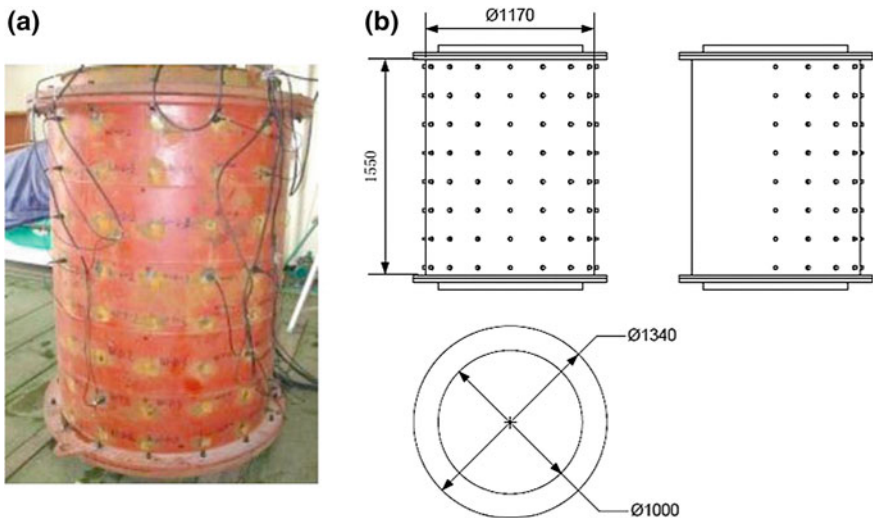
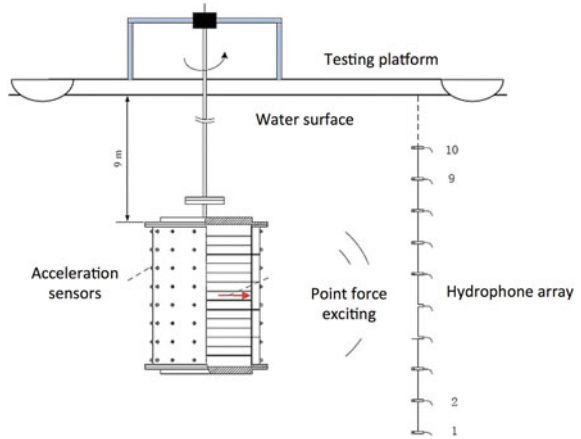


Fig. 2 Model of double cylindrical shell and layout of acceleration sensors

**Fig. 3** Testing field arrangement

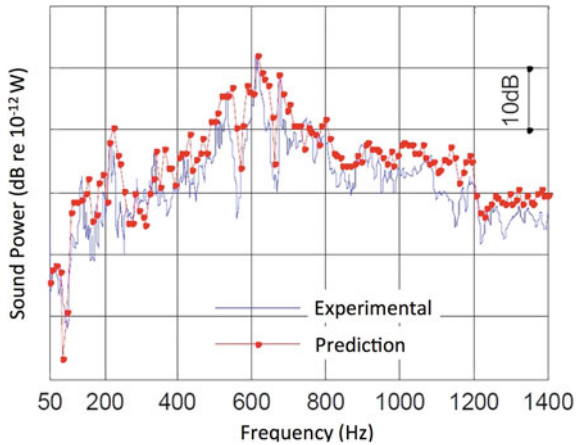


$$SWL = 10 \log_{10} \sum_{m=1}^M \left( \frac{|p_m|^2}{P_{ref}^2} \right) A_m \tag{7}$$

in which  $|p_m|$  is the mean square value of the  $m$ th grid,  $A_m$  is the area of the  $m$ th grid,  $p_{ref}$  is the reference sound pressure which equals to  $1 \mu Pa$ .

The spectrum of both the experimentally obtained from Eq. (7) and from BEM using interpolated velocity distribution are compared in Fig. 4. In the frequency interval below 1000 Hz, they have good agreement, the errors are less than 2 dB; in frequency interval from 1000 to 1400 Hz, the largest error is less than 5 dB, and the

**Fig. 4** Sound power level of experimental results and prediction results





average error is 2.8 dB. It can be found that the two results have the same trend, which indicates the prediction method of the radiated sound power of the cylindrical shell based on interpolation method has good practicability and can be used in engineering application.

## 4 Conclusion

In this work, a new interpolation method is proposed for the reestablishing of the surface velocity of cylindrical shell structures. The surface velocity is expressed by the Fourier series in the circumferential direction and the piecewise Lagrange functions in the axial direction. The coefficients of the series expression are computed from measured surface velocity. Once the coefficients are obtained, the series expression can be used to calculate the velocity at other positions on surface of the cylindrical shell structures. Then the sound power radiation of the cylindrical structures can be predicted based on boundary element method. In order to experimentally validate the numerical results, experiments on a double cylindrical shell was conducted in an underwater testing field. A similar trend in results of the radiated sound power obtained experimentally direct from the hydrophone data and from the interpolation method was observed. The interpolation method is shown to be an efficient technique and has engineering application.

**Acknowledgments** The work is supported by grant 11074170 of the National Natural Science Foundation of China.

## References

- Chen H, Li Q, Shang D (2014) Fast prediction of acoustic radiation from a hemi-capped cylindrical shell in waveguide. *J Mar Sci Appl* 13(4):437–448. doi:[10.1007/s11804-014-1270-x](https://doi.org/10.1007/s11804-014-1270-x)
- Guz AN, Kubenko VD (2002) Dynamics of shell systems interacting with a liquid. *Int Appl Mech* 38(3):260–301. doi:[10.1023/A:1016073909775](https://doi.org/10.1023/A:1016073909775)
- Liu D, Peters H, Kessissoglou N, Marburg S (2014) Prediction of the radiated sound power from a fluid-loaded finite cylinder using the surface contribution method. In: Paper presented at the 43rd international congress on noise control engineering: improving the world through noise control, INTERNOISE 2014
- Rahola J (1996) Diagonal forms of the translation operators in the fast multipole algorithm for scattering problems. *BIT Numer Math* 36(2):333–358
- Wu CJ, Chen HL, Huang XQ (2000) Sound radiation from a finite fluid-filled/submerged cylindrical shell with porous material sandwich. *J Sound Vib* 238(3):425–441. doi:[10.1006/jsvi.2000.3086](https://doi.org/10.1006/jsvi.2000.3086)
- Wu HJ, Jiang WK, Liu YJ (2010) Analysis of numerical integration error for Bessel integral identity in fast multipole method for 2D Helmholtz equation. *J Shanghai Jiaotong Univ (Sci)* 15(6):690–693. doi:[10.1007/s12204-010-1070-7](https://doi.org/10.1007/s12204-010-1070-7)
- Yang Q, Parvin B (2003) High-resolution reconstruction of sparse data from dense low-resolution spatio-temporal data. *IEEE Trans Image Process* 12(6):671–677. doi:[10.1109/TIP.2003.812389](https://doi.org/10.1109/TIP.2003.812389)

# Identification of Small Objects with Near-Field Data in Quasi-Backscattering Configurations

Housseem Haddar and Mohamed Lakhali

**Abstract** The aim of this work is the detection of small inclusions (or defects) in the three-dimensional free space, using near field acoustic data in a quasi-backscattering configuration. The latter is such that for any source point in the antenna path we have an orthogonal line of receivers. Our inversion algorithm is based on a Music type method adapted to the asymptotic form of the scattered field for small inclusions and the data configuration. The efficiency of the procedure is tested against synthetic data.

**Keywords** Data in quasi-backscattering configurations · Music type method · Near field operator

## 1 Introduction

We present a new sampling method (Cakoni and Colton 2014; Kirsch 2002) for detecting targets (small inclusions or defects) immersed in a homogeneous medium in three-dimensional space, from measurements of acoustic scattered fields created by point source incident waves. We consider the harmonic regime and a data setting that corresponds with quasi-backscattering configuration: the data is collected by a set of receivers that are distributed on a segment centered at the source position and the device is swept along a path orthogonal to the receiver line. We assume that the aperture of the receivers is small compared with the distance to the targets. Considering the asymptotic form of the scattered field as the size of the targets goes to zero and the small aperture approximation, one is able to derive a special

---

H. Haddar · M. Lakhali (✉)  
INRIA-Saclay Ile de France, Ecole Polytechnique CMAP,  
route de Saclay, 91128 Palaiseau Cedex, France  
e-mail: mohamed.lakhali@polytechnique.edu

H. Haddar  
e-mail: haddar.housseem@inria.fr

expression for the scattered field. In this expression a separation of the dependence of scattered field on the source location and the distance source-target is performed. This allows us to propose a sampling procedure that characterizes the targets location in terms of the range of a near-field operator constructed from available data. Our procedure is similar to the one proposed in Haddar and Jacob (2015) for far-field configurations. We then implement the procedure using Music type algorithm and well chosen combination of the multi-campaign measurements (varying the source-receivers path). Validation against synthetic data is performed for some toy examples.

The outline of this note is the following. In the first section, we present the direct problem corresponding to the acoustic wave propagation in the medium and its approximation in the case of small inclusions. We then describe the setting for the collected data that corresponds to quasi-backscattering configuration. In the second section, we give a characterization of targets in terms of the measurement operator range in the fashion of Music type algorithms. We treat both cases of mono-polar, di-polar and mixed inclusions. In the last section, we give details on how we use the Music method to solve our inverse problem and finally give numerical results to show the effectiveness of the technique.

## 2 Direct Problem

We begin discussing the mathematical formulation for the scattering problem in homogeneous media containing some inclusions in the case of three-dimensional space.

The direct problem corresponds with the determination of the total field  $u^t$  or the scattered field  $u^{sc}$  in some homogeneous medium containing some obstacles, from the knowledge of the incident field generated by a source point.

Let  $D$  be the set containing the targets composed of  $M$  inclusions  $D_j = C_j + \delta_j B_j$  where  $C_j$  represents the center,  $\delta_j$  is the size and  $B_j$  is the shape of the inclusion, with medium properties  $\rho^j, n^j$ .

Let  $u^{in}(x, x_0)$  be the incident field generated by the point source  $x_0$  in  $\Sigma$  a plane at altitude  $z = H$ ,

$$u^{in}(x, x_0) = \Phi(x, y) := \frac{\exp(ik|x - x_0|)}{4\pi|x - x_0|}, \quad \text{with } x_0 \in \Sigma \text{ and } x \in \mathbb{R}^3 \text{ and } x \neq x_0 \quad (1)$$

where  $k = \frac{2\pi}{\lambda}$  is the wave-number and  $\lambda$  is the wavelength in the homogeneous medium. Due to the in-homogeneity (presence of the inclusions) of the medium, this field induces a scattered field  $u^{sc}$ . The total field  $u^t = u^{in} + u^{sc}$  satisfies:

$$\nabla \left( \frac{1}{\rho_\delta} \nabla u_\delta^t(\cdot, x_0) \right) + k^2 n_\delta^2 u_\delta^t(\cdot, x_0) = -\delta_{x_0} \text{ in } \mathbb{R}^3 \quad (2)$$

subject to the Sommerfeld radiation condition:

$$\lim_{r \rightarrow +\infty} r \left( \frac{\partial u^{sc}}{\partial r} - iku^{sc} \right) = 0 \quad (3)$$

where  $r = |x|$  and  $\rho_\delta, n_\delta$  are defined as:

$$\rho_\delta(x) = \begin{cases} 1 \\ \rho_j \end{cases} \quad \text{and} \quad n_\delta(x) = \begin{cases} 1 \\ n_j \end{cases} \quad \text{if } x \in \begin{cases} \mathbb{R}^3 \setminus \cup_j D_j \\ \in D_j \end{cases}$$

In the case of small inclusions we have the following approximation for the scattered field (with  $\delta := \max_{j=1, \dots, M} \delta_j$ ):

$$u^{sc}(x, x_0) \sim \sum_{j=1}^M \gamma_\rho^j \mathcal{M}^{(j)} \nabla \Phi(C_j, x_0) \cdot \nabla \Phi(C_j, x) + |B_j| k^2 \gamma_n^j \Phi(C_j, x_0) \Phi(C_j, x) + O(\delta^3) \quad (4)$$

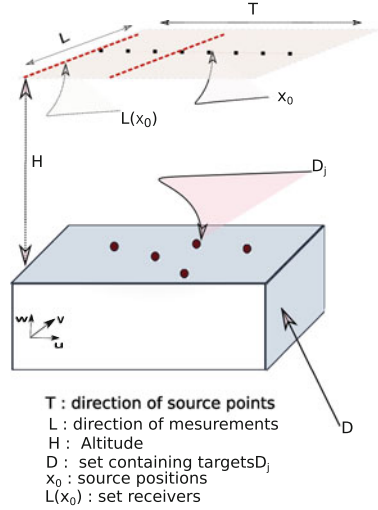
where  $\gamma_n^j = n_j^2 - 1$ ,  $\gamma_\rho^j = \rho_j - 1$ , and  $\mathcal{M}^{(j)}(\rho_j)$ ,  $|B_j|$  are respectively the polarization tensor and volume of  $B_j$  (Haddar and Mdimagh 2012). We consider the experimental setting where an array of receivers occupies a segment  $L$  is swept along a line  $T \in \Sigma$  orthogonal to  $L$  in the plane  $\Sigma := \{x \in \mathbb{R}^3, x_3 = H\}$  above the targets  $\{D_j, j = 1, \dots, M\}$  that belongs to the lower half plane  $\{x \in \mathbb{R}^3, x_3 \leq 0\}$ . We assume that a source is placed at the center of  $L$ . In this configuration one would collect measurements of  $u^{sc}(x, x_0)$ , for  $x_0 \in T$ ,  $x \in L(x_0)$ , where  $L(x_0) \subset \Sigma$  is the segment orthogonal to  $L$  at  $x_0$ .

In a backscattering configuration  $T(x_0)$  is reduced to  $\{x_0\}$  meaning that we have a single receiver at the source location (McDonough and Curlander 1991). In the quasi-back-scattering configuration we assume that the size of  $L(x_0)$  is small (but not reduced to a single point). More precisely  $|L(x_0)| = 2\theta$ , with  $\theta \ll H$ .

### 3 A Music Type Algorithm for the Inverse Problem

We now turn our attention to the inverse problem of reconstructing the location of the inhomogeneities from the quasi-backscattering near field data (described in the previous section) represented in Fig. 1.

**Fig. 1** Quasi-backscattering configuration



### 3.1 Approximation of the Scattered Field in the Quasi-Backscattering Configuration

Let  $\hat{\mathbf{v}}$  be a unit vector of  $\mathbb{R}^3$ , we consider the setting where we have:  $x_0 = |x_0|\hat{\mathbf{u}}$  and  $x = x_0 + \eta\hat{\mathbf{v}}$ , assume that  $\eta^{\frac{1}{2}} \ll |y - x_0|$ , let  $\eta \ll 1$  and  $\hat{\mathbf{w}}$  is such that  $(\hat{\mathbf{v}}, \hat{\mathbf{u}}, \hat{\mathbf{w}})$  form an orthonormal basis of  $\mathbb{R}^3$ . Then we simply have

$$|x - y| = |y - x_0 - \eta\hat{\mathbf{v}}| = |y - x_0| - \eta\hat{\mathbf{v}} \cdot y + O\left(\frac{\eta^2}{|x_0 - y|^2}\right) \quad (5)$$

and

$$\frac{x - y}{|x - y|} = \frac{x_0 - y + \eta\hat{\mathbf{v}}}{|y - x_0|} \left(1 + \frac{\eta}{|y - x_0|} \hat{\mathbf{v}} \cdot y + O\left(\frac{\eta^2}{|y - x_0|^2}\right)\right) \quad (6)$$

**The case of mono-polar inclusions:** It corresponds to  $\rho_j = 1$ , for all  $j \in \{1, \dots, N\}$  which implies that  $\mathcal{M}^{(j)} = 0$ . The scattered field is then given by:

$$u^{sc}(x, x_0) \simeq \sum_{j=1}^M |B_j| k^2 \gamma_n^j \Phi(C_j, x_0) \Phi(C_j, x) + O(\delta^3).$$

Let us set

$$\tilde{u}^{sc}(\eta, x_0) := \sum_{j=1}^M \tau_j \frac{e^{2ik|C_j - x_0|}}{(4\pi|C_j - x_0|)^2} e^{-ik\eta\hat{\nu}\cdot C_j} \quad (7)$$

with  $\tau_j = -k^2 \gamma_{n(x)}^j \delta_j^3 |B_j|$ ,  $|B_j|$ , volume of  $B_j$ ,  $\hat{\mathbf{u}} = \hat{\mathbf{v}}^\perp$  and  $\hat{\mathbf{v}}$  the incident and measurement directions. Then from approximation (5), we have:

$$u^{sc}(\eta, x_0) = \tilde{u}^{sc}(\eta, x_0) + O\left(\frac{\eta^2}{|x_0 - y|^2}\right).$$

**The case of dipolar inclusions:** they correspond with  $n_j = 1$  for all  $j = 1 : M$ . In this case

$$u^{sc}(x, x_0) = \sum_{j=1}^M \gamma_\rho^j \mathcal{M}^{(j)} \nabla \Phi(C_j, x_0) \cdot \nabla \Phi(C_j, x) + O(\delta^3).$$

Let us set in this case

$$\begin{aligned} \tilde{u}^{sc}(\eta, x_0) &= \sum_{j=1}^M \gamma_\rho^j \mathcal{M}^{(j)} \nabla \Phi(C_j, x_0) \cdot \nabla \Phi(C_j, x_0) e^{-ik\eta\hat{\nu}\cdot C_j} \\ &= \sum_{j=1}^M \gamma_\rho^j \mathcal{M}^{(j)} (C_j - x_0) \cdot (C_j - x_0) \frac{e^{2ik|x_0 - C_j|}}{16(\pi|x_0 - C_j|)^2} \left( ik - \frac{1}{|x_0 - C_j|} \right)^2 e^{-ik\eta\hat{\nu}\cdot C_j}. \end{aligned}$$

Then from approximation (6), the scattered field verifies

$$u^{sc}(\eta, x_0) = \tilde{u}^{sc}(\eta, x_0) + O\left(\frac{\eta^2}{|x_0 - y|^2}\right).$$

If in addition  $\mathcal{M}^{(j)} = \alpha_j I$ , with  $I$  the identity matrix, which corresponds to spherical inclusions,

$$\tilde{u}^{sc}(\eta, x_0) = \sum_{j=1}^M \gamma_\rho^j \alpha_j \frac{e^{2ik|x_0 - C_j|}}{16\pi^2} \left( ik - \frac{1}{|x_0 - C_j|} \right)^2 e^{-ik\eta\hat{\nu}\cdot C_j}. \quad (8)$$

### 3.2 A Music Algorithm

Let us consider as data  $\tilde{u}^{sc}(\eta, x_0)$ , where  $\tilde{u}^{sc}$  is given by Eq. (7) in the case of monopolar inclusions, and given by Eq. (8) in the case of dipolar spherical inclusions. We define the near-field operator as

$$F : L^2[-\theta, \theta] \rightarrow L^2(T)$$

given by

$$(Fg)(x_0) = \int_{-\theta}^{\theta} g(\eta) \tilde{u}^s(\eta, x_0) ds(y) \quad (9)$$

for  $z \neq x_0, x_0$ , with  $z \in \mathbb{R}^3$ . We also define the sampling function  $\psi_m$  (that we shall use in the inversion algorithm) as

$$\psi_m(x_0, z) := \Phi^2(x_0, z) = \frac{\exp(2ik|z - x_0|)}{(4\pi|z - x_0|)^2}$$

in the case of mono-polar inclusions and as sampling function  $\psi_b$

$$\psi_b(x_0, z) := \nabla \Phi(x_0, z) \cdot \nabla \Phi(x_0, z) = \frac{\exp(2ik|z - x_0|)}{16\pi^2} \left( ik - \frac{1}{|z - x_0|} \right)^2$$

this function in the case of dipolar inclusions. We observe from the expressions of  $\tilde{u}^s(\eta, x_0)$  that  $F$  has a finite rank. We denote by  $\Pi_{\perp}$  the orthogonal projection on  $T$ , and  $\Pi_{//}$  the orthogonal projection on the line  $\mathbb{R}\hat{\nu}$ . The inversion method we consider in this paper is based on the following result.

**Theorem 1** *Let  $z \in \mathbb{R}^3$  and  $\psi(\cdot, z)$  be the sampling function ( $=\psi_m(\cdot, z)$  in the monopolar case and  $=\psi_d(\cdot, z)$  in the dipolar case). Assume that  $\Pi_{//}(C_j) \neq \Pi_{//}(C_r)$  for all  $j \neq r$ . Then the following statements are equivalent:*

- (i)  $\psi(z, \cdot)$  is in the range of  $F$ ;
- (ii)  $|z - x_0| = |C_j - x_0|$ , for all  $x_0 \in T$  and for some  $j \in \{1, \dots, M\}$ .

Let us denote by  $\mathcal{C}_j$  for  $j \in \{1, 2, \dots, M\}$  the set of points  $z \in \mathbb{R}^3$  that satisfy (ii) in the theorem. This set is exactly the circle with center  $\Omega_j = \Pi_{\perp}(C_j)$  orthogonal to  $T$  and containing  $C_j$ .

As consequence of this theorem, one is able to identify from the operator  $F$  (and therefore the set of quasi-backscattering data)  $\mathcal{C}_j$  for  $j \in \{1, 2, \dots, M\}$ . Let us denote by  $\Sigma_j$  the plane containing  $\mathcal{C}_j$ .

If we consider another (path) line  $T'$  for the sources that is parallel to  $T$ , one can identify another set of circles  $\mathcal{C}'_j$  in the same plane  $\Sigma_j$ . It is then easy to reconstruct the points  $C_j$  for  $j \in \{1, 2, \dots, M\}$  as the intersections between  $\mathcal{C}_j$  and  $\mathcal{C}'_j$  (we exclude the intersection that have positive third components since we assume that the targets are located in the lower half plane). We have then obtained a characterization of the inclusions positions using the the range of  $\mathcal{R}(F)$  with two different backscattering data sets (associated with two parallel paths of the sources).

We now explain how one can reconstruct the circles  $\mathcal{C}_j$  using a Music type algorithm and how to automatically perform the intersections with different data sets. Let us consider  $\mathbb{P}$  the orthogonal projection onto the null space  $N(F^*)$  of  $F^*$ . It is well known that, since  $F$  has a finite rank,  $\psi(z, \cdot)$  is in the range of  $F$  if and only if  $\mathbb{P}\psi(z, \cdot) = 0$ . We then get from the theorem that the circles  $\mathcal{C}_j$  correspond with the points  $z$  such that  $\mathbb{P}\psi(z, \cdot) = 0$ . From the practical point of view, let us consider  $(U, S, V) = (u_k, s_k, v_k)_{k \geq 1}$  be the singular decomposition for  $F$  where  $u_k$  and  $v_k$  are respectively the left and right singular functions that correspond to the singular values  $s_k$ . Let  $r_0$  be the number of non vanishing singular values. Then

$$\|\mathbb{P}\psi(z, \cdot)\|^2 = \sum_{k > r_0} \left| \langle \psi(z, \cdot), v_k \rangle_{L^2(T)} \right|^2$$

We now introduce the imaging function:

$$I(z) := \frac{1}{\|\mathbb{P}\psi(z, \cdot)\|} \tag{10}$$

and observe that the circles  $\mathcal{C}_j$  are the points where  $I(z) = \infty$ .

From the algorithmic point of view, we observe that one can avoid evaluating  $I(z)$  for all points  $z \in \mathbb{R}^3$ . We can proceed in two steps. We first identify the planes  $\Sigma_j$  by evaluating  $I(z)$  on a plane  $P(T)$  containing  $T$ . The indicator function would have infinite values at the points  $\zeta_j = \mathcal{C}_j \cap P(T)$ . The planes  $\Sigma_j$  then correspond with the plane containing  $\zeta_j$  and orthogonal to  $T$ . One can also (in principle) obtain  $\mathcal{C}_j$  knowing  $\zeta_j$  and  $\Sigma_j$ . We rather prefer not to identify  $\mathcal{C}_j$  using this characterization since it would be sensitive to noise. We shall visualize  $\mathcal{C}_j$  by evaluating  $I(z)$  for all points  $z \in \Sigma_j$ . Let us denote  $I'(z)$  the indicator function associated with  $T'$ . Then the points  $C_j$  belonging to the plane  $\Sigma_j$  are identified as the peaks of  $I(z)I'(z)$ . This procedure has the advantage of being automatic and intrinsically handle the case of multiple points belonging to  $\Sigma_j$ . It can also be easily extended to the case of more than two sets of data (which would increase the precision and robustness with respect to noise).

## 4 Numerical Results

Before starting the presentation of some numerical results, we first give some details related to the implementation of our algorithm. We consider two parallel paths  $T$  and  $T'$  containing each  $N$  sources points and we assume that we have  $R$  receivers at each source position. Let us set  $K_j(x_0) = \tau_j \psi_m(x_0, C_j)$  in the monopolar case, and  $K_j(x_0) = \alpha_j \gamma_\rho^j \psi_d(x_0, C_j)$  in the dipolar case. The near field operator  $F$  is approximated by the matrix



$$F_{n,r} = \frac{2\theta}{R+1} \sum_{j=1}^M K_j(x_0^n) e^{-ik\eta_r \cdot \hat{v} \cdot C_j} \quad 1 \leq n \leq N \quad 1 \leq r \leq R.$$

In order to avoid inverse crime, we also consider the case of noisy measurements by applying our algorithm to the noisy operator

$$\tilde{F}_{n,r} := F_{n,r}(1 + \sigma N_{n,r}) \quad 1 \leq n \leq N \quad 1 \leq r \leq R$$

where  $(-1 \leq N_{n,r} \leq 1)$  are random numbers and  $\sigma$  denotes the noise level. The singular value decomposition of  $F$  or  $\tilde{F}$  is done using the predefined function `svd` in MATLAB.

In all the simulation, the region containing all the targets is taken as a volume  $\mathbb{V} = [-A, B] \times [-a, b] \times [-p, h]$ , of dimension  $20\lambda \times 20\lambda \times 11\lambda$ , with  $(A = B = a = b = p = 10\lambda)$  and  $h = \lambda$ .

We consider two parallel paths  $T$  and  $T'$  of the sources, which emit with a wavelength  $\lambda = 1$  cm. The corresponding imaging functions are  $I$  and  $I'$ . We shall express all the experiment parameters as functions of  $\lambda$ . The length of sources path is  $L = 20\lambda$ , with  $N = 81$  source points uniformly distributed with distance  $ds = \frac{\lambda}{4}$ . The aperture of the antenna is  $2\theta = 2\lambda$  containing  $R = 8$  detectors, equidistantly spaced with  $dm = \frac{\lambda}{7}$ . The line  $T$  is placed in the plane  $\Pi_0 = \{z_2 = y_0 | y_0 = -4\lambda\}$ , at the altitude  $H = 8\lambda$ . Each area in  $\mathbb{V}$  is uniformly sampled with a mesh size  $dz = \frac{\lambda}{6}$ . The circle centered at the exact position of defects with radius  $\frac{\lambda}{2}$  is indicated in all the images using a magenta color.

## 4.1 Reconstruction of One Inclusion

**A first example with a single defect:** The path  $T'$  is placed in the plane  $\Pi'_0 = \{z_2 = y'_0 | y'_0 = 4\lambda\}$ , at the altitude  $H' = 12\lambda$ . The inclusion is placed at  $C = (-2\lambda, 2\lambda, -\lambda)$ . In the **first step**, we evaluate the function  $I(z)$  for all the points  $z \in P(T) = \Pi_0$ . We denote by  $C_j^1$ ,  $j = 1 : r_0$ , the abscissa of the  $r_0$  first largest values of  $I(z)$  ( $r_0$  the number of non-vanishing singular values). In this case,  $r_0 = 1$  and one point  $C^1$  corresponds to the first component of  $C$  (see Fig. 2a). In the **second step**, we evaluate  $I(z)$  and  $I'(z)$  for all  $z \in \Sigma = \{z_1 = C^1\}$ , and the peaks of  $I(z)I'(z)$  give us the two other coordinates of  $C$  (see Fig. 2b).

**Influence of the distance  $T - T'$ :** To analyze the influence of the distance between the two paths  $T$  and  $T'$ , we vary the position of  $T'$  from the plane  $\Pi = \{z_2 = y | y = -4\lambda\}$  at the altitude  $z = 8\lambda$ , to the plane  $\Pi = \{z_2 = y | y = 4\lambda\}$  at altitude  $z = 12\lambda$ , with steps in space  $dy = \frac{\lambda}{2}$  and  $dh = \frac{\lambda}{8}$ . We set  $d = \sqrt{(y - y_0)^2 + (z - z_0)^2}$  the distance between the two line paths  $T$  and  $T'$ . In the same way as before, we

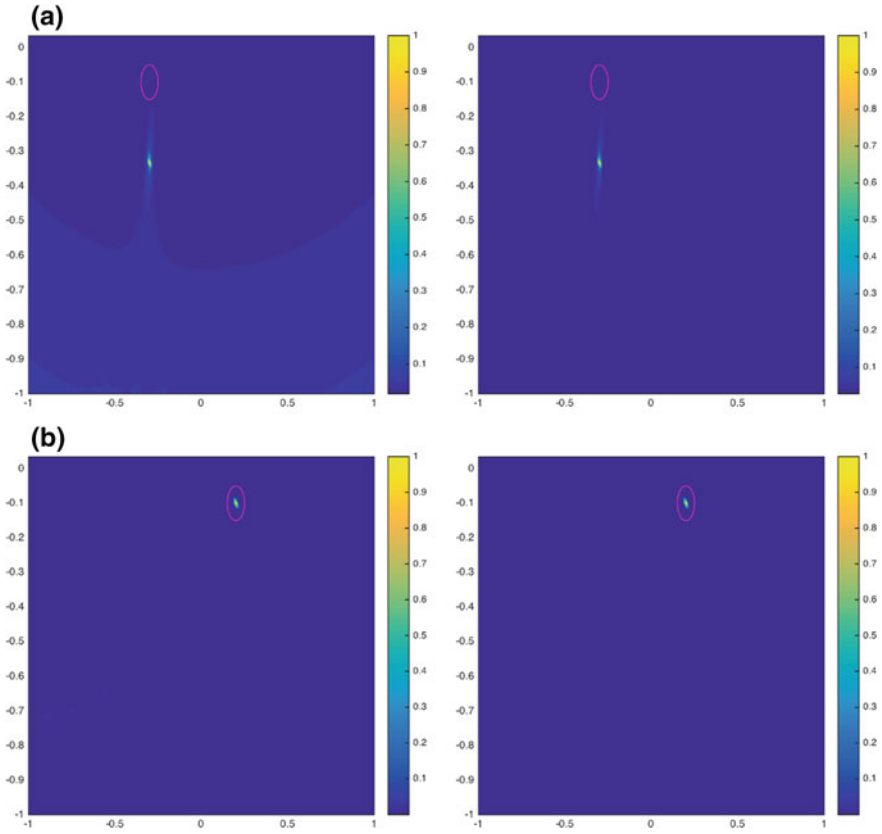


**Fig. 2** From *left to right*, the reconstruction of three component in the case of mono-polar and dipolar inclusion with 5 % noise. **a** Reconstruction of the component  $C_1$  in the plane  $P(T)$ . **b** Reconstruction of the two other the other components of the inclusion in the plane  $\Sigma$

reconstruct the inclusion  $C$  for all positions of  $T'$  corresponding with  $d \in [0, 4\sqrt{5}\lambda]$  by evaluating  $U_d(z) = I(z)I'_d(z)$ . Let us set  $\hat{U}_d(z) = \frac{U_d(z)}{\|U_d\|_\infty}$ . One defines the difference between  $\hat{U}_d$  and the theoretical  $U_d^{ex}(z)$  defined by  $U_d^{ex}(C) = 1$  and  $U_d^{ex}(z) = 0$  for  $z \neq C$  as  $\varepsilon(d) = \frac{\|\hat{U}_d - U_d^{ex}\|}{\|U_d^{ex}\|}$  (see Fig. 3).

As can be noted from these numerical results, increasing the distance  $T - T'$  improves the accuracy of the reconstruction of the inclusion. In the following, the path  $T'$  is placed in the plane  $\Pi'_0 = \{z_2 = y'_0\}$  and  $y'_0 = 4\lambda$ , at the altitude  $H' = 12\lambda$ .

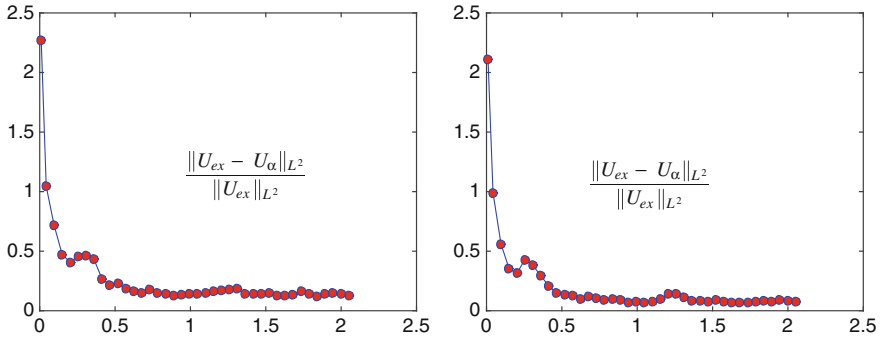


**Fig. 3** The difference between  $\hat{U}_d$  and  $U_d^{ex}$  as function of distance  $d$  between the two line  $T$  and  $T'$ , with 5 % of noise, in the *left* monopolar inclusion in the *right* dipolar one

### 4.2 Reconstruction of Multiple Inclusions

Here we consider the case of two inclusions;  $C_1 = (a_0, b_0, c_0) = (0, -4\lambda, -5\lambda)$  a fixed target in  $\mathbb{V}$  and  $C_2 = (a, b, c)$  that we shall vary the position and set  $d = \sqrt{(a - a_0)^2 + (b - b_0)^2 + (c - c_0)^2}$  the distance  $C_2 - C_1$  (Fig. 4).

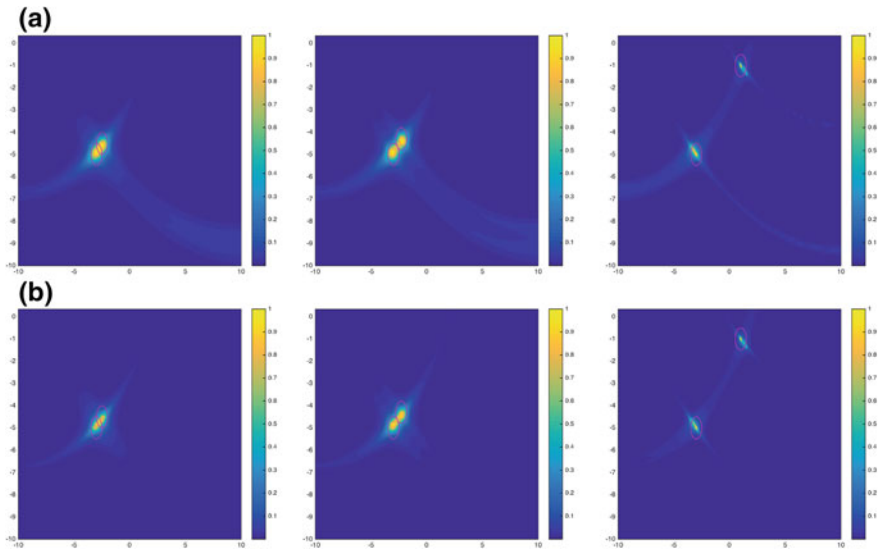


**Fig. 4** From the *left to right*, the reconstruction with 5 % of noise, with respectively distance between the two inclusions  $d = \frac{\sqrt{2}\lambda}{2}$ ,  $d = \lambda$  and  $d = 3\frac{\sqrt{2}\lambda}{2}$ . **a** Monopolar inclusions. **b** Dipolar inclusions

**First step**, we determine  $a = C_2^1$  and  $a_0 = C_1^1$  by evaluation of  $I(z)$  in all point with  $P(T) = \Pi_0$  the grid containing the line  $T$ , and identifying first  $r_0$  ( $=2$  in this case) abscissa of  $r_0$  largest values of  $I$ . In the **second step** for  $j = 1, 2$ , we evaluate  $I_{d,j}(z)$  and  $I'_{d,j}(z)$ , and therefore  $U_{d,j}(z) = I_{d,j}(z)I'_{d,j}(z)$  for all the grid point  $\in \Sigma_j = \{z_1 = C_j^1\}$ . Finally for all  $j = 1, 2$ , the imaging function  $\hat{U}_j(d) = \frac{U_j(d)}{\|U_j(d)\|_\infty}$  in  $\Sigma_j$ , which represent respectively the position of  $C_1$  and  $C_2$ . **Third step**: the concatenation  $\hat{U}_d = \hat{U}_1(d) + \hat{U}_2(d)$  (for example in the plane  $\Sigma = \{z_1 = 0\} // \Sigma_j, j = 1, 2$ ) of the two images should give us a grid with the components  $(y, z)$  of the two objects. In Fig. 4 are represented respectively the two monopolar and dipolar inclusions vertically, and horizontally the change in distance  $d$  from  $C_1$  to  $C_2$ .

We now analyze the influence of the distance between the targets on the quality of images obtained with our algorithm. To do that evaluate  $\varepsilon(d) = \frac{\|\hat{U}_d - U_d^{ex}\|}{\|U_d^{ex}\|}$  as in the previous example but where  $d$  denotes here the distance between the two inclusions. In Fig. 5 we present this variation in the case of two monopolar inclusions with 3 different noise levels.

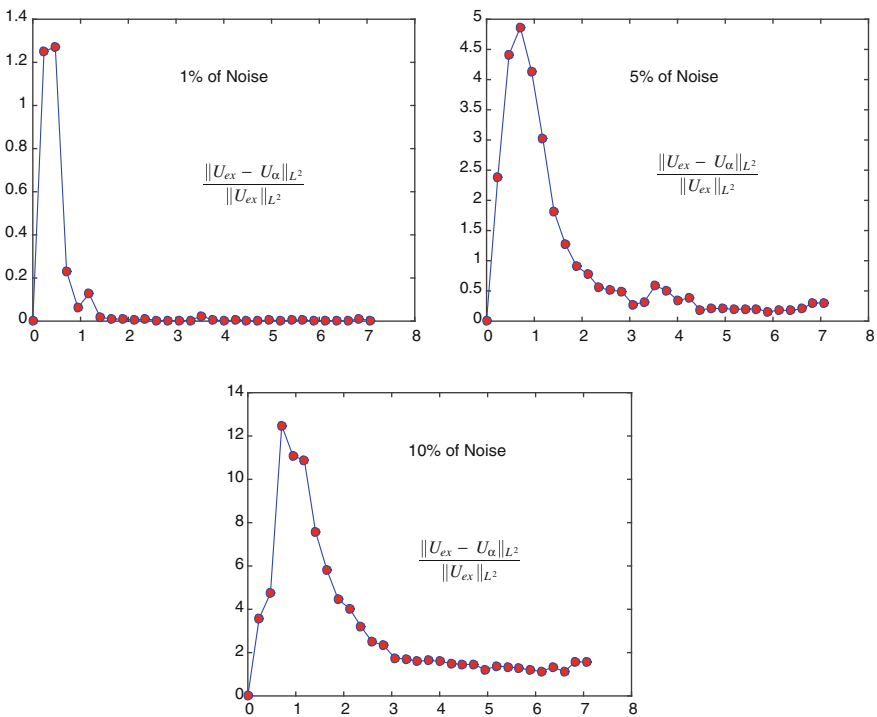


**Fig. 5** The difference between  $\hat{U}_d$  and  $U^{ex}$  as a function of distance between the two monopolar inclusions, with 1, 5 and 10 % of noise from left to right

As can be noted from the numerical results, the accuracy increases as the distance between the two inclusions increase. Our algorithm can clearly separate two different inclusions if the distance is greater than  $\lambda$ .

## References

- Cakoni F, Colton D (2014) *A qualitative approach to inverse scattering theory*. Springer, New York
- Haddar H, Mdimagh R (2012) Identification of small inclusions from multistatic data using the reciprocity gap concept. *Inverse Prob* 28(4):045011
- Haddar H, Rezac JD (2015) A quasi-backscattering problem for inverse acoustic scattering in the born regime. *Inverse Prob* 31(7):075008
- Kirsch A (2002) The MUSIC algorithm and the factorization method in inverse scattering theory for inhomogeneous media. *Inverse Prob* 18(4):1025–1040
- McDonough RN, Curlander JC (1991) *Synthetic aperture radar: systems and signal processing*, 1st edn. Wiley-Interscience, London

# Characterization of Sandwich Beams with Shear Damage by Linear Vibration Method

I. Ben Ammar, C. Karra, A. El Mahi, R. El Guerjouma and Mohamed Haddar

**Abstract** The purpose of this work is the study of the dynamic behavior of sandwich beams with shear damage. The linear vibration method is used in this study. The technique focuses on the response of the material's resonance modes as a function of the driving amplitude by sweeping the frequency. The sandwich materials used in this study is constructed with glass fiber laminates as skins and with PVC closed-cell foams with density 60 and 100 kg m<sup>-3</sup> as core. The response excitation of the shaker was established and the resonant frequencies and damping have been deduced for each frequency mode and each shear damage density.

**Keywords** Sandwich · Linear vibration · Shears damages · Dynamic behavior · Frequency · Damping

## 1 Introduction

Sandwich construction has found extensive application in aircraft, missile and spacecraft structures due to high strength to weight ratio. This type of construction consists of thin, stiff and strong sheets of metallic or fiber composite material separated by a thick layer of low density material.

They are more advantageous compared to the other traditional metallic materials.

---

I. Ben Ammar (✉) · C. Karra · A. El Mahi · R. El Guerjouma · M. Haddar  
Research Laboratory of Mechanics, Modeling and Manufacturing (LA2MP), National School of Engineers of Sfax (ENIS), <Code: 05/UR/11-13>, BP 1173, 3038 Sfax, Tunisia  
e-mail: benammarimene@gmail.com

C. Karra  
e-mail: chafik\_karra@yahoo.fr

I. Ben Ammar  
LUNAM University, Maine University, <CNRS UMR 6613>, Acoustic Laboratory of Maine University (LAUM), Avenue Olivier Messiaen, 72085 Le Mans Cedex 9, France

A sandwich construction has following advantages: High ratio of bending stiffness to weight as compared to monolithic construction; high resistance to mechanical and sonic fatigue; good damping characteristic...

During the use of the sandwich material, he can damage in several ways. The principal modes of damage of composites with foam cores are: fracture of skin, indentation, face wrinkling, debonding between skin and core, shear damage of the core.

Many damage detection methods have been developed for composite structures, such as acoustic emission (AE) (De Rosa et al. 2009; Lee and Lee 2002; Leone et al. 2012), thermography (Maldague 2001), X-ray (Shi et al. 2012), electrical resistance (Wen et al. 2011), ultrasonic C scan (Hsu 2009), guided-wave based (Su et al. 2006; Caminero et al. 2013; Li et al. 2013) and vibration-based (Fan and Qiao 2011; Yam et al. 2003) methods etc.

A great number of studies are reported in the literature on linear vibration of composite materials.

Vladimir et al. (2004) investigated the dynamic behavior of the sandwich beam with transverse damage on the foam. They observed that the frequency increase at the presence of the damage.

Idriss (2013) and Idriss et al. (2015) analyzed the dynamic behavior of sandwich with debonding. The Sandwich material used in this study is constructed with glass fibre laminates as skins and with PVC closed-cell foams as core. The linear vibration characterization showed that the frequency decrease and the loss factor increase when the debonding length increases. It also shown that when the density of the foam increases, the damping decreases slightly.

Okutan et al. (2009) studied the dynamic behavior of flat and curved sandwich with different position of debonding. They showed that the presence of the debonding damage causes the decrease of frequency and the curvature angle of sandwich.

Many researchers (Yang et al. 1998; Tenek et al. 1993; Lee et al. 2003) were studied the effects of delamination on the frequencies of composite.

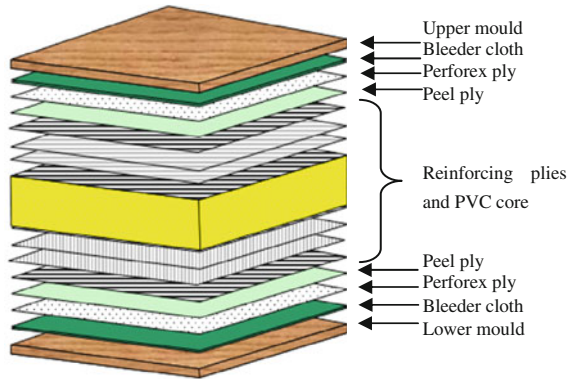
The purpose of the present article is to characterize the dynamic behavior of sandwich beams with shear damage on the foam by linear vibration method. The shear damage is initiated in the middle of the foam. The number of the shear damage is then increased two by two along the length of the specimens. The effects of the densities of damage on the frequency, loss factor were studied for each frequency mode.

## 2 Materials and Experimental Procedures

### 2.1 Materials

Sandwich material used in this study is constructed with glass fibre laminates as skins and with PVC closed-cell foams as core. The skins were cross-ply laminates with a total of 4 unidirectional layers of E-glass fibres in an epoxy matrix arranged

**Fig. 1** Schematic diagram of sandwich material assembly



in the sequence  $[0/90]_s$ . The sandwich beams are differentiated by the densities PVC core ( $60$  and  $100 \text{ kg m}^{-3}$ ) (Fig. 1).

The sandwich materials were prepared by hand lay-up process from epoxy resin, glass fibres and PVC closed-cell foams. Rectangular plates ( $600 \times 300 \text{ mm}$ ) of the composite were cured at room temperature with pressure ( $30 \text{ kPa}$ ) by using vacuum moulding process for  $10 \text{ h}$ . The plates were fabricated. The sandwich beams were cut with a diamond disk. The beam's dimensions are  $300 \times 40 \times 22 \text{ mm}$ .

## 2.2 Experimental Set up

The linear vibration tests are performed for both, i.e. the undamaged and damaged composite sandwich beams.

Figure 2 shows the experimental setup used to study the vibrations of specimens in a clamped-free configuration.

Generation of swept-sine signals is made up using an analyzer Stanford Research Systems SR785. The signals started by a start and end frequencies ranging from  $10 \text{ Hz}$  to  $2 \text{ kHz}$ . The signal excitation is amplified at a constant gain using a power amplifier, to excite the shaker BK 4809 attached at the extremity of the specimen. Vibrations are measured by an accelerometer attached at the free boundary of each sample and connected to a conditioning amplifier. The specimen is excited around resonance bending modes at intact as well as specimens with shear damage in the core using excitations from  $350 \text{ mV}$ , before amplification.

The shear damage is initiated in the middle of the foam. The number of the shear damage is then increased two by two along the length of the specimens (Fig. 3). The specimens were tested in linear (low amplitude of excitation) resonant experiment. For each material and each density of damage states, three samples were tested for repeatability three times.

Figure 4 shows an example of the Fourier transform of the response to an excitation level of a sandwich beam in a clamped-free configuration. This response



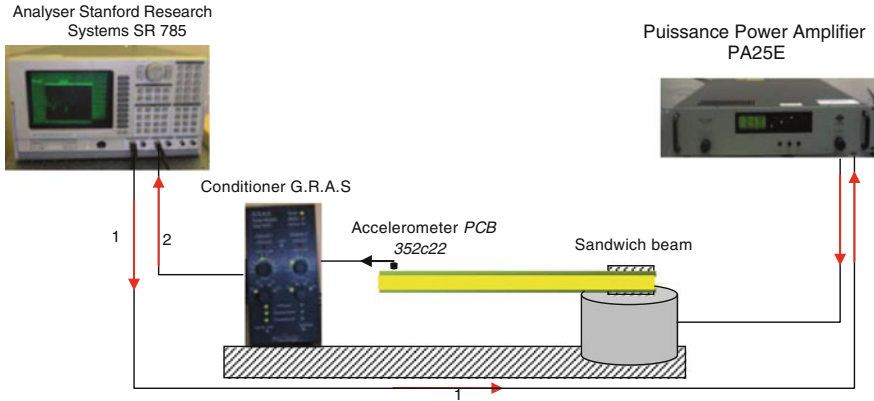


Fig. 2 Experimental setup

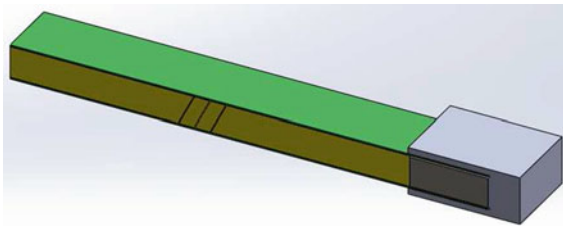


Fig. 3 Sandwich beam with 3 shear damages in the foam

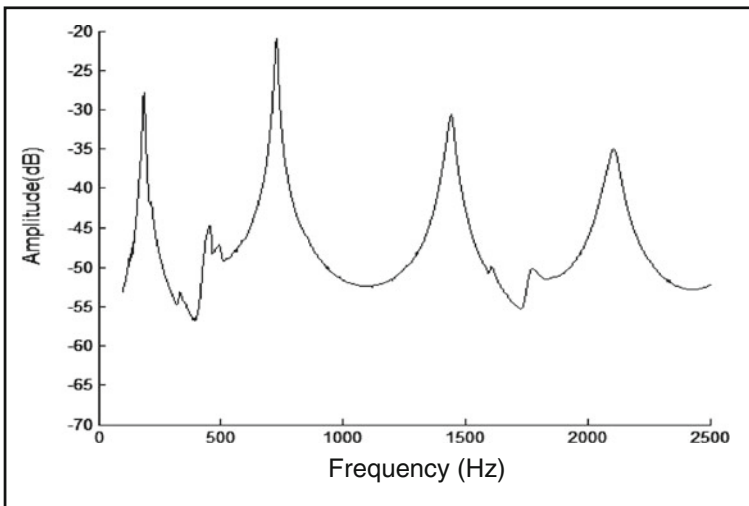


Fig. 4 Example of the Fourier transform of the response to an excitation level of a sandwich beam in a clamped-free configuration

shows the peaks corresponding to the natural frequencies of each mode (3 modes). The treatment of the experimental results is performed by polynomial interpolation of order up to 8. This method allows obtaining the values of the natural frequencies  $f_i$ , and the loss factor  $\eta_i$  of each mode. The loss factors are determined for different modes and different damage densities by the half-power bandwidth method (3 dB method).

### 3 Linear Vibration

The experimental vibration study is performed on sandwich beam with shear damage on the foam and in a clamped-free configuration. In this part, we studied the effect of damage densities on the frequencies and the loss factors.

#### 3.1 *Effects of Damage Densities on the Frequencies*

The specimens were tested at low amplitude excitation, to examine the effect of damage densities on frequency of sandwich beams in linear vibration.

Figure 5a, b show the evolution of natural frequency for four first modes versus the damage densities for two types of sandwich materials differentiated by the densities of their foams (60 and 100 kg m<sup>-3</sup>). The damage density is the ratio of the number of shear damage on the foams with the total length of the specimen.

The curves show that the natural frequencies decrease when the damage densities increase. This decrease is due to the rigidity loss, which is governed by the change of the mechanical properties of the sandwich materials (foam and skins). Then the natural frequencies depend on the damage and foam densities.

For the smaller damage densities, the higher order mode (mode 3) is much more sensitive than the others modes.

For example for core density of 60 kg m<sup>-3</sup>, the first and the third modes of the sandwich without shear damage are 186 and 1442 Hz. The sandwich beam with 12 m<sup>-1</sup> damage density, the first mode is about 173 Hz and for the third mode is 1165 Hz.

#### 3.2 *Effects of Damage Densities on the Loss Factors*

The loss factors are determined for different modes and different damage densities by the half-power bandwidth method (3 dB method).

Figure 6a, b show the evolution of loss factor for three first modes versus the damage densities for two types of sandwich materials differentiated by the densities of their foams (60 and 100 kg m<sup>-3</sup>). The results show that the loss factors increase with the increasing of damage densities.

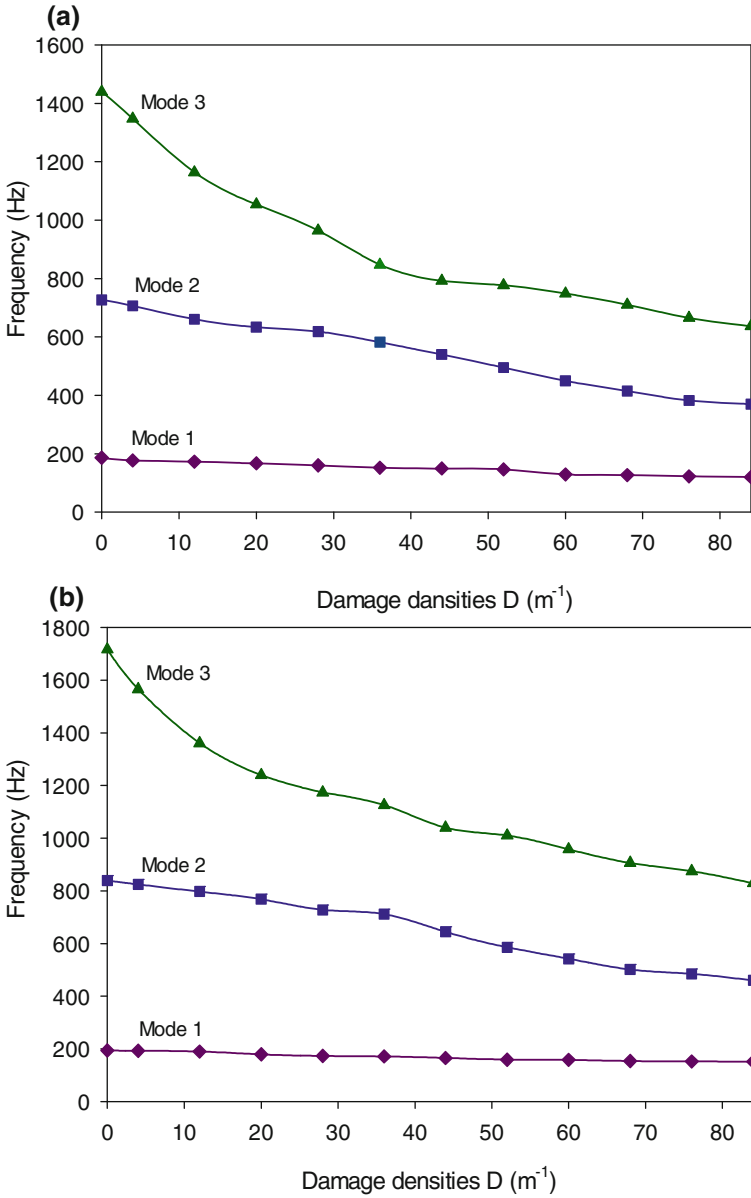


**Fig. 5** Evolution of the natural frequencies versus damage densities for sandwich specimens with foam density: **a**  $60 \text{ kg m}^{-3}$  and **b**  $100 \text{ kg m}^{-3}$

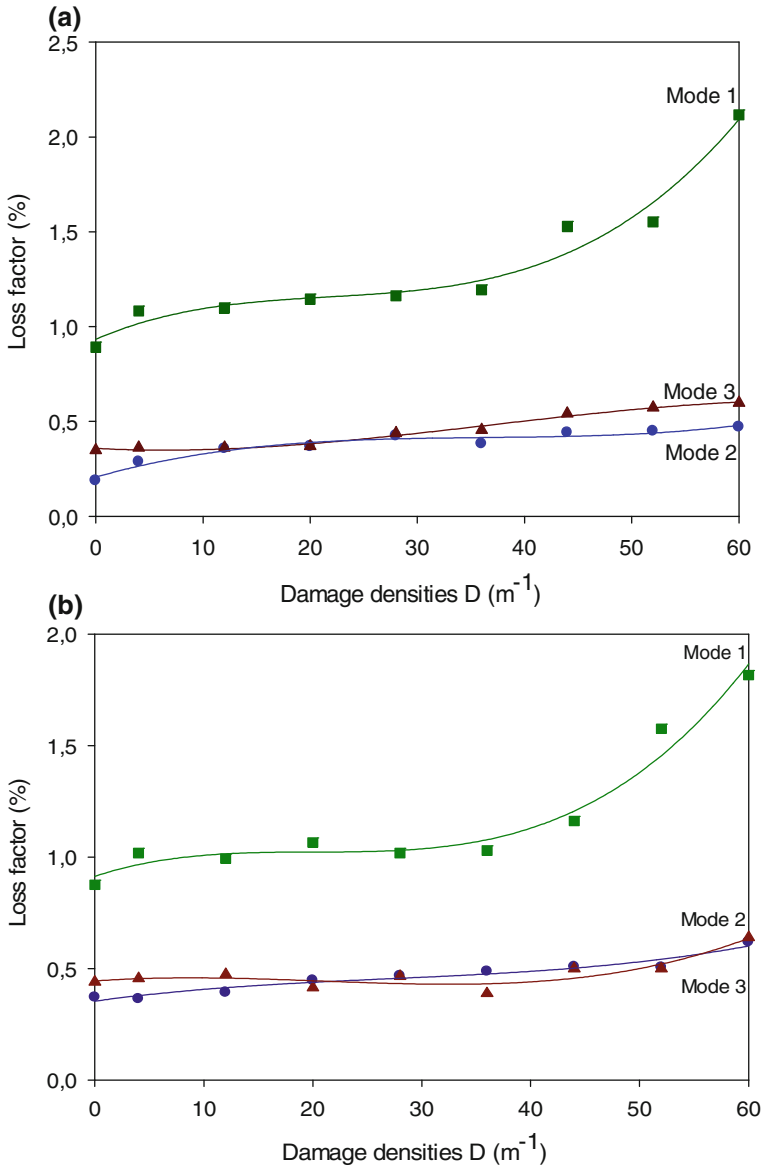


**Fig. 6** Evolution of the loss factor versus damage densities for sandwich specimens with foam density: **a**  $60 \text{ kg m}^{-3}$  and **b**  $100 \text{ kg m}^{-3}$

In the case of sandwich with foam of  $60 \text{ kg m}^{-3}$ , the value of the loss factor is 0.89 % for the undamaged specimens in first mode, while it is 2.12 % for sandwich with density of damage  $60 \text{ m}^{-1}$  in the foam.

For the sandwich with foam of  $100 \text{ kg m}^{-3}$ , the value of the loss factor is 0.87 % for the undamaged specimens, while it is 1.8 % for sandwich with  $60 \text{ m}^{-1}$  damage density in the foam. The variation of loss factor is considerably higher in case of the specimens with foam density of  $60 \text{ kg m}^{-3}$ . The density of the core plays an important role on the resistance.

## 4 Conclusion

The dynamic behavior of sandwich structures with shear damage by linear vibration method, are investigated. Two types of sandwich structures with different foam densities were considered. This study shows that the rigidity of the sandwiches increases with the increase of core and damage densities.

The main purpose of this study was to analyze the changes in linear parameter as function of densities of damage. The linear vibration characterization showed that the frequency decrease and the loss factor increase when the densities of damage increase. It also shown that when the density of the foam increases, the damping decreases slightly.

## References

- Caminero MA, Pavlopoulou S, Lopez-Pedrosa M, Nicolaisson BG, Pinna C, Soutis C (2013) Analysis of adhesively bonded repairs in composites: damage detection and prognosis. *Compos Struct* 95:500–517
- De Rosa IM, Santulli C, Sarasini F (2009) Acoustic emission for monitoring the mechanical behavior of natural fibre composites. *Compos: Part A* 40:1456–1469
- Fan W, Qiao PZ (2011) Vibration-based damage identification methods: a review and comparative study. *Struct Health Monit* 10:83–111
- Hsu DK (2009) Nondestructive evaluation of sandwich structures: a review of some inspection technique. *J Sandw Struct Mater* 11:275–291
- Idriss M (2013) Analyse expérimentale et par éléments finis du comportement statique et vibratoire des matériaux composites sandwich sains et endommagés. Thèse Université du Maine, Le Mans
- Idriss M, El Mahi A, El Guerjouma R (2015) Characterization of sandwich beams with debonding by linear and nonlinear vibration method. *Compos Struct* 120:200–207
- Lee JK, Lee JH (2002) Nondestructive evaluation on damage of carbon fiber sheet reinforced concrete. *Compos Struct* 58:139–147
- Lee S, Park T, Voyiadjis GZ (2003) Vibration analysis of multi-delaminated beams. *Compos B* 34:647–665
- Leone C, Lopresto V, Papa I, Caprino G (2012) Triangulation method as a valid tool to locate the damage in unidirectional CFRP laminates. *Compos Struct* 94:2418–2423
- Li B, Liu YQ, Gong KZ, Li Z (2013) Damage localization in composite laminates based on a quantitative expression of anisotropic wavefront. *Smart Mat Struct* 22:10
- Maldague X (2001) Theory and practice of infrared technology for nondestructive testing. Wiley, New York

- Okutan Baba B, Thoppul S (2009) Experimental evaluation of the vibration behavior of flat and curved sandwich composite beams with face/core debond. *Compos Struct* 91:110–119
- Shi Y, Swait T, Soutis C (2012) Modelling damage evolution in composite laminates subjected to low velocity impact. *Compos Struct* 94:2902–2913
- Su ZQ, Ye L, Lu Y (2006) Guided Lamb waves for identification of damage in composite structures: a review. *J Sound Vib* 295:753–780
- Tenek LH, Henneke EG II, Gunzburger MD (1993) Vibration of delaminated composite plates and some applications to non-destructive testing. *Compos Struct* 23:253–262
- Vladimir S, Hubertus F, Bremen V (2004) Higher-order free vibrations of sandwich beams with a locally damaged core. *Int J Solids Struct* 41:6529–6547
- Wen J, Xia ZH, Choy F (2011) Damage detection of carbon fiber reinforced polymer composites via electrical resistance measurement. *Compos Struct Part B-Eng* 42:77–86
- Yam LH, Yan YJ, Jiang JS (2003) Vibration-based damage detection for composite structures using wavelet transform and neural network identification. *Compos Struct* 60:403–412
- Yang S, Gibson RF, Gu L, Chen WH (1998) Modal parameter evaluation of degraded adhesively bonded composite beams. *Compos Struct* 43:79–91

# Parameter Identification of a Sandwich Beam Using Numerical-Based Inhomogeneous Wave Correlation Method

R. Ajili, O. Bareille, M.-L. Bouazizi, M.-N. Ichchou and N. Bouhaddi

**Abstract** To achieve low calculation-cost structural identification process, a numerical-based Inhomogeneous Wave Correlation (IWC) method is proposed in this paper as an extension to the experiment-based IWC. It consists, in a wave propagation framework also called wavenumber space (k-space), on identifying the propagation parameters such as the wavenumber and the spatial damping from the Frequency Response Functions (FRFs) computed using numerical simulations. The proposed method is applied to a sandwich beam with honeycomb cores in flexural vibration. Compared to its implementation based on experimentally-measured FRFs, the proposed numerical-based IWC proves to be an efficient tool for more inner structural parameter identification in wide frequency band with respect to the Mc Daniel method considered as reference.

**Keywords** Identification · Inhomogeneous wave correlation · Wavenumber space · Damping · Honeycomb-core sandwich

---

R. Ajili (✉)

National School of Engineers of Tunis (ENIT), University of Tunis el Manar,  
BP 37, Le Belvedere, 1002 Tunis, Tunisia  
e-mail: ajiliramis@gmail.com

R. Ajili · O. Bareille · M.-N. Ichchou

Laboratory of Tribology and Dynamics of Systems (LTDS),  
Ecole Centrale de Lyon, 36 Avenue Guy de Collongues, 69130 Ecully, France

R. Ajili · M.-L. Bouazizi

Preparatory Engineering Institute of Nabeul (IPEIN), Research Unit of Structural Dynamics,  
Modelling and Engineering of Multi-Physics, 8000 M'rzouga Nabeul, Tunisia

N. Bouhaddi

FEMTO-ST Institute UMR 6174, Department of Applied Mechanics,  
University of Franche-Comté, 24 Chemin de l'Épitaphe, 25000 Besançon, France

M.-L. Bouazizi

Mechanical Department, College of Engineering, Prince Sattam Bin Abdulaziz University,  
Al-Kharj, Kingdom of Saudi Arabia

© Springer International Publishing Switzerland 2017

T. Fakhfakh et al. (eds.), *Advances in Acoustics and Vibration*,  
Applied Condition Monitoring 5, DOI 10.1007/978-3-319-41459-1\_7

## 1 Introduction

Structural identification forms an ever growing emphasis in engineering applications, such as vibroacoustics. Since experiments are expensive, the use of numerical simulations becomes more and more inevitable in order to reduce the cost of the identification process for bulk structural property forecasting. In the literature, most works focus on the modal-based numerical approaches. In spite of their efficiency in low frequency range, these methods proved to be limited in mid and high frequencies. This disadvantage makes their use of limited interest. Other methods based on wave propagation approach are introduced as an alternative. The latter are based on the wavenumber space (k-space) analysis for parameter identification (Ichchou et al. 2008a).

With special emphasis on the k-space characteristics identification, the most frequently used approaches are the Mc Daniel (Mc Daniel et al. 2000a) and the Inhomogeneous Wave Correlation (IWC) (Berthaut et al 2005) methods. The principle of the Mc Daniel method is to adjust iteratively, for each frequency, the wavenumber using as initial estimate the wavenumbers for the neighboring frequencies. This method can also estimate the structural damping at any frequency. It was implemented in Mc Daniel et al. (2000b) for damping identification of a freely suspended beam excited by an arbitrary transient load. It proved to be efficient with respect to the modal approach. An extension of the application from one to two-dimensional structures was proposed in Ferguson et al. (2002) by combining a Continuous Fourier Transform (CFT) with a least square minimization. It permits to identify a single dominant homogeneous wave when using a windowed field far away from the near-field sources which would otherwise create disturbances.

The originality of the IWC lies in the use of inhomogeneous waves to describe the vibratory field. An introduced correlation index, depending on propagation parameters, allows extracting the parameters in each direction of propagation, and thus eliminating the near-field sources. Indeed, it builds a dispersion equation, from a space vibratory field, which depends on the frequency and direction. In the literature, the IWC method was applied in Berthaut et al. (2005) and Ichchou et al. (2008b) to parameter identification of isotropic and anisotropic ribbed panels and plates, in Ichchou et al. (2008a) to honeycomb beams and panels with bending load at wide frequency band, in Inqui  t   (2008) to identify the phase velocity of a quasi-isotropic laminated composite plate, in Carmona et al. (2007) to estimate the elasticity modulus of a plate with respect to a modal approach and in Rak et al. (2008), with the Mc Daniel, to identify the damping of an homogeneous beam covered with viscoelastic layers. The efficiency of these methods is proved with respect to standard Oberst tests. In this work, the IWC method is used for parameter identification and compared to the Mc Daniel method considered as reference.

Besides that, the growing industrial integration of composite materials, in particular for high technology sectors, is due to their interesting mechanical and material properties, high energy dissipation and resistance/weight ratios. In the present paper, the parameters identification of a sandwich composite beam of



honeycomb core with bending load is illustrated. The experimental and numerical Frequency responses functions (FRFs) computation permits to identify the structural damping of the beam by estimating the propagation parameters (wavenumber and special damping) using the IWC method compared to the Mc Daniel method.

## 2 Identification Methods

The main two identification methods which are considered in this paper are briefly described thereafter. The authors refer to the aforementioned literature concerning the Mc Daniel's method and the IWC one.

### 2.1 The Mc Daniel Method

In a mathematical framework, the Mc Daniel is based on the solving of a linear differential equation of motion of the neutral axe or surface of the structure of the form

$$-\omega^2 U = \mathcal{L}\{U\} \quad (1)$$

where  $\mathcal{L}\{U\}$  is a linear operator containing the displacement ( $U$ ) derivatives with respect to the space coordinate  $x$ .

The solution of Eq. (1) is thus expressed as

$$U(x) = \sum_{n=1}^N \left\{ F_n e^{ik_n x} + B_n e^{ik_n(L-x)} \right\} \quad (2)$$

where  $N$  is the number of different waves. Each wave  $n$  is characterized with a wavenumber  $k_n$  of complex value containing positive real and imaginary parts and an amplitude  $F_n$  or  $B_n$  according to forward or backward propagation, respectively, and computed using boundary conditions.

The wavenumber is computed according to the type of the propagated wave through the structure. It is, in fact, expressed, in the flexural, longitudinal and torsion wave case, respectively, as

$$k_f = \sqrt{4 \frac{\rho A \omega^2}{E(\omega)(1 - i\gamma(\omega))I}}, \quad k_l = \sqrt{\frac{\rho \omega^2}{E(\omega)(1 - i\gamma(\omega))}}, \quad k_t = \sqrt{\frac{\rho \omega^2}{G(\omega)(1 - i\gamma(\omega))}} \quad (3)$$

where  $E(\omega)$  and  $G(\omega) = E(\omega)/2(1 + \nu)$  are the real parts of the Young and shear modulus, respectively,  $\rho$  is the mass density,  $I$  the inertia moment,  $A$  the area of the transversal section and  $\gamma(\omega)$  the damping of the material.

The wavenumber being calculated, the damping can be identified as

$$\gamma = \left| \frac{\Im\{k_i^2\}}{\Re\{k_i^2\}} \right| \quad (4)$$

where the index  $i$  can refer to the indexes  $f$ ,  $l$  or  $t$  according to the specific case.  $\Im\{\cdot\}$  and  $\Re\{\cdot\}$  correspond respectively to the imaginary and real parts.

The wavenumber was initially supposed. To verify its validity, it is compared to the obtained wavenumber through the error function defined as

$$\varepsilon^2(k) = \sqrt{\frac{\sum_{m=1}^M |U^{mes}(x_m, \omega) - U(x_m, \omega)|^2}{\sum_{m=1}^M |U(x_m, \omega)|^2}} \quad (5)$$

where  $M$  is the number of considered measurement points and  $U^{mes}(x_m, \omega)$  and  $U(x_m, \omega)$  are the measured and real wave fields, respectively. To minimize this error, an optimization algorithm varying the wavenumber is implemented.

## 2.2 The IWC Method

The principle of the IWC method is to compute propagation parameters  $k$  and  $\gamma$  by correlating the vibratory field  $u(x, y, \omega)$  of the structure with an inhomogeneous wave:

$$u_{IWC} = \int_0^{2\pi} A(\theta) e^{-ik(\theta)(1+i\gamma(\theta))(x \cos(\theta) + y \sin(\theta))} d\theta \quad (6)$$

The correlation is performed through an *IWC* criterion defined as

$$IWC(k_{IWC}, \gamma_{IWC}, \theta) = \frac{\iint_S u \cdot \bar{u}_{IWC} dx dy}{\sqrt{\iint_S u \cdot \bar{u} dx dy \times \iint_S u_{IWC} \cdot \bar{u}_{IWC} dx dy}} \quad (7)$$

where  $\bar{u}_{IWC}$  is the complex conjugate of the wave  $u_{IWC}$ . This criterion represents the wave ( $u_{IWC}$ ) contribution in the field  $u(x, y, \omega)$  or also the ratio of the energy carried by the wave by the total energy contained in the field. Maximizing the *IWC* correlation criterion leads to optimizing the wavenumber and damping identification.

According to the works performed in Berthaut (2004) on plate structures, for a zero fixed damping ( $\gamma_0 = 0$ ) and direction ( $\theta_0 = 0$ ), the wavenumber  $k_0$  is calculated for a maximal *IWC* criterion. Then, the damping  $\gamma_0$  is computed. For the initial obtained couple  $(k_0, \gamma_0)$ , an iterative algorithm is implemented to calculate the couples  $(k_i, \gamma_i)$  for a finite set of directions  $\theta_i$ . The  $(k_i, \gamma_i)$  being calculated, they are

sorted and the damping values which correspond to vanishing waves ( $\gamma(\theta_i) > 1$ ) are eliminated. The final step consists in varying the frequency band of study and identifying the wavenumber  $k(\theta, \omega)$  and the damping  $\gamma(\theta, \omega)$  for each frequency iteration.

### 3 Experiments and Numerical Simulations

#### 3.1 Structure

The considered example is a sandwich composite beam with aluminum honeycomb core (Fig. 1) of length 1 m and width 0.029 m. The thickness of the core plate is 0.011 m. The face plates are made of 6-ply carbon-fiber composite oriented respectively according to the directions [45-45 45 45-45 45]. Materials properties of each component are listed in Table 1.

The beam is freely suspended. A point force is applied using an electrodynamic shaker Bruel&Kjær 4809. The normal velocity of the panel was measured by a Scanning Laser Vibrometer (Ometron VPI+). The phase reference was obtained by a force transducer Bruel&Kjær 8001. Both signals were sampled with a Hewlett Packard Paragon 35654A (Ichchou et al. 2008). 19 observation points are considered such as  $\Delta x = 0.05$  m in both experimental measurements and Finite Element Model (FEM) for numerical simulations.

The objective of the application is to identify the wavenumber and the spatial damping through two possible configurations: experiment-based and numerical-based identification. In fact, experimental and numerical FRFs results are

**Fig. 1** Honeycomb-core sandwich beam

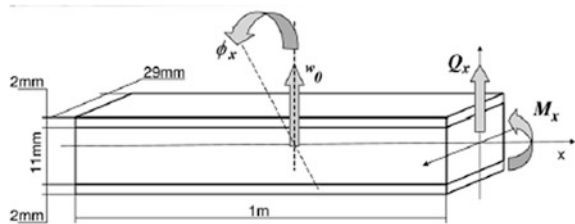


**Table 1** Material properties of the components of the sandwich beam

Material		Properties							
Type	Reference	$E_1$ (GPa)	$E_2$ (GPa)	$E_3$ (GPa)	$\nu$	$G_{12}$ (GPa)	$G_{13}$ (GPa)	$G_{23}$ (GPa)	$\rho$ ( $\text{kg m}^{-3}$ )
Face plates	Vicotex G803/914	60.27	60.27	–	0.029	5	5	5	1594
Core plate	5056 3.1 3/16.001	–	–	0.668	–	–	0.31	0.137	49.65

introduced to the identification process. The IWC method is used and its results are compared to those obtained when applying the Mc Daniel method.

The final goal is here to assess the ability of the IWC method to perform numerical predictions of the propagation characteristics of complex materials.

## 3.2 Results and Discussions

### 3.2.1 Experimental Results

The results presented below show a high sensitivity of the two methods to the measurement's disturbance and noise in the frequency range [3000, 6400 Hz], due to experimental conditions. The FRFs are less sharp and thus the wave numbers suffer some uneven changes at some frequencies. To overcome this issue, some functional regressions are required. This can be done through the least-squares technique: coarse regression corresponding to a low polynomial order regression and fine regression corresponding to a higher order one.

The effect of the noise on the identified wavenumber and damping is visible in Figs. 2 and 3, respectively, before applying the regression technique (blue and black curves). After regression, a good agreement between the identified wavenumber using the IWC and Mc Daniel methods can be shown in the same figures (brown and magenta curves for coarse regression and green and red curves for fine regression). Consequently, the IWC method proves to be an efficient tool for parameter identification from experimental FRFs.

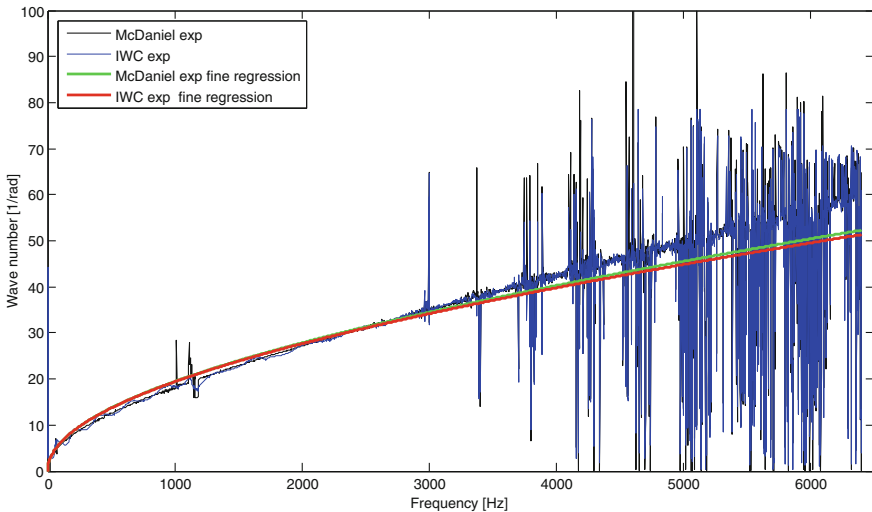


**Fig. 2** Evolution of the wavenumber identified using the IWC and Mc Daniel methods according to frequency (before and after regression)

### 3.2.2 Numerical Simulations Compared to Experimental Results

A comparison between the identified parameters using experimental and numerical FRFs after applying a fine regression is illustrated by Figs. 4 and 5. The

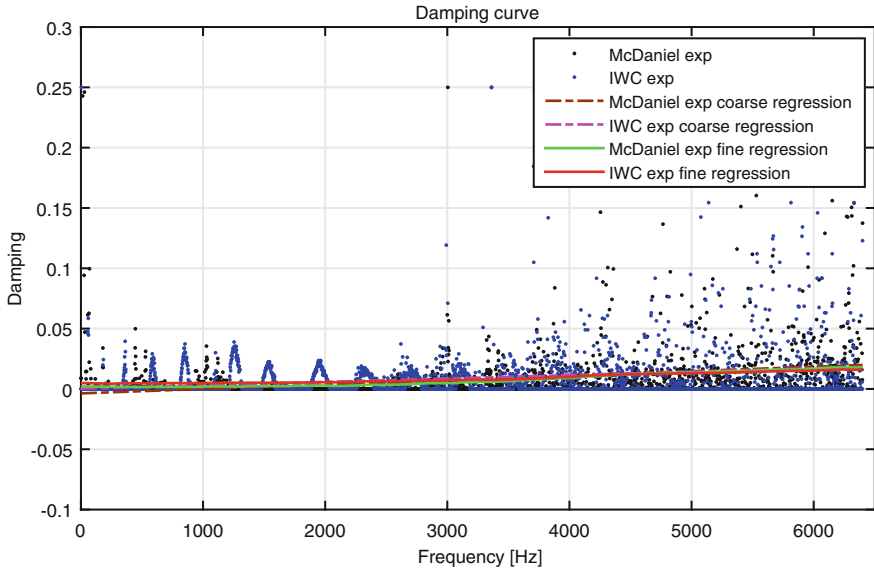


**Fig. 3** Evolution of the damping identified using the IWC and Mc Daniel methods according to frequency (before and after regression)

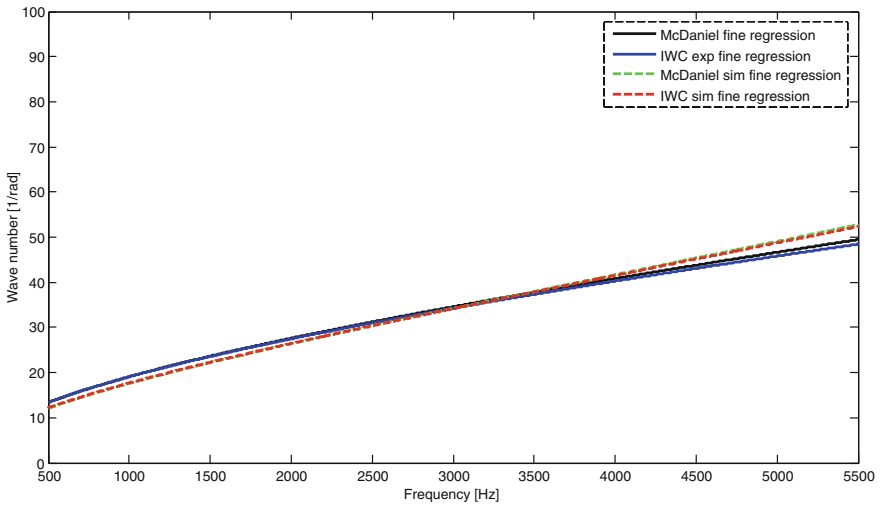


**Fig. 4** Comparison of the wavenumbers calculated using the IWC and MC Daniel methods according to the experimental and simulated FRFs

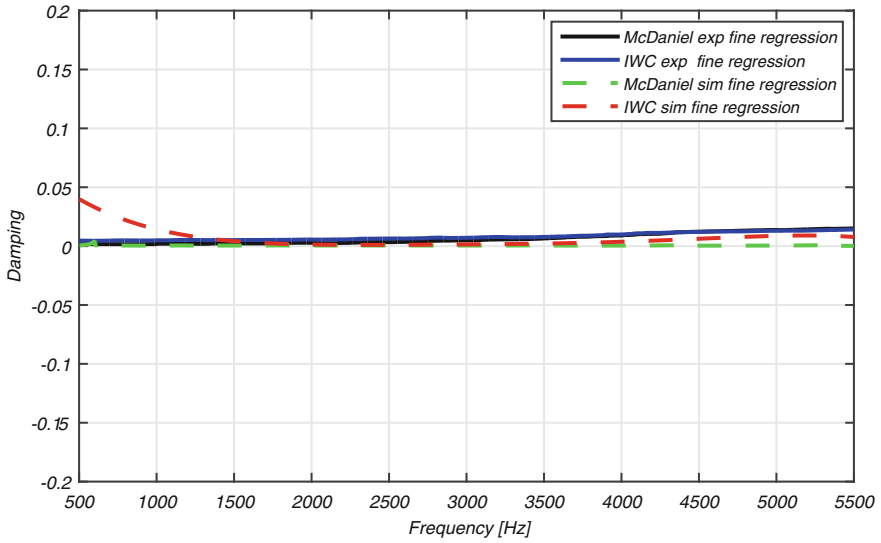


**Fig. 5** Comparison of the damping calculated using the IWC and MC Daniel methods according to the experimental and simulated FRFs

numerical-based identification process is in agreement with the experiment-based one. The efficiency of the IWC method is proved with respect to the Mc Daniel method in the two identification cases.

Either method can then be considered as predictive tools for bulk characteristics' predictions on composite material or on other complex substructures.

Note that the regression must be carefully done in order to filter the measurement noise and preserve the useful information contained in the displacement field and thus to correctly identify the wavenumber and the damping. To achieve this aim, the least squares method is implemented. It is based on the principle of minimizing the variance of the interpolation error by adequately choosing the interpolation polynomials order. First order polynomials are used in this work for coarse regression and fifth order polynomials for the fine regression.

### 3.2.3 Numerical Simulations

The numerical FRFs of the observation points, in the frequency range [500, 5500] Hz, are presented in Fig. 6.

As expected from the experimental applications, Figs. 7 and 8 show a good agreement between the identified wavenumber and spatial damping using the IWC and Mc Daniel methods. The IWC method is consequently an efficient tool for propagative characteristics identification from numerical FRFs.

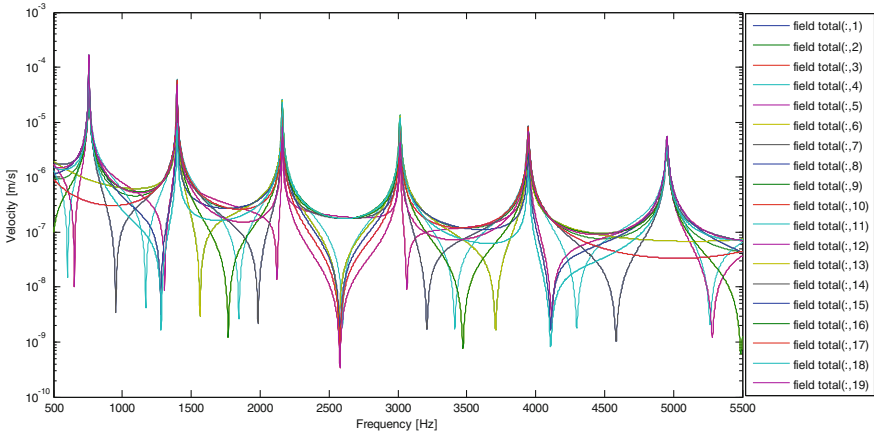


Fig. 6 Numerical velocity FRFs

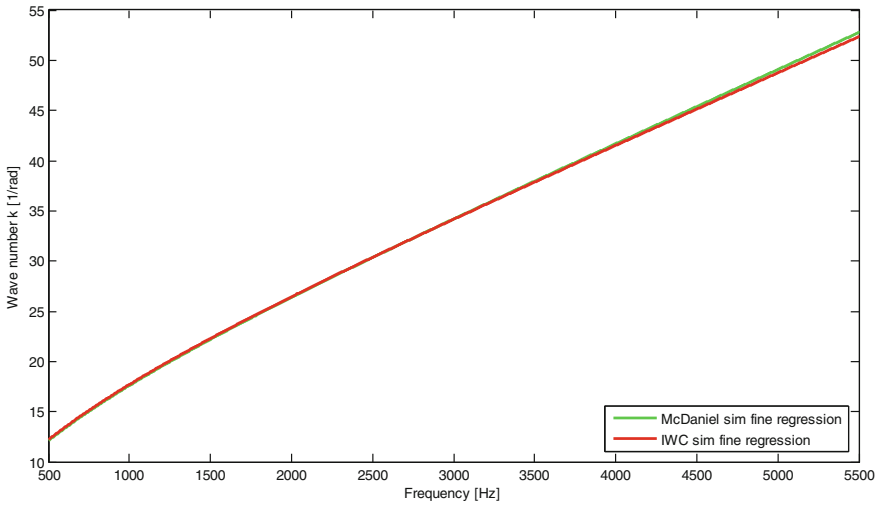
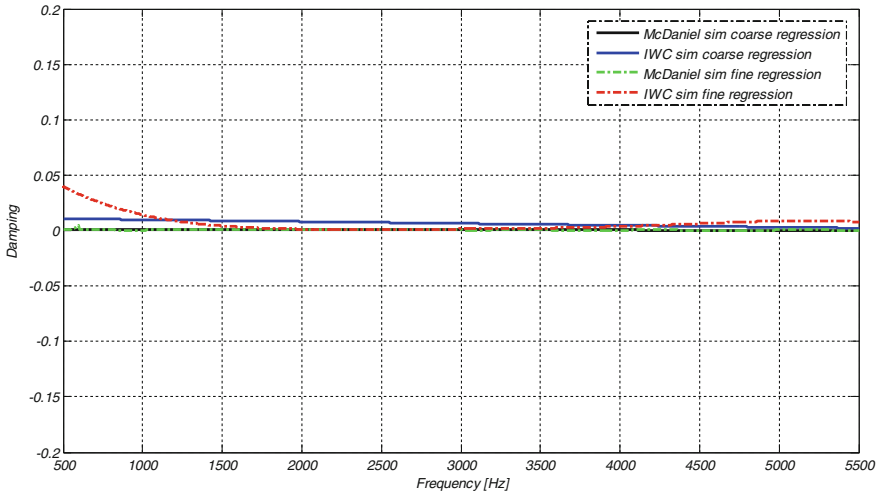


Fig. 7 Comparison of the wavenumbers calculated using the IWC and MC Daniel methods according to simulated FRFs



**Fig. 8** Comparison of the damping values calculated using the IWC and MC Daniel methods according to simulated FRFs

## 4 Conclusion

The agreement between the results of the IWC and the Mc Daniel methods, both according to experiments and simulations, proves that the numerical-based IWC method is an efficient tool for parameter identification in mid-high frequency range. It can be considered as an alternative to the modal-based methods.

The deterministic model parameters identification cannot perfectly agree with the experimental one. Therefore, extending the study to take into account uncertainties is an interesting perspective to this work which permits to achieve more realistic model parameters identification.

However, the results obtained for the damping identification are not sufficiently accurate. The identification process must be improved in order to achieve more accurate results. This is the current purpose of on-going researches.

## References

- Berthaut J (2004) Contribution à l'identification large bande des structures anisotropes— Application aux tables d'harmonie des pianos. PhD thesis: Ecole Centrale de Lyon
- Berthaut J, Ichchou MN, Jezequel L (2005) K-space identification of apparent structural behavior. *J Sound Vib* 280:1125–1131
- Carmona JC, Mazzoni D, Caillet J (2007) Plate moduli estimation using nearfield acoustic holography techniques. ICSV14: Cairns, Australia, 9–12 July
- Ferguson NS, Halkyard CR, Mace BG, Heron KH (2002) The estimation of wavenumbers in two dimensional structures. In *Proceedings of ISMA II*, pp 799–806



- Ichchou MN, Bareille O, Berthaut J (2008a) Identification of effective sandwich structural properties via an inverse wave approach. *Eng Struct* 30:2591–2604
- Ichchou MN, Berthaut J, Collet M (2008b) Multi-mode wave propagation in ribbed plates: Part I, wavenumber-space characteristics. *Int J Solids Struct* 45:1179–1195
- Inqui  t   G (2008) Numerical simulation of wave propagation in laminated composite plates. PhD thesis, Ecole Centrale de Lyon, France
- Mc Daniel JG, Shepard WS (2000a) Estimation of structural wave numbers from spatially sparse response measurements. *J Acoust Soc Am* 108(4):1674–1682
- Mc Daniel JG, Dupont P, Salvino L (2000b) A wave approach to estimating frequency-dependent damping under transient loading. *J Sound Vib* 231(2):433–449
- Rak M, Ichchou MN, Jan H-S (2008) Identification of structural loss factor from spatially distributed measurements on beams with viscoelastic layer. *J Sound Vib* 310:801–811

# Time Domain Stability Analysis for Machining Processes

Asia Maamar, Belhassen Chedli Bouzgarrou, Vincent Gagnol and Raouf Fathallah

**Abstract** In this paper, a time-domain simulation approach for stability analysis of machining processes is presented. Stability limits are detected by a new criterion. To ensure the reliability and the effectiveness of the proposed approach, the stability of the turning process is first studied, and then compared to the well-known semi analytical frequency-domain approach of Budak and Altintas, which gives exact stability predictions in this case. However, the proposed time-domain approach in milling process provides more conservative and realistic results in stability predictions. These results highlight the lack of precision of the classical frequency-domain approach for which several simplifying assumptions are made.

**Keywords** Turning · Milling · Stability lobes · Chatter

## 1 Introduction

The productivity is a key issue in machining operations. It depends on the cutting parameters but it is restricted by the phenomenon of chatter instability.

---

A. Maamar (✉) · B.C. Bouzgarrou · V. Gagnol  
Institut Pascal, Université de Clermont, Campus Universitaire de Clermont-Ferrand,  
Sigma-Clermont BP 10448, 63175 Aubière Cedex, France  
e-mail: [essia.maamer@sigma-clermont.fr](mailto:essia.maamer@sigma-clermont.fr)

B.C. Bouzgarrou  
e-mail: [belhassen-chedli.bouzgarrou@sigma-clermont.fr](mailto:belhassen-chedli.bouzgarrou@sigma-clermont.fr)

V. Gagnol  
e-mail: [vincent.gagnol@sigma-clermont.fr](mailto:vincent.gagnol@sigma-clermont.fr)

R. Fathallah  
Ecole Nationale D'Ingénieurs de Sousse (ENISo), Technopole de Sousse,  
Université de Sousse, BP 264 Sousse Erriadh 4023, Tunisie, Tunisia  
e-mail: [raouf.fathallah@gmail.com](mailto:raouf.fathallah@gmail.com)

Chatter has been widely studied (Altıntaş and Budak 1995; Tobias and Fishwick 1958). It consists in a feedback mechanism for the growth of the self-excited vibrations due to the vibrations in chip thickness, cutting force and tool vibrations (Gagnol et al. 2011). Many researches are performed to model this phenomenon, in order to avoid it (Altıntaş and Budak 1995; Merritt 1965; Tobias and Fishwick 1958). These studies have led to graphic charts, commonly known as stability lobe diagrams, showing the stability limits as a function of chip thickness and spindle speed. In 1983, Tlustý used a time domain simulation to predict machining stability of helical end mills and to develop the stability diagrams (Tlustý et al. 1983). In 1991, Smith highlighted the use of peak-to-peak force diagrams to plot cutting stability limit (Smith and Tlustý 1993; Tlustý et al. 1991). Altıntaş and Budak, in 1995, developed an analytical approach to develop the stability lobes in milling (Altıntaş and Budak 1995).

In the present study, machining stability prediction is developed by a time-domain simulation approach. The proposed approach allows evaluating stability prediction error attached to the hypotheses made in the frequency domain by Altıntaş and Budak.

## 2 Stability Prediction in Turning

In this section, a stability analysis in turning process is performed based on a time-domain approach. The objective of this work is to validate the proposed approach.

### 2.1 *Dynamic Cutting Model in Turning*

The cutting model, shown on Fig. 1, represents a rigid tool in interaction with a flexible workpiece in the radial direction.

The model is based on these hypotheses:

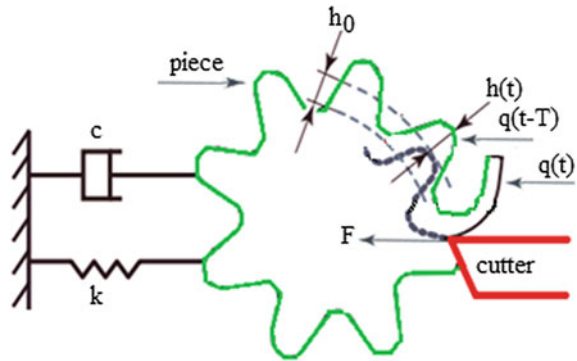
- An orthogonal cutting, so the effort is proportional to the depth and the width of cut.
- The dynamic behavior of the workpiece is assimilated to a one-DDL “mass-spring-damper” system.

The system’s equation of motion is given by the following relation:

$$m\ddot{q}(t) + c\dot{q}(t) + kq(t) = F(t) \quad (1)$$

where  $m$ ,  $c$ ,  $k$  are respectively the mass, damping and stiffness constants of the workpiece in the radial direction.

**Fig. 1** Dynamic cutting model in turning (Altintas 2012)



Initially and during the first round, the surface of the piece is smooth without waves, whereas in the next revolutions, the tool starts leaving a wavy surface due to the vibrations caused by the radial cutting force  $F$ .

Hence, the resulting dynamic chip thickness is no longer constant, but it varies in function of the vibration frequency and the speed of the workpiece.

The general dynamic chip thickness can be expressed as follows:

$$h(t) = h_0 - [q(t) - q(t - T)] \tag{2}$$

where  $h_0$  is the initial chip thickness.  $[q(t) - q(t - T)]$  is the dynamic chip thickness produced owing to vibrations at the present time  $t$  and one revolution period before  $T$ . This expression defines the contribution of the surface regeneration mechanism. The expression of the instantaneous cutting force is:

$$F(t) = k_f a h(t) \tag{3}$$

$k_f$  is the specific cutting pressure.

In the Laplace domain, the current vibrations, caused by the cutting force, is expressed as:

$$q(s) = k_f a h(s) \phi(s) \tag{4}$$

Were the transfer function of the single DOF of the workpiece is:

$$\phi(s) = \frac{q(s)}{F(s)} = \frac{1}{ms^2 + cs + k}$$

Figure 2 is a close loop block diagram that represents the chatter vibration system. In this diagram, the parameters of the dynamic cutting process are in the Laplace (frequency) domain. The input of the system is the initial chip thickness  $h_0$ , and the output of this feedback system is the current vibration  $q(t)$ , left on the inner surface.

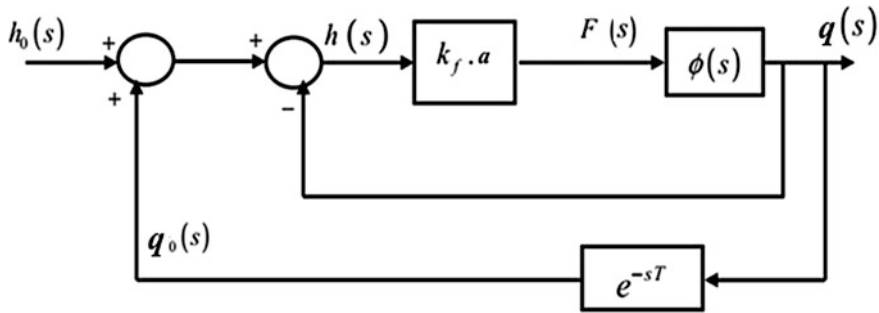


Fig. 2 Block diagram of chatter dynamics in turning process

The simulation of this diagram block, for different cutting conditions, gives us two cases of the time-domain workpiece trajectory, shown on Fig. 3a, b.

These simulations have been carried-out on Matlab-Simulink by using ODE45 integration scheme with a time step  $<10^{-4}$  s. At each instant, the actual depth of cut, as well as the force involved in the cutting, is computed.

In Fig. 3a, the instantaneous workpiece displacements are shown, from a rotational speed  $N = 5350$  rpm and an axial depth of cut  $a = 1.5 \times 10^{-5}$  m. With the same rotational speed, but with a depth of cut  $a = 1.5 \times 10^{-4}$  m (Fig. 3b), the vibrations rise to a level where the tool begins to lose contact with the workpiece.

## 2.2 Proposed Stability Criterion

From the instantaneous tool displacement, the stability identification requires defining an appropriate criterion. In this work, the proposed criterion is defined through these steps:

First, the creation of a vector  $Z$  that contains the values of displacement during the simulation:

$$Z = [q(t_1)q(t_2) \dots q(t_m)]^T$$

- Than two vectors  $X$  and  $Y$  contain the first and the last thousand values of the vector  $Z$  respectively:

$$X = Z(0 : 1000)$$

$$Y = Z(\text{length}(Z) - 1000 : \text{length}(Z))$$

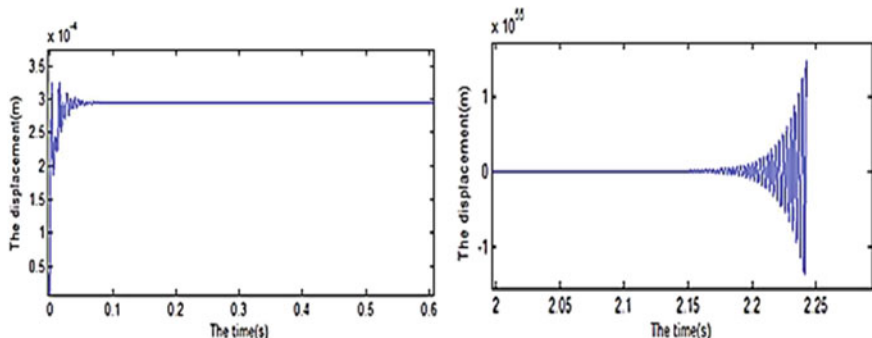


**Fig. 3** **a** Instantaneous displacement for stable cutting; **b** instantaneous trajectory for unstable cutting

- For each vector X and Y, the difference between the displacement and its mean value is calculated, then, the root mean square (RMS) values of this difference  $\gamma_X$  and  $\gamma_Y$  are determined by using these two expressions:

$$\gamma_X = \sqrt{\left(\frac{1}{T}\right) \int_0^T [q_X(t) - \overline{q_X}]^2 dt}, \quad \gamma_Y = \sqrt{\left(\frac{1}{T}\right) \int_0^T [q_Y(t) - \overline{q_X}]^2 dt} \quad (5)$$

- Finally, the stability criterion is defined:
- If  $\gamma_Y > \gamma_X$ , than the system is unstable and we mark in red the point (N, a) on the stability diagram.
- Else, the cutting system is stable and we mark in green the point (N, a) on the stability diagram.

A range of rotational speeds and a rotational speed step size, a range of axial depths of cut and an axial depth of cut step size are specified. The simulation program is then iteratively called for each combination of cutting conditions. After each run, the time displacements are scanned. In each case, the stability criterion is used to know if the cutting system is stable or not. The time-domain simulations lead to the limit of stability, which is in the form of lobes.

### 2.3 Verification of the Proposed Approach

In order to verify proposed approach, the stability prediction is carried out in the frequency domain by using the method of Altintas and Budak. In Fig. 4, both the time-domain and the frequency-domain stability limits are shown on the same graph. A total correlation between the two stability lobes is clearly seen with same stability limits.

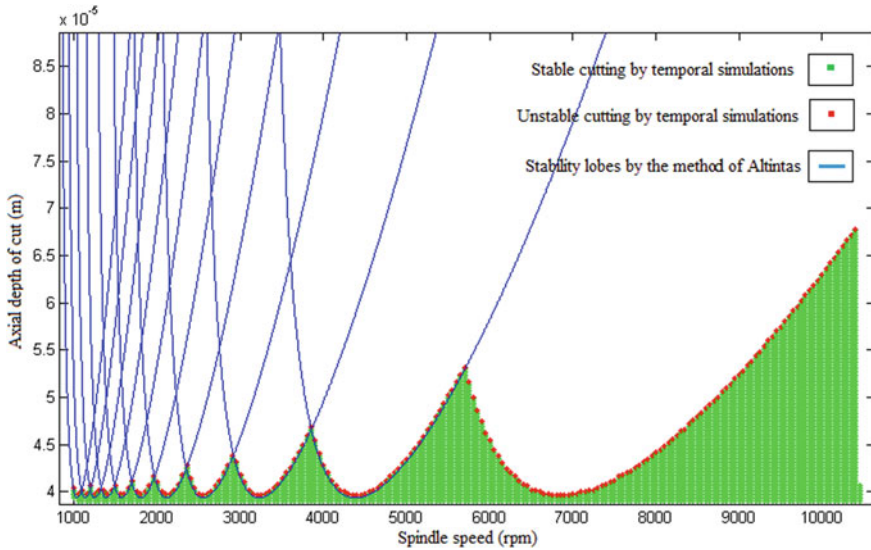


Fig. 4 Validation of the present method

This result is logic because, in frequency-domain approach, Altintas and Budak didn't use any approximation when modeling the dynamic behavior of the turning process. Finally, this correlation validates completely the proposed time-domain approach. Moreover, time-domain prediction gives more realistic results for spindle speeds higher than 5500 rpm.

### 3 Stability Prediction in Milling

#### 3.1 Dynamic Cutting Model in Milling

The dynamics of the milling process has been derived by Altintas and Budak, is considered to have two DOFs as shown in Fig. 5.

The cutting tool is assumed to have 4 teeth. The cutting forces excite the structure in the X and Y directions, causing dynamic displacements  $x(t)$  and  $y(t)$  of the tool, respectively.

The system's equations of motion are given by the following relations:

$$\begin{cases} m_x \ddot{x}(t) + c_x \dot{x}(t) + k_x x(t) = F_x(t) \\ m_y \ddot{y}(t) + c_y \dot{y}(t) + k_y y(t) = F_y(t) \end{cases} \quad (6)$$

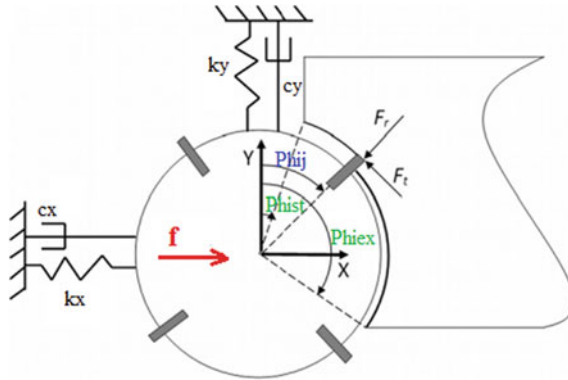


Fig. 5 Dynamic cutting model in milling (Altıntaş and Budak 1995)

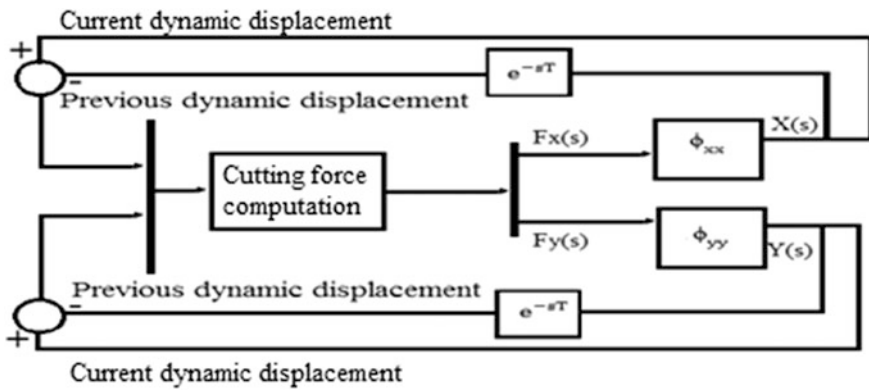


Fig. 6 Block diagram of chatter dynamics in milling process

Similarly, the stability analysis is performed firstly by the proposed time-domain approach and then by the well-known semi analytical approach of Altıntaş and Budak (1995), in the frequency domain.

Figure 6 is a close loop block diagram that represents the chatter vibration system, in the case of the cutting in milling. In this diagram, for each direction of the displacements X and Y, a transfer function,  $\phi_{xx}$  and  $\phi_{yy}$ , is integrated respectively. They are expressed as:

$$\phi_{xx} = \frac{1}{m_x s^2 + c_x s + k_x}, \quad \phi_{yy} = \frac{1}{m_y s^2 + c_y s + k_y} \tag{7}$$

These simulations have been carried-out on Matlab-Simulink by using ODE45 integration scheme with a time step  $<10^{-4}$  s. At each time step, the spindle angular position is updated, the forces in the two directions X and Y involved in the cutting



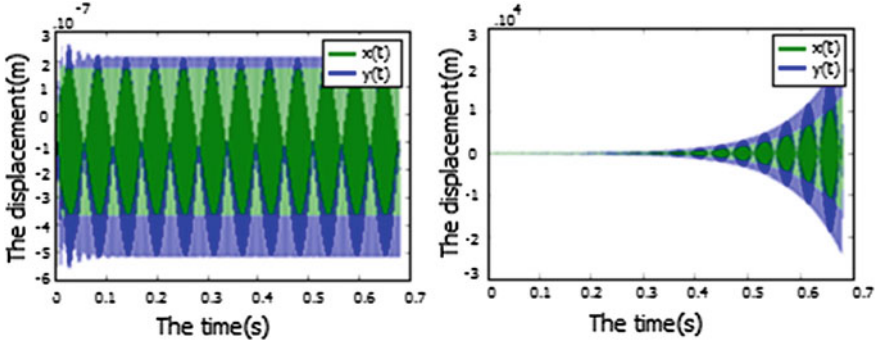


Fig. 7 Tool displacements in function of time **a** a stable cutting conditions; **b** unstable cutting

are calculated which allows determining the displacement of the tool in the directions X and Y.

For the elaboration of the stability lobes diagram, the simulation program is iteratively called for each combination of cutting conditions, which are the rotational speed and the depth of cut. After each run, the tool displacements in function of time can be plotted.

In Fig. 7a, the simulated tool displacements in function of time in the two direction X and Y are shown for a spindle speed  $N = 4000$  rpm and an axial depth of cut  $a = 1.2 \times 10^{-4}$  m. With the same rotational speed, but now with a depth of cut  $a = 3.1 \times 10^{-3}$  m (Fig. 7b), the vibrations rise to a level where the tool begins to lose contact with the workpiece.

### 3.2 Proposed Stability Criterion

In this case, the stability criterion is a little bit different from that used in the turning process, because the milling process is approximated to a two DOFs system. In the milling process, the proposed criterion is defined through these steps:

- First, the creation of two vectors Q1 et Q2 that contain the values of displacement during the simulation:

$$Q1 = [x(t1)x(t2) \dots x(tn)]^T, \quad Q2 = [y(t1)y(t2) \dots y(tn)]^T$$

- Then, we create a vector qx1 containing the first thousand values of the vector Q1:

$$qx1 = Q1(0 : 1000)$$

- A vector  $qx2$  will contain the last thousand values of the vector  $Q1$ :

$$qx2 = Q1(\text{length}(Q1) - 1000 : \text{length}(Q1))$$

- Then a vector  $qy1$  contains the first thousand values of the vector  $Q2$ :

$$qy1 = Q2(0 : 1000)$$

- A vector  $qy2$  will contain the last thousand values of the vector  $Q1$ :

$$qy2 = Q2(\text{length}(Q2) - 1000 : \text{length}(Q2))$$

- For each vector  $qx1$ ,  $qx2$ ,  $qy1$  and  $qy2$ , the difference between the displacement and its mean value is calculated.
- The RMS values of these differences:  $\gamma_{x1}$ ,  $\gamma_{x2}$ ,  $\gamma_{y1}$ , and  $\gamma_{y2}$  are determined by using the following expressions:

$$\gamma_{x1} = \sqrt{\left(\frac{1}{T}\right)^T \int_0^T \left[ qx1(t) - \frac{1}{T} \int_0^T qx1(t) \right]^2} \quad (8)$$

$$\gamma_{x2} = \sqrt{\left(\frac{1}{T}\right)^T \int_0^T \left[ qx2(t) - \frac{1}{T} * \int_0^T qx2(t) \right]^2} \quad (9)$$

$$\gamma_{y1} = \sqrt{\left(\frac{1}{T}\right)^T \int_0^T \left[ qy1(t) - \frac{1}{T} * \int_0^T qy1(t) \right]^2} \quad (10)$$

$$\gamma_{y2} = \sqrt{\left(\frac{1}{T}\right)^T \int_0^T \left[ qy2(t) - \frac{1}{T} * \int_0^T qy2(t) \right]^2} \quad (11)$$

- Finally,
  - If  $\gamma_{x2} > \gamma_{x1}$  or  $\gamma_{y2} > \gamma_{y1}$  than the system is unstable and we mark in red the point (N, a) on the stability diagram.
  - Else, the cutting system is stable and we mark in green the point (N, a) on the stability diagram.

Using the approach of Altintas and Budak, a stability analysis has been performed for the milling process. It is important to note that on the frequency-domain method, Altintas and Budak uses several simplifying approximations: A mean value of the cutting forces is used and the harmonic contributions are neglected.

Indeed, the instantaneous cutting forces are periodic at the tooth period. Their expression is the following:

$$\{F(t)\} = \begin{Bmatrix} F_x \\ F_y \end{Bmatrix} = \frac{1}{2} aK_t [A(t)] \begin{Bmatrix} \Delta_x \\ \Delta_y \end{Bmatrix} \quad (12)$$

Like the milling forces,  $[A(t)]$  matrix is periodic at the tooth period, and it can be expanded into Fourier series:

$$[A(t)] = \sum_{r=-\infty}^{\infty} [A_r] e^{-ir\omega t}, \quad [A_r] = \frac{1}{T} \int_0^T [A(t)] e^{-ir\omega t} dt \quad (13)$$

As a simplification, only the fundamental component of the Fourier series is considered:

$$[A_0] = \frac{1}{T} \int_0^T [A(t)] e^{-i\omega t} dt \quad (14)$$

The expression of the milling forces is therefore reduced to [3]:

$$\{F(t)\} = \frac{1}{2} aK_t [A_0] \begin{Bmatrix} \Delta_x \\ \Delta_y \end{Bmatrix} \quad (15)$$

A superposition of the two stability limits determined by the two different methods is shown in Fig. 8.

First, Fig. 8 indicates that the two stability lobes have the same peak locations.

The stability lobes obtained by time-domain simulations are more conservative than those resulting from the frequency-domain approach of Altintas and Budak.

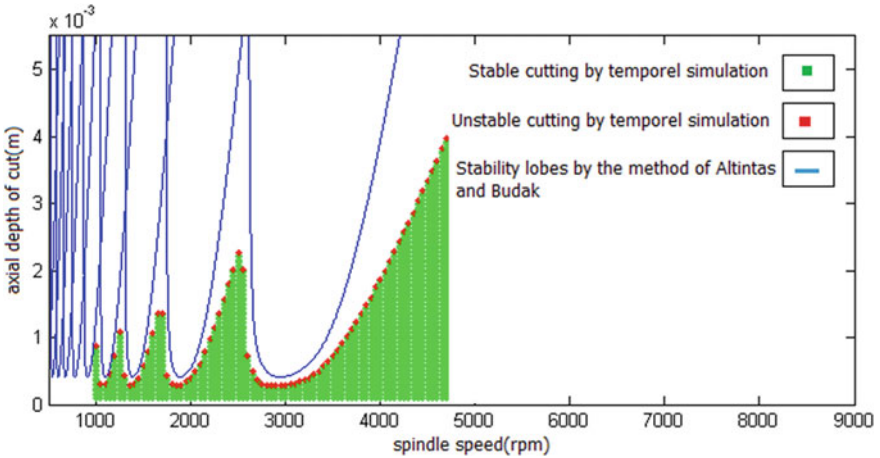


Fig. 8 Superposition of two limits of stability

This result is expectable, because in the frequency-domain method, the effect of the harmonic components of the variable cutting force is neglected.

The comparison between our approach and the frequency-domain-based stability limit shows clearly that the simplifying approximation has a significant effect on the stability limit.

## 4 Conclusion

In this work, a time-domain simulation approach for the prediction of stability in turning and milling is proposed. The dynamics of those machining processes are assimilated to mass-spring-damper systems, in which, the contribution of the surface regeneration mechanism is integrated. By simulating the block diagram of the cutting process, the instantaneous trajectories can be determined with good precision. In order to characterize the stability in the time domain, we have defined a criterion to detect the unstable growth of the displacements in the system. Thereafter, stability limits in terms of lobes are obtained. A stability prediction of a turning process, using the method of Altintas and Budak, is done to verify the effectiveness and the accuracy of the proposed approach. In the same manner, stability prediction in milling process is performed with the aim of highlighting the uncertainties of the simplifying approximations used in the frequency-domain method for stability prediction. Therefore, the proposed time-domain simulations are more accurate and best suited in this case for an optimal tuning of the cutting conditions that guarantee stability and high productivity of the machining process. Moreover, this approach allows rapid and efficient model refining as well as the integration of nonlinear dynamic effects in order to enhance the accuracy and the realism of the stability predictions.

## References

- Altintas Y (2012) *Manufacturing automation: metal cutting mechanics, machine tool vibrations, and CNC design*, 2nd edn. The United State of America
- Altıntaş Y, Budak E (1995) Analytical prediction of stability lobes in milling. *CIRP Ann Manuf Technol* 44(1):357–362. doi:[10.1016/S0007-8506\(07\)62342-7](https://doi.org/10.1016/S0007-8506(07)62342-7)
- Ding H, Ye D, Limin MZ (2012) On time-domain methods for milling stability analysis. *Chin Sci Bull* 57(33):4336–4345. doi:[10.1007/s11434-012-5499-y](https://doi.org/10.1007/s11434-012-5499-y)
- Gagnol V, Le TP, Ray P (2011) Modal identification of spindle-tool unit in high-speed machining. *Mech Syst Signal Process* 25(7):2388–2398. doi:[10.1016/j.ymssp.2011.02.019](https://doi.org/10.1016/j.ymssp.2011.02.019)
- Merritt HE (1965) Theory of self-excited machine-tool chatter: contribution to machine-tool chatter research. *J Eng Ind* 87(4):447–454. doi:[10.1115/1.3670861](https://doi.org/10.1115/1.3670861)
- Smith S, Tlustý J (1993) Efficient simulation programs for chatter in milling. *CIRP Ann Manuf Technol* 42(1):463–466. doi:[10.1115/1.3670861](https://doi.org/10.1115/1.3670861)

- Thusty J, Smith S, Zamudio C (1991) Evaluation of cutting performance of machining centers. CIRP Ann Manuf Technol 40(1):405–410. doi:[10.1016/S0007-8506\(07\)62017-4](https://doi.org/10.1016/S0007-8506(07)62017-4)
- Thusty J, Zaton W, Ismail F (1983) Stability lobes in milling. CIRP Ann Manuf Technol 32 (1):309–313. doi:[10.1016/S0007-8506\(07\)62017-4](https://doi.org/10.1016/S0007-8506(07)62017-4)
- Tobias S, Fishwick W (1958) The chatter of lathe tools under orthogonal cutting conditions. Trans ASME 80:1079–1088. doi:[10.1016/0043-1648\(59\)90080-8](https://doi.org/10.1016/0043-1648(59)90080-8)

# Modeling and Control for Lateral Rail Vehicle Dynamic Vibration with Comfort Evaluation

Mortadha Graa, Mohamed Nejlaoui, Ajmi Houidi, Zouhaier Affi and Lotfi Romdhane

**Abstract** Investigation of vibration is an important topic for the purposes of ride comfort in railway engineering. The vibration of rail vehicles becomes very complex because it is affected by the condition of vehicles, including suspensions and wheel profile, condition of track sections, including rail profile, rail irregularities, cant and curvature. The present study deals with the modeling and control for lateral rail vehicle active suspension by PID-ZN controller. For this, a numerical simulation of the dynamic behavior is made based on the Lagrangian approach in order to study the effect of vehicle speed in response to imperfections in the tracks. A model of 17 degrees of freedom is adopted which consists of one car body 2 bogies and 4 wheel-sets. A Sperling ride index (ISO2631) is calculated using filtered RMS accelerations in order to evaluate the ride comfort. Which allowing at the same time the evaluation of the dynamic behavior of the car body and the level of passenger comfort by analyzing the accelerations at the center of mass of the car body.

**Keywords** ISO 2631 · Active suspension · Passive suspension · PID controller · Comfort dynamic behavior · Ride comfort · Lateral dynamic vibration

---

M. Graa (✉) · M. Nejlaoui · Z. Affi  
Laboratoire de Génie Mécanique (LGM), Ecole Nationale d'Ingénieurs de Monastir,  
Université de Monastir, Monastir, Tunisia  
e-mail: graa\_mortadha@yahoo.fr

A. Houidi · L. Romdhane  
Laboratoire de Mécanique de Sousse (LMS), Ecole Nationale d'Ingénieurs de Sousse,  
Université de Sousse, Sousse, Tunisia

L. Romdhane  
College of Engineering, American University of Sharjah, Sharjah, United Arab Emirates

## 1 Introduction

Rail comfort is one of the priority axes of the designers of rail vehicles. However, the comfort that passengers experience is usually perceived differently from one individual to another. Proved in several research works, track defects present the main sources noise and vibration for the rail vehicles. The nature of vibration itself is random and covers a wide frequency range (Skarlatos et al. 2004). The improvement of the passenger comfort while travelling has been the subject of intense interest for many train manufacturers, researchers and companies all over the world. Although new techniques in manufacturing and design ensure better ride quality in railway carriages, it is sometimes impossible to completely eliminate track defects or various ground irregularities. This comfort is highly affected by the vehicle speed and the rail imperfections. Improving the rail vehicle suspension is the key to avoid high perturbations, to be transmitted from the wheels to the passenger. The classical passive suspensions are able to absorb only a limited part of these perturbations dynamic behavior of the car body comfort in a more efficient way.

Several studies have been performed on rail vehicle with passive suspensions. Nejlaoui et al. (2013) optimized the structural design of passive suspensions in order to ensure simultaneously passenger safety and comfort. Abood and Khan (2011) investigated the Railway carriage simulation model to study the influence of vertical secondary suspension stiffness on ride comfort of railway car body. Zhang et al. (2013) developed a finite elements optimization technique to find the best parameters of the passive suspension in order to improve the train riding comfort. The objective is to reach the best compromise between the ride quality and the suspension deflections.

Other works focused on the study of active suspension systems where a controlled actuator is embedded in the system. Zhou et al. (2010) developed an active lateral secondary suspension of railway vehicles in order to attenuate the vehicle body lateral vibration. This active suspension is controlled by the use of skyhook dampers. To decrease the effect of road vibration problems, Eski and Yıldırım (2009) controlled the vibration of the vehicle suspension by using a PID controller. The LQR method was also used in designing active suspensions (Pratt 2002; Vincent 1999).

Safety and comfort are evaluated with specific performance indices. To inspect the motion within the range of human comfort, a Sperling's ride index is measured for the ride comfort ISO 2631 (Kumar 2006). There exists complex dynamics between the rail and wheel. In fact, an accuracy modeling of the rail vehicle dynamics is often difficult. In the physical system, the input comes from the actual track. In a model, the user-defined input can be created analytically or can be based on actual measurements. For this study analytic track data are created using mathematical shapes, to represent the track geometry (Dukkipati and Amyot 1988).

## 2 Modeling of Rail Road Vehicle

To analyze the dynamic behavior of railway vehicles, usually the vehicle (and if necessary the environment) is represented as a multi body system. A multi body system consists of rigid bodies, interconnected via massless force elements and joints. Due to the relative motion of the system's bodies, the force elements generate applied forces and torques. Typical examples of such force elements are springs, dampers, and actuators combined in primary and secondary suspensions of railway vehicles.

### 2.1 Assumptions

The assumptions made in formulating the model are as follows:

- Bogie and car body component masses are rigid.
- The springs and dampers of the suspension system elements have linear characteristics.
- Friction does not exist between the axle and the bearing.
- The vehicle is moving with constant velocity on a rigid and constant gauge.
- All wheel profiles are identical from left to right on a given axle and from axle to axle and all wheel remain in contact with the rails.
- Straight track.
- An irregularity in the vertical direction with the same shape for left and right rails.

### 2.2 Rail Road Vehicle Model

Figure 1 illustrates the train vehicle model adopted in this study. It consists of a vehicle body, two bogies frames and four wheel-sets. Each bogie consists of the bogie frame, and two wheel sets. The car body is modeled as a rigid body having a mass  $M_c$ ; and having moment of inertia  $J_{bx}$  and  $J_{cz}$  about the longitudinal and vertical axes, respectively. Similarly, each bogie frame is considered as a rigid body with a mass  $m_b$  ( $m_{b1}$  and  $m_{b2}$ ) with moment of inertia  $J_{bx}$  and  $J_{bz}$  about the longitudinal and vertical axes, respectively. Each axle along with the wheel set has a mass  $m_w$  (for four axles  $m_{w1}$ ;  $m_{w2}$ ;  $m_{w3}$  and  $m_{w4}$ ). The spring and the shock absorber in the primary suspension for each axle are characterized by a spring stiffness  $K_p$  and a damping coefficient  $C_p$ , respectively. Likewise, the secondary suspension is characterized by spring stiffness  $K_s$  and damping coefficient  $C_s$ , respectively. As the vehicle car body is assumed to be rigid, its motion may be described by the lateral displacement and rotations about the vertical axis (yaw or  $\Psi_c$ ) and about the



longitudinal axis (roll or  $\theta_c$ ). Similarly, the movements of the two bogies units are described by three degrees of freedom  $y_{bi}$ ;  $\Psi_{bi}$  and  $\theta_{bi}$  ( $i = 1, 2$ ), each about their centers. Each axle set is described by two degrees of freedom  $y_w$ ; and  $\Psi_w$  about their centers. Totally, 17 degrees of freedom have been considered in this study for the vehicle model shown in Fig. 1. The detailed parameters regarding the moment of inertia and mass of different component are given in Table 1.

Some parameters regarding the rigid bodies are already given in Table 1; however, the other parameters, which are essential for the simulation of the vehicle, are presented in Table 2. A typical rail road vehicle system is composed of various components such as car body, springs, dampers, Bogies, Wheel-set, and so forth.

When such dynamic systems are put together from these components, one must interconnect rotating and translating inertial elements with axial and rotational springs and dampers, and also appropriately account for the kinematics of the system structure.

To minimize the car body vibrations, tow lateral actuators are designed: one controller actuator per bogie in a vehicle (Fig. 1). The lateral controllers are designed to suppress car body lateral, yaw and roll angular vibrations caused by lateral rail disturbances.

The control force vector can be given as: ( $i = 1, 2, j = 1 \dots 4$ )

$$[F_u] = [F_c^u \quad F_{bi}^u \quad F_{wj}^u] \tag{1}$$

where  $F_c^u$ ,  $F_{bi}^u$  and  $F_{wj}^u$  are the car body, bogie  $i$  and wheel-set  $j$  control forces, respectively, given in following:

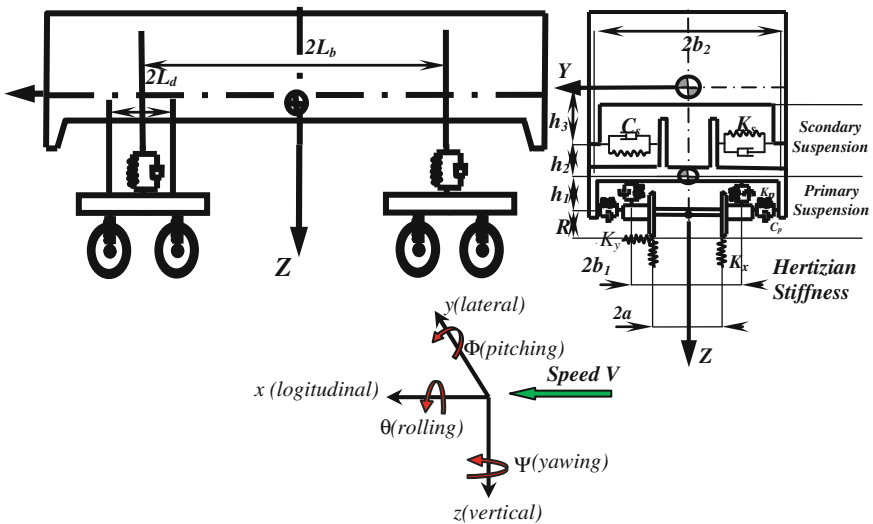


Fig. 1 Physical model of railway vehicle

**Table 1** Detailed parameter of rigid bodies

Name of rigid bodies	Mass (kg)	Moment of inertia (kg m <sup>2</sup> )	
		I <sub>xx</sub>	I <sub>zz</sub>
Car body	$6.7 \times 10^5$	$10^5$	$10^6$
Bogie-I and II	$10^5$	$10^5$	$10^5$
Wheel-set-I, II, III and IV	4000	4000	4000

**Table 2** Vehicle parameters

Parameter	Nomenclature	Values
Primary spring stiffness	$K_p$	$10^6$ N/m
Secondary spring stiffness	$K_s$	$1.7 \times 10^6$ N/m
Primary damping coefficient	$C_p$	$6 \times 10^4$ Ns/m
Secondary damping coefficient	$C_s$	$10^5$ Ns/m
Lateral hertz spring stiffness	$K_{hz}$	$35 \times 10^9$ N/m
Longitudinal distance between bogies I and II and car body mass center	$L_b$	6 m
Longitudinal distance between wheel-set and corresponding bogie origin	$L_d$	1.4 m
Lateral distance between a longitudinal primary suspension and corresponding wheel-set	$d_p$	1 m
Lateral distance between longitudinal secondary suspension and corresponding bogie origin	$d_s$	1 m
Lateral distance between contact point of wheel-rail and corresponding wheel-set origin	$a$	0.7163 m
Lateral distance between vertical primary suspension and corresponding wheel-set origin	$b_1$	1 m
Lateral distance between vertical secondary suspension and car body mass center	$b_2$	1 m
Nominal wheel radius	$R_1$	0.61 m
Vertical distance between wheel-set and bogie mass centers	$h_1$	0.3 m
Vertical distance between bogie mass center and lateral secondary suspension	$h_2$	0.2 m
Vertical distance between lateral secondary suspension and car body mass center	$h_3$	1.3 m

$$\mathbf{F}_c^u = \begin{bmatrix} \sum_{i=1}^2 u_{yi} \\ h_3 \sum_{i=1}^2 u_{yi} \\ L_b [u_{y1} - u_{y3}] \end{bmatrix}^T \quad (2)$$

$$\mathbf{F}_{ii}^u = [-u_{yi} \quad h_2 u_{yi} \quad 0] \quad (3)$$

$$\mathbf{F}_{wj}^u = [0 \quad 0 \quad 0 \quad 0] \quad (4)$$

### 2.3 Equation of Motion

The equations of motion of the railway vehicle are obtained by means of the Lagrange equation. We obtained the following equations of motion for the wheel-set  $j$ :

$$\begin{aligned} m_{wj} \ddot{y}_{wj} + 2C_p \left[ -\dot{y}_{bi} + \dot{y}_{wj} - h_1 \dot{\theta}_{bi} + (-1)^i L_d \dot{\psi}_{bi} \right] \\ + 2K_p \left[ -y_{bi} + y_{wj} - h_1 \theta_{bi} + (-1)^i L_d \psi_{wj} \right] \\ + k_{hy} \left[ y_{wj} \left( 1 + R_1 \frac{\lambda}{a} \right) - y_{rj} \right] + 2 \left[ f_{11} \left( \frac{\dot{y}_{wj}}{V} - \psi_{wj} \right) + f_{12} \left( \frac{\dot{\psi}_{wj}}{V} \right) \right] = 0 \end{aligned} \quad (5)$$

$$\begin{aligned} J_{z_{wj}} \ddot{\psi}_{wj} + 2d_p^2 C_p \left[ -\dot{\psi}_{bi} + \dot{\psi}_{wj} \right] + 2d_p^2 K_p \left[ -\psi_{bi} + \psi_{wj} \right] \\ + 2 \left[ f_{11} \left( \frac{\dot{y}_{wj}}{V} - \psi_{wj} \right) + f_{12} \left( \frac{\dot{\psi}_{wj}}{V} \right) \right] = 0 \end{aligned} \quad (6)$$

where  $j = 1, 2$  when  $i = 1, j = 3, 4$  when  $i = 2, k = 1$  when  $j = 1, k = 3$  when  $j = 2, k = 5$  when  $j = 3, k = 7$  when  $j = 4$ ; the dot indicates differentiation with respect to time variable  $t$ ;  $f_{11}$  is the lateral creep coefficient;  $f_{12}$  is the lateral/spin creep coefficient.

The equations of motion of the bogie  $i$  are:

$$\begin{aligned} m_{bi} \ddot{y}_{bi} + 2C_p \left[ 2\dot{y}_{bi} - (\dot{y}_{wj} + \dot{y}_{w(j+1)}) + 2h_1 \dot{\theta}_{bi} \right] \\ + 2C_s \left[ -\dot{y}_c + \dot{y}_{bi} - (h_3 \dot{\theta}_c + h_2 \dot{\theta}_{bi}) - kL_b \dot{\psi}_c \right] \\ + 2K_p \left[ 2y_{bi} - (y_{wj} + y_{w(j+1)}) + 2h_1 \theta_{bi} \right] \\ + 2K_s \left[ -y_c + y_{bi} - (h_3 \theta_c + h_2 \theta_{bi}) - kL_b \psi_c \right] = -u_{yi} \end{aligned} \quad (7)$$

$$\begin{aligned}
& J_{xbi}\ddot{\theta}_{bi} + 2h_1C_p \left[ 2h_1\dot{\theta}_{bi} + 2\dot{y}_{bi} - (\dot{y}_{wj} + \dot{y}_{w(j+1)}) \right] \\
& + 2h_2C_s \left[ h_3\dot{\theta}_c + h_2\dot{\theta}_{bi} + \dot{y}_c - \dot{y}_{bi} + kL_b\dot{\psi}_c \right] \\
& + 2b_1^2C_p \left[ 2\dot{\theta}_{bi} - \frac{\lambda}{a}(\dot{y}_{wj} + \dot{y}_{w(j+1)}) \right] + 2b_2^2C_s \left[ -\dot{\theta}_{bi} + \dot{\theta}_c \right] \\
& + 2h_1K_p \left[ 2h_1\theta_{bi} + 2y_{bi} - (y_{wj} + y_{w(j+1)}) \right] \\
& + 2h_2K_s \left[ h_3\theta_c + h_2\theta_{bi} + (y_c - y_{bi}) + kL_b\psi_c \right] \\
& + 2b_1^2K_p \left[ 2\theta_{bi} - \frac{\lambda}{a}(y_{wj} + y_{w(j+1)}) \right] + 2b_2^2K_s \left[ \theta_{bi} - \theta_c \right] = h_2u_{yi}
\end{aligned} \tag{8}$$

$$\begin{aligned}
& J_{zbi}\ddot{\psi}_{bi} + 2d_p^2C_p \left[ 2\dot{\psi}_{bi} - (\dot{\psi}_{wj} + \dot{\psi}_{w(j+1)}) \right] \\
& + 2L_dC_p \left[ 2L_d\dot{\psi}_{bi} - (\dot{y}_{wj} - \dot{y}_{w(j+1)}) \right] \\
& + 2d_p^2K_p \left[ 2\psi_{bi} - (\psi_{wj} + \psi_{w(j+1)}) \right] + 2d_s^2K_s(\psi_{bi} - \psi_c) \\
& + 2L_dK_p \left[ 2L_d\psi_{bi} - (\psi_{wj} + \psi_{w(j+1)}) \right] = 0
\end{aligned} \tag{9}$$

where  $j = 1$  and  $k = 1$  when  $i = 1$ ;  $j = 3$  when  $i = 2$ ;  $j = 5$  and  $k = -1$  when  $i = 3$ .

Finally, the equations of motion of the car body are:

$$\begin{aligned}
& m_c\ddot{y}_c + 2C_s \left[ 2(\dot{y}_c + h_3\dot{\theta}_c) - \sum_{p=1}^2 \dot{y}_{bp} + h_2 \sum_{p=1}^2 \dot{\theta}_{bp} \right] \\
& + 2K_s \left[ 2(y_c + h_3\theta_c) - \sum_{p=1}^2 y_{bp} \right] + h_2(\theta_{b1} + \theta_{b2}) = \sum_{p=1}^2 u_{yp}
\end{aligned} \tag{10}$$

$$\begin{aligned}
& J_{xc}\ddot{\theta}_c + 2h_3C_s \left[ 2(h_3\dot{\theta}_c + \dot{y}_c) + h_2 \sum_{p=1}^2 \dot{\theta}_{bp} - \sum_{p=1}^2 \dot{y}_{bp} \right] + 2b_2^2C_s \left[ 2\dot{\theta}_c - \sum_{p=1}^2 \dot{\theta}_{bp} \right] \\
& + 2h_3K_s \left[ 2(h_3\theta_c + y_c) + h_2 \sum_{p=1}^2 \theta_{bp} - \sum_{p=1}^2 y_{bp} \right] + 2b_2^2K_s \left[ 2\theta_c - \sum_{p=1}^2 \theta_{bp} \right] = h_3 \sum_{p=1}^2 u_{yp}
\end{aligned} \tag{11}$$

$$\begin{aligned}
& J_{zc}\ddot{\psi}_c + 2L_bC_s \left[ 2L_b\dot{\psi}_c + (-\dot{y}_{b1} + \dot{y}_{b2}) - h_2(-\dot{\theta}_{b1} + \dot{\theta}_{b2}) \right] \\
& + \left[ 2d_s^2 \left[ \begin{array}{c} K_s(2\psi_c - (\psi_{b1} + \psi_{b2})) + K_s(\psi_c - \psi_{b2}) \\ + 2L_bK_s \left[ \begin{array}{c} 2L_b\psi_c + (-y_{b1} + y_{b2}) \\ + h_2(-\theta_{b1} + \theta_{b2}) \end{array} \right] \end{array} \right] \right] = L_b(u_{y1} - u_{y3})
\end{aligned} \tag{12}$$

### 3 Track Inputs to Rail Road Vehicle

The dynamic wheel loads generated by a moving train are mainly due to various wheel/track imperfections. These imperfections are considered as the primary source of dynamic track input to the railroad vehicles. Normally, the imperfections that exist in the rail-track structure are associated with the vertical and lateral track profile, cross level, rail joint, wheel flatness, wheel/rail surface corrugations and sometimes uneven support of the sleepers.

In actual practice different types of periodic, a-periodic or random track irregularities may exist on the track, but in the present study a lateral local discontinuity type of irregularity is considered as shown in Fig. 2. The shape of the irregularity is assumed to be similar on the left and the right rails.

The excitations of the left wheels of leading bogies are as follows:

$$Y_{ri} = \begin{cases} H & \text{for } t_{di} \leq t \\ 0 & \text{otherwise} \end{cases} \quad (i = 1..4) \tag{13}$$

where

$$[t_{d1}, t_{d2}, t_{d3}, t_{d4}] = \left[ 0, \frac{2L_d}{V}, \frac{2L_b}{V}, \frac{2L_b + 2L_d}{V} \right] \tag{14}$$

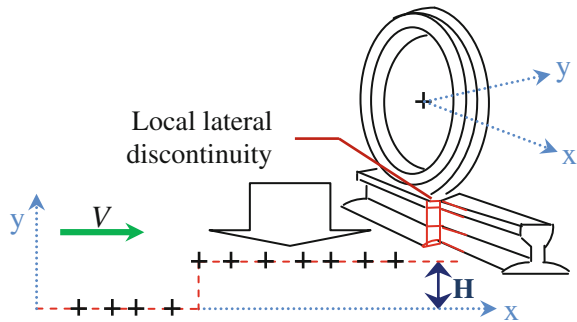
In the present study,  $H$  is taken as 0.03 m.

### 4 Control Strategies and Design

In this section, the design of the PID controller for improving the ride passenger comfort is presented.

The different controller gains will be determined according to the rail vehicle dynamic. The PID controller block diagram is given in Fig. 3. The objective of the

**Fig. 2** Model of track irregularity



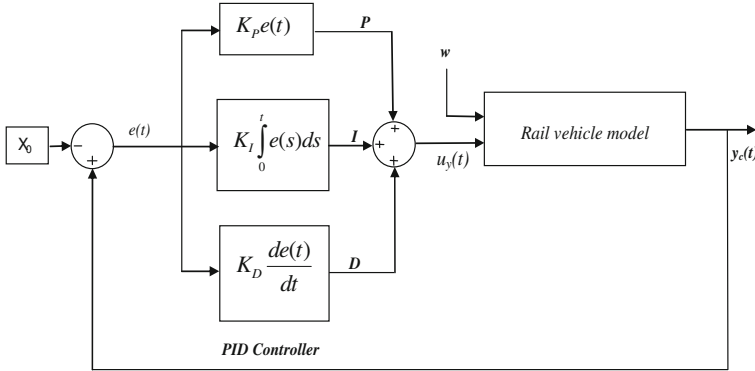


**Fig. 3** The block diagram of PID controller

**Table 3** PID gains

Lateral control force	$K_P$	$K_D$	$K_I$
$u_{yi} (i = 1,2)$	121	2432	42,654

PID is to minimize an error  $e(t)$  through the control of the active suspension. The output of the PID controller is given by:

$$u_{yi}(t) = K_P e(t) + K_I \int_0^t e(s) ds + K_D \frac{de(t)}{dt} \tag{15}$$

where  $K_P, K_I$  and  $K_D$  are proportional, integral and derivative gains, respectively.  $u_{yi}(t)$  is the control force.

We will substitute the PID controller and the open loop return with a level step. To find the values of the PID gains, we have used the step response Ziegler-Nichols method (Ang et al. 2005; Wolfgang 2005). Table 3 presents these gains.

## 5 Simulation and Comfort Evaluation

The models were built in the MATLAB/Simulink<sup>®</sup> environment. The fixed step solver ODE-45 (Dormand-Prince) was utilized, with the sampling time  $T_s = 0.0001$ .

Dynamic analysis was carried out for the vehicle at different speeds: 15, 30, 45 and 60 m/s.

**Fig. 4** The lateral Car body displacement for 60 m/s

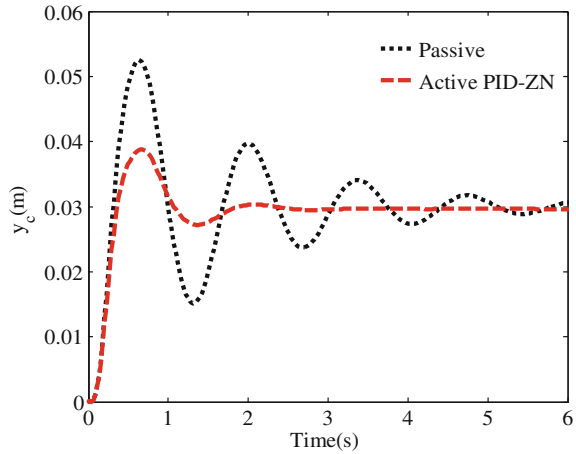


**Table 4** Sperling’s ride index evaluation for different vehicle velocities (passive system)

Vehicle speed (m/s)	Sperling index ( $W_z$ )	Ride comfort evaluation
15	3.17	Strong, irregular, but still tolerable
30	2.54	More pronounced but not unpleasant
45	2.15	Clearly noticeable
60	2.03	Clearly noticeable

Figure 4 presents the lateral car body displacement for the speed 60 m/s. It can be observed that, in the case of the active PID-ZN controller, the reduction of the car body’s lateral displacement peak is approximately 63 % compared to passive suspension.

To calculate the Sperling ride comfort index (European Rail Research Institute 1993; Chen et al. 2005). The FFT plot is generated for a frequency range between 0 and 1000 Hz, as the human beings are most sensitive in the frequency range of 4–12.5 Hz. Ride comfort analysis has been performed for speeds ranging from 15 to 60 m/s.

The analysis has been performed on the system model to calculate the vertical acceleration of the system. FFT output is taken to get the peak acceleration frequency component. Comfort index for passive system has been presented in Table 4.

The maximum and minimum ISO Sperling Index values are respectively 3.17 and 2.03 for the rail vehicle speed respectively 15 and 60 m/s. These values respectively indicate “Strong, irregular, but still tolerable” and “Clearly noticeable” zones.

This means that the passengers are not much affected by the vibration as they are exposed to low level of vibrations for this type of irregularity. From Table 5, the

**Table 5** Sperling's ride index evaluation for different vehicle velocities (active system)

Vehicle speed (m/s)	Sperling index ( $W_z$ )	Ride comfort evaluation
15	1.17	Just noticeable
30	1.54	Just noticeable
45	1.15	Just noticeable
60	1.03	Just noticeable

active PID-ZN controller keeps the passenger in a “just noticeable” level of comfort for all speed values.

## 6 Conclusion

Lateral control dynamic analysis has been carried out for a Railway Vehicle. A 17 degree of freedom model is used for the analysis. A lateral acceleration response at the car body has been calculated in the frequency domain. The Sperling Ride index has been calculated and presented for the above vehicle at different speeds. The calculated values of the Sperling index are found well in the satisfactory limits defined by the ISO 2631 standard which means that the passengers are not much affected by the vibration as they are exposed to low level of vibrations. It should be noticed that the control model was carried out to improve  $W_z$  index for all speeds.

## References

- Abood KHA, Khan RA (2011) The railway carriage simulation model to study the influence of vertical secondary suspension stiffness on ride comfort of railway carbody. *J Mech Eng Sci* 225:1349–1359
- Chen H et al (2005) Application of constrained  $H^\infty$  control to active suspension systems on half-car models. *Trans ASME J Dyn Syst Measure Control* 127(3):345–354
- Zhou R et al (2010) 9 DOF railway vehicle modeling and control for the integrated tilting bolster with active lateral secondary suspension. In: *IEEE, UKACC international conference on systems technology control*, vol 465, pp 1–6
- Ang KH, Chong GCY, Li Y (2005) PID control system analysis, design, and technology. *IEEE Trans Control Syst Technol* 13(4):559–576
- Dukkipati V, Amyot J (1988) *Computer aided simulation in railway dynamics*. Marcel Dekker, New York
- Eski I, Yıldırım S (2009) Vibration control of vehicle active suspension system using a new robust neural network control system. *Simul Model Pract Theory* 17:778–793
- European Rail Research Institute (1993) B153/RP21: application of ISO standard to railway vehicles comfort index  $N_{mv}$  comparison with the ISO/SNCF comfort note and with the  $W_z$
- Kumar H (2006) Sujata: vertical dynamic analysis of a typical indian rail road vehicle. In *Proceedings on computational mechanics and simulation*, IIT, India, pp 8–10



- Nejlaoui M et al (2013) Multiobjective robust design optimization of rail vehicle moving in short radius curved tracks based on the safety and comfort criteria. *Simul Model Pract Theory* 30:21–34
- Pratt I (2002) Active suspension applied to railway trains. PhD thesis, Department of Electronic and Electrical Engineering, Loughborough University
- Skarlatos D et al (2004) Railway fault diagnosis using a fuzzy logic method. *Appl Acoust* 65 (10):951–966
- Vincent J (1999) Etude du concept de suspensions actives: applications aux voitures ferroviaires
- Wolfgang A (2005) Practical control for engineers and technicians, 115–117
- Zhang YW et al (2013) Riding comfort optimization of railway trains based on pseudo-excitation method and symplectic method. *J Sound Vib* 332:5255–5270

# Vibration Detection in Gas Turbine Rotor Using Artificial Neural Network Combined with Continuous Wavelet

Benrabeh Djaidir, Ahmed Hafaiifa and Abdallaha Kouzou

**Abstract** The current development in surveillance methods as well new supervisory approaches meets many requirements in the design and operation of industrial equipment. This article proposes the development of vibration fault detection in gas turbines. Indeed, the presence of one or more defects of vibration in these machines results in the emergence of new usable frequency for monitoring these rotating machines. This work proposes to implement an approach based on artificial neural network methods, combined with continuous wavelet technique for the construction of fault diagnostic tool based on the information data on the state of the examined gas turbine bearing.

**Keywords** Faults detection · Gas turbine · Continues wavelet · Generation of residues · Monitoring system · Neural networks system · Varying conditions · Vibration modeling

## 1 Introduction

Gas turbines are widely used in industry, because of their frequent use in various applications; dice the importance of these machines in the oil facilities and other industrial fields. However, many shortcomings and problems affected such systems, which can lead to dangerous vibrations on their mode of operation and degrades its mechanical condition. Vibration monitoring of gas turbines, is widely used in several industrial applications technique, given its efficiency is taking a very

---

B. Djaidir · A. Hafaiifa (✉) · A. Kouzou  
Applied Automation and Industrial Diagnostics Laboratory,  
University of Djelfa, 17000 DZ Djelfa, Algeria  
e-mail: hafaiifa.ahmed.dz@ieee.org

B. Djaidir  
e-mail: B.djaidir@univ.djelfa.dz

A. Kouzou  
e-mail: kouzouabdellah@ieee.org

important place in the framework of the implementation of condition-based maintenance (Hafaifa et al. 2013a, b, 2014, 2015a, b; Djeddi et al. 2015a, b; Mohamed et al. 2015; Bendjama et al. 2010). It allows you to track the status of the turbine in operation to prevent unwanted downtime. To perform vibration analysis, different tools are used, firstly to detect a failure and to assess the severity of the problem on the state of the machine.

This work proposes the use of a monitoring system for the detection of vibrations of a gas turbine using an approach based on artificial neural networks; this technique is based on the existence of basic data learning for the examined turbine. Next, a combination with the wavelet method associated with spectral analysis and based on the Fourier transform is developed. The results are satisfactory and validated by an experimental procedure for monitoring of certain abnormalities (lineage default), and to identify the causes and nature of faults affecting the examined system.

## 2 Neural Networks Supervision

A supervisory strategy based on neural network techniques, makes it possible to develop a diagnostic procedure defects of generating indicators of defects (residual generation), designed to detect and locate faults. And allows for localization and identification of the type of failure, the principle is calculated from the difference between the measurements of the process signals and the theoretical value provided by the system model to monitor. In this work, the neural network approach is proposed to describe the dynamic behavior of the process, which can be characterized by deterministic relationships between defects causes and effects. In order to improve the performance of the proposed diagnostic strategy, that is to say the development of its outputs according to the input thereof. The artificial neural networks are suitable for such problems as an effective monitoring tool. Among the different types of neural networks, multilayer perceptron (MLP Multi Layer Perceptron) are quite popular and used at present in many industrial applications (Djaidir et al. 2014; Eshati et al. 2013; Ablay 2013; Jurado and Carpio 2006; Kim et al. 2011; Lee et al. 2013).

In this work an neural networks approach are used, the parameters of acceleration and rotational speed as input variables in this system, as they are the most representative of the defects, their paces vary considerably in case of application of a fault, and their measurements, may be accessed by sensors which provide physical quantities. The network settings can write using the following vector:

$$[x_1 \quad x_2 \quad \dots \quad x_N]^T \quad (1)$$

With in the activation function  $f_j$ ,  $u_j$  is the output of  $j^{eme}$  neurons in the hidden layer is obtained as follows:

$$u_j = f_1 \left( \sum_{i=1}^N w_{ij}^1 x_i + b_j^1 \right) \tag{2}$$

With  $b_j^1$  and  $w_{ij}^1$  represented respectively bias and weight between  $j^{eme}$  neurons of the hidden layer and the  $i^{eme}$  neuron of the input layer.

The desired output vector is given by:

$$[y_1 \quad y_2 \quad \dots \quad y_N]^T \tag{3}$$

The transformed to an intermediate vector of hidden variables, the general laws for calculating outputs of the neurons  $k$  in the hidden layer may be expressed as follows:

$$y_k = f_2 \left( \sum_{l=1}^N w_{lk}^2 u_l + b_k^2 \right) \tag{4}$$

The index above 2 shows the connection (secondary) between neurons layers input/hidden.

With  $f_1(v) = \frac{2}{1+e^{-2v}} - 1$  and  $f_2(v) = v$  are the sigmoid and linear activation functions respectively.

The modeling algorithm is performed according to the type of application studied in this work, which is a gas turbine, as shown in Fig. 1.

The stage of development of the gradient back propagation neural networks is made by a supervised learning algorithm. This algorithm is designed to make associations between pairs of vectors (data input, desired output). Indeed, the basic idea of this algorithm is to minimize the squared error criterion relative to weight connections, once the weights are updated according to the error, from layer to layer in the layer output is given by the following formula (Mohamed et al. 2015;

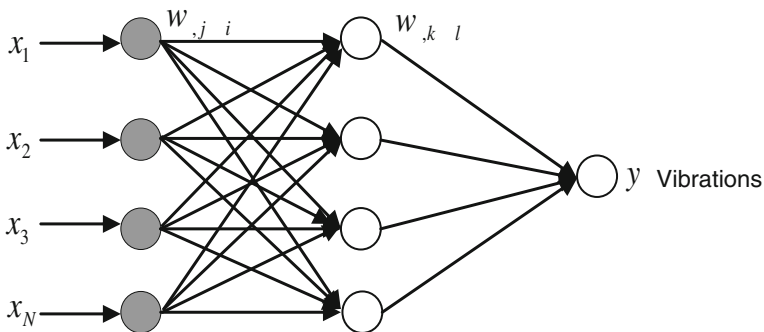


Fig. 1 Structure of used multilayer neural networks

Guemana et al. 2015; Nikpey et al. 2014; Jagaduri and Radman 2007; Sanaye and Tahani 2010; Simani and Patton 2008):

$$E = \frac{1}{2} \sum_{i=1}^M (y d_i - y_i)^2 \quad (5)$$

The aim of this learning algorithm of back propagation error gradient is to find the set of weights, ensuring output of the neural network as possible following the desired reference value. In the implementation section will be supervised learning neural network from a database, to accommodate the detection and classification of defects in the examined vibration gas turbine.

### 3 Industrial Applications

In this work, a gas turbine type GE 3002-MS installed in SC2 compression station in north of Hassi R'Mel gas field, Algeria, as shown in Fig. 2, was examined in the context of a diagnostic study of this gas turbine. Deferent vibratory phenomena emitted at the bearing (No. 01 and 03) of the gas turbine have had tested.

The examined gas turbine is designed for driving a compressor of natural gas, along a pipeline. So to identify the origin of the high level of vibration signal in the control room, oversee a system was proposed and to propose practical solutions to make the machine compatible with a normal exploitation of corrective actions on the modes of operation of this turbine.

In practical fact, some defects in gas turbines are characterized by shocks, resulting from non-local stationary of the vibration signals, because these vibrations contain all the information regarding the state of defective mechanical turbine bodies. Therefore, vibrations are the result of a set of forces exerted by the turbine itself, or the result of the interaction with the environment in which the machine is

**Fig. 2** Examined gas turbine GE 3002



**Table 1** Gas turbine GE3002 vibrations measurement

SC2	Speed HP = 7100 rpm		Levels of vibration (mm/s)			
	Speed LP = 6500 rpm		Turbine		Centrifuge compressor	
	HP speed (%)	LP speed (%)	Bearing 04°	Bearing 03°	Bearing 02°	Bearing 01°
			LP (mm/s)	HP (mm/s)	CC (mm/s)	CC (mm/s)
Gas turbine MS 3002 TC301	60	2.6	0.47	1.59	0.95	0.36
	61	32.46	1.56	1.8	0.99	0.56
	69.5	43.56	1.53	2.32	0.82	0.438
	75.5	51	1.535	3.39	0.843	0.43
	82.67	55.34	1.537	4.36	1.06	0.931
	85	56.69	2.2	4.4	1.42	1.2
	86	57.837	2.46	4.6	2.6	1.35
	91.99	67.13	2.37	5.9	1.95	1.52
	100	85.32	2.337	6.43	1.46	1.63
	98.78	97	2.84	9.5	1.54	1.85
	99	100	2.98	9.61	2.01	2.73
	98.8	89.4	3.89	9.754	2	2.89
	100	100	3.85	10	2.63	2.854
	98.9	95	3.3	10.5	2.49	1.34

operated. Indeed the analysis of their signals provides information on the degradation process, which may be internal in general. Vibration monitoring by measuring and analyzing the dynamic behavior demonstrates that the turbine is adapted, or on the contrary it should be improved mechanically to fulfill its mission.

The problem knows which method is possible to strengthen the management of analysis of vibration signals from the components of the gas turbine, as a complementary indicator for better optimal vibration monitoring strategy. A preliminary reading of the train operating parameters was performed on the examined turbine, action was recorded from sensors installed on this machine, in Table 1, unstable vibration values over the tree line are given.

Supervised learning of the used neural network from a data base was made and well adapted, through learning by the multilayer perceptron, for the detection and classification of defects turbine studying this, to optimize optimal settings for the used neural network, as shown in Fig. 3.

The MSE performance obtained for the gas turbine after modeling are given in Table 2.

Figures 4, 5 and 6 shows successively the evolution of the spectral structure, when a lineage of defect in the bearing No. 03 of the gas turbine. The imbalance generates strong vibrations in the rotational speed of the high pressure turbine (HP), it appears when the center of gravity of the rotor does not correspond to its axis of

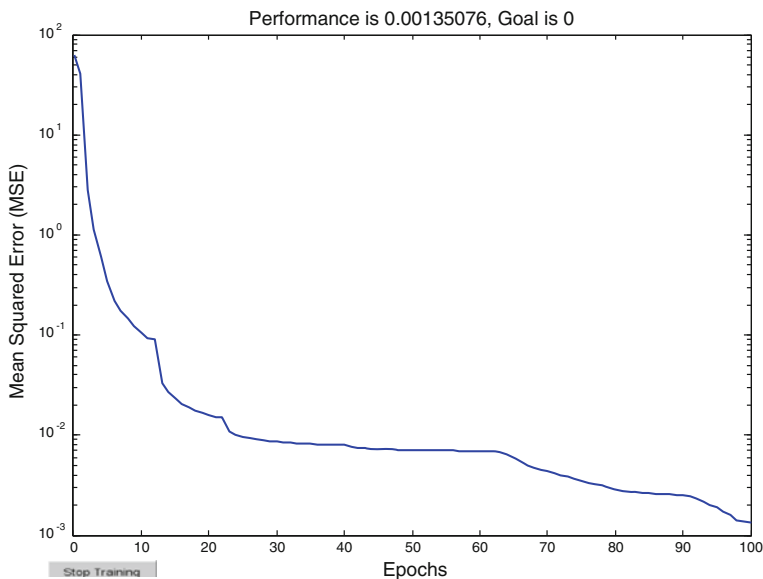


**Fig. 3** Performance of the used neural network

**Table 2** MSE performance using neural network modeling

Tests	Performance (MSE) of ANN				
	Training function	Number of neurons	Transfer function in hidden layer	Transfer function in output layer	MSE for best average performance
Test 1	traingd	18	tansig	logsig	0.00135
Test 2	traingd	8	logsig	logsig	0.00105

rotation. From the results obtained, and the modeling done by supervised learning techniques of selected neural network shows that the architecture of the network is better. Because the values of the squared error is tolerable and obtained little computing time, as shown in Fig. 7, which explains that the desired outputs are very close to the actual outputs. This learning is to change the parameters of the neural network, to minimize the error between the target output and the actual output of the neural network.

The simulation results have shown the ability of the obtained neural model to reproduce the dynamic bearings of the turbine, and which can detect defects that occur in the shaft line for different amplitudes. Neural networks can thus be successfully applied, because learning is in this case to change the parameters to minimize the error between the target output and the actual output of the neural network.

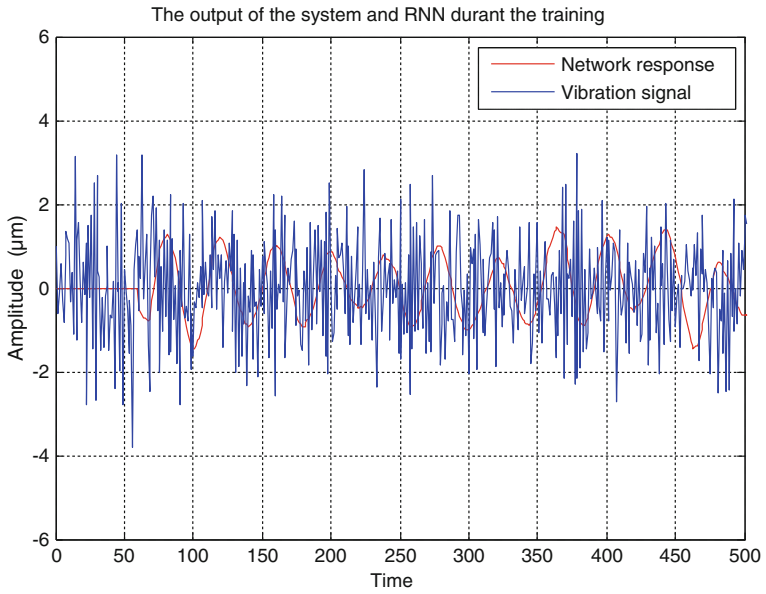


Fig. 4 Evolution of the spectral vibration structure

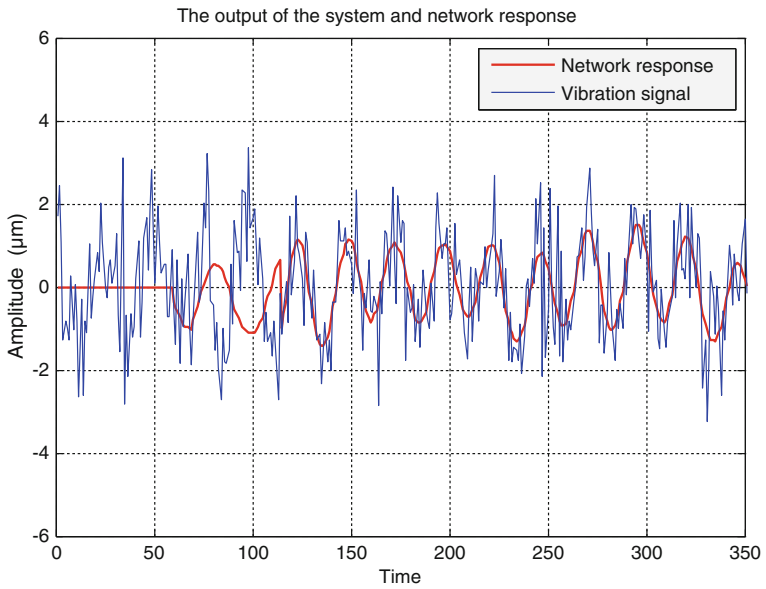


Fig. 5 Lineage defect amplitude/test 1



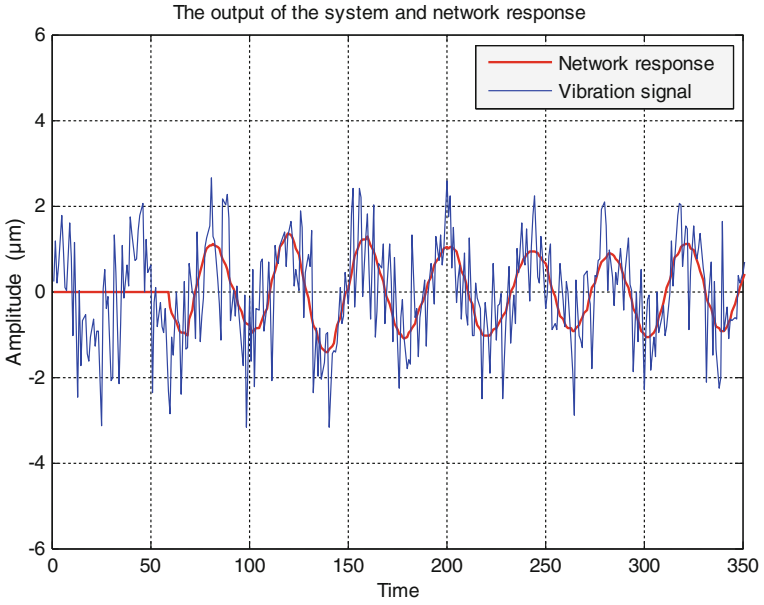


Fig. 6 Lineage defect amplitude/test 2

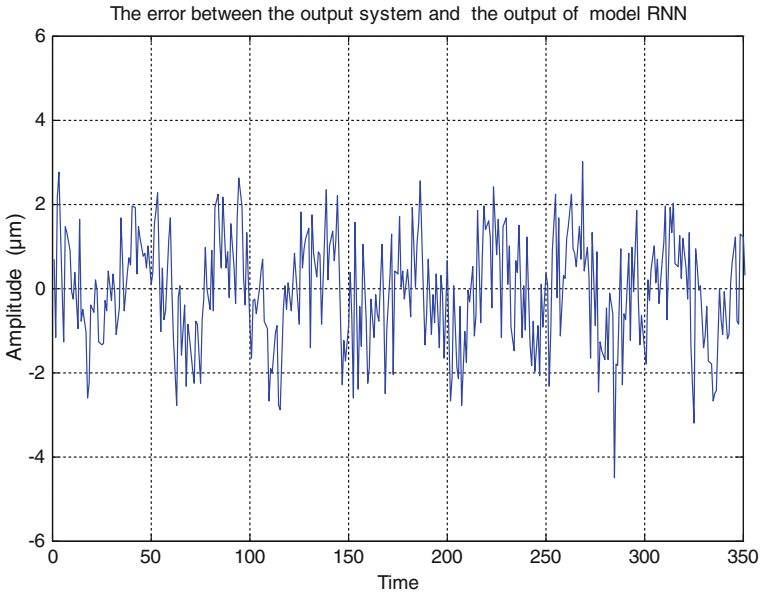


Fig. 7 Error between the output system and the output of neural network model

### 3.1 Validation Tests Using Wavelet Analysis

In this part of the work, wavelet analysis for the validation tests was performed; the wavelet transform is used to apply a multi-resolution analysis of the vibration signal obtained in the previous section. Indeed, the continuous wavelet transform is thus defined by the convolution  $f(t)$  with all translated and dilated wavelet  $\psi_{b,a}(t)$ , is give by:

$$TOC(b, a) = \frac{1}{\sqrt{|a|}} \int_{-\infty}^{+\infty} f(t) \psi\left(\frac{t-b}{a}\right) dt \quad (6)$$

With  $\psi_{b,a}(t)$  is generated by translations and dilatations of  $\psi(t)$  the latter is expanded with a scale parameter  $a$  and by translated parameter  $b$  given by:

$$\psi_{b,a} = \frac{1}{\sqrt{|a|}} \psi\left(\frac{t-b}{a}\right) \quad (7)$$

This means that any energy signal can be written as a linear combination of wavelets  $\psi_{b,a}(t)$  and wavelet coefficients of this combination are the scalar products, given by:

$$\int_{-\infty}^{+\infty} f(t) \psi_{b,a}(t) dt \quad (8)$$

With  $f(t)$  is being the studied signal.

We use the mathematical formula of the wavelet Morlet following:

$$\psi(x) = e^{-\pi x^2} e^{10i\pi x} \quad (9)$$

By expansion and translation in time, there is dilated and translated wavelet function  $\psi_{b,a}(t)$  which is represented in the following formula:

$$\psi_{b,a}(x) = \frac{1}{\sqrt{|a|}} e^{-\pi\left(\frac{x-b}{a}\right)^2} e^{10i\pi\left(\frac{x-b}{a}\right)} \quad (10)$$

Thus, the wavelet transform is a time-frequency resolution which depends on the scale, if it satisfies the following condition of eligibility:

$$C_\psi = \int_{-\infty}^{+\infty} \frac{|\hat{\psi}(x)|^2}{|x|} dx < +\infty \quad (11)$$

For the validation tests, the form used is the wavelet of Morlet shown in Fig. 8.

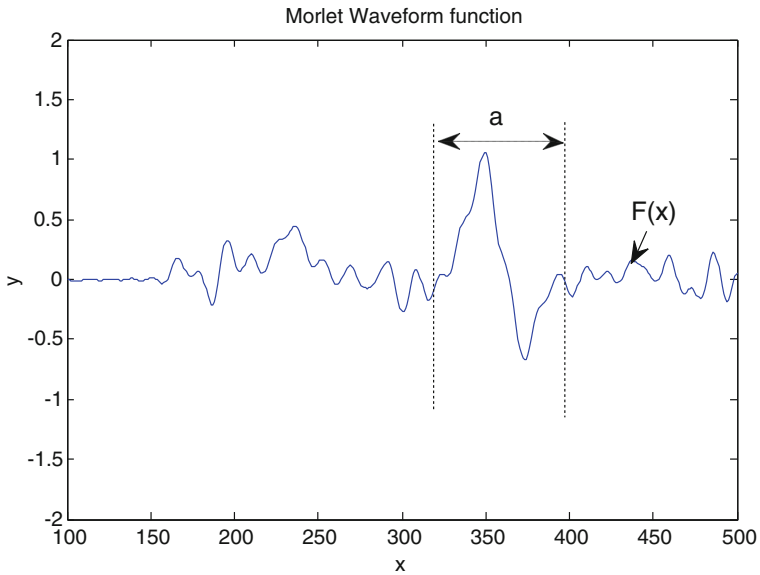


Fig. 8 Form of the used wavelet

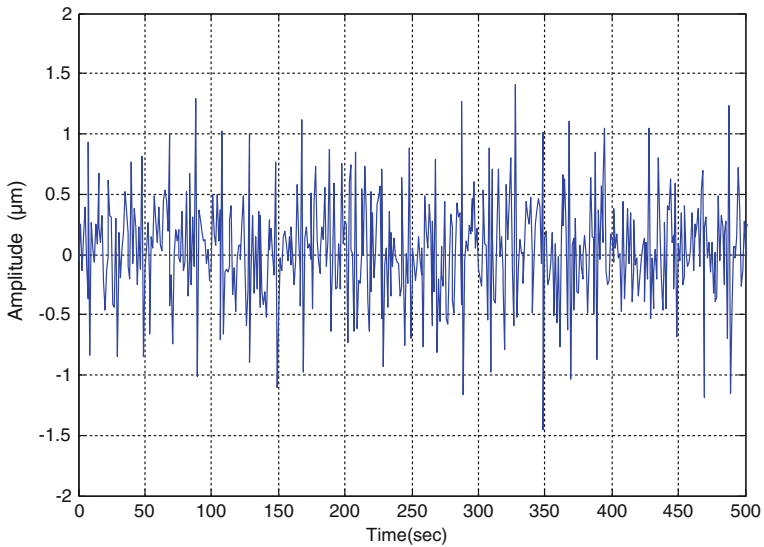


Fig. 9 Vibration signal with a lineage default

Figure 9 shows the results of validation tests, by applying the wavelet transform on the vibration signal measured at the bearing No. 03 of the high pressure (HP) turbine and Fig. 10 shows the spectrum obtained by the wavelet validation test.

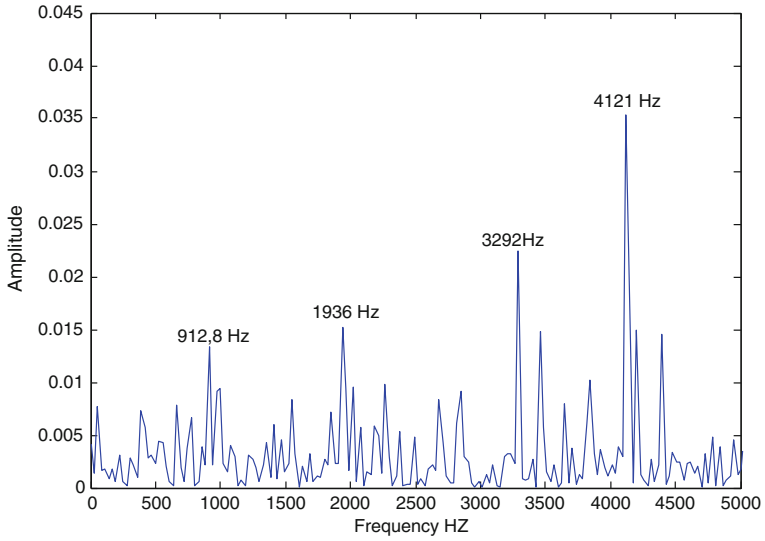


Fig. 10 Spectrum envelope of the wavelet coefficients

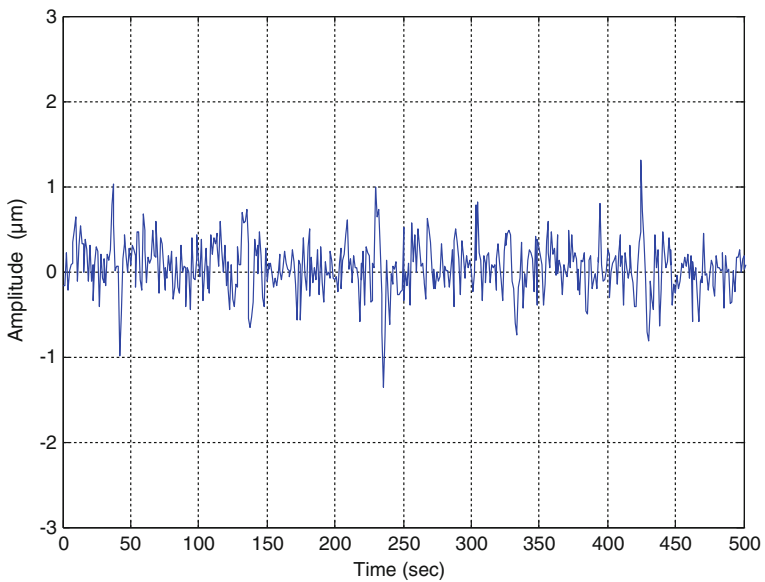
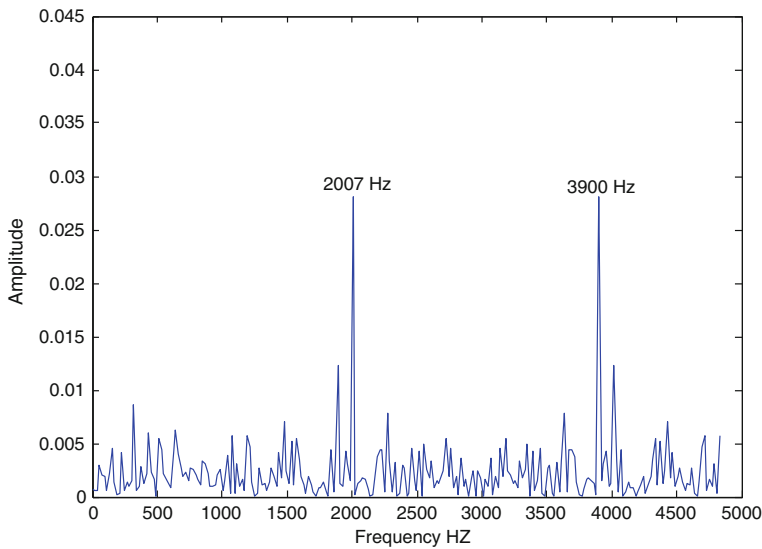


Fig. 11 Acceleration signal in the presence of defects in bearings

From the results obtained, defects of the bearings are manifested by the appearance of periodic impacts at particular frequencies. To overcome such defects, the wavelet application to this vibration signal measured was used on the bearing



**Fig. 12** Spectrum envelope of the wavelet coefficients

No. 03, the results of this test is shown in Fig. 11 and their spectrum envelope of the wavelet coefficients Fig. 12.

Experimental results obtained by following the experimental conditions are presented in this section, showing amplitude as a function of the vibration frequency signal. The bearing life depends on the load acting on the shaft, the rotational speed and the action point of the force.

## 4 Conclusion

The model developed in this work model the dynamic behavior of a gas turbine rotor type MS 3002, operated at high speed for defect detection vibration. The alignment effect is manifested as a component of high amplitude at the frequency of rotation of the rotor in radial direction, sometimes in the axial direction in the case of rotor cantilever. The monitoring approach offered by neural networks allows for the relationships between vibration signatures holders lineage defects. From this input variable, the neural network provides a representation for characterizing the output variables for proper monitoring strategy. And combining with the wavelet method, for the diagnosis of strategies was validated, and vibration signature, and allows a very precise analysis of vibration signals of defects of different types in multiple configurations in temporal mode frequency.

## References

- Ablay G (2013) A modeling and control approach to advanced nuclear power plants with gas turbines. *Energy Convers Manag* 76:899–909
- Bendjama H, Boucherit MS, Bouhouche S, Mansour M (2010) Vibration signal analysis using Wavelet—PCA-NN technique for fault diagnosis in rotating machinery. *Mediterr J Meas Control* 6(4):145–154
- Djaidir B, Hafaifa A, Abdallaha K (2014) Synthèse et surveillance des défauts de vibrations des turbines à gaz pour la prise de décision de contrôle. 1er Colloque International sur les Hydrocarbures, Energies et Environnement (HCEE), Ouargla, Algérie, 23–24 Novembre 2014
- Djeddi AZ, Hafaifa A, Salam A (2015a) Operational reliability analysis applied to a gas turbine based on three parameter Weibull distribution. *Mechanics* 21(3):187–192
- Djeddi AZ, Hafaifa A, Salam A (2015b) Gas turbine reliability model based on tangent hyperbolic reliability function. *J Theoret Appl Mech* 53(3):723–730
- Eshati S, Abu A, Laskaridis P, Khan F (2013) Influence of water–air ratio on the heat transfer and creep life of a high pressure gas turbine blade. *Appl Therm Eng* 60(1–2):335–347
- Guemana M, Hafaifa A, Rahmoune MB (2015) Reliability study of gas turbines for improving their availability by ensuring optimal exploitation. *OIL GAS Eur Mag* 2:88–91
- Hafaifa A, Djeddi AZ, Daoudi A (2013a) Fault detection and isolation in industrial control valve based on artificial neural networks diagnosis. *J Control Eng Appl Inform CEAI* 15(3):61–69
- Hafaifa A, Guemana M, Daoudi A (2013b) Fault detection and isolation in industrial systems based on spectral analysis diagnosis. *Intell Control Autom* 4(1):36–41
- Hafaifa A, Rachid B, Mouloud G (2014) Modelling of surge phenomena in a centrifugal compressor: experimental analysis for control. *Syst Sci Control Eng Open Access J* 2(1):632–641
- Hafaifa A, Benyounes A, Guemana M (2015a) Control of an industrial gas turbine based on fuzzy model. In: 16th IFAC conference on technology, culture and international stability, Sozopol, Bulgaria, 24–27 Sept 2015
- Hafaifa A, Guemana M, Daoudi A (2015b) Vibration supervision in gas turbine based on parity space approach to increasing efficiency. *J Vib Control* 21:1622–1632
- Jagaduri RT, Radman G (2007) Modeling and control of distributed generation systems including PEM fuel cell and gas turbine. *Electr Power Syst Res* 77(1):83–92
- Jurado F, Carpio J (2006) Improving distribution system stability by predictive control of gas turbines. *Energy Convers Manag* 47(18–19):2961–2973
- Kim KH, Ko H-J, Perez-Blanco H (2011) Analytical modeling of wet compression of gas turbine systems. *Appl Therm Eng* 31(5):834–840
- Lee MC, Chung JH, Park WS, Park S, Yoon Y (2013) The combustion tuning methodology of an industrial gas turbine using a sensitivity analysis. *Appl Therm Eng* 50(1):714–721
- Mohamed BR, Hafaifa A, Mouloud G (2015) Vibration modeling improves pipeline performance, costs. *Oil Gas J Mars* 113:98–100
- Nikpey H, Assadi M, Breuhaus P, Mørkved PT (2014) Experimental evaluation and ANN modeling of a recuperative micro gas turbine burning mixtures of natural gas and biogas. *Appl Energy* 117:30–41
- Rahmoune MB, Hafaifa A, Guemana M (2015) Neural network monitoring system used for the frequency vibration prediction in gas turbine. In: The 3rd international conference on control, engineering & information technology CEIT'2015, Tlemcen, Algeria, 25–27 May 2015
- Sanaye S, Tahani M (2010) Analysis of gas turbine operating parameters with inlet fogging and wet compression processes. *Appl Therm Eng* 30(2–3):234–244
- Simani S, Patton RJ (2008) Fault diagnosis of an industrial gas turbine prototype using a system identification approach. *Control Eng Pract* 16(7):769–786

# A Finite Element Model for Elastic-Viscoelastic-Elastic Composite Structures

Zhicheng Huang, Zhaoye Qin and Fulei Chu

**Abstract** A finite element model is developed to investigate the vibration and energy dissipation characteristics of elastic-viscoelastic-elastic composite (EVEC) beams. The theoretical energy dissipation characteristics of the EVEC beams are quantized by the loss factors. Two energy dissipation mechanisms, namely the shear and compression damping are combined in the finite element model. Numerical examples are provided to verify the finite element model. The instructive conclusions are important to make the EVEC beam more suitable for controlling structural vibrations and noise.

**Keywords** Viscoelastic material · Composite structure · Combined damping · Finite element method · Vibration analysis

## 1 Introduction

Elastic-viscoelastic-elastic composite (EVEC) structures have been extensively applied to various structures in order to attenuate their vibration response noise (Nashif et al. 1985). It is very important to study their energy-dissipation Characteristics.

Most of researchers in this area make the assumption that the shear damping is the only mechanism, and the compressional damping does not occur or is negligible. Kerwin (1959) first studied the viscoelastic damping based on the theory that the damping only came from the shear strain of the viscoelastic layer. Ungar (1962) extended this work to a more general analysis for complicated viscoelastic

---

Z. Huang (✉) · Z. Qin · F. Chu  
Department of Mechanical Engineering, Tsinghua University,  
Beijing 100084, China  
e-mail: huangwu555@sina.com

Z. Huang  
College of Mechanical and Electronic Engineering, Jingdezhen Ceramic Institute,  
Jingdezhen 333001, Jiangxi, China

geometries. DiTaranto (1965) accounted for the extensional deformations in the viscoelastic. Mead and Markus (1969) derived sixth-order equation of motion for EVEC beam. Johnson and Kienholz (1982) used Modal strain Energy (MSE) method to predict the damping characteristics of EVEC structures. Later, many researchers such as, Galucio et al. (2004), Kumar and Singh (2009), Daya and Potier-Ferry (2001) and Bilasse et al. (2011) developed some numerical model models for EVE sandwich beams and plates.

On the other hand, some researchers experimentally found the compressional damping of the EVEC structures, and some analytical models based on compressional assumption of dissipating energy were established. Douglas and Yang (1978) and Douglas (1986) presented a mathematical model for compressional damping of EVEC beam, and they proved the transverse compressional damping by experiment. Sisemore et al. (1999) and Sisemore and Darvennes (2002) presented cantilever EVEC beam experiments, and the results showed the compressional damping in the viscoelastic core.

The models of EVEC structures in above-cited works were analytical models. Moreover, they considered only one damping mechanism. In fact, there exist two damping mechanisms in the viscoelastic core, namely, the shear and compressional damping mechanisms. The shear strains results from the longitudinal relative motion of the two elastic layers. The compression strains of the viscoelastic core results from the transverse relative vibration of the two elastic layers.

The purpose of this research is to develop a refined finite element (FE) model to investigate the vibration and energy dissipation characteristics of EVEC beams. The FE model simultaneously considers the shear and compression deformation of the viscoelastic layer.

## 2 Finite Element Modeling

### 2.1 Model and Basic Assumptions

The FE model is briefly outlined in this section to describe the behavior of EVEC beam. It is assumed that the base beam and the constraining layer follow the Euler–Bernoulli beam theory. The base beam and the constraining layer have different transverse deflection. The transverse displacement of the viscoelastic layer is the linear interpolation of the ones between the constraining layer and the base beam. The structural damping is caused by the shear and compression deformation of the viscoelastic layer. Every layer is pasted solidly and there is no relative sliding between layers.



### 2.2 Kinematics

Based on the above assumptions, with the geometry and deformation of the EVEC beam, the longitudinal and transverse displacements of the viscoelastic layer can be derived, respectively:

$$u_v = \frac{1}{2} \left[ (u_c + u_b) + \frac{1}{2} \left( h_c \frac{\partial w_c}{\partial x} - h_b \frac{\partial w_b}{\partial x} \right) \right], \quad w_v = \frac{1}{2} (w_c + w_b) \quad (1a, b)$$

The shear strain and the transverse compression strain can respectively given by

$$\beta = \frac{1}{h_v} \left[ (u_c - u_b) + \frac{(h_c + h_v)}{2} \frac{\partial w_c}{\partial x} + \frac{(h_b + h_v)}{2} \frac{\partial w_b}{\partial x} \right], \quad \varepsilon_v = \frac{1}{h_v} (w_c - w_b) \quad (2a, b)$$

where  $u_c$  and  $u_b$  are the longitudinal deflections of the constraining layer and the base beam,  $h_c$ ,  $h_v$  and  $h_b$  are the thickness of the constraining layer, the viscoelastic layer.

### 2.3 Degrees of Freedom and Shape Functions

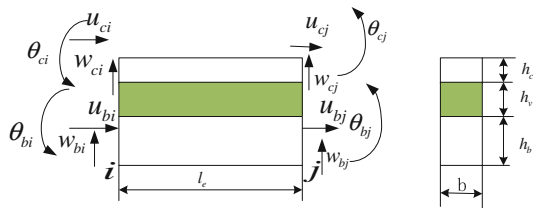
The beam elements considered in this study are integral one-dimensional elements bounded by two nodes. Each node has six degrees of freedom to describe the longitudinal, transverse and angular displacement of the constraining layer and the base beam. Figure 1 shows an EVEC beam element.

The nodal displacements are given by

$$\{\Delta^e\} = \{w_{ci} \ \theta_{ci} \ u_{ci} \ w_{bi} \ \theta_{bi} \ u_{bi} \ w_{cj} \ \theta_{cj} \ u_{cj} \ w_{bj} \ \theta_{bj} \ u_{bj}\}^T \quad (3)$$

The transverse displacement  $w_c$ , the rotation  $\theta_c$  and the axial displacement  $u_c$  of the constraining layer, the transverse displacement  $w_b$ , the rotation  $\theta_b$  and the axial displacement  $u_b$  of the beam are expressed in the nodal displacements by finite shape functions

**Fig. 1** Nodal displacement of a EVEC beam element



$$\begin{aligned} w_c &= [N_1]\{\Delta^e\}, & \theta_c &= [N_2]\{\Delta^e\}, & u_c &= [N_3]\{\Delta^e\} \\ w_b &= [N_4]\{\Delta^e\}, & \theta_b &= [N_5]\{\Delta^e\}, & u_b &= [N_6]\{\Delta^e\} \end{aligned} \quad (4a-f)$$

where the shape functions are given by

$$\begin{aligned} N_1 &= \left[ 2\left(\frac{x}{le}\right)^3 - 3\left(\frac{x}{le}\right)^2 + 1 \quad \frac{x^3}{le^2} - 2\left(\frac{x^2}{le}\right) + x \quad 0 \quad 0 \quad 0 \quad 0 \right. \\ &\quad \left. -2\left(\frac{x}{le}\right)^3 + 3\left(\frac{x}{le}\right)^2 \quad \frac{x^3}{le^2} - \frac{x^2}{le} \quad 0 \quad 0 \quad 0 \quad 0 \right] \\ N_2 &= \left[ 6\left(\frac{x^2}{le^3}\right) - 6\left(\frac{x}{le^2}\right) \quad 3\left(\frac{x}{le}\right)^2 - 4\left(\frac{x}{le}\right) + 1 \quad 0 \quad 0 \quad 0 \quad 0 \right. \\ &\quad \left. -6\left(\frac{x^2}{le^3}\right) + 6\left(\frac{x}{le^2}\right) \quad 3\left(\frac{x}{le}\right)^2 - 2\left(\frac{x}{le}\right) \quad 0 \quad 0 \quad 0 \quad 0 \right] \\ [N_3] &= \left[ 0 \quad 0 \quad 1 - \frac{x}{le} \quad 0 \quad 0 \quad 0 \quad 0 \quad 0 \quad \frac{x}{le} \quad 0 \quad 0 \quad 0 \right] \\ N_4 &= \left[ 0 \quad 0 \quad 0 \quad 2\left(\frac{x}{le}\right)^3 - 3\left(\frac{x}{le}\right)^2 + 1 \quad \frac{x^3}{le^2} - 2\left(\frac{x^2}{le}\right) \right. \\ &\quad \left. + x \quad 0 \quad 0 \quad 0 \quad 0 \quad -2\left(\frac{x}{le}\right)^3 + 3\left(\frac{x}{le}\right)^2 \quad \frac{x^3}{le^2} - \frac{x^2}{le} \quad 0 \right] \\ N_5 &= \left[ 0 \quad 0 \quad 0 \quad 6\left(\frac{x^2}{le^3}\right) - 6\left(\frac{x}{le^2}\right) \quad 3\left(\frac{x}{le}\right)^2 - 4\left(\frac{x}{le}\right) + 1 \quad 0 \quad 0 \quad 0 \quad 0 \right. \\ &\quad \left. -6\left(\frac{x^2}{le^3}\right) + 6\left(\frac{x}{le^2}\right) \quad 3\left(\frac{x}{le}\right)^2 - 2\left(\frac{x}{le}\right) \quad 0 \right] \\ [N_6] &= \left[ 0 \quad 0 \quad 0 \quad 0 \quad 0 \quad 1 - \frac{x}{le} \quad 0 \quad 0 \quad 0 \quad 0 \quad 0 \quad \frac{x}{le} \right] \end{aligned} \quad (5a-f)$$

Applying shape functions, Eqs. (1) and (2) can be expressed in the nodal displacement as follows:

$$u_v = [N_7]\{\Delta^e\}, \quad w_v = [N_8]\{\Delta^e\}, \quad \beta = [N_9]\{\Delta^e\}, \quad \varepsilon_v = [N_{10}]\{\Delta^e\} \quad (6a-d)$$

where

$$\begin{aligned} [N_7] &= \frac{1}{2} \left[ (N_3 + N_6) + \frac{1}{2}(h_c N_2 - h_b N_5) \right], & [N_8] &= \frac{1}{2}(N_1 + N_4), \\ [N_9] &= \frac{1}{h_v} \left[ (N_3 - N_6) + \frac{(h_c + h_v)}{2} N_2 + \frac{(h_b + h_v)}{2} N_5 \right], & [N_{10}] &= \frac{1}{h_v}(N_1 - N_4) \end{aligned} \quad (7a-d)$$

## 2.4 Energy Expressions

In this section, the energy expressions of the element are derived to obtain the mass and stiffness matrices. The nomenclature used in this section is present as follows:  $E_i, A_i, I_i$  and  $\rho_i (i = c, v, b)$  are the Young's modulus, the cross-sectional area, the

moment of inertia and the density of the constraining layer, the viscoelastic layer and the base beam, respectively.  $G_v$  is the shear modulus of the viscoelastic layer.

### 2.4.1 Potential Energy

#### 1. The constraining layer

$$U_c = \frac{1}{2} \int_0^{l_c} \left[ E_c A_c \left( \frac{\partial u_c}{\partial x} \right)^2 + E_c I_c \left( \frac{\partial^2 w_c}{\partial x^2} \right)^2 \right] dx = \frac{1}{2} \{\Delta^e\}^T ([K_{ec}] + [K_{bc}]) \{\Delta^e\} \quad (8a, b)$$

where

$$[K_{ec}] = E_c A_c \int_0^{l_c} \left[ \frac{\partial N_3}{\partial x} \right]^T \left[ \frac{\partial N_3}{\partial x} \right] dx, \quad [K_{bc}] = E_c I_c \int_0^{l_c} \left[ \frac{\partial^2 N_1}{\partial x^2} \right]^T \left[ \frac{\partial^2 N_1}{\partial x^2} \right] dx \quad (9a, b)$$

#### 2. The base beam layer

$$U_b = \frac{1}{2} \int_0^{l_c} \left[ E_b A_b \left( \frac{\partial u_b}{\partial x} \right)^2 + E_b I_b \left( \frac{\partial^2 w_b}{\partial x^2} \right)^2 \right] dx = \frac{1}{2} \{\Delta^e\}^T ([K_{eb}] + [K_{bb}]) \{\Delta^e\} \quad (10a, b)$$

where

$$[K_{eb}] = E_b A_b \int_0^{l_c} \left[ \frac{\partial N_6}{\partial x} \right]^T \left[ \frac{\partial N_6}{\partial x} \right] dx, \quad [K_{bb}] = E_b I_b \int_0^{l_c} \left[ \frac{\partial^2 N_4}{\partial x^2} \right]^T \left[ \frac{\partial^2 N_4}{\partial x^2} \right] dx \quad (11a, b)$$

#### 3. The viscoelastic layer

$$U_v = \frac{1}{2} \int_0^{l_c} [G_v A \beta^2 + E_v h_v b \varepsilon_v^2] dx = \frac{1}{2} \{\Delta^e\}^T ([K_{sv}] + [K_{pv}]) \{\Delta^e\}^T \quad (12a, b)$$

where

$$[K_{sv}] = G_v A_v \int_0^{l_e} [N_9]^T [N_9] dx, \quad [K_{pv}] = E_v h_v b \int_0^{l_e} ([N_{10}]^T [N_{10}]) dx \quad (13a, b)$$

The total stiffness matrix of the EVEC beam element is

$$[K^e] = [K_{ec}] + [K_{bc}] + [K_{eb}] + [K_{bb}] + [K_{sv}] + [K_{pv}] \quad (14)$$

## 2.4.2 Kinetic Energy

### 1. The constraining layer

$$T_c = \frac{1}{2} \int_0^{l_e} \left[ \rho_c A_c \left( \frac{\partial u_c}{\partial t} \right)^2 + \rho_c A_c \left( \frac{\partial w_c}{\partial t} \right)^2 \right] dx = \frac{1}{2} \{ \dot{\Delta}_e \}^T ([M_{ec}] + [M_{bc}]) \{ \dot{\Delta}_e \} \quad (15a, b)$$

where

$$[M_{ec}] = \rho_c A_c \int_0^{l_e} [N_3]^T [N_3] dx, \quad [M_{bc}] = \rho_c A_c \int_0^{l_e} [N_1]^T [N_1] dx \quad (16a, b)$$

### 2. the base beam layer

$$T_b = \frac{1}{2} \int_0^{l_e} \left[ \rho_b A_b \left( \frac{\partial u_b}{\partial t} \right)^2 + \rho_b A_b \left( \frac{\partial w}{\partial t} \right)^2 \right] dx = \frac{1}{2} \{ \dot{\Delta}_e \}^T ([M_{eb}] + [M_{bb}]) \{ \dot{\Delta}_e \} \quad (17a, b)$$

where

$$[M_{eb}] = \rho_b A_b \int_0^{l_e} [N_6]^T [N_6] dx, \quad [M_{bb}] = \rho_b A_b \int_0^{l_e} [N_4]^T [N_4] dx \quad (18a, b)$$

### 3. the viscoelastic layer

$$T_v = \frac{1}{2} \int_0^{l_e} \left[ \rho_v A_v \left( \frac{\partial u_v}{\partial t} \right)^2 + \rho_v A_v \left( \frac{\partial w}{\partial t} \right)^2 \right] dx = \frac{1}{2} \left\{ \dot{\Delta}_e \right\}^T ([M_{ev}] + [M_{bv}]) \left\{ \dot{\Delta}_e \right\} \quad (19a, b)$$

where

$$[M_{ev}] = \rho_v A_v \int_0^{l_e} [N_7]^T [N_7] dx, \quad [M_{bv}] = \rho_v A_v \int_0^{l_e} [N_8]^T [N_8] dx \quad (20a, b)$$

The total mass matrix of the EVEC beam element is

$$[M^e] = [M_{ec}] + [M_{bc}] + [M_{eb}] + [M_{bb}] + [M_{ev}] + [M_{bv}] \quad (21)$$

## 2.5 Equations of Motion

Using Hamilton's principle, the equations of motion for the EVEC beam element can be written as:

$$M^e \ddot{\Delta}^e + K^e \Delta^e = R^e \quad (22)$$

For the whole EVEC beam, by assembling the mass matrix and the stiffness matrix with standard FEM assembling procedures, the global dynamic equation can be derived as:

$$M \ddot{\Delta} + K \Delta = R \quad (23)$$

where  $M$  is the total mass matrix of the EVEC beam,  $K$  is the total stiffness matrix of the EVEC beam, and  $R$  is the force exerted on the EVEC beam system.

## 3 Finite Element Model Validation

A cantilever EVEC beam case is used to validate the presented FE model. The material and geometrical parameters of the sandwich beam are presented in Table 1. The natural frequencies and associated loss factors of the clamped-free sandwich beam corresponding to the first three modes are presented in Table 2. The results from the present FE model are compared with the experimental values

**Table 1** Material and geometrical parameters of cantilever EVEC beams

Constraining layer and base beam	Young's modulus	$E_c = E_b = 6.87 \times 10^{10}$ Pa
	Poisson's ratio	$\nu_c = \nu_b = 0.33$
	Mass density	$\rho_c = \rho_b = 2.69 \times 10^3$ kg/m <sup>3</sup>
	Thickness	$h_c = h_b = 3$ mm
Viscoelastic core	Young's modulus	Depend on frequency
	Poisson's ratio	$\nu_v = 0.25$
	Mass density	$\rho_v = 795$ kg/m <sup>3</sup>
	Loss factor	Depend on frequency
	Thickness	$h_v = 2$ mm
Structure size	Length	$L1 = 500$ mm
	Width	$b = 24$ mm

**Table 2** Comparisons between experimental and numerical results of the first three natural frequencies for the EVEC beam

Mode	Experimental result (Barbosa and Farage 2008)		Present FE model			
	Natural frequency (Hz)	Loss factor	Natural frequency (Hz)	Error (%)	Loss factor	Error (%)
1	16.95	0.1748	17.15	1.17	0.1797	2.80
2	79.33	0.1350	76.91	3.05	0.1361	0.81
3	184.44	0.0765	184.76	0.17	0.0822	7.45

(Barbosa and Farage 2008). When the presented FE model is used, the cantilever EVEC beam is discretized into 30 elements.

The Young's modulus and loss factor of the viscoelastic core can be expressed as, respectively:

$$E_v = \varepsilon + \frac{\alpha\omega^2(\omega^2 - \delta + \beta^2)}{(\delta - \omega^2)^2 + \beta^2\omega^2} \quad (28)$$

$$\eta_v = \frac{\alpha\beta\omega\delta}{(\delta - \omega^2)^2 + \beta^2\omega^2} \frac{1}{E_v} \quad (29)$$

where  $\alpha = 5.26$  MPa,  $\beta = 55.59 \times 10^6$  s<sup>-1</sup>,  $\delta = 6.98 \times 10^9$  s<sup>-2</sup>, and  $\varepsilon = 0.58$  MPa.

Table 2 shows the natural frequencies and the associated loss factors of the clamped-free sandwich beam corresponding to the first three modes by using the presented FE method and the experimental results, respectively. Compared with the experimental results, the errors of the FE method are showed in Table 2 as well.

It can be seen from Table 2 that the presented FE model has good accuracy in predicting the natural frequency and the loss factor of the EVEC beam structure.

The error range is from 0.17 to 3.05 %, and the average error is 1.46 %. It can be seen from Table 2 that the theoretical predictions are very close to the experimental values for the first three loss factors as well. The error range of the loss factors is from 0.81 to 7.45 %, and the average error is 3.69 %.

The results presented in Table 2 show a good agreement between the theoretical predictions and experimental values for the first three natural frequencies and loss factor. This provides validation for the present complex finite element model.

## 4 Conclusions

A refined FE numerical model is developed to analyze the vibration and damping characteristics of EVEC beam structure. A type of one-dimensional sandwich beam element with eight DOF is used to discretize the composite beam structure. The viscoelastic material of the core layer is assumed to be compressible. Both of the shear and compressional deformations of the viscoelastic core are considered in the FE model. The energy-dissipation characteristics of the EVEC beams are quantized by the loss factors. The natural frequencies and loss factors of the EVEC beams are investigated by the FE model. The results of the present finite element method are compared with the experimental ones to verify the validity of the FE method.

**Acknowledgments** This research is funded by the Natural Science Foundation of China (11272170, 11102096), and the authors are grateful to them for supporting the research.

## References

- Barbosa FS, Farage MCR (2008) A finite element model for sandwich viscoelastic beams: experimental and numerical assessment. *J Sound Vib* 317(1–2):91–111
- Bilasse M, Azrar L, Daya EM (2011) Complex modes based numerical analysis of viscoelastic sandwich plates vibrations. *Comput Struct* 89(7–8):539–555
- Daya EM, Potier-Ferry M (2001) A numerical method for nonlinear eigenvalue problems application to vibrations of viscoelastic structures. *Comput Struct* 79(5):533–541
- DiTaranto RA (1965) Theory of vibratory bending for elastic and viscoelastic layered finite length beams. *J Appl Mech* 87:881–886
- Douglas BE (1986) Compressional damping in three-layer beams incorporating nearly incompressible viscoelastic cores. *J Sound Vib* 104(2):343–347
- Douglas BE, Yang JCS (1978) Transverse compressional damping in the vibratory response of elastic–viscoelastic–elastic beams. *Am Inst Aeronaut Astronaut J* 16(9):925–930
- Galucio AC, Deu JF, Ohayon R (2004) Finite element formulation of viscoelastic sandwich beams using fractional derivative operators. *Comput Mech* 33(4):282–291
- Johnson CD, Kienholz DA (1982) Finite element prediction of damping in structures with constrained layers. *AIAA J* 120(9):1284–1285
- Kerwin EM (1959) Damping of flexural waves by a constrained viscoelastic layer. *J Acoust Soc Am* 31(7):952–962

- Kumar N, Singh SP (2009) Vibration and damping characteristics of beams with active constrained layer treatments under parametric variations. *Mater Des* 30(10):4162–4417
- Mead DJ, Markus S (1969) The forced vibration of a three-layer damping sandwich beam with arbitrary boundary conditions. *J Sound Vib* 10(2):163–175
- Nashif AD, Jones D, Henderson J (1985) *Vibration damping*. Wiley, New York
- Sisemore CL, Darvennes CM (2002) Transverse vibration of elastic-viscoelastic-elastic sandwich beams: compression-experimental and analytical study. *J Sound Vib* 252(1):155–167
- Sisemore CL, Smaili AA, Darvennes CM (1999) Experimental measurement of compressional damping in an elastic–viscoelastic–elastic sandwich beam. In: *Proceedings of the American Society of Mechanical Engineers Noise Control and Acoustics Division*, pp 223–227
- Ungar EE (1962) Loss factor of viscoelastically damped beam structures. *J Acoust Soc Am* 34(8):1082–1089



# Application of the Operational Modal Analysis Using the Independent Component Analysis for a Quarter Car Vehicle Model

Dorra Ben Hassen, Mariem Miladi, Mohamed Slim Abbes,  
S. Caglar Baslamisli, Fakher Chaari and Mohamed Haddar

**Abstract** This paper investigates the dynamic behavior of a quarter car vehicle system using the Operational Modal Analysis (OMA). This method is applied using one of the major techniques of the Blind Source Separation (BSS) which is the Independent Component Analysis (ICA). Compared to the classical modal analysis, the Operational Modal Analysis presents the advantage that it is only based on the vibratory responses of the structure in order to identify its modal parameters. To validate this approach in the case of a quarter car vehicle model, the estimated results obtained by the OMA methods are presented and compared with those obtained by the modal recombination method.

**Keywords** Operational modal analysis · Independent component analysis · Quarter car vehicle model

---

D.B. Hassen (✉) · M. Miladi · M.S. Abbes · F. Chaari · M. Haddar  
Mechanics, Modeling and Production Laboratory, National Engineering School  
of Sfax (ENIS), BP 1173–3038, Sfax, Tunisia  
e-mail: dorra.benhassen@yahoo.fr

M. Miladi  
e-mail: mariam.mi@hotmail.fr

M.S. Abbes  
e-mail: ms.abbes@gmail.com

F. Chaari  
e-mail: fakher.chaari@gmail.com

M. Haddar  
e-mail: Mohamed.haddar@enis.rnu.tn

S.C. Baslamisli  
Department of Mechanical Engineering, Hacettepe University,  
06800 Beytepe, Ankara, Turkey  
e-mail: caglar.baslamisli@gmail.com

# 1 Introduction

The modal analysis is an interesting research area. In fact, this method allows the determination of the dynamic characteristics of a system such as: the eigenfrequencies, the mode shapes and the damping coefficients. Classical modal analysis requires the measurement of the vibratory responses of the system and the knowledge of the applied forces on it. But in real structures, it is hard to identify exactly the excitation force such as for the case big machines vibrations or the wind acting on the buildings.... Thus, the major difficulty of such problem resides in the existence of any information about these forces For this purpose, this paper deals with the use of the Operational Modal Analysis (OMA) based on the Independent Component Analysis (ICA) in order to identify the modal parameters of a system knowing only its vibratory responses. Many authors were interested in this technique, for example Abbes et al. (2011) showed that the ICA can be used in the OMA in order to determine the modal characteristics of vibrations of a double panel system. Others like (Akrouf et al. 2012) used the ICA as a method of the OMA in the case of laminated double-glazing system and determined the modal parameters of the structure. They validated this technique by calculating three types of performance criteria. Kershen et al. (2007) showed the relation between the vibration modes and those obtained by the ICA technique in the case of structural dynamics.

In this paper, the use of The ICA as a technique of the OMA is applied in the case of a quarter car vehicle model to identify its dynamic characteristics. In fact, the determination of the modal parameters of this system is very important in order to avoid the resonance when using such system. Nevertheless, the suspension system is a very important part in the vehicle. It permits the minimization of the vibrations due to the road profile also, it ensures the vehicle handling (Li et al. 2014; Purushotham 2013). Basha and Rao (2012) examined the MacPherson suspension system using a finite element formulation and concluded that it is possible to ensure a good road handling using the parameters of the considered suspension. Maher and Young (2007) achieved an experimental test for a suspension system and compared the results with those obtained numerically using the modal analysis.

This paper is structured as follows: In the first section a brief presentation of the OMA method is done, then, a description of the studied system is carried out. Finally, comparison between estimated and theoretical modal parameters responses is performed.

## 1.1 Description of the ICA

The vector of the observed signals  $X$  can be written as (Jutten and Héroult 1991)

$$X(t) = [A]\{S\} \quad (1)$$

where:  $A$  is the mixing matrix and  $S$  is the vector of the source signals.

The ICA concept consists on estimating both  $A$  and  $S$  based only on the knowledge of the vector  $X$ . This estimation must be done under many assumptions (Hyvärinen and Oja 2000; Taktak et al. 2012) which are defined as follows:

- The components of the vector  $S$  are statistically independent.
- These independent components must be uncorrelated.
- The components of the vector  $S$  must have a non Gaussian distribution.

## 1.2 Application of the ICA in the OMA

The modal response of a given mechanical system using the modal superposition method can be written as follows:

$$y(t) = \sum_{i=1}^n a_i \exp(-\xi_i \omega_i t) \sin(\omega_{di} t + \varphi_i) \quad (2)$$

With:  $\xi_i$ : damping coefficients,  $\omega_i$ : natural frequencies,  $\omega_{di}$ : damped frequencies,  $\varphi_i$ : phasing and  $a_i$ : Constants determined from the initial conditions,  $t$ : time.

Starting from this response, the dynamic response of the system can be written as:

$$x = \psi y \quad (3)$$

With:  $x$ : the measured signal (displacement),  $\psi$ : the modal matrix.

By combining the two Eqs. (2) and (3),  $x(t)$  can be written as:

$$x(t) = \sum_{i=1}^n \psi_i a_i \exp(-\xi_i \omega_i t) \sin(\omega_{di} t + \varphi_i) \quad (4)$$

The principal idea is to consider the vibratory responses  $x(t)$  as virtual sources with different spectral contents. They are considered as the observed signals of the ICA algorithm. Then, we apply the ICA concept; in this case, the ICA provides the mixing matrix  $A$  which is close to the matrix  $\psi$  and the estimated signals  $S$  which are close to the modal responses. From these responses the eignfrequencies and the damping coefficients are determined.

So, it can be noticed that the ICA technique is close to the Operational Modal Analysis which aims to determine the modal matrix  $\psi$ , the damping coefficients and the natural frequencies of the system by knowing only the measured signal  $X(t)$ .

## 2 Description of the Studied System

### 2.1 Presentation of the System

The studied system is presented by Fig. 1.

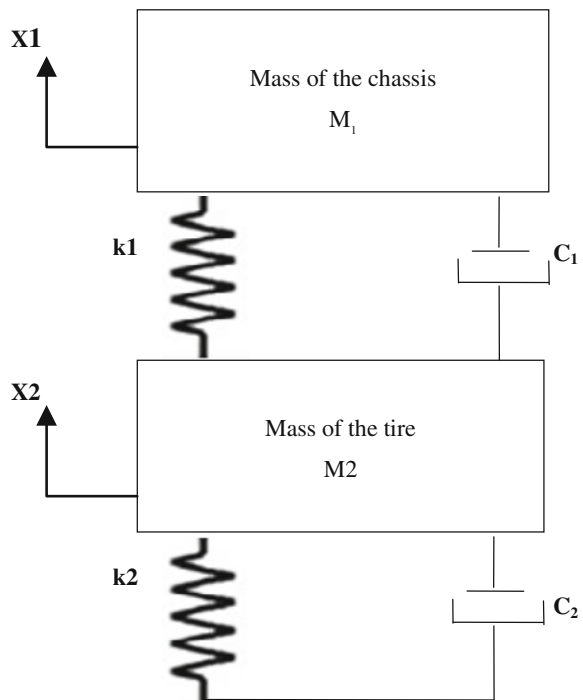
This system has two degrees of freedom.  $X_1$  is related to the sprung mass  $M_1$  and  $X_2$  is related to the unsprung mass  $M_2$ . The mathematical formulation of the equations of motion is described in the following section.

### 2.2 Equations of Motion

The two equations of motion of the system can be written in a matrix form as follows:

$$[M]\{\ddot{X}\} + [C]\{\dot{X}\} + [K]\{X\} = 0 \quad (5)$$

**Fig. 1** Quarter car vehicle model



where:

$\{X\}$ ,  $\{\dot{X}\}$  and  $\{\ddot{X}\}$  are respectively displacement, velocity and acceleration vectors.

$[M]$  is the mass matrix (Kg) described as follow:  $[M] = \begin{bmatrix} M_1 & 0 \\ 0 & M_2 \end{bmatrix}$ .

$[C]$  is the damping matrix (Ns/m) which is written as:  $[C] = \begin{bmatrix} c_1 & -c_1 \\ -c_1 & c_1 + c_2 \end{bmatrix}$ .

$[K]$  is the stiffness matrix (N/m) which is equal to:  $[K] = \begin{bmatrix} k_1 & -k_1 \\ -k_1 & k_1 + k_2 \end{bmatrix}$ .

In our case, we are going to use the parameters values as written below:

$$[M] = \begin{bmatrix} 1085 & 0 \\ 0 & 40 \end{bmatrix}; [C] = \begin{bmatrix} 100 & -100 \\ -100 & 200 \end{bmatrix}; [K] = \begin{bmatrix} 10000 & -10000 \\ -10000 & 140000 \end{bmatrix}$$

The vibratory responses of the suspension system is numerically computed, taking into consideration these initial conditions:

$$\text{Initial displacements: } \{X_0\} = \begin{bmatrix} 10^{-3} \\ 10^{-3} \end{bmatrix}$$

$$\text{Initial velocities: } \{\dot{X}_0\} = \begin{bmatrix} 10^{-3} \\ 10^{-3} \end{bmatrix}$$

In Fig. 2 we present the vibratory responses of the quarter car vehicle model with their frequency spectrum.

It can be noticed that the frequency spectrum of the observed signals  $X$  contains the eigenfrequencies of the studied system which are equals to ( $f_1 = 0.5$  Hz and  $f_2 = 10$  Hz).

### 3 Results of the Application of the ICA

Starting only from the vibratory responses presented in Fig. 2, the modal parameters of the quarter car vehicle model are estimated via the ICA method.

Figure 3 presents the two estimated modal responses of the quarter car vehicle model as well as their spectrum.

From these figures, it can be concluded that the ICA can identify the modal parameters of the quarter car vehicle system. In fact, for each estimated modal response, the spectral contents show only one eigenfrequency which is the estimated eigenfrequency of the corresponding mode.

**Fig. 2** Vibratory responses of the quarter car vehicle model **a**  $X_1$  **b**  $X_2$

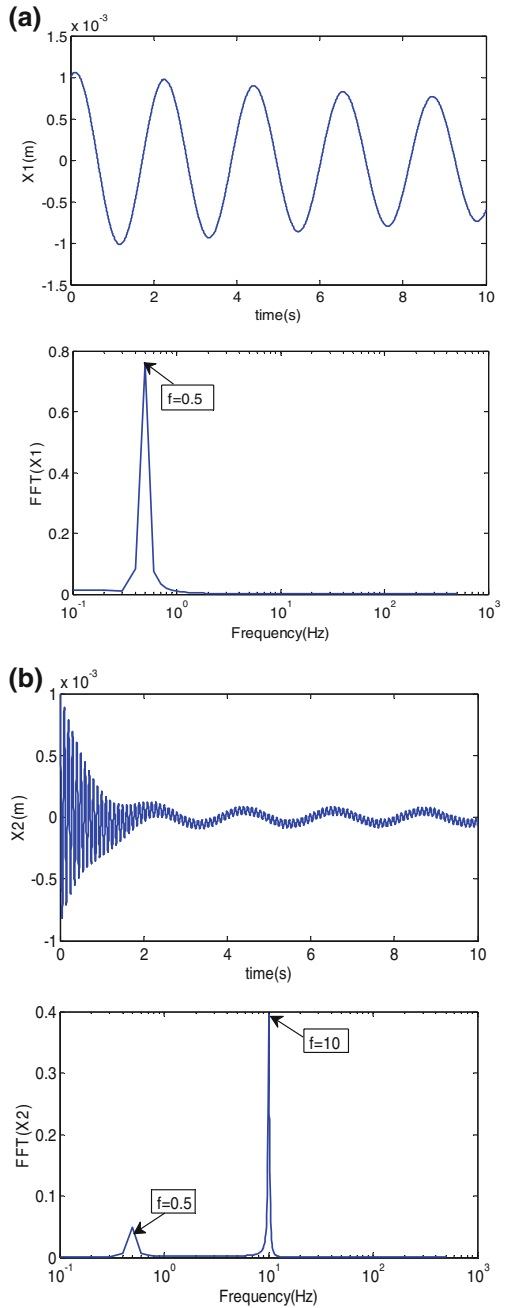


**Fig. 3** Modal responses and frequency spectrum of the quarter car vehicle **a** mode 1  
**b** mode 2

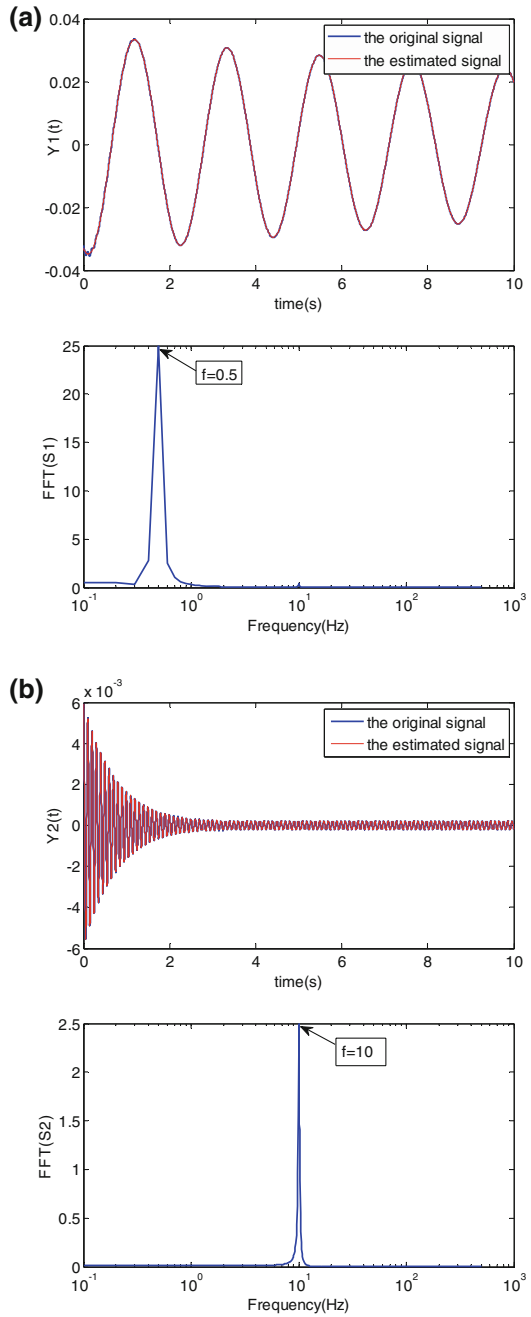


**Table 1** Comparison between the eignfrequencies

Mode	Theoretical frequency (Hz)	Estimated theory (Hz)	Relative error (%)
1	F1 = 0.46	F1 = 0.5	8
2	F2 = 10.066	F2 = 10	0.66

**Table 2** Comparison between the damping coefficients

Mode	Theoretical damping coefficient	Estimated damping coefficient	Relative error (%)
1	$\zeta_1 = 0.32$	$\zeta_1 = 0.3$	6
2	$\zeta_2 = 0.16$	$\zeta_2 = 0.162$	1.2

Table 1 summarizes both the theoretical eignfrequencies and the estimated ones. A good agreement is obtained when comparing the two results.

The damping coefficients of each mode are presented in Table 2.

It is noticed that the relative error between the estimated and the theoretical damping coefficients is small, so it can be concluded that the ICA can also identify the damping coefficients of a dynamic system.

## 4 Conclusion

For this paper, one of the important techniques of the BSS which is the ICA is used in the OMA. For the studied system which is a quarter car vehicle model, the OMA allows identifying the modal properties (modal response, natural frequencies). By calculating the relative error of the parameters (eignfrequencies, damping coefficients) obtained by the modal recombination method and those estimated by the ICA, we obtained satisfactory results. Thus, the Independent Component Analysis (ICA) can be applied in the Operational Modal Analysis (OMA) in order to determine the modal characteristics of a system using only its measured vibratory responses.

**Acknowledgments** The authors are grateful to Vicent Zarzoso and Pierre Comon for making RobustICA package available at <http://www.i3s.unice.fr/~zarzoso/robustica.html>. The authors also gratefully acknowledge the helpful comments and suggestions of the reviewers, which have improved the presentation.

## References

- Abbès MS, Akrouit MA, Fakhfekh T, Haddar M (2011) Vibratory behavior of double panel system by the operational modal analysis. *Int J Model Simul Sci Comput* 2(4):459–479
- Akrouit A, Chaabene MM, Hammami L, Haddar M (2012) Edge stiffness effects on thin-film laminated double glazing system dynamical behavior by the operational modal analysis. *J Mech Mater Struct*. doi:10.2140/jomms.2012.7.837



- Basha SIA, Rao NAN (2012) Dynamic analysis of Mac Pherson suspension system by using FE method. *Int J Math Eng* 3(1):1423–1433
- Hyvärinen A, Oja E (2000) Independent component analysis: algorithms and applications. *IEEE Trans Neural Netw* 13(4–5):411–430
- Jutten C, Héroult J (1991) Blind separation of sources, part I: an adaptive algorithm based on neuromimetic architecture. *Sig Process* 24:1–10
- Kerschen G, Poncelet F, Golinval JC (2007) Physical interpretation of independent component analysis in structural dynamics. *Mech Syst Signal Process* 21:1561–1575
- Li P, Lam J, Cheung KC (2014) Multi-objective control for active vehicle suspension with wheelbase preview. *J Sound Vib* 333:5269–5282
- Maher D, Young P (2007) Modelling of road vehicle suspension systems for performance evaluation. <http://www.iomac.dk/sync/uploads/48eb2ddce997c08530b8c43231afb29e.pdf>
- Purushotham A (2013) Comparative simulation studies on Mac Pherson suspension system. *Int J Mod Eng Res* 3:1377–1381
- Taktak M, Tounsi D, Akrouit A, Abbès MS, Haddar M (2012) One stage spur gear transmission crankcase diagnosis using the independent components method. *Int J Veh Noise Vib* 8(4): 387–400

# Feature Extraction Using S-Transform and 2DNMF for Diesel Engine Faults Classification

Ezzeddine Ftoutou and Mnaouar Chouchane

**Abstract** This paper investigates the supervised classification of a distribution fault of an internal combustion Diesel engine using vibration measurement. For 3 inlet valve clearance values, the standard S-transform is used to produce a time-frequency representations of the vibration signals. The large size of time frequency images is then reduced to a set of lower sizes using two-dimensional non-negative matrix factorization. A multilayers perceptron neural network is then trained and applied to classify the test data. The optimal size of feature set is computed, for the best classification and the lowest elapsed *CPU* time at the training and testing classification phases. It has been found that the performance of the multilayers perceptron neural network classifier is, generally, enhanced and the *CPU* time is minimized for a reduced feature set size.

**Keywords** Feature extraction · S-transform · Two-dimensional non negative matrix factorization · Distribution fault classification · Diesel engine

## 1 Introduction

Vibration signals measured on the engine block are generally non-stationary (Antoni et al. 2002). Time-frequency analysis is often considered as the adequate signal processing tool in this case (Ftoutou et al. 2012; Li et al. 2011; Wang et al. 2008).

In the internal combustion Diesel engine faults classification domain, many transformations are used to transform the acquired signals in the time domain to the time-frequency domain. Among these methods, we cite the short-time Fourier

---

E. Ftoutou (✉) · M. Chouchane  
Laboratory of Mechanical Engineering (LGM), National Engineering School of Monastir (ENIM), University of Monastir, Avenue Ibn Eljazzar, 5019 Monastir, Tunisia  
e-mail: ezzeddine.ftoutou@gmail.com

M. Chouchane  
e-mail: mnaouar.chouchane@enim.rnu.tn

transform (*STFT*), the continuous wavelet transform, Wigner-Ville transforms (*WV*), etc. A recently developed method called S-transform (*ST*) (Stockwell et al. 1996) is used as a joint time-frequency representation of the vibration signals.

This method is known for its local spectral phase properties that combines elements of wavelet transform and short-time Fourier transform. *ST* is unique in that it provides frequency-dependent resolution while maintaining a direct relationship with the Fourier spectrum. In addition, the S-transform is shown to have a frequency invariant amplitude response in contrast to the continuous wavelet transform which attenuates high frequency signals relative to the low frequency signals. In the case of additive noise, the linear property of the S-transform insures the easy removal of this noise from the time frequency representation if it was not completely removed before. This advantage is not present in the other transforms, as Wigner-Ville transforms. For these reasons, *ST* will be used in this paper as time-frequency transform to transform the acquired signals in the time domain to the time-frequency domain.

The high number of pixels in time-frequency representations or images prohibits the direct exploitation of the pixel values as features. Thus, a method of reduction of the image matrix to a reasonable number of features should be used.

For a given matrix, many factorization methods exist, such as: singular value decomposition (*SVD*), non-negative matrix factorization (*NMF*) (Lee and Seung 2001), *LU* decomposition, *QR* decomposition, Cholskey decomposition, etc.

The difference between these methods comes from the applicability and physical significance that can be deduced from these based on the domain in which they are applied. In the internal combustion Diesel engine faults classification domain, the most common decomposition methods are *SVD* and *NMF*. Both are matrix decomposition techniques. But, the *SVD* yields unique factors, whereas *NMF* factors are non-unique. In addition, *SVD* factors contain both positive and negative entries while *NMF* factors are strictly positive. This constraint of positivity makes the resulting matrices easier to inspect. Also, *NMF* is additive combinations, and can be easily understood and linked to physical meanings. In contrast to *NMF* which applies for only a single matrix, and finds only one base matrix, *2DNMF* aims to find two base matrices to represent the input matrices in a low dimensional matrix subspace. *2DNMF* not only inherits the advantages of *NMF*, but also owns the properties low computational complexity, as well as high recognition accuracy. For these reasons, the new technique called two dimensional non-negative matrix factorization (*2DNMF*) (Li et al. 2011) based on the non-negative matrix factorization (*NMF*) will be used in this paper for feature sets extraction and reduction by reducing the number of columns (time) and/or lines (frequency) of each high dimensional time-frequency representation.

Before the classification step, an important question must be asked: what is the optimal size of feature set, which must be used, while retaining the most important information in the time frequency representations, have the best classification rate and with the minimum *CPU* time?

In this paper, we try to give the answer to this question by using a multilayers perceptron neural network (*MLP*) as a supervised classifier, to discriminate the test data into three fault classes, and to find the optimal size of feature set. The

percentage accuracy rate (Ftoutou et al. 2011) and the elapsed *CPU* time at the training and testing phases of classification process are computed and compared to select the optimal size of feature set.

In this paper, the classification of a distribution fault of an internal combustion (IC) diesel engine is investigated. The classification is based on the features extracted from time-frequency domain using two recent methods S-transform and two-dimensional non negative matrix factorization. Vibration signals are measured at the middle of the engine block for three levels of the inlet valve clearance fault at the idle speed. Using the S-transform (*ST*), all vibration signals are transformed to time-frequency images. Feature set extraction and reduction is then applied using *2DNMF* to the time-frequency matrix. Subsequently, a *MLP* with back-propagation algorithm is used to classify the test data into three fault classes and to evaluate the performances of the *2DNMF* algorithm.

This paper is organized as follows. Section 2 describes the time-frequency representation of temporal signals using S-transform, the feature extraction in time-frequency domain and feature set reduction by the *2DNMF* and the supervised fault classification using *MLP*. The measurement set up and the signal acquisition and processing system as well as the simulated fault are described in Sect. 3. The methods presented in Sect. 2 are then applied in Sect. 4. The percentage accuracy rate (*PAr*) and the elapsed *CPU* time for the classification and matrix size reduction, with *2DNMF*, are computed and compared. The paper is concluded in Sect. 5.

## 2 Fault Classification

To classify the distribution Diesel engine fault, three steps have been applied.

In the first step, all vibration signals, acquired in the time domain, are transformed to the time-frequency domain using the *ST*. In the second step, the sizes of the time-frequency representations are decreased using *2DNMF*. In the last step, a *MLP* method is used to discriminate the 3 fault classes.

### 2.1 Time-Frequency Transformation Using ST

In this paper, the recently developed S-transform (Stockwell et al. 1996) is used as a time frequency transformation of the vibration signals. The discrete S-transform  $ST\left[jT, \frac{n}{NT}\right]$  of a temporal discrete signal  $x[kT]$ , of  $N$  points and acquired with a sampling period  $T$ , is defined as:

$$ST\left[\frac{n}{NT}\right] = \sum_{m=0}^{N-1} X\left[\frac{m+n}{NT}\right] e^{-\frac{2\pi^2 m^2}{n^2}} e^{\frac{i2\pi mn}{N}}, \quad n \neq 0 \quad (1)$$

where  $X\left[\frac{m+n}{NT}\right]$  is the discrete Fourier transform of the discrete signal  $x[kT]$  and defined as:

$$X\left[\frac{m+n}{NT}\right] = \frac{1}{N} \sum_{k=0}^{N-1} x[kT] e^{-\frac{j2\pi nk}{N}}, n \neq 0 \quad (2)$$

with  $j, k$  and  $m = 0, 1, \dots, N-1$  and  $n = 1, 2, \dots, N$ .

## 2.2 Feature Set Extraction and Reduction Using 2DNMF

In 2DNMF method (Li et al. 2011), each time-frequency matrix  $\mathbf{A}_k$ , obtained by  $ST$ , is transformed into a low dimensional matrix  $\mathbf{D}_k$  following two steps.

At first step, for each  $p \times q$  (with  $q = N, p = N/2$  and  $N$  is the number of sample in the  $k$ -th measured temporal signal) time-frequency matrix  $\mathbf{A}_k$ , 2DNMF finds  $p \times d$  non-negative matrix  $\mathbf{L}$  and  $d \times q$  non-negative matrix  $\mathbf{H}_k$  such that  $\mathbf{A}_k$  can be written as a weighted sum of the column bases  $\mathbf{L}$  as follows:

$$\mathbf{A}_k \approx \mathbf{L}\mathbf{H}_k \quad (3)$$

At the second step of 2DNMF, the  $q \times p$  time-frequency matrix transpose  $\mathbf{A}_k^T$  of  $\mathbf{A}_k$  is written as:

$$\mathbf{A}_k^T \approx \mathbf{R}\mathbf{C}_k \quad (4)$$

where  $\mathbf{R}$  and  $\mathbf{C}_k$  are  $q \times g$  row bases and  $g \times p$  combining coefficients matrices respectively. By now, we have obtained the  $p \times d$  dimensional column bases  $\mathbf{L}$  and the  $q \times g$  dimensional row bases  $\mathbf{R}$ . A matrix  $\mathbf{D}_k$  of a reduced size giving a new representation of the matrix  $\mathbf{A}_k$  can be obtained by projection of matrix  $\mathbf{A}_k$  on the column bases  $\mathbf{L}$  and the row bases  $\mathbf{R}$ . Thus,

$$\mathbf{D}_k = \mathbf{L}^T \mathbf{A}_k \mathbf{R} \quad (5)$$

$\mathbf{D}_k$  is a  $d \times g$  matrix called the encoding matrix of  $\mathbf{A}_k$  and contains the most important information contained in the matrix  $\mathbf{A}_k$ .

To find the approximate factorization  $\mathbf{A}_k \approx \mathbf{L}\mathbf{H}_k$ , we need to define cost functions ( $F$ ) that quantifies the quality of the approximation. One useful measure is simply the square of the Euclidean distance defined as:

$$F(\mathbf{W}, \mathbf{H}) = \|\mathbf{A} - \mathbf{W}\mathbf{H}\|_F^2 \quad (6)$$

with  $\|\cdot\|_F$  is the Frobenius norm. To get  $\mathbf{L}$  and  $\mathbf{H}_k$  matrices (or  $\mathbf{R}$  and  $\mathbf{C}_k$ ) the update propagation rule, given by (Lee and Seung 1999), is used.

### 2.3 Fault Classification Using MLP

MLP is the most famous and the most widely used type of artificial neural networks with applications as diverse as finance (forecasting), manufacturing (process control), and science (speech and image recognition, health monitoring, fault classification, etc.) MLP have an input layer, a number of hidden layers and an output layer. For additional information's see (Magnus et al. 2010).

## 3 Measurement Set-up and Faults Simulation

Vibration signals are measured on the external structure of an IC diesel engine, mounted on a testing bench, having four cylinders in line, a power of 50 kW at 4600 rpm and a maximum torque of 110 Nm at 2000 rpm. The engine is mounted on a testing bench. The fuel is injected indirectly into the combustion chambers in the following order: 1–3–4–2. The engine events timing are presented in Table 1.

Vibration signals are measured at the middle of the camshaft cover of the IC diesel engine using B&K piezoelectric accelerometers type 4384, and B&K charge amplifier type 2634 as shown in Fig. 1. At the same time, an inductive proximity sensor is also used to detect the top dead center (TDC) in cylinder 4 as shown in Fig. 1. The output of the amplifier is connected to a PC plug-in data acquisition card NI PCI-6025E.

The measurement is carried out at a crankshaft speed of 800 rpm, which corresponds to the idle speed, and at a roughly constant oil pressure and water temperature and without external load.

Figure 2 shows typical measured signals, from top to bottom: the TDC signal and a vibration signal measured by an accelerometer placed at point P1 (*cf.* Fig. 1).

The vibration signal in Fig. 2b shows that the main sources of excitation likely to affect the engine vibration response include impacts related to fuel injection, high rise of gas pressure during combustion and the impacts of intake and exhaust valves. It can also be noticed that the vibration energy related to combustion in cylinders 2 and 3 is higher than that of cylinders 1 and 4 because the accelerometer is fixed closer to cylinders 2 and 3 during measurement.

**Table 1** Timing of valves events for the IC engine with BDC: bottom dead center and TDC: top dead center

Engine event	Relative position
Exhaust valve open (EVO)	56° B-BDC
Inlet valve open (IVO)	20° B-TDC
Exhaust valve close (EVC)	13° A-TDC
Inlet valve close (IVC)	37° A-BDC

Suffix 'B' represents 'Before' and 'A' represents 'After'

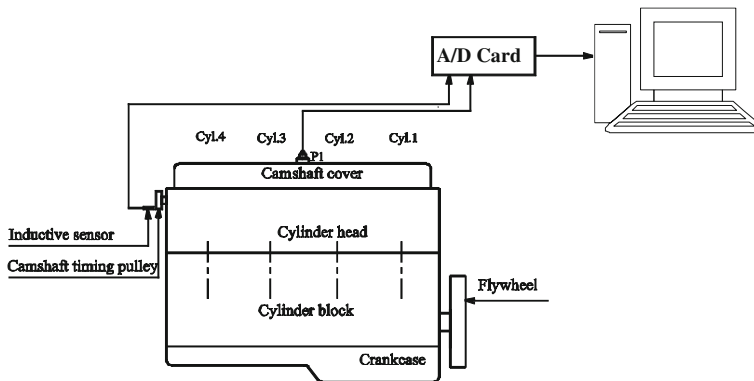


Fig. 1 Measurement set-up for vibration data acquisition on an IC diesel engine

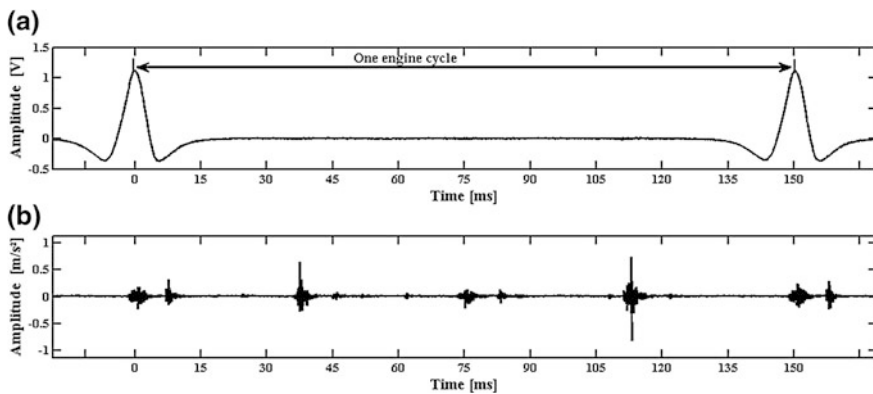


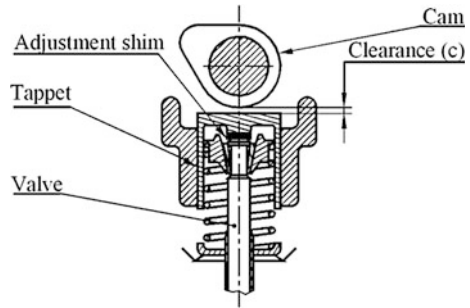
Fig. 2 Acquired signals. **a** Top dead center signal, **b** vibration signal

The distribution fault consists of changing the intake valve clearance of cylinder 2 from its normal value of 0.25 mm to two higher values of 0.35 and 0.45 mm. Three fault classes are therefore considered, *C1*, *C2* and *C3*, corresponds respectively to valve clearances 0.25, 0.30 and 0.35 mm. Valve clearance is modified by reducing the thickness of the adjustment shim located between the valve stem and the tappet, as shown in Fig. 3, respectively by 0.1 and 0.2 mm.

## 4 Results and Discussions

For the engine speed and for each fault class among the 3 fault classes, the measured temporal vibration signal has a length of 800 engine cycles. Each cycle contains 1024 data points or samples. Twenty signals were selected randomly from

**Fig. 3** The valve control mechanism



each class. The set of 20 signals is also, randomly, divided into two equal sets. One set is used in the training phase and the other set for the test phase of the *MLP* classifier. All selected signals are transformed to time-frequency domain using *ST*. Mathematically, each vector of length 1024 is converted into a matrix of size  $512 \times 1024$ .

For both kinds of faults, all time–frequency images (i.e. matrices) sizes are reduced to extract low-dimensional feature subset using *2DNMF*, described in Sect. 2.2. The parameters  $d$ ,  $g$  were set to one of the values [512, 256, 128, 64, 32, 16, 8, 4, 2] and the maximum number of iterations of the *2DNMF* algorithm was fixed to 100. The size of the reduced matrix is therefore  $g_r \times d_c$  features extracted from each time-frequency image with  $r = 1, 2, \dots, 10$  and  $c = 1, 2, \dots, 9$ .

Randomly, sixty time–frequency matrices for each fault class and speed are used to calculate the encoding matrices  $\mathbf{D}_k$ . Thirty  $\mathbf{D}_k$  matrices are used to train the *MLP* classifier and the remainder for him testing. The *MLP* classifier is constructed with three layers, the input layer, one hidden layer containing five neurons, and the output layer, and trained by the back-propagation learning rule until the mean squared errors are less than  $1.10^{-20}$ . The sigmoid function is used as the activation function in the *MLP* classifier.

The percentage accuracy rate (*PAr*) used by Ftoutou et al. (2011) and the average elapsed *CPU* time to carry out the training and the test tasks at classification phases are used, in this subsection, to compare and evaluate the performance of the *2DNMF* algorithm for different matrix size. A low value of *PAr* indicates a bad fault classification result and vice versa.

Figure 4 shows the average elapsed *CPU* time to reduce the time-frequency images size using the *2DNMF* algorithm for the 3 distribution fault classes *C1*, *C2* and *C3*. From this figure, we conclude that the average *CPU* time is between a few seconds, for a low matrix size, and more than 400 s for a matrix of size  $(512 \times 512)$ . A general conclusion can be interpreted, that the average elapsed *CPU* time to reduce the time-frequency images decreases with the size of matrix to compute.

Table 2, shows the average percentage of perfect classification values as a function of  $\mathbf{D}_k$  size ( $g \times d$ ). Examining this table, a decisive relationship between



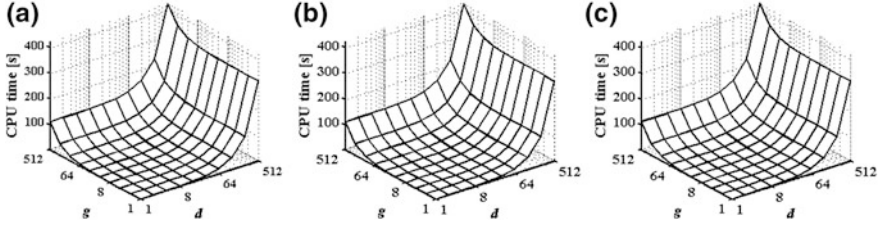


**Fig. 4** Average elapsed CPU time required to reduce the time-frequency images size ( $g \times d$ ) using the 2DNMF algorithm for: **a** valve clearance = 0.25 mm, **b** valve clearance = 0.35 mm, and **c** valve clearance = 0.45 mm

**Table 2** Percentage of accuracy rate values for different dimensions of time-frequency matrix ( $g \times d$ )

		$d$									
$g$		512	256	128	64	32	16	8	4	2	
	512	33.2	37.4	50.1	36.9	58.7	53.8	63.0	66.2	72.4	
	256	62.2	34.6	50.2	60.5	64.6	63.7	53.5	59.5	73.1	
	128	40.4	48.6	64.9	55.3	65.0	45.2	54.4	63.5	65.6	
	64	33.9	46.9	45.7	63.2	66.0	49.9	63.2	59.3	76.1	
	32	50.3	69.7	55.6	63.3	58.6	72.7	54.5	64.6	68.2	
	16	48.5	61.7	55.9	78.6	63.5	78.6	67.0	59.8	79.9	
	8	64.1	59.5	59.6	69.4	64.2	66.3	64.7	66.2	75.1	
	4	60.7	66.4	58.5	65.9	64.4	54.5	58.0	58.5	87.6	
	2	74.0	80.2	79.6	75.6	77.6	68.0	64.6	66.7	65.5	

$PAR$  and different matrix size ( $g \times d$ ) is not easy to interpret. However, a number of general interpretations can be deduced such as:

- the use of  $ST$ ,  $2DNMF$  and  $MLP$  algorithms to classify the distribution fault, gives a  $PAR$  values between 33.2 % for a  $\mathbf{D}_k$  size ( $g \times d$ ) =  $(512 \times 512)$  and 87.6 % for a size ( $g \times d$ ) =  $(4 \times 2)$ ,
- generally, the  $PAR$  values increase when  $\mathbf{D}_k$  size ( $g \times d$ ) decrease,
- the best values of  $PAR$  are localized below the diagonal of Table 2  $((2, 512), (512 \times 2))$ .

Figure 5 shows the average elapsed CPU time for the  $MLP$  algorithm to classify the 3 fault classes, at the training and testing phases, respectively, in Fig. 5a, b. From this figure we notice that the average elapsed CPU time for the  $MLP$  algorithm to classify the 3 fault classes, at both training and testing phases, increase with the size of  $\mathbf{D}_k$ . Also, we conclude that the average elapsed CPU time for the  $MLP$  algorithm to classify the 3 fault classes, at the training phase is between a few seconds and about 300 s for a large  $\mathbf{D}_k$  size. While at the testing phase, the average

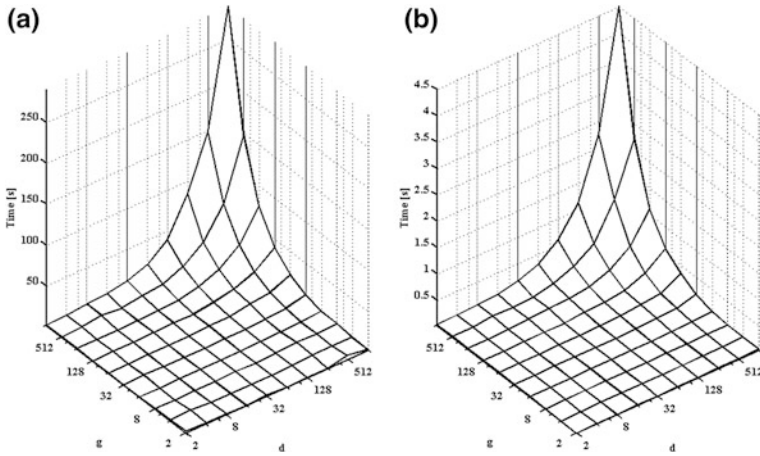


**Fig. 5** Average elapsed CPU time for the MLP algorithm at the training phase (a) and the testing phase (b)

elapsed CPU time for the *MLP* algorithm to classify the 3 fault classes does not exceed 5 s.

## 5 Conclusion

In this paper, the classification of a diesel engine distribution fault using vibration analysis is investigated. Vibration signals are measured on the engine bloc and transformed to the time-frequency domain using the S-transform. To construct a set of features for each measured signal, the *2DNMF* algorithm has been applied to reduce the size of the matrix representation of the time frequency images. A *MLP* neural network algorithm is used as a supervised classifier.

## References

Antoni J, Danière J, Guillet F (2002) Effective vibration analysis of IC engines using cyclostationarity. Part I: A methodology for condition monitoring. *J Sound Vib* 257(5):815–837

Ftoutou E, Chouchane M, Besbès N (2011) Internal combustion engine valve clearance fault classification using multivariate analysis of variance and discriminant analysis. *Trans Inst Meas Control* 34(5):566–577

Ftoutou E, Chouchane M, Besbès N (2012) Feature selection for diesel engine fault classification. In: Fakhfakh T et al (eds) *Condition monitoring of machinery in non-stationary operations*. Springer, Heidelberg, pp 309–318

- Lee DD, Seung HS (1999) Learning the parts of objects by non-negative matrix factorization. *Nature* 401(6755):788–791
- Lee DD, Seung HS (2001) Algorithms for non-negative matrix factorization. *Adv Neural Info Proc Syst* 13:556–562
- Li B, Zhang PL, Liu DS et al (2011) Feature extraction for rolling element bearing fault diagnosis utilizing generalized S-transform and two-dimensional non-negative matrix factorization. *J Sound Vib* 330:2388–2399
- Magnus N et al (2010) *Neural networks for modeling and control of dynamic systems: practitioner's handbook*. Springer, London
- Stockwell RG, Mansinha L, Lowe RP (1996) Localization of the complex spectrum: the S-transform. *IEEE Trans Signal Process* 44(4):998–1001
- Wang C, Zhong Z, Zhang Y (2008) Fault diagnosis for diesel valve trains based on time-frequency images. *Mech Syst Signal Process* 22:1981–1993

# Experimental Study of Combined Gear and Bearing Faults by Sound Perception

Younes Ramdane, Ouelaa Nouredine, Hamzaoui Nacer  
and Djebala Abderrazek

**Abstract** One presented in this work a vibro acoustic analysis of various signals in the case of one or several combined defects such as bearings and gears defects. The objective is to identifying each of the defects even when it combined. We begin by studying the temporal and spectral scalar indicators; a perceptive analysis of the sounds corresponding to different types of defects have been established to investigate the sensitivity of listeners to the combined defects, and the ability to distinguish between defects with different types and natures. According to the study of the vibrational indicators and of the listening test, the results are well preventative of the evolution of different defects gravity. For sound perception, the listeners could classify the sounds according to the type and the level of defects gravities.

**Keywords** Vibro-acoustics · Sound perception · Gear defects · Bearing defects · Combined defects

---

Y. Ramdane · O. Nouredine (✉) · D. Abderrazek  
Mechanics and Structures Laboratory, University of Guelma,  
B.P. 401, Guelma, Algeria  
e-mail: n\_ouelaa@yahoo.fr

Y. Ramdane  
e-mail: ramdane\_ys@yahoo.com

D. Abderrazek  
e-mail: djebala\_abderrazek@yahoo.fr

H. Nacer  
Laboratory of Vibration-Acoustics, INSA of Lyon, Bâtiment A.  
St. Exupéry, 25 bis Avenue Jean Capelle, 69621 Villeurbanne cedex, France  
e-mail: nacer.hamzaoui@insa-lyon.fr

## 1 Introduction

The gears and bearings are driveline effort and movement by physical contact between parts. This type of transmission generates vibrations and consequently emits noise. Main vibrations are produced by the input shock contacting gear teeth.

The monitoring and the diagnosis of the defects of rotating machines belong to the programs of conditional maintenance, and are 75 % based on vibration analysis. Several researchers are still working on the improvement or the development of new indicators resulting from vibration and acoustic signals. In this study an acoustic approach of perception was used in order to propose an optimization of the monitoring indicators to improve the detection of defects. Indeed, subjective analyses used by maintenance technicians, based on the experience feedback, are often correlated with the worsening of the defects. The use of dissimilarity test, as acoustic perception, allowed to correlate a dimension of obtained perceptual space with Gears defects (Younes et al. 2015a, b).

Listening to the vibration signals of the different defects configurations, we hope to build a linear correlation between the aggravation of the defect and a combination of 2 scalar indicators used in monitoring. The advantage will be to build a defect detection model with scalar indicators, ranging from birth to the defect aggravation. To design this type of model in a new real case, should constitute a basis for signals coming from healthy and defective configurations. This approach is quite similar to a method of artificial intelligence as neural networks, but does not require any learning stage to adjust optimization settings. The originality of this article is at the level of the contribution of a subjective approach by human hearing in addition to the current physical methods.

In complement with work concerning the study of the real and simulated gears defects (Younes et al. 2015a, b), we presents in what follows a study of the combined defects of gears and bearings by acoustic perception; the purpose here is to extend the application of the perceptive approach presented in Younes et al. (2015a, b) for the case of the defects of different nature and gravity.

## 2 Experimental Setup

### 2.1 Test Rig

One uses a device designed by the Mechanics and Structures Laboratory University of Guelma Algeria, for the realization of simulations of isolated defects on bearings and/or in gears (Fig. 1). This experimental design is made for different speeds and different frequency bands.

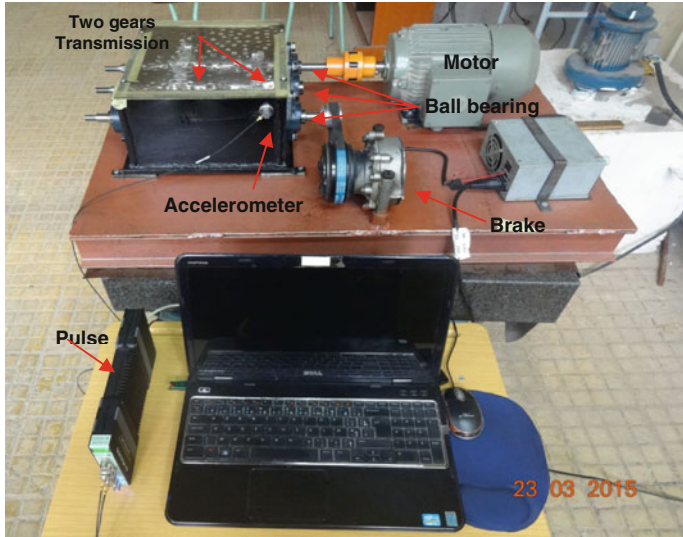


**Fig. 1** Experimental setup

## 2.2 Configurations of the Simulated Defects

In this experimental design, we made the acquisition of vibration signals for two rotations frequencies and two frequencies bands for different types of defects. We started by the case without defect, after that we have created three defects, small, average and great on three different bearings to ensure the possibility to combine these defects with three gears defects (small, average and great) that we created on the surface of a pinion tooth 2, see Table 1.

## 3 Results and Discussion

### 3.1 Scalar Indicators

The evolution of scalar indicators over time can give information about the defect aggravation. One present in Table 2, the values of these indicators calculated from different time signals collected by accelerometers. The evolution of each indicator is not linear with the worsening of the combined defects; It is therefore difficult to monitor the status of defect with a single indicator.

The kurtosis is a sensitive indicator to signal shape and not to its energy, this is confirmed by the histogram in Fig. 2, where we note the increase with the severity of the defect in two cases of isolated defects on bearing and gear. The combination of the two defects decreases its sensitivity and causes a decrease in its level.

**Table 1** The values of the scalar indicators

Sounds	Corresponding defects
<b>S1</b>	<b>Healthy Case HC</b>
<b>S2</b>	<b>Small Defect on Bearing2 SDB2</b>
<b>S3</b>	<b>Average Defect on Bearing2 ADB2</b>
<b>S4</b>	<b>Great Defect on Bearing1 GDB1</b>
<b>S5</b>	<b>Small Defect on PinionG2 SDG2 + Without Defect Bearing SDG2 + WDB2</b>
<b>S6</b>	<b>Average Defect on PinionG2 SDG2 + Average Defect on Bearing2 ADG2 + ADB2</b>
<b>S7</b>	<b>Small Defect on PinionG2 SDG2 + Small Defect on Bearing2 PDG2 + SDB2</b>
<b>S8</b>	<b>Moyen Défaut PignonG2 MDG2 + Moyen Défaut Roulement Palier2 MDG2 + MDRP2</b>
<b>S9</b>	<b>Grand Défaut PignonG2 GDG2 + Sans Défaut Roulement Palier2 GDG2 + SDRP2</b>
<b>S10</b>	<b>Grand Défaut PignonG2 GDG2 + Grand Défaut Roulement Palier2 GDG2 + GDRP2</b>

**Table 2** The values of the scalar indicators

		Pv	RMS	CF	K	OL	KF	SCG
Without defect	S1	15.60	3.28	4.75	4.03	2.68	51.21	351.28
Bearing defect	S2	21.60	3.47	4.83	4.80	2.84	75.04	363.88
	S3	23.30	4.04	5.77	5.22	3.30	94.03	401.96
	S4	30.80	4.01	7.67	6.02	3.28	123.65	433.38
Gear defect	S5	16.80	3.33	5.04	4.37	2.72	55.96	334.74
	S7	18.50	3.66	5.05	4.65	2.99	67.72	361.28
	S9	29.60	4.07	7.28	5.66	3.32	120.42	342.69
Combined defect	S6	18.70	3.50	6.49	6.13	2.86	65.45	359.42
	S8	19.70	3.66	5.38	4.21	2.99	72.19	339.63
	S10	19.90	3.80	5.23	4.38	3.10	75.67	361.73

### 3.2 *Perceptive Approach*

One chose for the treatment, only the signals measured at a speed of 15 Hz and a 12800 Hz frequency band. These are exported from Labshop Pulse software on \*.wav format. We have selected 10 sounds that will be the subject of the listening test.

The listening test was conducted on the different sounds, using the paired comparison method, multidimensional analysis INDSCAL MDS was applied thereafter for the results treatment of Younes et al. (2015a, b).

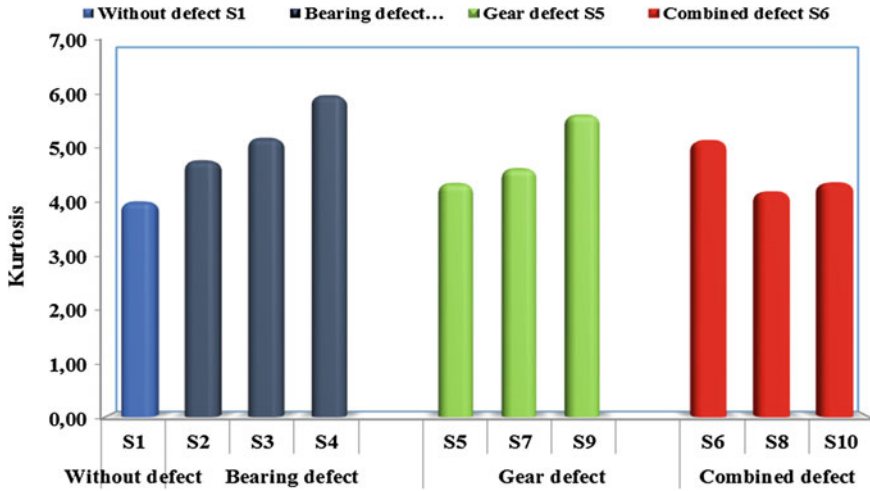


Fig. 2 Evolution of kurtosis according to the defect type

### 3.2.1 Perceptual Space with Two Dimensions

One present in Fig. 3, the perception space in 2 dimensions; we found according to DIM1, that sounds appear in the of defect degradation order from least degraded (S1) to the most degraded (S10) and this for different degradation degrees and defects types (bearing or gear).

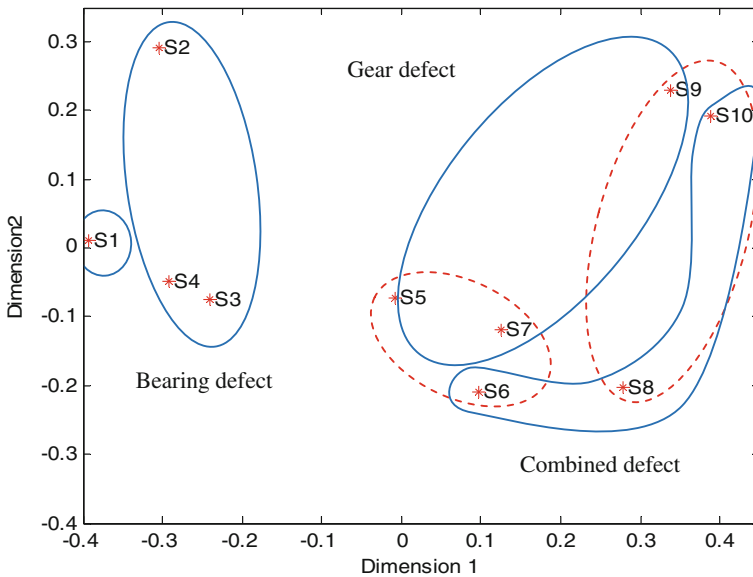
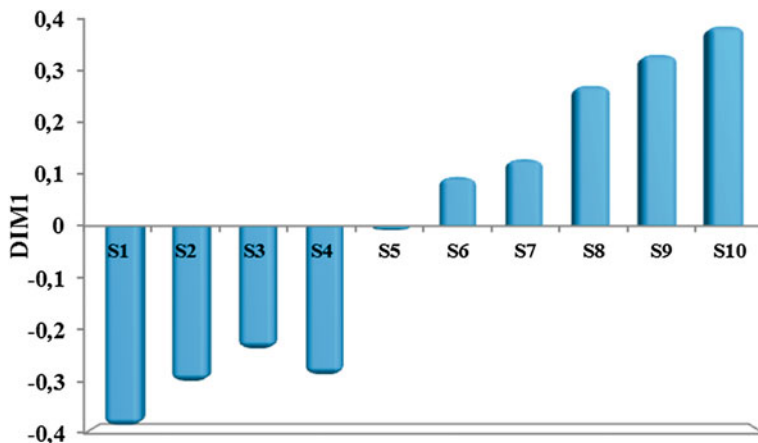


Fig. 3 Perceptual space





**Fig. 4** DIM1 values of the 10 sounds

The first group of sounds S2, S3 and S4 corresponding to small, average and great bearing defect. Listeners have classified them just after the S1 sound (healthy case).

The second group of sounds (S5, S7 and S9) corresponding to the small, medium and large gear defect. Referring to the analysis of DIM1, listeners have classified the gear defects as being more degraded defects (important) than bearing defects, including the great defect S9, which has been classified with the defect S10 which is the combination of two great defects on the bearing and the gear.

The third group of combined defects sounds S6, S8 and S10 corresponding to the small–small, average–average and great–great defects of bearing and gear. The S6 can be grouped with S5 and S7 of the gear sounds, view to the little influence of bearing defect over the gear defect. While the S8 and S10 sounds were perceived by listeners as the more degraded defect than small and average gear defect. The S8 and S9 and S10 sounds can be grouped together as defects with great severity.

One presents by histogram of the Fig. 4 coordinates sounds of DIM1 of the 10 sounds. The results of this figure, confirm the analysis which we presented in Younes et al. (2015b), where we found that the passage of DIM1 values from negative to the positive means that that we have achieved a stage of deterioration that requires stopping the machine.

### 3.2.2 Correlations Between Scalar Indicators and Dimensions

The correlation of scalar indicators in Table 2 with the results of sound perception, does not give a good result except for the DIM2 with two indicators: the kurtosis and crest factor. We get a mathematical model (1) with a correlation coefficient  $R^2 = 0.72$ .

$$\text{DIM2} = -0.462 * \text{Kurtosis} + 0.287 * \text{Crest factor} + 0.598 \quad (1)$$

The dimension DIM1 that is physically correlated with the degradation state (bearing and/or gear) can be modeled via a linear combination of indicators in Table 1; it will therefore analyze other indicators.

## 4 Conclusion

The objective of this work is to extend the application of perceptual approach to the study of single and combined defects of different nature (gear and bearing). The aim is to propose mathematical models to DIM1 and DIM2 allowing the correlation of some indicators with sound perception.

For sound perception, listeners were able to classify the sounds according to the type and the level of defects severity. While the correlation between scalar indicators and sound perception, does not give a good result except for the second dimension with two indicators: the kurtosis and crest factor.

The application of perceptive approach has proven effective in cases investigated in Younes et al. (2015a, b), real and simulated gear defects, but its application in the case of several defects with different type and nature can be still useful extending it to other indicators.

## References

- Younes R, Ouelaa N, Hamzaoui N, Djebala A (2015a) Experimental study of real gear transmission defects using sound perception. *Int J Adv Manuf Technol* 76(5–8):927–940
- Younes R, Hamzaoui N, Ouelaa N, Djebala A (2015b) Perceptual study of the evolution of gear defects. *Appl Acoust* 99:60–67

# Modal Analysis of Spur Gearbox with an Elastic Coupling

Atef Hmida, Ahmed Hammami, Fakher Chaari,  
Mohamed Taoufik Khabou and Mohamed Haddar

**Abstract** Coupled shafts are considered as the main source of vibration in rotating systems. In this work, a mechanical system composed of an electric motor, an elastic coupling and one stage spur gear is investigated to analyze dynamic behavior of elastic coupling, its influence on the natural frequencies, the vibrations, and the response of the system. A lumped parameter model of the corresponding system is developed to identify the natural frequencies and vibration modes. In addition, distributions of modal kinetic and strain energies are studied.

**Keywords** Elastic coupling · Gearbox · Natural frequencies · Distributions of modal kinetic and strain energies

## 1 Introduction

The dynamic characterization of an elastic coupling that connects two shafts, in terms of the equivalent stiffness and damping coefficients, are associated with the angular and translation displacements of the coupling. Accurate models for rotating systems are important for the prediction of their dynamic behavior (Genta et al. 2005; Chatelet et al. 2005). Some components are difficult to model accurately, and

---

A. Hmida (✉) · A. Hammami · F. Chaari · M.T. Khabou · M. Haddar  
Laboratory of Mechanics, Modeling and Production (LA2MP),  
National School of Engineers of Sfax, BP1173–3038 Sfax, Tunisia  
e-mail: abdallahatef@yahoo.fr

A. Hammami  
e-mail: ahmed.hammami2109@gmail.com

F. Chaari  
e-mail: fakher.chaari@gmail.com

M.T. Khabou  
e-mail: mtkhabou@hotmail.com

M. Haddar  
e-mail: mohamed.haddar@enis.rnu.tn

several researchers have attempted to characterize them experimentally to gain physical insight into their behavior (Ding et al. 2000). For example, Nordmann (1984) identified modal parameters from an elastic rotor supported by oil film bearings, and Edwards et al. (2000) and Sinha et al. (2002) used the machine itself to determine the dynamic characteristics of the structure supporting the machine. Few practical works has been done on the dynamic characterization of torsional flexible couplings that are found in many rotor dynamic systems. Recently, Tapia and Cavalca compared some models of flexible couplings. Four models of flexible couplings are considered; the first model proposed by Kramer (1993) considers the flexibility of mechanical connections as a frictionless coupling which is rigid in the radial direction. In this model, the coupling has the effect of the decreased degrees of freedom of translation in the nodes, making the translational movement both nodes equal. The coupling mass should be added to both nodes of the coupling as a rigid body. The second model proposed by Kramer (1993) considers the torsional stiffness and the damping of the coupling. But in this case, the stresses of the first model are always maintained. The third model defined by Nelson and Crandall (1992) considers that the elastic coupling has a translational stiffness and a torsional stiffness. It takes into account also internal damping and inertial effects of the coupling. Inertial effects are considered in the model and two rigid disks are added in each point of connection.

Gears are widely used in many power transmission applications and are characterized by their high efficiency. However, they can be subjected to severe operating conditions giving rise to dynamic problems. Many researchers studied modal properties of gears highlighting the relationship between natural frequencies and parameters of the system. Cunliffe et al. (1974) focused on a numerical model of a planetary gear with a fixed carrier and characterized vibration modes.

Bartelmus (2001) showed the influence of error mode parameters and the influence of clutch damping on the dynamic factor.

This paper presents a modal analysis of a mechanical system composed of a gearbox driven by a motor via an elastic coupling. Natural frequencies are identified and the distribution of modal kinetic energies and modal strain energies are analyzed.

## 2 Dynamic Model

The system is composed of a motor and a receiver connected through an elastic coupling and one stage spur gearbox. The transmission shafts are supported by 3 bearings (Fig. 1).

The corresponding dynamic model is presented in Fig. 2. It is composed by three blocks:

- The first block is constituted by a driving wheel and the first part of the elastic coupling. They are connected through a transmission shaft (1).

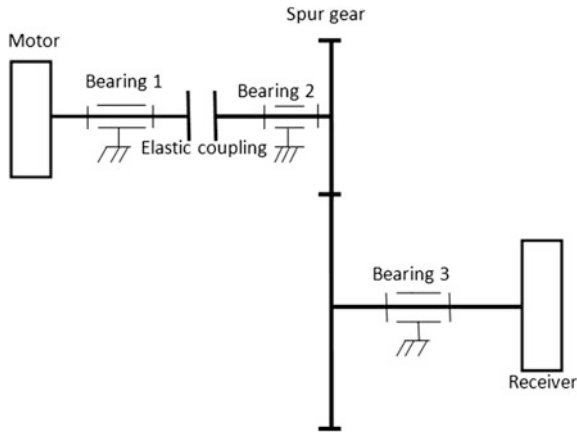


Fig. 1 Kinematic layout of the system

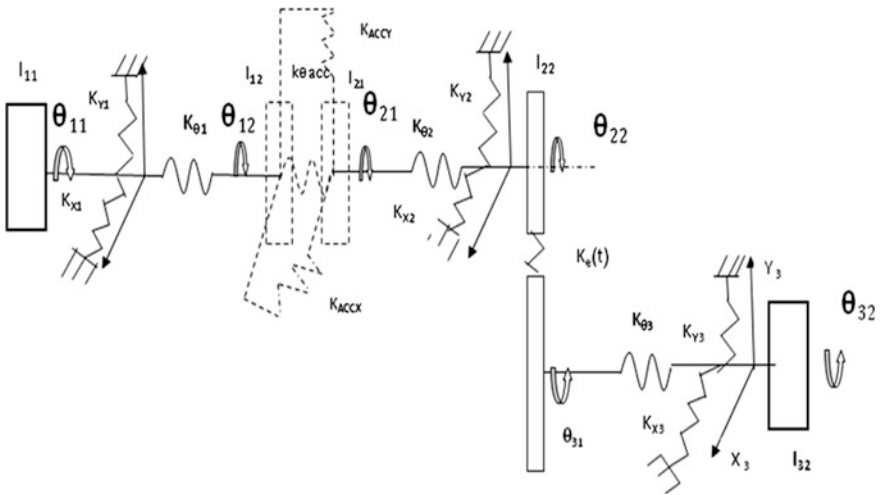


Fig. 2 Dynamic model of the system

- The second block is composed of the second part of the coupling and the pinion gear (spur gear (22)) connected through the shaft (2).
- The third block is composed of the spur gear (31) and the receiving wheel (32) connected to each other by a transmission shaft (3).

The wheels are assumed rigid body. Shafts are assumed massless and have torsional stiffness  $k_{\theta i}$  ( $i = 1, 2, 3$ ). They are supported by bearings modeled as linear springs.

The second model proposed by Nelson and Crandall is adopted for the elastic coupling with two translation stiffness and damping ( $k_t, C_t$ ), torsional stiffness and

damping ( $k_r, C_r$ ). The coupling inertial effects are included in the model as two rigid disks in the first and the second blocks.

Using Lagrange formalism, the equation of motion can be written as:

$$M\ddot{q} + C\dot{q} + (K(t) + \dot{K}s)q = F(t) \quad (1)$$

$M$  is the global mass matrix which is defined as:

$$M = \begin{bmatrix} I_{11} & 0 & 0 & 0 & 0 & 0 & 0 & 0 & 0 & 0 & 0 & 0 \\ 0 & I_{12} & 0 & 0 & 0 & 0 & 0 & 0 & 0 & 0 & 0 & 0 \\ 0 & 0 & I_{21} & 0 & 0 & 0 & 0 & 0 & 0 & 0 & 0 & 0 \\ 0 & 0 & 0 & I_{22} & 0 & 0 & 0 & 0 & 0 & 0 & 0 & 0 \\ 0 & 0 & 0 & 0 & I_{31} & 0 & 0 & 0 & 0 & 0 & 0 & 0 \\ 0 & 0 & 0 & 0 & 0 & I_{32} & 0 & 0 & 0 & 0 & 0 & 0 \\ 0 & 0 & 0 & 0 & 0 & 0 & M_1 & 0 & 0 & 0 & 0 & 0 \\ 0 & 0 & 0 & 0 & 0 & 0 & 0 & M_1 & 0 & 0 & 0 & 0 \\ 0 & 0 & 0 & 0 & 0 & 0 & 0 & 0 & M_2 & 0 & 0 & 0 \\ 0 & 0 & 0 & 0 & 0 & 0 & 0 & 0 & 0 & M_2 & 0 & 0 \\ 0 & 0 & 0 & 0 & 0 & 0 & 0 & 0 & 0 & 0 & M_3 & 0 \\ 0 & 0 & 0 & 0 & 0 & 0 & 0 & 0 & 0 & 0 & 0 & M_3 \end{bmatrix} \quad (2)$$

$C$  is the global damping matrix which is written as:

$$C = \begin{bmatrix} C_{01} & -C_{01} & 0 & 0 & 0 & 0 & 0 & 0 & 0 & 0 & 0 & 0 & 0 \\ -C_{01} & C_{01} + C_{0acc} & -C_{0acc} & 0 & 0 & 0 & 0 & 0 & 0 & 0 & 0 & 0 & 0 \\ 0 & -C_{0acc} & C_{02} + C_{0acc} & -C_{02} & 0 & 0 & 0 & 0 & 0 & 0 & 0 & 0 & 0 \\ 0 & 0 & -C_{02} & C_{02} & 0 & 0 & 0 & 0 & 0 & 0 & 0 & 0 & 0 \\ 0 & 0 & 0 & 0 & C_{03} & -C_{03} & 0 & 0 & 0 & 0 & 0 & 0 & 0 \\ 0 & 0 & 0 & 0 & -C_{03} & C_{03} & 0 & 0 & 0 & 0 & 0 & 0 & 0 \\ 0 & 0 & 0 & 0 & 0 & 0 & C_{x1} + C_{xacc} & 0 & -C_{xacc} & 0 & 0 & 0 & 0 \\ 0 & 0 & 0 & 0 & 0 & 0 & 0 & C_{y1} + C_{yacc} & 0 & -C_{yacc} & 0 & 0 & 0 \\ 0 & 0 & 0 & 0 & 0 & 0 & -C_{xacc} & 0 & C_{x2} + C_{xacc} & 0 & 0 & 0 & 0 \\ 0 & 0 & 0 & 0 & 0 & 0 & 0 & -C_{yacc} & 0 & C_{y2} + C_{yacc} & 0 & 0 & 0 \\ 0 & 0 & 0 & 0 & 0 & 0 & 0 & 0 & 0 & 0 & C_{x3} & 0 & 0 \\ 0 & 0 & 0 & 0 & 0 & 0 & 0 & 0 & 0 & 0 & 0 & C_{y3} & 0 \end{bmatrix} \quad (3)$$

$K_s$  is the structural stiffness matrix of the system.

$$K_s = \begin{bmatrix} K_{01} & -K_{01} & 0 & 0 & 0 & 0 & 0 & 0 & 0 & 0 & 0 & 0 & 0 \\ -K_{01} & K_{01} + K_{0acc} & -K_{0acc} & 0 & 0 & 0 & 0 & 0 & 0 & 0 & 0 & 0 & 0 \\ 0 & -K_{0acc} & K_{02} + K_{0acc} & -K_{02} & 0 & 0 & 0 & 0 & 0 & 0 & 0 & 0 & 0 \\ 0 & 0 & -K_{02} & K_{02} & 0 & 0 & 0 & 0 & 0 & 0 & 0 & 0 & 0 \\ 0 & 0 & 0 & 0 & K_{03} & -K_{03} & 0 & 0 & 0 & 0 & 0 & 0 & 0 \\ 0 & 0 & 0 & 0 & -K_{03} & K_{03} & 0 & 0 & 0 & 0 & 0 & 0 & 0 \\ 0 & 0 & 0 & 0 & 0 & 0 & K_{x1} + K_{xacc} & 0 & -K_{xacc} & 0 & 0 & 0 & 0 \\ 0 & 0 & 0 & 0 & 0 & 0 & 0 & K_{y1} + K_{yacc} & 0 & -K_{yacc} & 0 & 0 & 0 \\ 0 & 0 & 0 & 0 & 0 & 0 & -K_{xacc} & 0 & K_{x2} + K_{xacc} & 0 & 0 & 0 & 0 \\ 0 & 0 & 0 & 0 & 0 & 0 & 0 & -K_{yacc} & 0 & K_{y2} + K_{yacc} & 0 & 0 & 0 \\ 0 & 0 & 0 & 0 & 0 & 0 & 0 & 0 & 0 & 0 & K_{x3} & 0 & 0 \\ 0 & 0 & 0 & 0 & 0 & 0 & 0 & 0 & 0 & 0 & 0 & K_{y3} & 0 \end{bmatrix} \quad (4)$$

$K(t)$ : time dependant stiffness matrix.

$$K(t) = K_m(t) \begin{bmatrix} 0 & 0 & 0 & 0 & 0 & 0 & 0 & 0 & 0 & 0 & 0 & 0 & 0 \\ 0 & 0 & 0 & 0 & 0 & 0 & 0 & 0 & 0 & 0 & 0 & 0 & 0 \\ 0 & 0 & 0 & 0 & 0 & 0 & 0 & 0 & 0 & 0 & 0 & 0 & 0 \\ 0 & 0 & 0 & S_{10} & S_{12} & 0 & 0 & 0 & S_7 & S_6 & -S_7 & -S_6 \\ 0 & 0 & 0 & S_{12} & S_{11} & 0 & 0 & 0 & S_9 & S_8 & -S_9 & -S_8 \\ 0 & 0 & 0 & 0 & 0 & 0 & 0 & 0 & 0 & 0 & 0 & 0 \\ 0 & 0 & 0 & 0 & 0 & 0 & 0 & 0 & 0 & 0 & 0 & 0 \\ 0 & 0 & 0 & 0 & 0 & 0 & 0 & 0 & 0 & 0 & 0 & 0 \\ 0 & 0 & 0 & S_7 & S_9 & 0 & 0 & 0 & S_3 & S_5 & -S_3 & -S_5 \\ 0 & 0 & 0 & S_6 & S_8 & 0 & 0 & 0 & S_5 & S_4 & -S_5 & -S_4 \\ 0 & 0 & 0 & -S_7 & -S_9 & 0 & 0 & 0 & -S_3 & -S_5 & S_3 & S_5 \\ 0 & 0 & 0 & -S_6 & -S_8 & 0 & 0 & 0 & -S_5 & -S_4 & S_5 & S_4 \end{bmatrix} \quad (5)$$

where  $K_m(t)$  is the gear mesh stiffness.  $F(t)$  is the external force vector.  
 $q$  is the degree of freedom vector and it is defined as:

$$q = (\theta_{11}, \theta_{12}, \theta_{21}, \theta_{22}, \theta_{31}, \theta_{32}, x_1, y_1, x_2, y_2, x_3, y_3) \quad (6)$$

The technological and dimensional parameters of the model are presented on the Table 1.

**Table 1** Parameter of the system

<b>Gear box parameters</b>	
Teeth number	$Z_{12} = 20; Z_{21} = 30$
Pressure angle	$\alpha = 20^\circ$
Teeth module (m)	$m_n = 2 \times 10^{-3}$
Contact ratio	$\epsilon_\alpha = 1.6$
Average mesh stiffness (N/m)	$K_{moy} = 2.11 \times 10^8$
<b>Motor's Characteristics</b>	
Torque (N m)	20
Inertia (kg/m <sup>2</sup> )	$4 \times 10^{-3}$
Speed (rpm)	1200
<b>Characteristics of receiving</b>	
Torque (N m)	-40
Inertia (kg/m <sup>2</sup> )	$6 \times 10^{-3}$
<b>Coupling's Characteristics</b>	
Inertia (kg/m <sup>2</sup> )	$4 \times 10^{-3}$
Torsional stiffness (N/m)	352
Translation stiffness (N/m)	$462 \times 10^2$
<b>Characteristics of shafts and bearings</b>	
Torsional shaft stiffness (N/m/rad)	$5 \times 10^8$
Bearing stiffness (kg/m <sup>2</sup> )	$5 \times 10^8$

### 3 Modal Analyses

#### 3.1 Natural Frequencies and Vibration Modes

The natural frequencies and vibration modes are determined from equation of motion (1) and the associated eigenvalue problem given by

$$\omega_i^2 [M] V_i = ([K_s] + [\dot{K}]) V_i \tag{7}$$

where  $\omega_i$  are the natural frequencies and  $V_i$  are the vibration modes.

$\dot{K}$  is the average matrix of mesh stiffness matrix depend of time  $K(t)$ .

In order to identify the natural frequencies, the Frequency Response Function (FRF) on the third bearing in the  $X_3$  direction is showed when the first degree of freedom is excited (Fig. 3). Several peaks located in 26.1, 878, 1679.6, 1972.3, 1974.2, 2591.1 and 3470.3 Hz and corresponding to the natural frequencies appear in this figure.

Meanwhile, there are other natural frequencies which don't appear in this figure. They are 1902, 2344 and 3470 Hz.

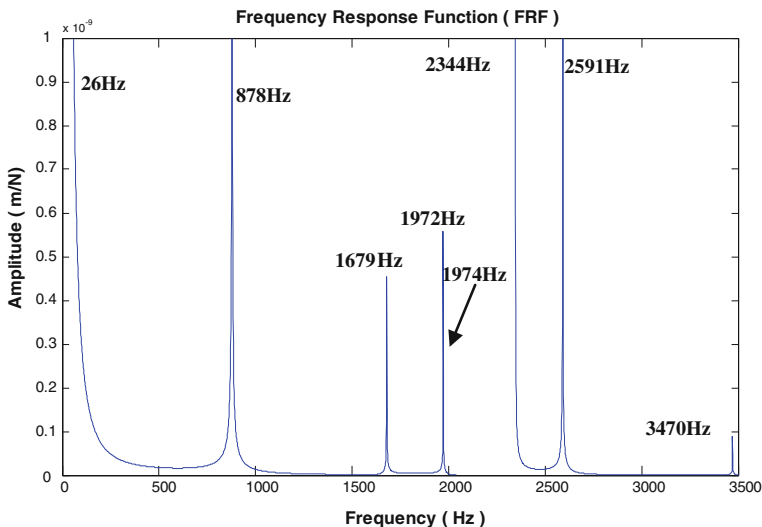


Fig. 3 Frequency response function (FRF) on the third bearing (X3)



### 3.2 Analysis of the Distribution of Modal Strain and Modal Kinetic Energies

The modal strain energy and the modal kinetic energy distributions are computed in order to give information on bodies sought to critical speeds in terms of dominant motion and deformation.

#### 3.2.1 Analysis of the Distribution of Modal Strain Energies

The total modal strain energy is defined as:

$$E_p = \frac{1}{2} q_i^t (\tilde{K} + K_s) q_i \quad (8)$$

Figure 4 shows the distribution of modal strain energies, where the  $X$ -axis is defined in Table 2.

In  $X$ -axis is represented the contribution of each degree of freedom in the total modal strain energy. Details are given in Table 2.

#### 3.2.2 Analysis of the Distribution of Modal Kinetic Energies

The modal kinetic energy can be written as:

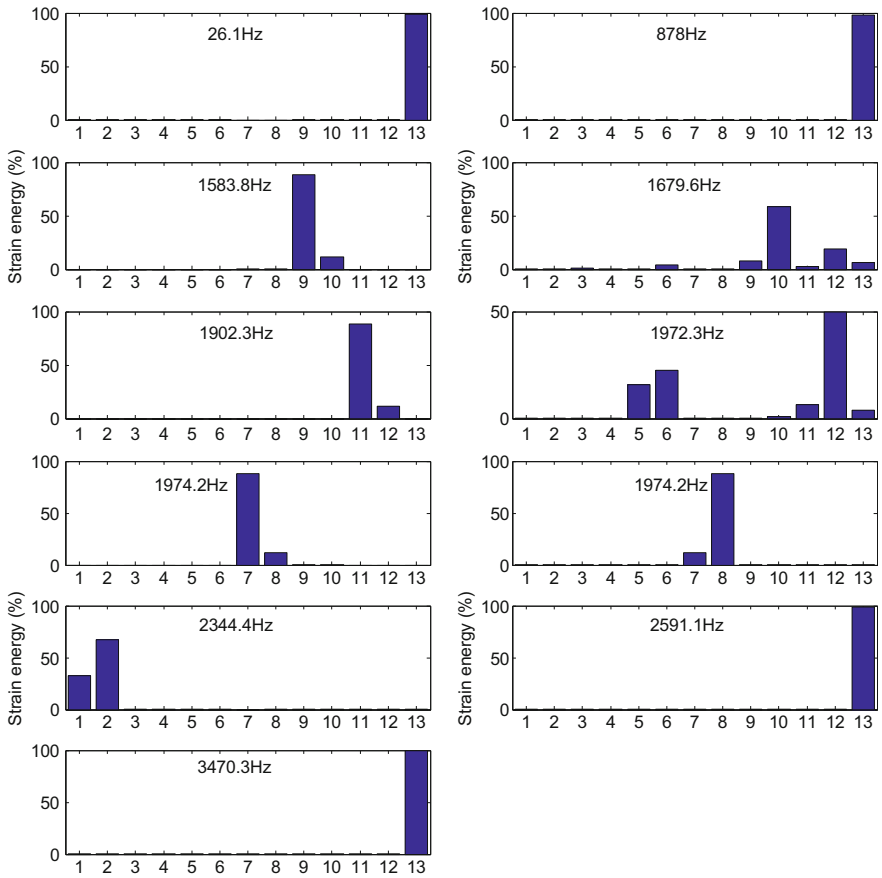
$$E_c = \frac{1}{2} w_i^2 q_i^{\bullet t} M \dot{q}_i \quad (9)$$

Figure 5 shows the distribution of modal kinetic energies.

In  $X$ -axis is represented the contribution of each degree of freedom in the total modal kinetic energy. Details are given in Table 3.

Table 4 shows a recapitulation of the modal dominant kinetic and strain energies distributions. It can be noticed that the natural frequencies can be divided into two bands:

- The first band where the natural frequencies are less than 1500 Hz. This band can be called “gear modes” and it is characterized by the dominant strain energy in the gear meshing zone and a dominant rotational motion of the components. Movement are rotation of components.
- The second band concerns the natural frequencies more than 1500 Hz. This band can be called “bearing modes” and it is characterized by the dominant strain energy in bearings and the dominant movement are in translations of shafts.



**Fig. 4** Modal strain energies

**Table 2** X-axis of the contribution of the modal strain energy

1	Inertia of the motor	7	Bearing 1( $x_1$ )
2	Inertia of the 1st part of coupling	8	Bearing 1( $y_1$ )
3	Inertia of the 2nd part of coupling	9	Bearing 2( $x_2$ )
4	Inertia of the 1st gear	10	Bearing 2( $y_2$ )
5	Inertia of the 2nd gear	11	Bearing 3( $x_3$ )
6	Inertia of the receiver	12	Bearing 3( $y_3$ )
		13	Gear meshing

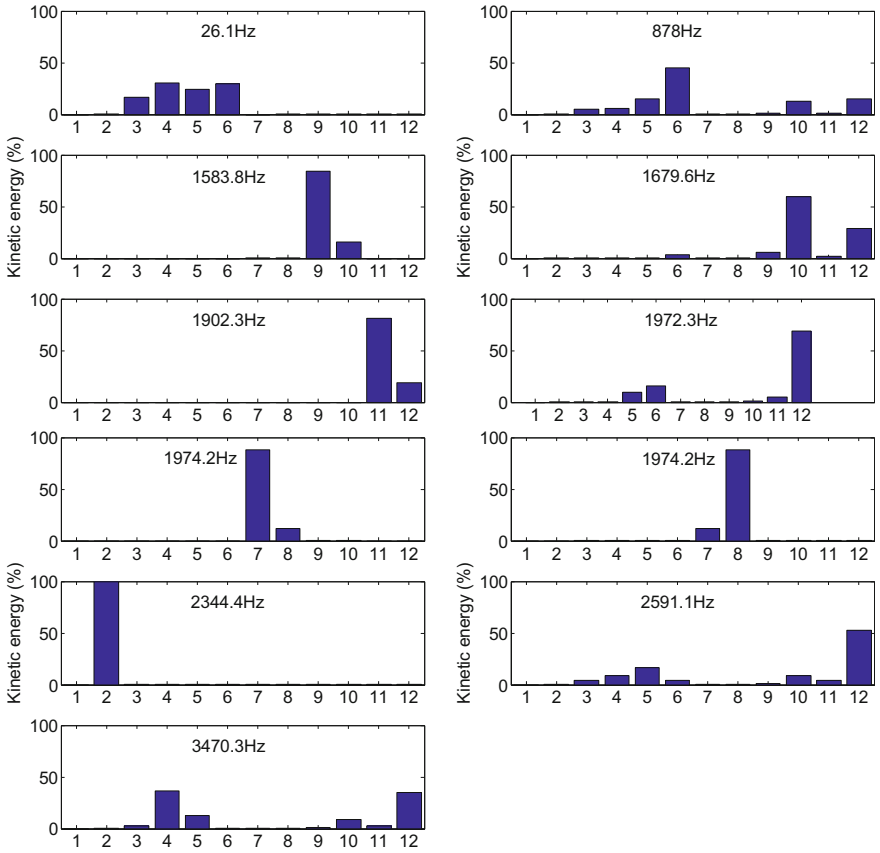


Fig. 5 Modal kinetic energies

Table 3 X-axis of the contribution of the modal kinetic energy

1–2	Rotation of shaft 1( $\theta_{11}, \theta_{12}$ )	7–8	Translation in bearing 1( $x_1, y_1$ )
3–4	Rotation of shaft 2( $\theta_{21}, \theta_{22}$ )	9–10	Translations in bearing 2( $x_2, y_2$ )
5–6	Rotation of shaft 3( $\theta_{31}, \theta_{32}$ )	11–12	Translations in bearing 3( $x_3, y_3$ )

**Table 4** Summary of the modal dominant kinetic and strain energies distributions

Frequency (Hz)	Dominant kinetic energy	Dominant strain energy
26.1	Rotation motion in 2 and 3 shafts	Gear meshing
878.3	Rotation motion in the 3 shaft	Gear meshing
1583.8	Translation in bearing 2(X2)	Bearing 2(x2)
1679.6	Translation in bearing 2 and 3(Y2 and Y3)	Bearing 2(y2)
1902.3	Translation in bearing 3(X3)	Bearing 3(x3)
1972.3	Translation in bearing 3(Y3)	Bearing 3(y3)
1974.2	Translation in bearing 1(Y1)	Bearing 1(x1)
1974.2	Translation in bearing 2(X2)	Bearing 1(y1)
2344.4	Rotation motion in 1 shaft	Inertia of the 1st part of coupling
2591.1	Translation in bearing 3(Y3)	Gear meshing
3470.3	Rotation motion in 2 shaft and Translation in bearing 3(Y3)	Gear meshing

## 4 Conclusion

Using elastic coupling to connect two shafts and model it following Nelson and Crandall showed that this coupling was most important in controlling the dynamic response.

According to the distribution of modal strain energies and modal kinetic energies, the natural frequencies can be classified into two bands: below and above 1500 Hz. Modes located in the first band called “gear modes” are characterized by the dominant strain energy in the meshing zone and a rotational dominant movement whereas modes located in the second band are called “bearing modes” and they are characterized by the dominant strain energy in bearings and a translational dominant motion of shafts. This study can help designers to avoid critical frequencies on the system by changing parameters of the system. It allows one also to localize critical components susceptible to damage when crossing natural frequencies.

## References

- Bartelmus W (2001) Gearbox dynamic modelling. *J Theoret Appl Mech* 39(4):989–999
- Chatelet E, D’Ambrosio F, Jacquet-Richardet G (2005) Toward global modelling approaches for dynamic analyses of rotating assemblies of turbomachines. *J Sound Vibr* 282(1–2):163–178
- Cunliffe F, Smith JD, Welbourn DB (1974) Dynamic tooth loads in epicyclic gears. *J Eng Ind* 95:578–584
- Ding JJ, Al-Jumaly A (2000) A linear regression model for the identification of unbalance changes in rotating machines. *J Sound Vibr* 231(1):125–144
- Edwards S, Lees AW, Friswell MI (2000) Experimental identification of excitation and support parameters of flexible rotor–bearings—foundation system from a single run-down. *J Sound Vibr* 232(5):963–992

- Genta G (2005) Dynamics of rotating systems. Mechanical Engineering Series, Springer
- Krämer E (1993) Dynamics of rotors and foundations. Springer, London
- Nelson HD, Crandall SH (1992) Analytic prediction of rotor dynamic response. In Ehrich FE (ed) Handbook of rotor dynamics. McGraw-Hill Inc, NewYork
- Nordmann R (1984) Identification of modal parameters of an elastic rotor with oil film bearings. J Vib Acoust Stress Reliab Des 106:107–112
- Sinha JK, Friswell MI, Lees AW (2002) The identification of the imbalance and the foundation model of a flexible rotating machine from a single run-down. Mech Syst Signal Process 16(2–3):255–271

# Planet Load Sharing Behavior During Run Up

Ahmed Hammami, Alfonso Fernandez Del Rincon, Fakher Chaari,  
Fernando Viadero Rueda and Mohamed Haddar

**Abstract** The objective of this paper is to study the effects of meshing phase between planets and the planet position error on the load sharing behavior in planetary gear set during run up regime. These effects will be studied numerically and will be validated experimentally through a back-to-back planetary gear test bench by comparing strains in the pinhole of each planet.

**Keywords** Planetary gear · Load sharing · Run up · Meshing phase · Planet position error

## 1 Introduction

Planetary gear can transmit higher power because they use multiple power paths formed by each planet branches. This allows the input torque to be divided between the  $n$  planet paths, reducing the force transmitted by each gear mesh.

---

A. Hammami (✉) · F. Chaari · M. Haddar  
Laboratory of Mechanics, Modeling and Production (LA2MP),  
National School of Engineers of Sfax, BP1173–3038 Sfax, Tunisia  
e-mail: ahmed.hammami2109@gmail.com

F. Chaari  
e-mail: fakher.chaari@gmail.com

M. Haddar  
e-mail: mohamed.haddar@enis.rnu.tn

A. Hammami · A. Fernandez Del Rincon · F. Viadero Rueda  
Department of Structural and Mechanical Engineering, Faculty of Industrial  
and Telecommunications Engineering, University of Cantabria,  
Avda de los Castros s/n, 39005 Santander, Spain  
e-mail: alfonso.fernandez@unican.es

F. Viadero Rueda  
e-mail: fernando.viadero@unican.es

Each planet path carries an equal load under ideal conditions. Nevertheless, planetary gears have inevitable manufacturing and assembly errors. So, the load is not equally shared amongst the different planet-ring and sun-planet paths, which can be a problem in terms of both durability and dynamic behavior.

Many significant works on the subject of planetary gear load sharing have been done. These works were based on transmission modeling and assessed by experimental tests. Kahraman (1994) used a discrete model to study the influence of carrier pin hole and planet run-out errors on planet load-sharing characteristics of a four-planet system under dynamic conditions. He employed later (Kahraman 1999) a planet load-sharing model to determine the static planet load sharing of four-planet systems and presented experimental data for validation of the model predictions. Iglesias et al. (2013) studied the effect of planet position error on the load sharing and transmission error. Singh (2005) found that the tangential pin position error has a greater effect on the load sharing than the radial pin position error. Ligata et al. (2008) proved experimentally that for the same amount of error, the degree of inequality in the planet load-sharing behavior increases with the number of planets in the system. Guo and Keller (2012) presented a three-dimensional dynamic model which take into account to the addressing gravity, bending moments, fluctuating mesh stiffness, nonlinear tooth contact, and bearing clearance. They validated this model against the experimental data.

All works on the subject of planetary gear load sharing are in the static, quasi-static or stationary operations.

In this paper, the effects of meshing phase and the error position of the pin hole of planets on the load sharing characteristics are studied during the run up regime numerically and validated experimentally through back-to-back planetary gear.

## 2 Description of the Test Bench

The test bench is composed of two identical planetary gear sets with the same gear ratio allowing the mechanical power circulation (Fig. 1). The first planetary gear is a “test gear set” and the second planetary gear is a “reaction gear set” having a free ring. An arm is fixed on this ring and allowing the introduction of external load (Hammami et al. 2014a, b). The two planetary gears are connected back-to-back: the sun gears of both planetary gear sets are connected through a common shaft and the carriers of both planetary gear sets are connected to each other through a rigid hollow shaft (Hammami et al. 2014c).

Three strains gauges are used in quarter bridge configuration in order to compare the load sharing between the tests planets. They are installed in the pin holes of each planet in the tangential direction of the test carrier (Fig. 1).

The wires from the strain gauges are connected to the Programmable Quad Bridge Amplifier module (PQBA) of the acquisition system “LMS SCADAS 316

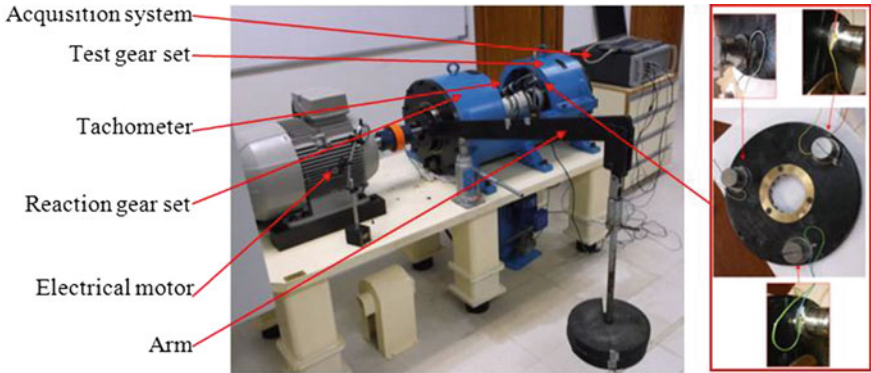


Fig. 1 Back-to-back planetary gear test bench

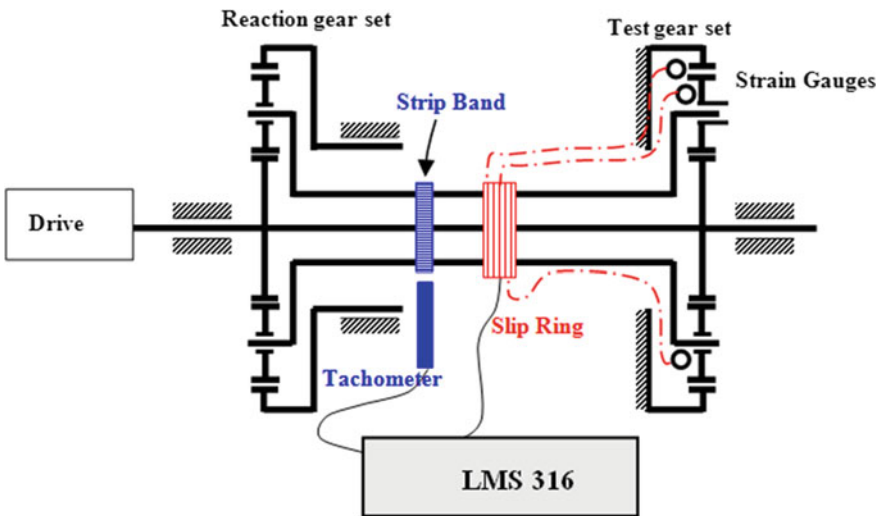


Fig. 2 Instrumentation layout

system” through a hollow slip ring which is installed with the hollow shaft that connects the carriers (Fig. 2).

Additionally, an optic tachometer (Compact VLS7) which is placed along the hollow carriers’ shaft measure its instantaneous angular velocity.

The data will be processed with the software “LMS Test.Lab” to visualize time history of strains.



### 3 Numerical Results

In this part, effects of meshing phase and the position error of planets on the load sharing behavior are studied during the run up regime. The variation of speed during this regime is controlled by the frequency converter “Micromaster 440” which commands linearly the variation of the rotational speed of motor as shown in Fig. 3.

First of all, we define the planet load sharing ratio (LSR) as the ratio of the meshing torque due to sun-planet (i) and ring-planet (i) meshes of planet (i) by the meshing torque of all planets.

$$L_{Pi} = \frac{T_{mesh(Pi)}}{\sum_{i=1}^n T_{mesh(Pi)}}. \quad (1)$$

#### 3.1 Effect of Meshing Phase

For the case of equally spaced planets and in phase meshes gear (sun planets and ring planets), the planet load sharing factor is equal to  $1/N$  (N: number of planets).

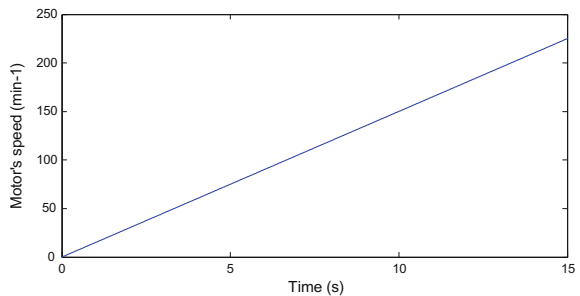
In our case, planets are equally spaced and gear meshes functions are sequentially phased.

$$\frac{Z_j \psi_i}{2\pi} \neq n \text{ and } \sum_{i=1}^N Z_j \psi_i = m\pi \quad (j = r, s) \quad (2)$$

$Z_j$  is the number of tooth of the gear (j).  $\psi_i$  is the angle position of the planet (i). n and m are integer.

For run up regime, the period of mesh stiffness function decrease as speed increases (Khabou et al. 2011; Viadero et al. 2014). Meshes stiffness between gears

**Fig. 3** Evolution of the motor’s speed during run up



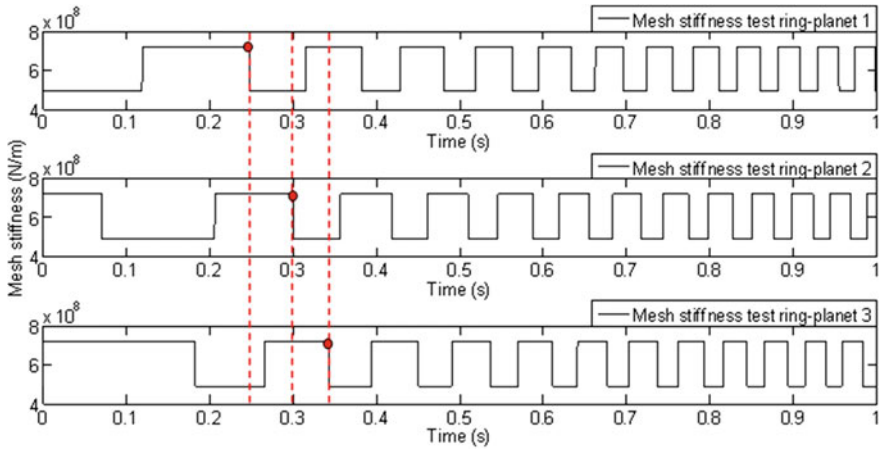


**Fig. 4** Evolution of the mesh stiffness ring-planets during run-up

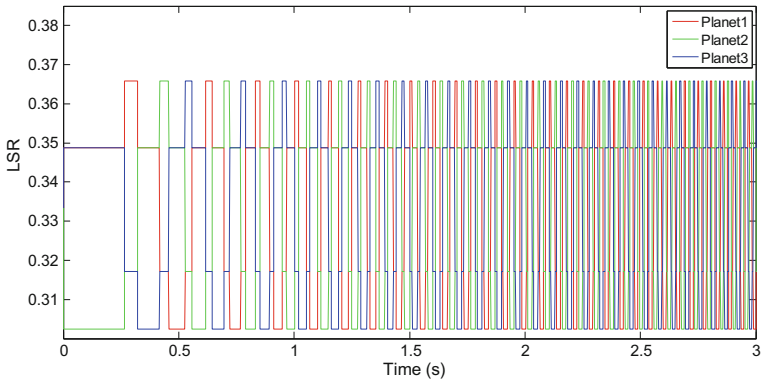


**Fig. 5** Planet load sharing ratio for the nominal position of planets

are modelled as square functions. Figure 4 shows the evolution of mesh stiffness for ring-planets on the test gear set during run up taking into account mesh phasing.

The dynamic response is computed according to the procedure given in (Kahraman 1994) and the load sharing ratio is computed according to Eq. (1). Figure 5 shows the planet load sharing ratio for the nominal position of planets (faultless system) for 100 N.m of input torque.

In this case, the LSR for all planets fluctuates slightly around the  $1/N$  value ( $N = 3$ : number of planets) because the number of tooth in contact changes. The fluctuation of LSR of each planet is with a phase shift of  $2\pi/3$ . This phase is induced by the fact that gear mesh sun-planets and ring-planets are sequentially phased. In addition, the period of fluctuation of LSR of each planet decrease with time which is explained by the evolution of the mesh stiffness ring-planets during run-up.

### 3.2 Effect of Planet Position Error

If a planet has an error “ $e$ ” on the position of its pin hole, and all other planets are at their ideal position, then the force due to this error is given by (Singh 2010):

$$F_e = K_{eff} \cdot e \quad (4)$$

$K_{eff}$  is the cumulative stiffness due to meshing stiffness of the contact at the sun-planet  $K_{ps}$  and planet–ring  $K_{pr}$ , and the planet bearing stiffness  $K_b$ .

$K_{eff}$  is defined as (Ligata et al. 2009):

$$\frac{1}{K_{eff}} = \frac{1}{K_b} + \frac{1}{K_{ps} + K_{pr}} \quad (5)$$

In our case, the planet 1 has an error “ $e_1 = 60 \mu\text{m}$ ”, the planet 2 has an error “ $e_2 = -5 \mu\text{m}$ ” and the planet 3 has an error “ $e_3 = -60 \mu\text{m}$ ”. The LSR in this case is represented in Fig. 6.

The position errors of planets 1 and 2 have an important effect in the LSR. Planet 1 which has a positive error anticipates the contact, being preloaded before planets 2 and 3 begin to transmit load; whereas planet 3 which has a negative error is preloaded after planet 2 and 1. This defects are in tangential direction and they have an effect very important in the LSR (Bodas and Kahraman 2004). In addition, planet load sharing ratio tends towards fair values in the run up regime which is explained by the fact that the transmitted load decrease in each planet as the speed increase.

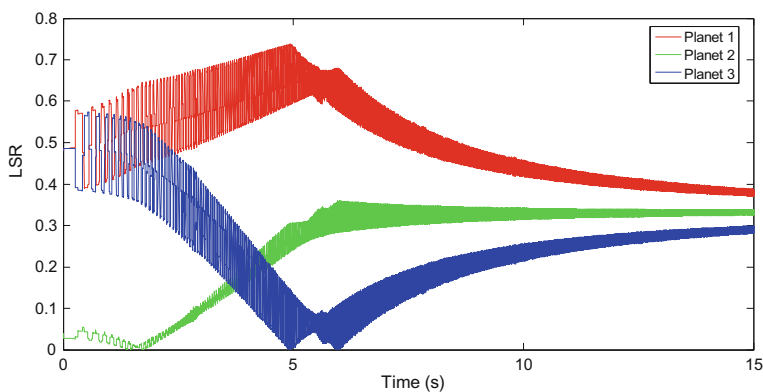


**Fig. 6** Planet load sharing ratio with planets position errors

### 4 Correlation with Experimental Results

Strain-time histories for three planets system having errors “ $e_1 = 60 \mu\text{m}$ ” and “ $e_2 = -5 \mu\text{m}$ ” and “ $e_2 = -60 \mu\text{m}$ ” are shown in Fig. 7. It is clear that the positioning error has an important effect in the strain of each pin hole of planet. Also, strains tend towards fair values as the speed increase.

The computational results of the load sharing ratio are compared to the measured LSR (Fig. 8). In general, the calculated load sharing agrees with the measured data. In fact, the effect of meshing phase is observed only in the numerical results because the recorded signals presents noise due to the contact between brushes and slip ring. So, a signal processing was necessary.

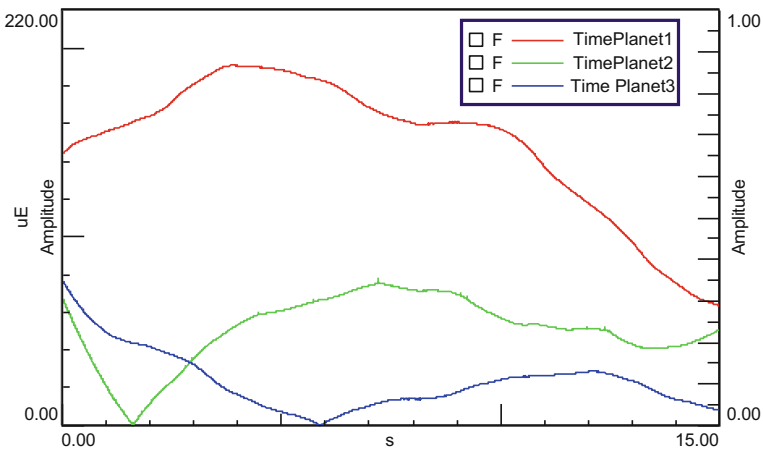


Fig. 7 Variation of the measured planets strains for the speed motor 165 rpm

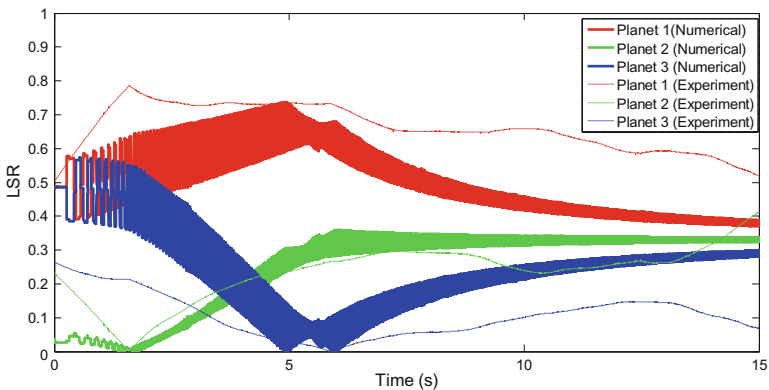


Fig. 8 Evolution of measured and calculated LSR

## 5 Conclusion

In this paper, the planets load sharing behaviour is studied during the run up regime and correlated with those obtained experimentally using strain gages on planets of a back-to-back planetary gear test bench.

The effect that planets are sequentially phased is included to the model and as results; the load sharing ratio for all planets fluctuates slightly around the  $1/N$  value and the period of fluctuation of each planet decreases with time. The planets position errors have an important effect on the LSR of each planet which tends towards fair values in the run up regime. The final numerical results with the two effects agree with the measured strains on planets.

**Acknowledgments** This paper was financially supported by the Tunisian-Spanish Joint Project No. A1/037038/11.

The authors would like also to acknowledge project “Development of methodologies for the simulation and improvement of the dynamic behavior of planetary transmissions DPI2013-44860” funded by the Spanish Ministry of Science and Technology.

Acknowledgment to the University of Cantabria cooperation project for doctoral training of University of Sfax’s students.

## References

- Bodas A, Kahraman A (2004) Influence of carrier and manufacturing errors on the static load sharing behavior of planetary gear sets. *Bull Jpn Soc Mech Eng* 47(3):908–915
- Guo Y., Keller J (2012) Combined effects of gravity, bending moment, bearing clearance, and input torque on wind turbine planetary gear load sharing. American Gear Manufacturers Association technical paper, 12FTM05
- Hammami A, Fernández A, Viadero F, Chaari F, Haddar M (2014a) Modal analysis of back-to-back planetary gear: experiments and correlation against parameter model. *J Theor Appl Mech* 53(1):125–138
- Hammami A, Fernández A, Viadero F, Chaari F, Haddar M (2014b) Dynamic behaviour of back-to-back planetary gear in run up and run down transient regimes. *J Mech* 31(4):481–491
- Hammami A, Fernández A, Chaari F, Viadero F, Haddar M (2014c) Dynamic behaviour of two stages planetary gearbox in non-stationary operations. In: *Mechatronic system: theory and application*, pp 23–35
- Iglesias M, Fernandez A, De-Juan A, Sancibrian R, Garcia P (2013) Planet position errors in planetary transmission: effect on load sharing and transmission error. *Front Mech Eng* 8:80–87
- Kahraman A (1994) Load sharing characteristics of planetary transmissions. *Mech Mach Theory* 29:1151–1165
- Kahraman A (1999) Static load sharing characteristics of transmission planetary gear sets: model and experiment. SAE Paper No. 1999-01-1050
- Khabou MT, Bouchaala N, Chaari F, Fakhfakh T, Haddar M (2011) Study of a spur gear dynamic behavior in transient regime. *Mech Syst Signal Process* 25:3089–3101
- Ligata H, Kahraman A, Singh A (2008) An experimental study of the influence of manufacturing errors on the planetary gear stresses and planet load sharing. *J Mech Des* 130
- Ligata H, Kahraman A, Singh A (2009) A closed-form planet load sharing formulation for planetary gear sets using a translational analogy. *J Mech Des* 131:021007

- Singh A (2005) Application of a system level model to study the planetary load sharing behavior. *J Mech Des* 127:469–476
- Singh A (2010) Load sharing behavior in epicyclic gears: physical explanation and generalized formulation. *Mech Mach Theory* 45:511–530
- Viadero F, Fernández A, Iglesias M, de-Juan A, Liaño E, Serna MA (2014) Non-stationary dynamic analysis of a wind turbine power drivetrain: offshore considerations. *Appl Acoust* 77:204–211

# Multi-objective Design Optimization of the NBTTL Mechanism

B. Najlawi, M. Nejlaoui, Z. Affi and L. Romdhane

**Abstract** This work deals with the multi-objective design optimization of NBTTL mechanism. The needle jerk (NJ) and the maximum angular velocity ratio (MAVR) are minimized simultaneously. The goal is to minimize the machine input torque and vibration. The multi-objective imperialistic competitive algorithm (MOICA) is used to find the optimal link lengths of the NBTTL mechanism. Compared to Juki 8700, the obtained results show that the optimized mechanism can reduce the MAVR by 80 % and the NJ by 70 %.

**Keywords** NBTTL mechanism · Multi-objective optimization · MOICA · Needle jerk · MAVR

## 1 Introduction

The application of several engineering fields in textile industry has found a great attention in recent years. Many researchers focused on optimizing the design of sewing machines in order to improve their mechanical performances. In particular, synthesizing the needle-bar-and-thread-take-up-lever (NBTTL) mechanism is one

---

B. Najlawi (✉) · M. Nejlaoui · Z. Affi  
LGM, ENIM, University of Monastir, Monastir, Tunisia  
e-mail: najlawibilelali@gmail.com

M. Nejlaoui  
e-mail: nejlaouimohamed@gmail.com

Z. Affi  
e-mail: zouhaier.affi@enim.rnu.tn

L. Romdhane  
Department of Mechanical Engineering, American University of Sharjah,  
Sharjah, UAE  
e-mail: lotfi.romdhane@gmail.com

of the most important studies in this area. This mechanism consists of a four bar linkage and a slider crank mechanism driven by the same crank.

Several studies deal with the dimensional synthesis of four bar mechanisms. Vasiliu and Yannou (2001) optimized the design of four bar mechanisms using a neural network method. In the same lines, Matekar et al. (2011) presented an optimization study of a four bar mechanism with the differential evolution algorithm. Ebrahimi and Payvandy (2015) used an objective function with penalty weighting factors to minimize the coupler tracking error and the Jerk of the thread take-up lever.

Other works dealt with the design of slider crank mechanisms. Gotlih et al. (2007) minimized the needle velocity using a nonlinear optimization procedure. The aim is to decrease the heat caused by friction between the needle and the fabric in the penetration zone. However, the reduction of the needle velocity in the penetration zone may affect the amount of the required needle force, which in turn depends on the transmission angle of the slider crank mechanism (Eschenbach and Tesar 1971). In this context, Tanik (2011) has introduced the transmission angle criterion to design a compliant slider crank mechanism.

However, to the best of our knowledge, there is no study which considers simultaneously the optimization of the four bar linkage and the slider crank mechanism (as a single system) in order to design the NBTTL mechanism. In this paper, a multi-objective optimal design of the NBTTL mechanism is developed. The aim is to reduce the sewing machine vibration and minimize the input to output torques ratio by minimizing, simultaneously, the needle jerk (NJ) and the maximum angular velocity ratio (MAVR) of the coupler point.

The rest of the paper is organized as follows: In Sect. 2, a description of different parts of the NBTTL is presented. In Sect. 3, a kinematic analysis of the NBTTL mechanism is developed. In Sect. 4, a multi-objective optimization problem for the design of the NBTTL mechanism is formulated. Then, the MOICA algorithm is described. The obtained optimal results are discussed in Sect. 5 and some concluding remarks are shown in Sect. 6.

## 2 The NBTTL Mechanism

Figure 1 presents the NBTTL mechanism of a sewing machine. The thread take-up lever mechanism is the four-bar linkage OABC. OEF represents the slider-crank mechanism in which point F denotes the needle. The function of the thread take-up lever in the stitch formation process is to ensure appropriate thread feeding. The function of the needle, which is fixed to the needle bar, is to penetrate the fabric. The rotation of the input link (OA) is transformed to the translation of the needle bar through the slider-crank mechanism. The displacement of the needle bar is represented by the distance 's'.



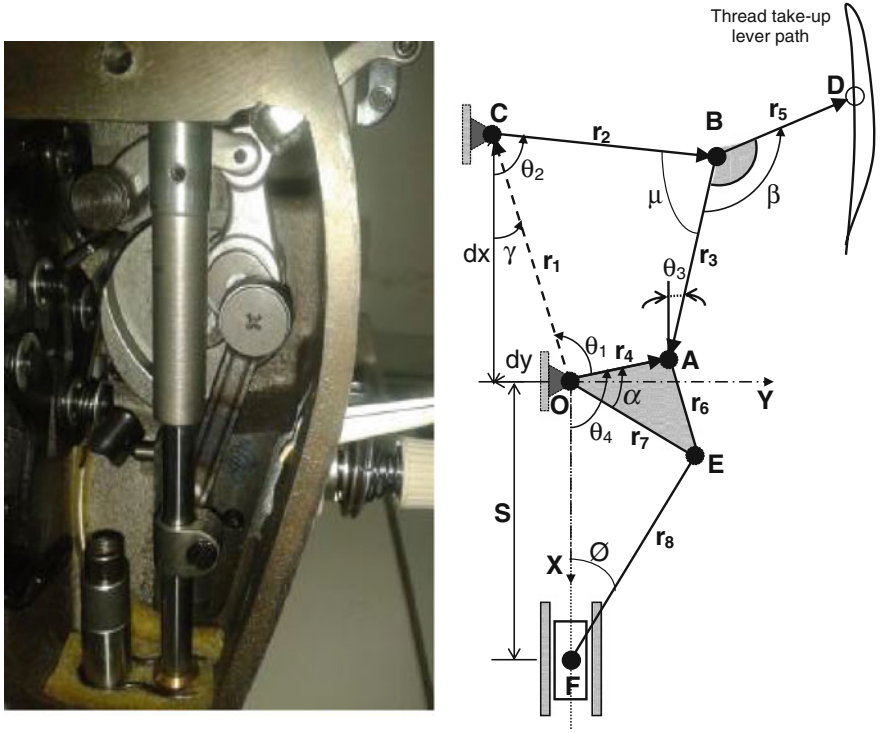


Fig. 1 The NBTTL mechanism

### 3 Kinematics of the NBTTL Mechanism

To optimize the NBTTL mechanism, it is mandatory to find:

- The input-output relation between the crank OA angular displacement and the coupler point D displacement.
- The needle jerk in point F.

In this section, the modeling of the NBTTL mechanism is presented. The angle  $\theta_4$ , the velocity  $\dot{\theta}_4$  and the acceleration  $\ddot{\theta}_4$  describing the input of the machine are supposed to be known during the functioning of the sewing machine.

The needle displacement, with respect to  $(OX,OY)$  frame, is given by (Fig. 1):

$$r_7 \sin(\theta_4 - \alpha) - r_8 \cos \phi = 0 \tag{1}$$

$$s = r_7 \cos(\theta_4 - \alpha) + r_8 \cos\left(\sin^{-1}\left(\frac{r_7}{r_8} \sin(\theta_4 - \alpha)\right)\right) \tag{2}$$

By taking the time derivative of Eq. (3), we can find the needle jerk:

$$\begin{aligned} \ddot{s} = & -r_7 \left[ \ddot{\theta}_4 \sin(\theta_4 - \alpha) + 3\dot{\theta}_4 \ddot{\theta}_4 \cos(\theta_4 - \alpha) - \dot{\theta}_4^3 \sin(\theta_4 - \alpha) \right] \\ & - \left[ 3r_7 \left[ \frac{r_7}{r_8} \frac{df(\theta_4)}{dt} \dot{\theta}_4 + \frac{r_7}{r_8} f(\theta_4) \ddot{\theta}_4 \right] f(\theta_4) \dot{\theta}_4 \cos(\sin^{-1}(\frac{r_7}{r_8} \sin(\theta_4 - \alpha))) \right] \\ & - \left[ r_7 \sin(\theta_4 - \alpha) \frac{d}{dt} \left[ \frac{r_7}{r_8} \frac{df(\theta_4)}{dt} \dot{\theta}_4 + \frac{r_7}{r_8} f(\theta_4) \ddot{\theta}_4 \right] \right] + \left( \frac{r_7}{r_8} f(\theta_4) \dot{\theta}_4 \right)^3 r_7 \sin(\theta_4 - \alpha) \end{aligned} \tag{3}$$

$$\text{Where } f(\theta_4) = \frac{\cos(\theta_4 - \alpha)}{\sqrt{1 - \left(\frac{r_7}{r_8}\right)^2 \sin^2(\theta_4 - \alpha)}}$$

In textile engineering, sewing machines have been basically designed for work at high speed. This can lead to high vibration. To decrease the vibration of the sewing machine, we reduce the jerk of its needle given by:

$$NJ = \int_0^{2\pi} |\ddot{s}| d\dot{\theta}_4 \tag{4}$$

NJ defines the first objective function to be minimized.

The maximum angular velocity ratio (MAVR) is given by:

$$MAVR = \max(AVR) = \max\left(\frac{\dot{\theta}_2}{\dot{\theta}_4}\right) = \max\left(\frac{r_4}{\lambda}\right) \tag{5}$$

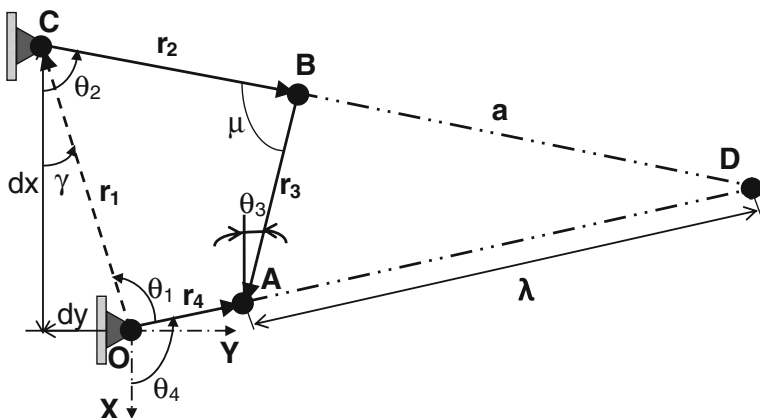


Fig. 2 Position virtual loop of four-bar linkage

Generally, the MAVR is treated geometrically (Barker 1987). In this work we will give a closed form solution of the MAVR. Referring to Fig. 2, the closed loop equations of the virtual loop ABD can be given by:

$$\overrightarrow{AB} + \overrightarrow{BD} + \overrightarrow{DA} = \overrightarrow{0} \quad (6)$$

Equation (6) can be projected into their X and Y components.

$$\begin{cases} -r_3 \cos \theta_3 + a \cos \theta_2 - \lambda \cos \theta_4 = 0 \\ r_3 \sin \theta_3 + a \sin \theta_2 - \lambda \sin \theta_4 = 0 \end{cases} \quad (7)$$

By using Eq. (6), we can express  $\lambda$  as follows:

$$\lambda = r_3 \frac{\sin(\theta_3 + \theta_2)}{\sin(\theta_4 - \theta_2)} \quad (8)$$

From Eq. (5), the maximum angularity ratio is given by:

$$\text{MAVR} = \max \left( \frac{r_4 \sin(\theta_4 - \theta_2)}{r_3 \sin(\theta_3 + \theta_2)} \right) \quad (9)$$

In fact, minimizing the maximum angular velocity ratio yields the minimization of the input to output torques ratio. Minimizing this ratio allows the minimization of accelerations and hence minimizing the inertial forces exerted on the mechanism. Hence, The MAVR represent the second objective function.

## 4 Multi-objective Optimization Design of the NBTTL Mechanism

The optimization problem can be defined as minimizing simultaneously the NJ and the MAVR while respecting some constraints. In order to ensure that the input crank of the thread take-up lever can make a complete rotation, the mechanism should satisfy the Grashof law. Moreover, the set of input link angles  $\theta_4$  has to be sorted in an increasing order ( $\theta_4(i) < \theta_4(i + 1)$ ). The displacement of the needle is limited ( $30 \text{ mm} \leq s \leq 62 \text{ mm}$ ) and the optimization variables have to be limited to some bounds due to the practical limitations in the construction of the mechanism. Hence, the multi-objective optimization problem can be formulated as:

$$\text{Minimize} \begin{cases} \text{NJ} = \int_0^{2\pi} |\ddot{s}| d\theta_4 \\ \text{MAVR} = \max \left( \frac{r_4 \sin(\theta_4 - \theta_2)}{r_3 \sin(\theta_3 + \theta_2)} \right) \end{cases} \quad (10)$$

**Table 1** Range of the design variables

Parameter	dx (mm)	dy (mm)	r <sub>i</sub> (mm)	α (°)
Range	[0–60]	[0–60]	[0–60]	[0–360]

$$\text{Subject to : } \begin{cases} 2[\max(r_1, r_2, r_3, r_4) + \min(r_1, r_2, r_3, r_4)] < r_1 + r_2 + r_3 + r_4 \\ \theta_4^i - \theta_4^{i+1} < 0 \\ \sin(\theta_3 + \theta_2) \neq 0 \\ x_i \in [x_{i \min}, x_{i \max}], x_i \in X \\ 30 \text{ mm} \leq s \leq 62 \text{ mm} \end{cases} \quad (11)$$

The search domains of the design variables are shown in Table 1.

We have proposed in a previous work (Najlawi et al. 2015) a multi-objective imperialist competitive algorithm (MOICA) inspired from the socio-political process of imperialist competition. Figure 3 shows the flowchart of the MOICA algorithm. This algorithm starts by a random generation of initial countries. The cost of a country is determined by evaluating the objective functions. The most powerful country is called “imperialist” and the remaining countries are considered as “colonies”. Each initial empire is composed of one imperialist and several colonies. After forming initial empires, colonies start moving towards the relevant imperialist. In each empire, the multi-points crossover and the random replacement mutation operators enhance the colonies with a new one that can have more power and eventually constitute imperialists. In this case, the colony and the imperialist permute positions. Then, non-dominated imperialists are kept in an archive based on the fast non dominated sorting approach (Deb et al. 2002). This archive represents the Pareto front.

Based on their power, any empire that does not improve in imperialist competition will be diminished. As a result, the imperialistic competition will increase the power of great empires and weaken the frail ones. Thus, weak empires will collapse. Finally, The MOICA algorithm stops when only one empire remains.

## 5 Results and Discussion

Using the MOICA algorithm, the Pareto front of NJ and MAVR objective functions can be determined to find the optimal non-dominated solutions (Fig. 4).

In Fig. 4, each non dominated solution represents an optimal design vector of the NBTTL mechanism. One can note that for the best MAVR, we have the worst NJ and vice versa. Table 2 presents the design vectors of the extreme optimal solutions S<sub>1</sub> and S<sub>2</sub> taken from the Pareto front. For comparison reason, we give in the same table the design vector of the known existing sewing machine Juki 8700.

From Fig. 5 and Table 2 one can note that, compared to Juki 8700, we can reduce the MAVR by about 80 % by using the optimal S<sub>1</sub> solution.

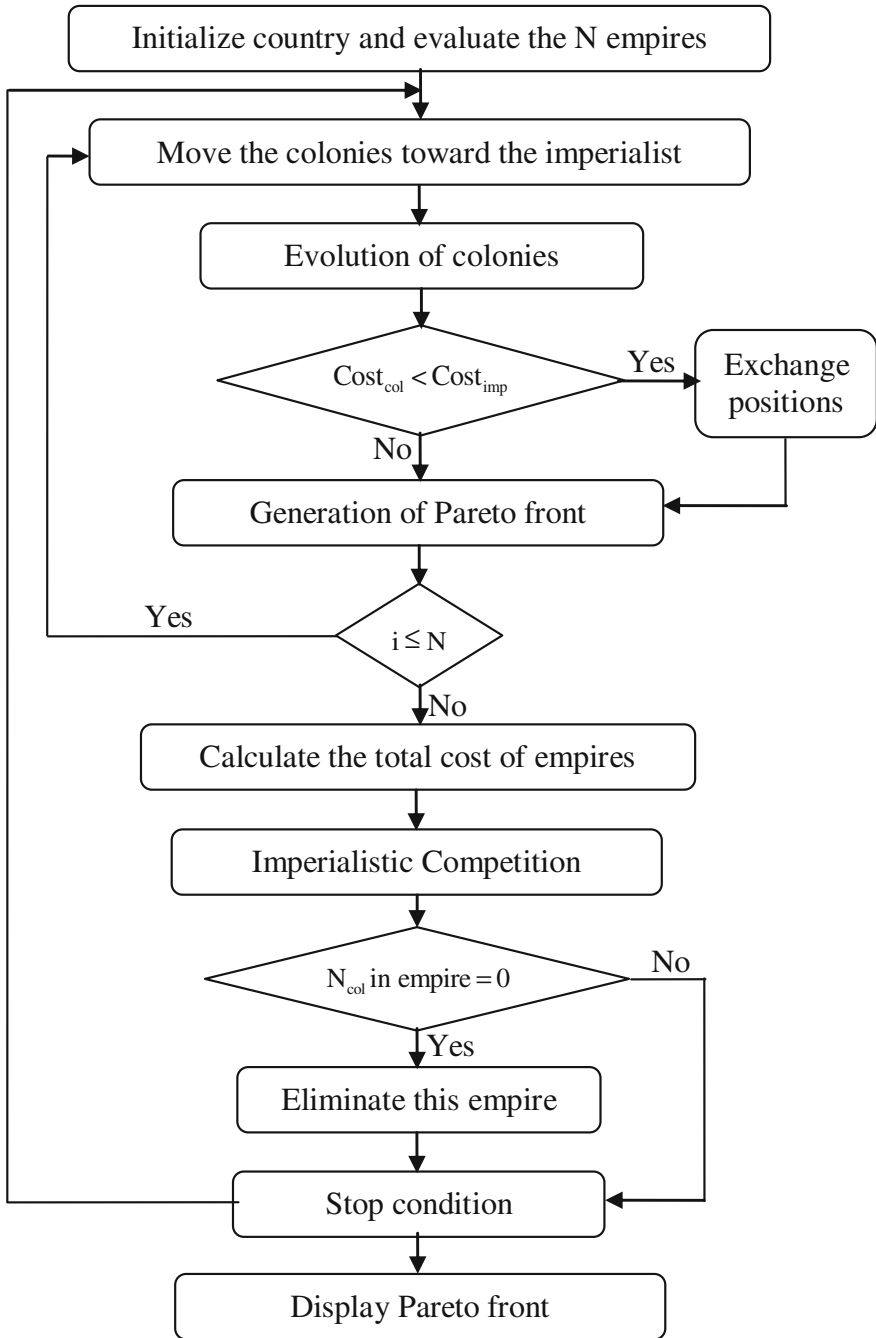
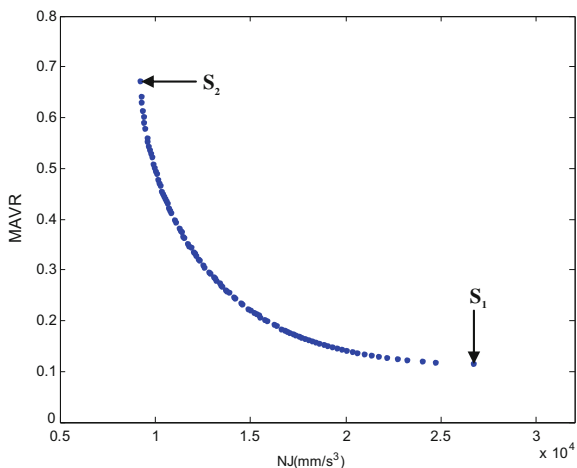


Fig. 3 Flowchart of the MOICA method

**Fig. 4** Pareto front of optimal solutions



**Table 2** Design vector of  $S_1$ ,  $S_2$  and Juki 8700

Parameters	$S_1$	$S_2$	Juki 8700
dx (mm)	28.64	36.17	38.64
dy (mm)	38.12	29.42	33.22
$r_2$ (mm)	37.76	43.89	44.80
$r_3$ (mm)	33.07	26.81	30.31
$r_4$ (mm)	7.06	8.42	7.68
$r_5$ (mm)	38.51	41.32	40.26
$r_7$ (mm)	12.63	13.04	11.57
$r_8$ (mm)	44.26	47.79	49.82
$\alpha$ (°)	19.76	16.81	18
MAVR	0.12	0.66	0.73
NJ (mm s <sup>-3</sup> )	2.67E + 4	9.25E + 3	2.81E + 4

**Fig. 5** Evolution of the angular velocity ratio

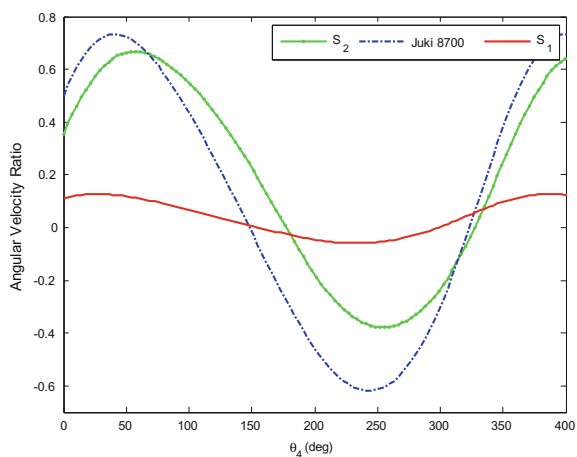


**Fig. 6** Evolution of the needle jerk

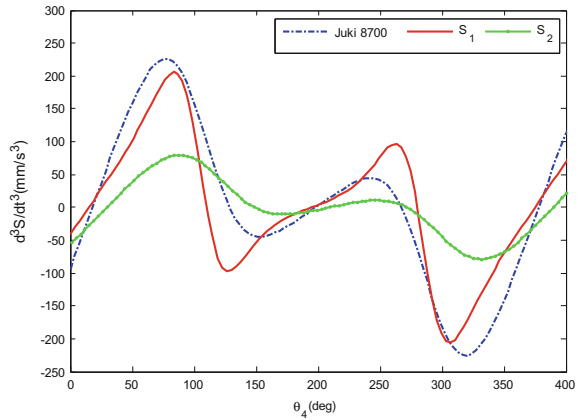


Figure 6 shows the evolution of the needle Jerk, for the extreme optimal solutions  $S_1$  and  $S_2$ , as a function of the input link angle  $\theta_4$ . We present also, in the same figure, the evolution of the needle jerk, obtained by the sewing machine Juki 8700. One can note that by using the  $S_2$  design vector, we decrease the needle jerk down by 70 % compared to the one for the Juki 8700.

## 6 Conclusion

This work deals with the multi-objective design optimization of a NBTTL mechanism used in the sewing machine. The goals are minimizing the machine vibration and its input to output torque ratio. These two criteria are ensured by minimizing the needle jerk and the maximum angular velocity ratio. The MOICA algorithm was used for this purpose. The obtained results show that the performance of optimized mechanism can reduce the MAVR and Needle Jerk by 80 and 70 % respectively, compared to Juki 8700.

## References

- Barker CR (1987) Characteristic surfaces for extreme values of angular velocity ratio in planar four-bar mechanisms. *Mech Mach Theor* :351–358
- Deb K, Pratap A, Agarwal S, Meyarivan T (2002) A fast and elitist multi-objective genetic algorithm: NSGA-II. *IEEE Trans Evol Comput* 6(2):182–197
- Ebrahimi S, Payvandy P (2015) Efficient constrained synthesis of path generating four-bar mechanisms based on the heuristic optimization algorithms. *Mech Mach Theor* 85:189–204
- Eschenbach PW, Tesar D (1971) Link length bounds on the four-bar chain. *J Manuf Sci Eng* 93:287–293

- Gotlih K, Lojen DZ, Vohar B (2007) Optimization of needle penetration velocity using the link drive mechanism in a sewing machine. *Fibres Text Eastern Euro* 15:66–71
- Matekar SB, Gogate GR (2011) Optimum synthesis of path generating four-bar mechanisms using differential evolution and a modified error function. *Mech Mach Theor* 52:158–179
- Najlawi B, Nejlaoui M, Affi Z, Romdhane L (2015) An improved imperialist competitive algorithm for multi-objective optimization. *Engineering Optimization* (to be published)
- Tanik E (2011) Transmission angle in compliant slider crank mechanism. *Mech Mach Theor* 46:493–508
- Vasiliu A, Yannou B (2001) Dimensional synthesis of planar mechanisms using neural networks: application to path generator linkage. *Mech Mach Theor* 36:299–310



# Appropriation Effects in the Estimation of Modal Damping

Mohamed Krifa, Nouredine Bouhaddi and Scott Cogan

**Abstract** Damping presents one of the most important physical aspects to model and estimate, since it plays a large role in determining the performance of a dynamic system and the amplitude of vibrations. The present study employs the modal strain energy method to estimate the modal damping associated with the localized dissipative interfaces of a global linear structure. This method is accurate in the case of proportional or classical damping model. But in the real case when modes are coupled with damping due to the localization of the dissipation, as in the case of most assembled structures, this method may present significant errors. In this paper an appropriation method is proposed and associated to the modal strain energy method in order to get a good estimation of the modal damping. The impact of appropriation on the modal damping estimation in the case of non-proportional viscous damping model is studied for a multi-degree of freedom system. Results are compared with the reference one obtained by the state space method. Simulated academic examples, where accurate estimations of the exact solutions are available, will be used to illustrate the methodology and to explore the potential difficulties that may arise in more complex industrial applications.

**Keywords** Appropriation method · Non-proportional damping · Modal strain energy method · Bolted joints · Localized dissipation

---

M. Krifa (✉) · N. Bouhaddi · S. Cogan  
Department of Applied Mechanics, FEMTO-ST Institute, University of Franche-Comté  
UBFC, 24, Rue de l'Épitaphe, 25000 Besançon, France  
e-mail: mohamed.krifa@femto-st.fr

N. Bouhaddi  
e-mail: noureddine.bouhaddi@femto-st.fr

S. Cogan  
e-mail: scott.cogan@univ-fcomte.fr

## 1 Introduction

Analytical techniques for estimating structural vibration have become increasingly sophisticated. However the estimation of damping remains difficult and uncertain, due to the variety and complexity of its physical origin. Indeed, damping can arise from many different sources, such as (Mead 1999): intrinsic damping of the structural material, coulomb friction and partial-impact energy loss at structural interfaces (Bograd et al. 2011; Caignot et al. 2010), energy lost into surrounding air, water or ground and into contained fluids; friction between the structure and mounted equipment, furnishings, payload and people, and viscous damping (Adhikari 2013; Krifa et al. 2015) between sliding and lubricated machines surfaces.

In all generality, the dissipated forces can be expressed as a non-linear function of the displacement  $y$  and the velocities  $\dot{y}$ .

$$f_d = f_d(y, \dot{y}) \quad (1)$$

For simplification reasons, in this study the damping is assumed to be linear with respect to the velocities (viscous damping) and independent of  $y$ .

The main purpose of this paper is to highlight the performance of appropriation method for the estimation of modal damping in the case of localized dissipation modeled with viscous damping model. Advantages and drawbacks of the modal strain method with and without appropriation will be presented and compared to the reference one obtained by the state space method, in order to explore the potential difficulties that may arise in more complex industrial applications.

## 2 Theoretical Background

In order to estimate the damping of structures with a multi-degree of freedom when the modes are well separated, we can use the following methods: the state space method, modal strain energy and the appropriation method. We describe here briefly these methods.

Assuming a linear and dissipative problem of assembled structures, the discrete form of the damped vibration problem may be governed by the following equation:

$$M\ddot{y}(t) + C\dot{y}(t) + Ky(t) = f(t) \quad (2)$$

where  $K$ ,  $M$  and  $C$  are respectively the stiffness, mass and damping matrices,  $y$  is the response of the system,  $f$  is the vector of the external loads. We distinguish two cases: proportional damping (Rayleigh 1896) and non-proportional damping. In both cases the frequency response of the system governed by Eq. (2) is equal to

$$y(\omega) = (K + j\omega C - \omega^2 M)^{-1} \times f \quad (3)$$

Unfortunately, the use of Eq. (3) may be computationally very expensive especially for large order systems. The assumption of proportional damping is generally used in order to resolve the system with an acceptable cost and duration by projecting on the undamped modal basis:

$$y(\omega_v) = \sum_{i=1}^n \phi_i q_i \quad (4)$$

where  $\phi_i$  and  $q_i$  are respectively the eigenmode and the modal amplitude corresponding to the  $i$ th eigenfrequency  $\omega_i$ . The contribution of all modes is taken into account using this equation. But the contribution of all these modes can contribute to a non accurate estimation of the modal damping of a specific mode as demonstrated later in the numerical simulations.

To avoid this problem, a projection of the response on a single mode of vibration is generally used, thus ensuring an accurate estimation of the modal damping, so the Eq. (4) becomes

$$y(\omega_v) = \phi_v q_v \quad (5)$$

## 2.1 Reference Method

The reference method is the state space method (Geradin and Rixen 2014). It is chosen for two main reasons: first for its accuracy in computing the modal damping, and secondly for its capacity to be used in both non-proportional (localized) and proportional damping cases. The state space equation is classically written in the following form:

$$\begin{bmatrix} C & M \\ M & 0 \end{bmatrix} \begin{bmatrix} \dot{y}(t) \\ \ddot{y}(t) \end{bmatrix} = \begin{bmatrix} -K & 0 \\ 0 & M \end{bmatrix} \begin{bmatrix} y(t) \\ \dot{y}(t) \end{bmatrix} \quad (6)$$

However, the state space method uses complex eigenvalue solutions by solving a double size system ( $2n \times 2n$ ). So, this method is time-consuming for large finite element model. And there is no physical meaning behind the use of complex variables.

The resolution of the Eq. (6) gives  $n$  complex eigenvalues  $s_v$  and  $n$  conjugate complex eigenvalues  $\bar{s}_v$ . When the modal damping factor  $\zeta_v$  verifies  $\zeta_v \ll 1$ , these eigenvalues can be expressed as follows:

$$s_v = -\zeta_v \omega_v \pm j \omega_v \sqrt{1 - \zeta_v^2} \quad (7)$$

Eigenfrequency and modal damping are deduced from the Eq. (7) by the following expressions:

$$\omega_v = \sqrt{\text{Re}^2(s_v) + \text{Im}^2(s_v)} \quad (8)$$

$$\zeta_v = -\frac{\text{Re}(s_v)}{\omega_v} \quad (9)$$

This method has been implemented in Matlab and will be considered as the reference one, as it generates “the exact” estimation of the modal damping.

## 2.2 Modal Strain Method (MSE)

The Modal Strain Energy method (MSE) was firstly suggested by Ungar and Kerwin (1962), and has been used since to address viscoelastic damping problems of sandwich structures by Johnson and Klenholz (1982). Later, a modified MSE was proposed by Dokainish (1995) in order to improve the estimation of modal damping. The advantage of the MSE method is that it allows one to compute modal damping by a real instead of a complex, eigenvalue solution. Consequently, the computational cost is greatly reduced. The objective of the modal strain energy is to determine the damping factor corresponding to each vibration mode of the structure. It is based on the concept of the dissipated energy in the interfaces for which the close form expression of the loss factor is the ratio between dissipated energy and maximal potential energy, over a cycle of periodic vibration (Krifa et al. 2015), as shown in this relation:

$$\zeta_v = \frac{1}{4\pi} \frac{E_v^{diss}}{E_v^{pot}} \quad (10)$$

where  $E_v^{diss}$  and  $E_v^{pot}$  are respectively the dissipated energy and maximal potential energy.

Dissipated energy is calculated by the following expression:

$$E_v^{diss} = \int_0^\tau \dot{y}(t)^T f_d(t) dt \quad (11)$$

where

- $\tau = \frac{2\pi}{\omega_v}$  cycle of periodic vibration of mode  $v$ .
- $f_d(t) = C\dot{y}(t)$  dissipative force

–  $\dot{y}(t) = \text{Re}(j\omega_v y(\omega_v) e^{j\omega_v t})$  velocity

The potential energy is calculated as follows:

$$E_v^{pot} = \frac{1}{2} y(\omega_v)^T K y(\omega_v) \tag{12}$$

Equation (5) supposes that only one mode, in the same time, is responsible for the vibration, and that the others neighbouring modes are not involved when a forced harmonic excitation is applied. This is of course true only if an appropriate force is applied.

### 3 Proposed Appropriation Method

The force appropriation method is widely used in the aeronautical community to perform modal testing (Ewins 1995). The specificity of force appropriation testing is its ability to identify one by one the normal modes of vibration of the associated undamped system through the cancellation of the damping forces by the excitation system (Piranda 2001).

From the Eq. (2) one can deduce the frequency expression for a given angular frequency  $\omega$ .

$$(K + j\omega C - \omega^2 M)y(\omega) = f \tag{13}$$

The appropriated force is then deduced from the Eq. (13) when the structure is oscillated at the resonance frequency  $\omega_v$ :

$$f_v = (K + j\omega_v C - \omega_v^2 M)\phi_v = j\omega_v C\phi_v \tag{14}$$

In the case of a complex structure where the physical damping matrix C is unknown, it is sufficient to apply a force proportional to the eigenmode in the following form:

$$f_v = \alpha_v \times \phi_v \text{ where } \alpha_v = cte \tag{15}$$

Later we will discuss examples to show the effectiveness of this choice of appropriation in calculating the coefficients of modal damping by modal strain energy.

### 4 Numerical Simulations

The results of an academic example consisting of a system with 8 dofs masses, springs, and dampers located (between dofs 1 and 2, 4 and 5, 7 and 8) will be presented in this part (Fig. 1). We show here the influence of extra-diagonal damping coefficients on the dynamic responses of the damped system, using the proposed method.

The natural frequencies of the undamped system are summarised in the Table 1.

In the case of localized dissipation, the modal damping estimated by modal strain energy depends on the applied excitation. In the following, we will compare the influence of the type of the external force on the estimation of the modal damping.

If one applies a non-appropriated force to the localized spring mass damper system, the MSE method may not provide a good estimation of damping for all modes. For instance, the first excitation (a) applied gives a reasonable estimation for just the first five modes about 0.25 % (Table 2a), while the two coefficients  $\xi_6$  and  $\xi_8$  are miscalculated. One can notice an error equals to 13.98 and 18.91 % respectively for modes 6 and 8, which is not acceptable.

Figure 2a shows a comparison of the coefficients of damping estimated between the reference method and the modal strain energy without force appropriation. The corresponding errors committed are given in Fig. 2b.

The errors of estimation can be explained by the importance of non-diagonal terms in the generalized damping matrix. In order to solve this problem of coupled modes by damping, one can apply an appropriated force using Eq. (14).

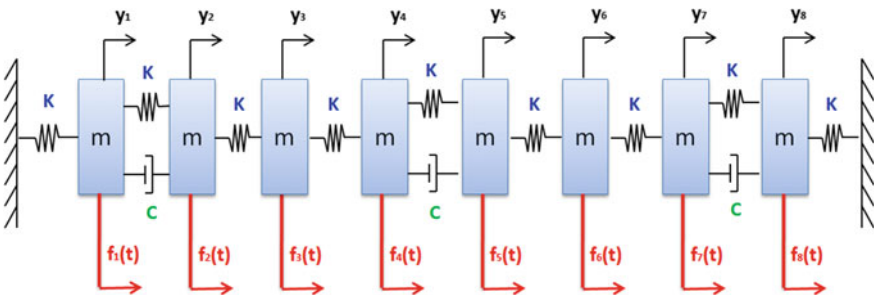


**Fig. 1** Linear array of  $n$  spring-mass oscillators,  $n = 8$ ,  $m = 10$  kg,  $k = 10^5$  N/m. Localized dampers are between 1st and 2nd, 4th and 5th, 7th and 8th masses,  $c = 50$  Ns/m

**Table 1** Eigenfrequencies of the undamped system

Mode	1	2	3	4	5	6	7	8
Eigen frequency (Hz)	5.53	10.89	15.92	20.46	24.38	27.57	29.91	31.35

**Table 2** Impact of the appropriation force on the modal damping estimation

(a) Excitation $f_v = \{10000000\}^T$								
Mode	1	2	3	4	5	6	7	8
$\xi_v$ (%)	0.29	0.57	0	1.07	1.28	2.48	1.62	1.95
<i>err</i> (%)	0.04	0.25	0	-0.04	-0.21	<b>13.98</b>	-3.12	<b>-18.91</b>
(b) Appropriated excitation $f_v = \omega_v C \phi_v$								
$\xi_v$ (%)	0.29	0.57	0	1.07	1.27	2.88	1.57	1.64
<i>err</i> (%)	-0.01	-0.06	0	0.03	-0.07	<b>0</b>	0.08	<b>0.02</b>
(c) Quasi-appropriated excitation $f_v = \alpha \phi_v$								
$\xi_v$ (%)	0.29	0.57	0	1.07	1.26	2.88	1.56	1.64
<i>err</i> (%)	-0.01	0.07	0	0.26	1.05	<b>0</b>	0.86	<b>0.17</b>

Three studied cases: (a) non appropriated force, (b) appropriated force, and (c) quasi-appropriated force

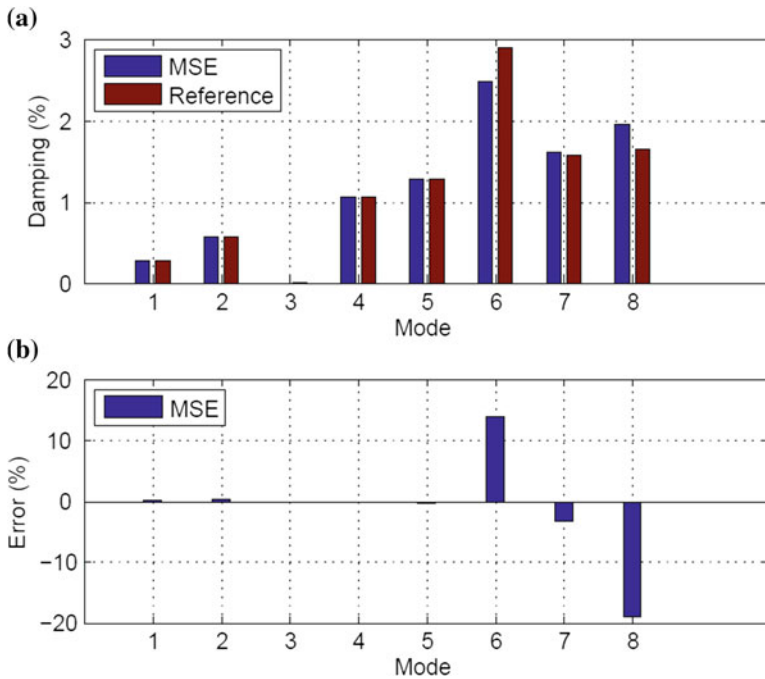


**Fig. 2** a Comparison of estimated damping coefficients. b Estimation error

Consequently, a good estimation of the modal damping by the appropriate force method is ensured.

For each eigenfrequency, the simulation with an appropriated excitation is run and the corresponding modal coefficient is obtained using the appropriate response. The advantage of this method is that appropriation guarantees the excitation of only

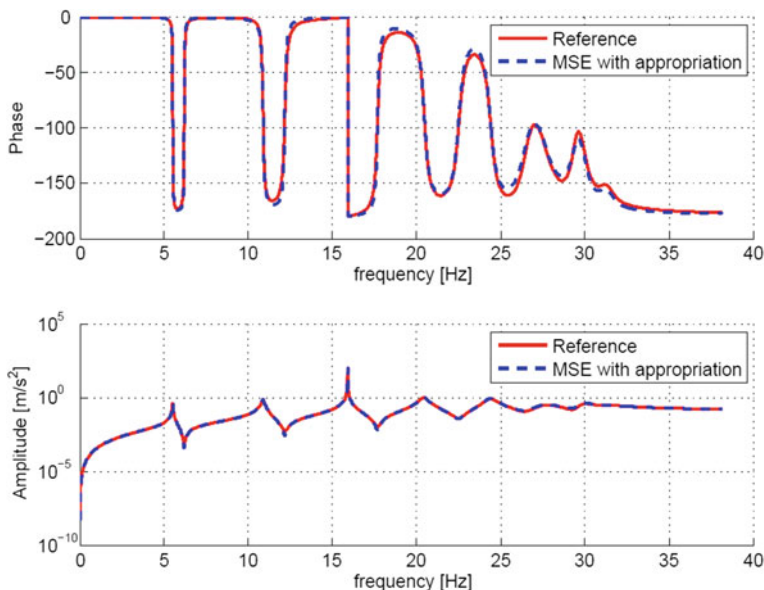


**Fig. 3** Forced response related to the non-proportional case using modal damping estimated by the proposed method

one mode at a given time, so thereafter a good estimation of the modal damping is obtained (Table 2b).

However, the drawback of the appropriation method is that the appropriated force is expressed in terms of the damping matrix  $C$  which is not necessarily known in practical problems. To overcome this difficulty it is proposed to apply a quasi-appropriate force which is proportional to the eigenvector as expressed by the Eq. (15).

As illustrated in the Table 2c, this quasi-appropriate force gives a good prediction of modal damping.

Figure 3 shows the frequency response using the modal damping estimated by the modal strain energy approach associated to the appropriation force method. The estimated FRF coincides with the reference FRF obtained using the reference state space method.

## 5 Conclusion

The modal strain energy (MSE) method has been presented to estimate the modal loss factor of structures with viscous dampers. An appropriation approach has been proposed and associated to the MSE method. This method estimates the modal loss factor of structures with respect or not to the condition of proportionality. The



results obtained by different methods (reference state space method and MSE method) are generally consistent with respect to the prediction of the modal loss factor, particularly when the structure has a proportional matrix damping. However, for a non-proportional matrix damping, both methods can give different results for certain excitations. This problem was address by using an appropriated excitation. Finally the modal strain energy associated with the appropriation method was illustrated by a 8 DOF spring-mass system with proportional and non-proportional matrix damping.

**Acknowledgments** Authors are grateful to the National Research Agency for their financial support of this project (contract ANR-12-MONU-00016-01).

## References

- Adhikari S (2013) Structural dynamic analysis with generalized damping models: analysis. Wiley
- Bograd S, Reuss P, Schmidt A, Gaul L, Mayer M (2011) Modeling the dynamics of mechanical joints. *Mech Syst Signal Process* 25(8):2801–2826
- Caignot A, Ladeveze P, Neron D, Durand J-F (2010) Virtual testing for the prediction of damping in joints. *Eng Comput* 5:621–644.15
- Dokainish MA, Mansour WM (1995) A modified MSE method for viscoelastic systems: a weighted stiffness matrix approach. *J Vib Acoust* 1001:227
- Ewins DJ (1995) Modal testing: theory and practice, vol 6. Research studies press, Letchworth
- Géradin M, Rixen DJ (2014) Mechanical vibrations: theory and application to structural dynamics. Wiley
- Johnson CD, Kienholz DA (1982) Finite element prediction of damping in structures with constrained viscoelastic layers. *AIAA J* 20(9):1284–1290
- Krifa M, Bouhaddi N, Cogan S (2015) Estimation of modal damping for structures with localized dissipation. In: Special topics in structural dynamics, vol 6. Springer International Publishing, pp 179–191
- Mead DJ (1999) Passive vibration control. Wiley
- Piranda J (2001) Analyse modale expérimentale. *Techniques de l'ingénieur* 6180:1–29
- Rayleigh JWSB (1896) The theory of sound, vol 2. Macmillan
- Ungar EE, Kerwin EM Jr (1962) Loss factors of viscoelastic systems in terms of energy concepts. *J Acoust Soc Am* 34(7):954–957

# Simulation of Resonance Phenomenon in Pipelines Caused by Water Hammer

Noura Bettaieb and Ezzeddine Haj Taieb

**Abstract** Excessive piping vibrations are a major cause of machinery downtime, leaks, fatigue failure, high noise, fires, and explosions in hydraulic plants. High vibration levels usually occur when an acoustic natural frequency of the piping system is excited by some pulsations or mechanical sources. The aim of this study is the numerical modelling and simulation of the resonance occurred in a cylindrical pipe caused by a variable rotational speed of a centrifugal pump and a linear closure of a valve. The governing equations for such flow are two coupled hyperbolic partial differential equations which are the equations of continuity and motion. MATLAB software was used in modeling the resonance along the pipeline and a comparison between different cases was done.

**Keywords** Simulation · Pipe vibration · Resonance · Centrifugal pump · Characteristic curve

## 1 Introduction

Resonance in piping systems is an undesirable phenomenon which isn't easy to prevent. It is the source of noise, fatigue, vibration, instability and in severe cases it can lead to destruction of the hydraulic system including its equipment. This phenomenon, if it is possible, should be taken into account in the phase of design and be included in the transient analysis (Tijsseling et al. 2010).

---

N. Bettaieb (✉) · E. Haj Taieb  
Research Laboratory “Applied Fluid Mechanics, Process Engineering and Environment”,  
National Engineering School of Sfax, BP 1173, 3038 Sfax, Tunisia  
e-mail: Noura\_bettaib1@hotmail.fr

E. Haj Taieb  
e-mail: Ezed.Hadj@enis.rnu.tn

From a practical standpoint, the most important problem with forced vibration in a piping system is resonance. Resonance occurs when the vibration forcing frequency is at or very close to an acoustical or mechanical natural frequency of the system (Mignosa et al. 2008). Since most structures and piping systems have very little damping, the vibration amplitude becomes very high if resonance occurs. If it occurs, it will usually be at the fundamental (i.e., first) or one of the other lower order natural frequencies.

When occurring in hydraulic pressure systems, this phenomenon can lead to very high stresses on pipelines and equipment: in the most severe cases documented in the scientific and technical literature (Wylie and Streeter 1967; Jaeger 1977), pipes collapse and significant damage to artifacts connected to them were recorded. However, the prediction of such phenomenon is less unpretentious than it seems. As a start, natural frequencies are not always based on simple formulas. Second, attention must be allocated to correctly model the excitation mechanisms as well as the mechanism that are influenced by the system response itself. And finally, damping mechanisms must be modeled properly especially with reference to beat phenomena and suppressing fluid transient.

This paper is studying a simple case of acoustic resonance occurring in a pipeline system due to the variable rotational speed of the pump.

## 2 Mathematical Model

Equations for the conservation of mass and momentum describe the transient flow in closed conduits. These equations are usually referred to as the continuity and momentum equations. Some authors call a simplified form of the latter, the equation of motion or the dynamic equation. These equations are a set of two partial differential equations since the flow velocity and pressure in transient flow are functions of time as well as distance. This equations can be adapted from the analytical model developed by Wylie et al. (1993). Applying the law of conservation of mass and momentum yields to the following equations of continuity and motion:

$$\frac{\partial H}{\partial t} + \frac{C^2}{gA} \frac{\partial Q}{\partial x} = 0 \quad (1)$$

$$\frac{\partial Q}{\partial t} + gA \frac{\partial H}{\partial x} + \frac{\lambda Q|Q|}{2DA} = 0 \quad (2)$$

where  $Q$  is the fluid discharge,  $H$  is the head,  $C$  is the pressure wave's celerity,  $\rho$  is the fluid density,  $\lambda$  is the coefficient of friction,  $A$  is the cross section area of the pipe,  $D$  is the circle pipe diameter,  $t$  is the time and  $x$  is the distance along the pipe.

### 3 Resolution by the Method of Characteristics

The method of characteristics (Fox 1977) is applied to transform the system of partial differentials Eqs. (1) and (2) into a system of ordinary differential equations that can be integrated numerically without difficulty. One gets:

$$dH \pm \frac{C}{gA} dQ + Jdx = 0 \text{ and } dx = \pm Cdt \quad (3)$$

Equation 3 determine the evolution of the head pressure and the discharge according to the time and the space. They are much appropriated to be solved numerically on a microcomputer. The obtained solution constitutes a solution to the original system of the Eqs. (1) and (2). Each pipe is subdivided into N equal reaches. If we start with known steady-state conditions at  $t = 0$ , then we will know Q and H at the N + 1 section of the pipe. If we specify the time interval  $\Delta t = \Delta x/C$ ,  $B = \frac{C}{gA}$  and  $R = \frac{\lambda \Delta x}{2gDA^2}$  the integration of Eq. (3) along the characteristic lines permits to write:

$$H_{Pi} - H_{i-1} + B(Q_{Pi} - Q_{i-1}) + RQ_{i-1}|Q_{i-1}| = 0 \quad (4)$$

$$H_{Pi} - H_{i+1} - B(Q_{Pi} - Q_{i+1}) - RQ_{i+1}|Q_{i+1}| = 0 \quad (5)$$

The calculation of the discharge and head at any section  $i$  is obtained by solving for  $H_{Pi}$  and  $Q_{Pi}$ . These equations may be written:

$$H_{Pi} = C_P - BQ_{Pi} \quad (6)$$

$$H_{Pi} = C_M + BQ_{Pi} \quad (7)$$

where:

$$C_P = H_{i-1} + BQ_{i-1} - RQ_{i-1}|Q_{i-1}| \quad (8)$$

$$C_M = H_{i+1} - BQ_{i+1} + RQ_{i+1}|Q_{i+1}| \quad (9)$$

$R$  is the resistance coefficient of the pipeline.

Eliminating  $Q_{Pi}$  from Eqs. (6) and (7) we get:

$$H_{Pi} = \frac{C_P + C_M}{2} \quad (10)$$

Then  $Q_{Pi}$  may be found directly from either Eq. (6) or (7).

### 3.1 Boundary Conditions

At either end of a single pipe only one of the compatibility Eqs. (6) or (7) is available in the two variables. For the upstream end (Fig. 1), Eq. (7) holds along the  $C^-$  characteristic, and for the downstream boundary (Fig. 1), Eq. (6) is valid along the  $C^+$  characteristic. These are linear equations in  $Q_{Pi}$  and  $H_{Pi}$ ; each conveys to its respective boundary the complete behavior and response of the fluid in the pipeline during the transient. An auxiliary equation is needed in each case that specifies  $Q_{Pi}$ ,  $H_{Pi}$ , or some relation between them.

In this paper, we consider two boundary conditions. At the upstream end; the pipe is supplied by a centrifugal pump driven by an electric motor, and, at the downstream end, the pipe is connected to a constant level reservoir with a valve upstream it.

### 3.2 Centrifugal Pump at the Upstream End

The head-discharge curve for a centrifugal pump running at a constant speed is shown in Fig. 2. This curve can be approximated by an equation (Bettaieb et al. 2015) of the form:

$$H_{P1} = C_5 + C_6 Q_{P1}^2 \tag{11}$$

Fig. 1 Boundary conditions

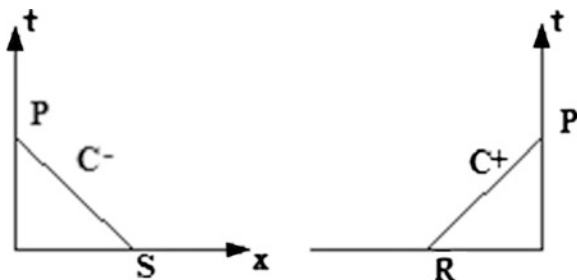
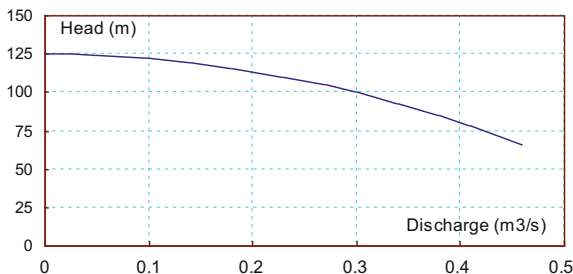


Fig. 2 Characteristic curve of a centrifugal pump



Solving this equation simultaneously with Eq. (7):

$$Q_{P1} = \frac{1}{2C6} \left[ B - \sqrt{B^2 + 4C6(C_M - C5)} \right] \quad (12)$$

Now  $H_{P1}$  can be determined from Eq. (11).

### 3.3 Valve Closure at the Downstream End

Steady-state flow through a valve can be written as

$$Q_0 = (C_d A_G)_0 \sqrt{2gH_{V0}} \quad (13)$$

in which subscript 0 indicates steady-state conditions,  $C_d$  is the coefficient of discharge,  $H_{V0}$  is the head upstream of the valve, and  $A_G$  is the area of the valve opening.

An equation similar to Eq. (13) may be written for the transient state as:

$$Q_{PN+1} = (C_d A_G) \sqrt{2gH_{PN+1}} \quad (14)$$

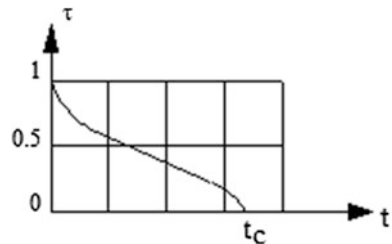
Dividing Eq. (14) by Eq. (13), taking square of both sides and defining the relative valve opening  $\tau = \frac{C_d A_G}{(C_d A_G)_0}$  (Fig. 3), one can obtain:

$$\frac{Q_{PN+1}}{Q_0} = \tau \sqrt{\frac{H_{PN+1}}{H_{V0}}} \quad (15)$$

Substitution for  $H_{PN+1}$  from the positive characteristic equation Eq. (6) into Eq. (15) yields:

$$Q_{PN+1} = -BC_V + \sqrt{(BC_V)^2 + 2C_V C_P} \quad (16)$$

**Fig. 3** Closing of a valve at downstream end



where  $C_V = (Q_0\tau)^2 / (2H_{V0})$ .

Now  $H_{P_{N+1}}$  may be determined from Eqs. (6) or (15).

### 4 Case Study

In order to understand this phenomenon, and thus to identify the causes of these malfunctions, some configurations were performed on the hydraulic system.

We consider the hydraulic installation (Fig. 4) composed of a pump driven by an electric motor. The fluid is pumped through a cylindrical pipe, with 300 m long and 0.6 m in diameter, to supply a constant level reservoir placed at the downstream end (reservoir not shown). A valve, placed at the discharge end of the pipe, permits to control the flow of the liquid entering the reservoir.

The initial flow is  $Q_0 = 0.5 \text{ m}^3/\text{s}$  which corresponds to an initial head of  $H_0 = 100 \text{ m}$ . The head of the pump at  $Q = 0 \text{ m}^3/\text{s}$  is equal to  $H_s = 125 \text{ m}$ . The head losses coefficient is  $\lambda = 0.02$  and the wave speed is  $C = 1020 \text{ m/s}$ .

Identifying the elements of Eq. (11):  $C_5 = H_s = 125 \text{ m}$ ;  $C_6 = \frac{(C_5 - H_0)}{V_0^2}$  and  $V_0 = \frac{Q_0}{\pi D^2/4}$ .

To evaluate the effect of the pump characteristic on the resonance phenomenon, the head was considered variable along the time as the rotational speed of the pump is varying in a sinusoidal way.

$$N = N_0[1 + a\sin(\omega t)] \tag{17}$$

with  $\omega = \frac{2\pi}{T}$ ,  $T = \frac{4L}{C}$ ,  $f = \frac{1}{T} = 0.85 \text{ Htz}$ ,  $a = 0.01$

To compute the variable head of the pump, the similitude equation is used:

$$\frac{H}{(N)^2} = \frac{H_0}{(N_0)^2} \tag{18}$$

Fig. 4 Hydraulic installation

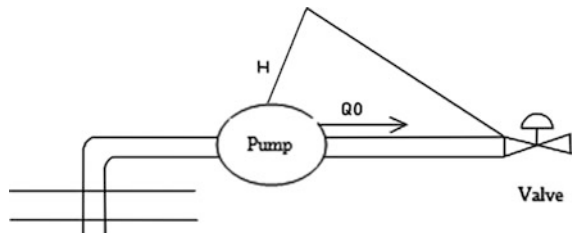
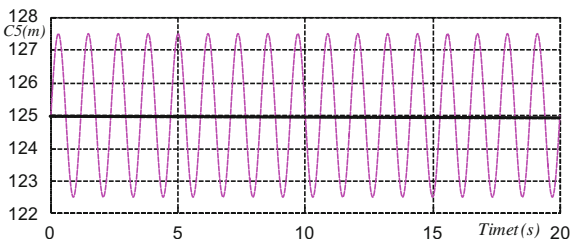


**Fig. 5** Sinusoidal variation of the head  $C_5$



So:

$$C_5 = 125 \left( \frac{N}{N_0} \right)^2 = 125 [1 + 0.01 \sin(\omega t)]^2 \quad (19)$$

The variation of  $C_5$  is illustrated in Fig. 5.

The calculation of the transient regime begins with computing the head for different intermediate nodes of the pipe in the steady state condition using the head loss formula of Darcy-Weisbach (Shames (1982)) deduced from Eq. (2):

$$\frac{dH}{dx} = - \frac{\lambda Q |Q|}{2gDA^2} \quad (20)$$

The space step  $\Delta x = L/N$  and the time step  $\Delta t = \Delta x/C$  should be firstly calculated in order to integrate the former equation,  $N$  is the number of section of the pipe.

To simulate the resonance condition for a closing valve,  $\tau$  versus  $t$  may be specified either in a tabular form or by an algebraic expression (Fig. 3).  $\tau = 1$  corresponds to the valve opening at which the flow through the valve is  $Q_0$  under a head of  $H_{V_0}$ .

$$\tau = \begin{cases} 1 - t/t_c & \text{if } t \leq t_c \\ 0 & \text{else} \end{cases} \quad (21)$$

with  $t_c$  is the time needed for the valve to close.

## 5 Numerical Results

In order to study the resonance phenomenon, a MATLAB code was developed. Firstly, the valve downstream the pipe was kept fully open. The pressure fluctuation shown in Fig. 6 are due to the sinusoidal variation of the pump's rotational speed. In this case, the resonance phenomenon do not exist in the installation.

To produce resonance in the pipe, the valve was closed linearly resulting in high pressure fluctuation.



**Fig. 6** Pressure versus time with an open valve downstream

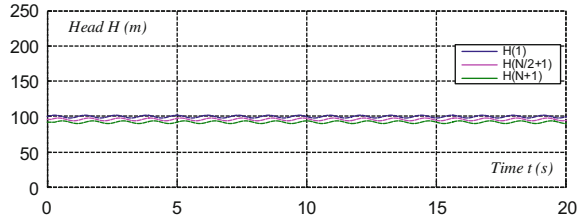


**Fig. 7** Pressure versus time at the beginning of the resonance process

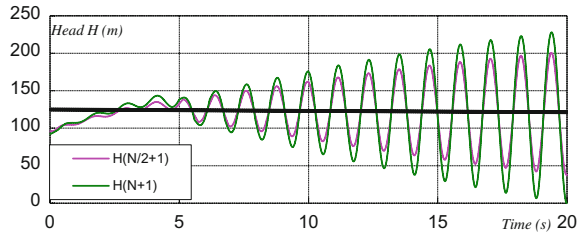
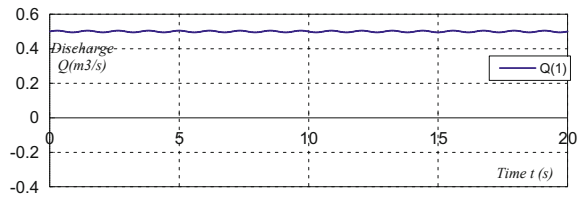


**Fig. 8** Flow versus time with an open valve downstream



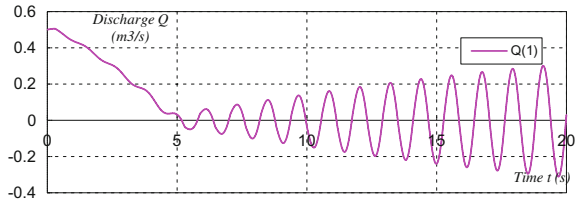
Acoustical resonance in a piping system occurs when reflected pressure pulses from a piping discontinuity (e.g., closed valve) travel back to and arrive at their source in time to join in phase with the next pulse. The resultant larger pressure pulse travels down the pipe, is reflected back again, increases in size again, and so on. The final amplitude of this reinforcement process is limited by the dynamic friction forces in the piping system.

From Fig. 7, it is obvious that the amplitude of pressure oscillations is quite remarkable: pressure grows fast reaching the maximum value of about 230 m, 15 s after the beginning of the closure. Moreover, the pressure fluctuation in the pipe is at the frequency of the pipe.

The same process was done to evaluate the flow fluctuation in both cases. Results are shown in (Fig. 8).

For the resonance case, before completely closing the valve, it is clear from Fig. 9 that the flow of the pump started decreasing gradually from  $Q_0 = 0.5 \text{ m}^3/\text{s}$  to approximately  $Q = 0.05 \text{ m}^3/\text{s}$  at the time in which the valve is completely closed. After  $t = 5 \text{ s}$ , it starts to fluctuate in a sinusoidal form reaching  $Q = 0.3 \text{ m}^3/\text{s}$ .

**Fig. 9** Flow versus time at the beginning of the resonance process



## 6 Conclusion

Piping systems are subject to vibration-induced failures. This excessive vibrations are significant risks for an organization such as piping failures, loss of containment, and machinery downtime. In this paper we have studied one of the reasons causing this dangerous problem. The resonance are likely caused by hydraulic water hammer and it has been shown in the numerical model the high amplification of the pressure head.

## References

- Bettaieb N, Hadj Taieb E (2015) Theoretical study and measurement of the characteristic curves of a centrifugal pump? In: The 6th international congress on design and modeling of mechanical systems. Hammamet, Tunisia, Mar 23–25
- Fox JA (1977) Hydraulic analysis of unsteady flow in pipe networks. The Mac Millan Press LTD., London
- Jaeger C (1977) Fluid transients. Blackie, Glasgow, London
- Mignosa P et al (2008) Analysis of a resonance phenomenon in a water supply system. In: The 10th annual water distribution systems analysis conference. Kruger National Park, South Africa, Aug 17–20
- Streeter VL, Wylie EB (1967) Hydraulic transients. McGraw-Hill Book Company, New York
- Tijsseling AS et al (2010) Acoustic resonance in a reservoir-pipeline-orifice system. In: Proceedings of the ASME 2010 pressure vessels & piping division/ K-PVP Conference. Bellevue, Washington, USA, July 18–22
- Wylie EB, Streeter VL, Suo L (1993) Fluid transients in systems. Prentice Hall, Englewood Cliffs, NJ

# Sensitivity of GFRP Composite Integrity to Machining-Induced Heat: A Numerical Approach

Ali Mkaddem, Muhammad Zain-ul-Abdein, Salah Mezlini,  
Abdullah S. Bin Mahfouz and Abdessalem Jarraya

**Abstract** This paper aims at investigating the temperature effects during abrasive milling of glass fiber reinforced plastic composites (GFRP). A 3D thermal model using volumetric heat source with Gaussian distributed cylindrical flux was developed as DFLUX subroutine and implemented into Abaqus/Standard code. The model employs linear power law for simulating the temperature variation during tool advance. The composite plate is made of glass fibers oriented perpendicular to the tool trajectory. The tool feed was simulated by the source constant motion while speed was taken variable. Four equidistant thermocouples were simulated within the medium plan of the specimen in order to record the temperature evolution. The predictions highlighted the sensitivity of temperature histories to cutting speed. The conductivity and heat capacity played for controlling heating and cooling phases of the curves. The peak temperature exhibited maximum value at TC3 irrespective to

---

A. Mkaddem (✉) · M. Zain-ul-Abdein · A.S. Bin Mahfouz · A. Jarraya  
Mechanical Engineering Department, Faculty of Engineering,  
University of Jeddah, P.O. Box 80327, 21589 Jeddah, Saudi Arabia  
e-mail: amkaddem@uj.edu.sa

M. Zain-ul-Abdein  
e-mail: mzainulabdein@gmail.com

A.S. Bin Mahfouz  
e-mail: asbinmahfouz@uj.edu.sa

A. Mkaddem  
MSMP-EA7350, Arts et Métiers ParisTech, Rue Saint Dominique,  
BP. 508, 51006 Châlons-en-Champagne, France

S. Mezlini  
LGM, École Nationale d'Ingénieurs de Monastir, Université de Monastir,  
Monastir, Tunisia  
e-mail: salah.mezlini@gmail.com

A. Jarraya  
LA2MP, National Engineering School of Sfax, University of Sfax, BP W3038 Sfax, Tunisia  
e-mail: ajarraya@uj.edu.sa

speed value. The pure thermal analysis showed sufficient ability to predict the heat affected zone in the GFRP, which is, in turn, a function of tool spindle speed.

**Keywords** FE · GFRP · Milling · Heat source · Temperature · Damage

## 1 Introduction

The exciting potentiality (low weight-to-strength ratio, good thermal resistance, high endurance, resistance to corrosion, etc.) of fibre reinforced polymers (FRP) classifies them as excellent substitute solution to metals for better energy saving in automotive, aeronautical and maritime sectors. However, their machining still remain challenging topic in spite of the wide researches have been conducted within the last decades, (e.g. Arola et al. 2002; Mkaddem et al. 2008). The material structure (disparate phases' properties, imperfect fibre-matrix adhesion, fibre abrasiveness, etc.) is commonly pointed out as the main obstacles prohibiting the good control of the material removal process MRP (Ben Soussia et al. 2014). Success of cutting operation passes necessary through a deep analysis of cutting behaviour for identifying the main factors controlling the mechanisms involved. The thermo-mechanical behaviour governing the tool-material interface is widely considered as responsible of the most physical phenomena generated throughout the cutting system (Grzesik and Nieslony 2004; Mkaddem et al. 2013; Brinksmeier et al. 2011; Tian and Zhou 2011; Liu et al. 2014a, b). Besides mechanical damage resulting in interphases' decohesion, matrix degradation etc., heat localization substantially alters the composite structures integrity. The difference in phases' properties plays to accentuate the localization phenomenon. If the matrix vitrifying temperature  $T_g$  was exceeded, heat critically localizes leading to surface burning under severe machining conditions. Up to  $T_g$ , the polymeric composites maintain their glassy state with very low elastic deformations. By this reason, a special attention must be given to keep the cutting temperature  $T_c$  within the active zone under  $T_g$  while machining (Yashiro et al. 2013). In spite of researches addressing thermo-integral response of composites (Summers 2012; Kerboua 2012; Johnson 2014), the fundamental still remain understood due to composite structure variability, and environment conditions. Obviously, accurate prediction of effective properties of composites prevents catastrophic failure of components (Mahesha 2015). Spănu and Iliescu (2008) investigated the generated heat when cylindrical milling of GFRP. The experimental set-up used technological systems equipped with IR camera for capturing temperature frames during machining. The authors outlined the significant variance of temperature versus the independent machining variables. As to Pecat et al. (2012), they studied the damage evolution in circumferential milling of unidirectional CFRP when the part

temperature ranges in  $-40$  to  $120$  °C. Liu et al. (2014a, b) developed a heat transfer model in the prospective of optimizing helical milling and to restrain damage in CFRP composites. They used the Conjugate Gradient Method to solve heat partition transferred into the CFRP workpiece. The consistency of the model was proved by comparison to experiment.

## 2 FE Model

### 2.1 B.C. and Mesh Structure

Finite element (FE) model was developed upon Abaqus/Standard commercial code in order to simulate the temperature fields. After the material removal, the GFRP plate dimensions were  $100 \times 24.8 \times 4$  mm<sup>3</sup>. Since, the heat transfer within the test specimen was to be simulated. A 3D mesh was generated using the test plate dimensions at the end of milling operation, where a total of 13,500 solid continuum brick elements (type: DC3D8) and 4500 prism elements (type: DC3D6) with linear interpolation between nodes were used. A so fine mesh discretization was adopted in the vicinity of heat source, while a gradual decrease in mesh density was maintained in the transverse direction. Figure 1 shows the test plate geometry, mesh and thermocouple locations.

The tool feed was simulated by the source motion at  $250$  mm min<sup>-1</sup> while speeds are fixed to three different values, namely, 360, 480 and 600 m min<sup>-1</sup>.

### 2.2 Heat Flux Modeling

The heat generated within the composite specimen as a result of friction between the tool and the GFRP material was imposed as volumetric heat flux. Computation of a transient temperature field in space ( $x, y, z$ ) and time ( $t$ ) requires solution of the following heat equation:

$$\frac{\partial}{\partial x} \left( \lambda \frac{\partial T}{\partial x} \right) + \frac{\partial}{\partial y} \left( \lambda \frac{\partial T}{\partial y} \right) + \frac{\partial}{\partial z} \left( \lambda \frac{\partial T}{\partial z} \right) + Q_v = \rho \cdot C_p \cdot \frac{\partial T}{\partial t} \quad (1)$$

where  $\rho$  is the density in kg m<sup>-3</sup>,  $C_p$  the specific heat capacity in J kg<sup>-1</sup> C<sup>-1</sup>,  $\lambda$  the thermal conductivity in W m<sup>-1</sup> C<sup>-1</sup>,  $T$  the temperature in °C, and  $Q_v$  the volumetric heat flux in W m<sup>-3</sup>.

In practice, heat loss in the surrounding of the plate was largely due to the convection and radiation. In addition, some heat loss occurs at the plate/fixtures interfaces. A combined heat transfer coefficient may be defined as,

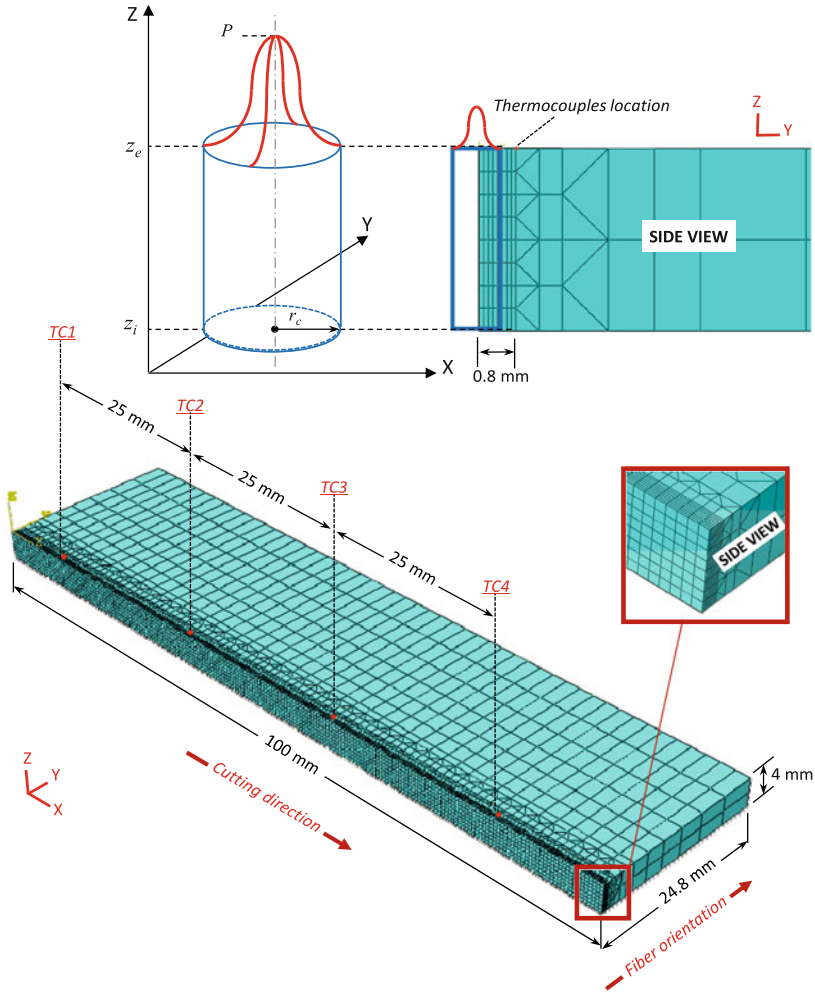


**Fig. 1** Plate geometry, dimensions and mesh

$$q = h(T - T_0) \tag{2}$$

where  $q$  is the heat loss per unit area in  $W m^{-2}$ ,  $h$  a combined heat transfer coefficient in  $W m^{-2} \text{ } ^\circ C^{-1}$ ,  $T_0$  the ambient temperature in  $^\circ C$ , and  $T$  the current temperature of the component in  $^\circ C$ . The heat transfer coefficient used in this work was  $h = 20 W m^{-2} \text{ } ^\circ C^{-1}$ , which was close to the values used in literature for free convection in air (Zain-ul-Abdein et al. 2009).

A moveable cylindrical heat source with Gaussian distribution was programmed in DFLUX subroutine to apply the volumetric heat flux ( $Q_v$ ) within the composite plate:

$$Q_v = \frac{3\eta P \cdot e^3}{\pi \cdot (e^3 - 1)} \cdot \frac{1}{r_c^2(z_e - z_i)} \cdot e^{-\frac{3r^2}{r_c^2}} \quad (3)$$

where  $Q_v$  is the heat flux in  $\text{W m}^{-1}$  and  $P$  the heat flux in  $W$ .  $z_e$  and  $z_i$  the coordinates of the top and bottom surfaces, respectively,  $r_c$  the radius of the cylinder,  $r$  the current radius as a function of Cartesian Coordinates  $x$  and  $y$ . Here, the efficiency of the process  $\eta$  was assumed to be 1. The height of the cylinder ( $z_e - z_i$ ) equals the plate thickness while  $r_c$  was set at 0.5 mm to calibrate the  $P$  values.

Note that the Gaussian distribution is more realistic than the linear distribution, since it involves an exponential decay of heat flux in the radial direction.

### 2.3 EHOM Assumption

The equivalent homogeneous orthotropic material (EHOM) assumption was considered for modeling glass/epoxy behavior with volume fractions  $V_f = 0.52$  and  $V_m = 0.48$ , respectively. Since thermal conductivity governs the temperature rate and distribution within the specimen, it is treated as orthotropic in nature. Table 1 provides the material properties used in modeling.

The thermal conductivities in the directions parallel and perpendicular to the fiber orientation were estimated using Wiener model (Wiener 1912) stating that:

$$\lambda_{\parallel} = V_f \lambda_f + (1 - V_f) \lambda_m \quad (4)$$

$$\lambda_{\perp} = \frac{\lambda_f \lambda_m}{V_f \lambda_f + (1 - V_f) \lambda_m} \quad (5)$$

where  $\lambda_{\parallel}$  and  $\lambda_{\perp}$  are the conductivities in parallel and perpendicular orientations, respectively.  $\lambda_f$  and  $\lambda_m$  are respectively the thermal conductivities of fiber and matrix in  $\text{W m}^{-1} \text{ } ^\circ\text{C}^{-1}$ . Substituting the values given in Table 1 in the Eqs. (4) and (5) leads to  $\lambda_{\perp} = \lambda_{xx} = \lambda_{zz} = 0.035 \text{ W m}^{-1} \text{ } ^\circ\text{C}^{-1}$ , and  $\lambda_{\parallel} = \lambda_{yy} = 0.11 \text{ W m}^{-1} \text{ } ^\circ\text{C}^{-1}$ .

**Table 1** Material properties used in the proposed model

Material	Property	Value	References
Glass fiber	$\rho$ ( $\text{kg m}^{-3}$ )	2600	Jeon et al. (2014)
	$C_p$ ( $\text{J kg}^{-1} \text{ } ^\circ\text{C}^{-1}$ )	840	Jeon et al. (2014)
	$\lambda_f$ ( $\text{W m}^{-1} \text{ } ^\circ\text{C}^{-1}$ )	0.02	Wang et al. (2003)
Epoxy matrix	$\rho$ ( $\text{kg m}^{-3}$ )	1250	Jeon et al. (2014)
	$C_p$ ( $\text{J kg}^{-1} \text{ } ^\circ\text{C}^{-1}$ )	1300	Aadmi et al. (2014)
	$\lambda_m$ ( $\text{W m}^{-1} \text{ } ^\circ\text{C}^{-1}$ )	0.2	Wang et al. (2003)

### 3 Results and Discussion

#### 3.1 Temperature Histories' Predictions

Consider Fig. 2a–c for a comparative analysis of temperature history predictions. It may be noticed an overall tendency for all curves presenting, in turn, heating period succeeded by a cooling period. However, some discrepancies may be outlined during heating and cooling, inter-alia, in peak values.

It is worth noting that predictions refer physically to heating and cooling phases during tool passage. For instance, the slopes at simulated heating curves at all the thermocouple locations are higher than those at cooling phase.

On the other hand, cooling curves marks higher duration to reach room temperature value and more disparity in path slope. The most probable reason for this difference is the temperature independent thermal conductivity values.

Since thermal conductivity is, in general, a function of temperature, its effect is predominant in transient analysis. However, one can outline the sensitive evolution of peak temperature with the speed.

The increase recorded in peak temperature with the speed confirms relatively that the conductivity values used for simulation were good enough to reproduce physical tendencies, and to capture the thermal behavior at thermocouple locations. In fact, an increase in speed should enhance frictional forces at interfaces which favor heat generation within the cut material. Note that at TC3, the peaks' temperatures obtained at 360 and 600  $\text{m min}^{-1}$  increase by 37 and 56 % respectively if compared with peak temperature obtained at 360  $\text{m min}^{-1}$ .

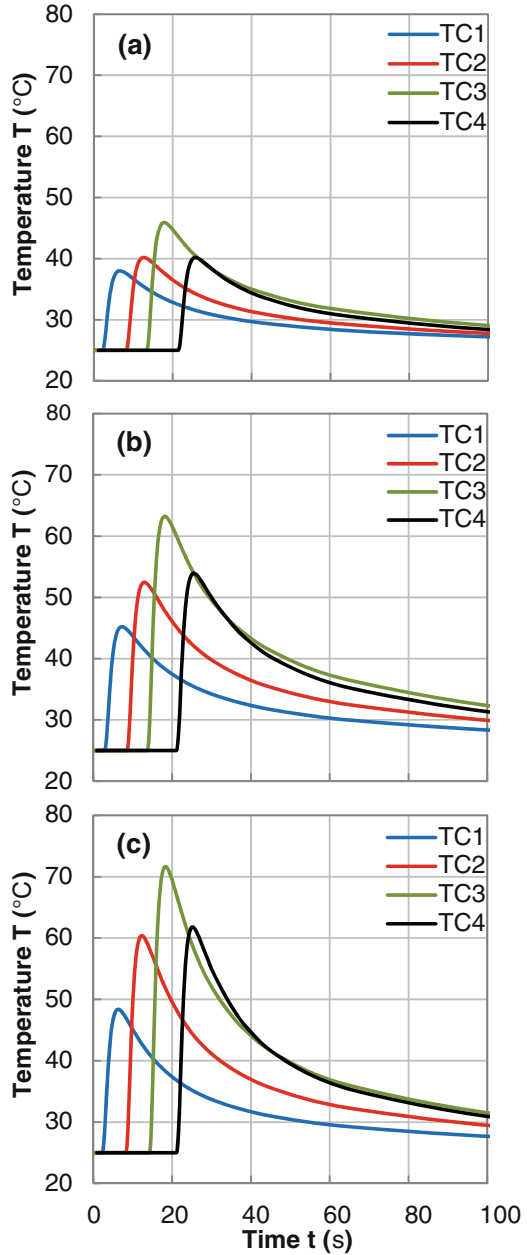
In all cases, it can be observed that TC1 records lower peak temperature than TC4 while they were both located close to the free extreme sides of the plate. It was revealed that the direction of heat source motion played its role to induce thermal inertia in front of the tool hence over-heating towards the end of the test plate. Thus, the heat loss through the left side (next to TC1) and right side (next to TC4) of the plate appears asymmetric.

#### 3.2 Heat Affected Zone (HAZ)

Figure 3a shows typical temperature contours in the test plate during the application of heat flux for the test case of 360  $\text{m min}^{-1}$  spindle speed. The temperature contours for the cases 360, and 600  $\text{m min}^{-1}$  were also identical with an only difference of peak temperature. The top and front cross-section views are shown along the cutting plane indicated as L1. Note that the temperature distribution within the thickness direction is uniform (Fig. 3b) at both the front face and cross-section because of cylindrical distribution of heat flux, whereas the contours are uneven on the top surface (Fig. 3c) because of the orthotropic conductivity values. Continuous profiles may only be observed in case of isotropic properties.



**Fig. 2** Temperature histories versus time predicted for  
**a** 360, **b** 480 and  
**c** 600 m min<sup>-1</sup>



When the cutting speed increases from 360 to 600 m min<sup>-1</sup>, the temperature at the tool-plate interface, along the plane L1, increases approximately from 173 to 378 °C.

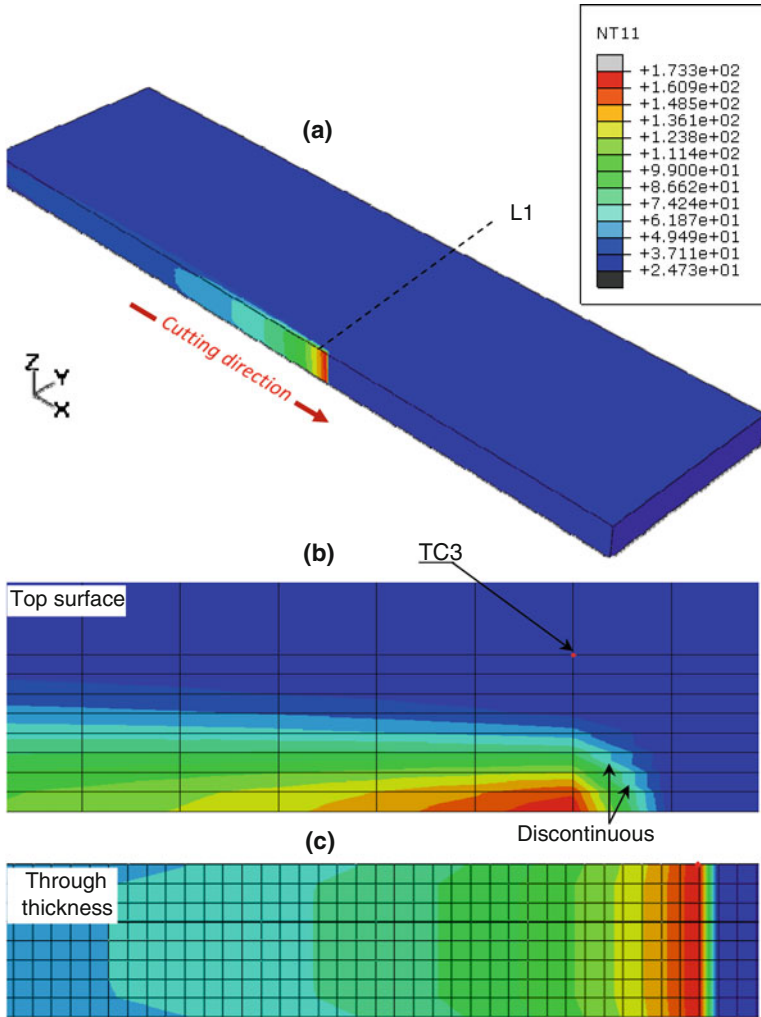


Fig. 3 Temperature contours: heat affected zone

Preliminary simulations showed that when cutting direction-to-fiber orientation varies from  $0^\circ$  to  $90^\circ$ , the temperature rises by a factor of  $2 \pm 0.1$ . This was fundamentally attributed to the ability of the composite to dissipate heat parallel and perpendicular to the fiber orientation in close correlation with the conductivity of the constituents.

Since the glass fibers are of poor thermal conductivity ( $\lambda_f = 0.02 \text{ W m}^{-1} \text{ }^\circ\text{C}^{-1}$ ), they act as thermal barriers and consequently prevent in-depth heat propagation when cutting parallel to fiber orientation. In contrast, in-depth heat propagation was

accelerated when cutting perpendicular to fiber orientation because of epoxy ‘columns’ resulting in relatively higher thermal conductivity ( $\lambda_m = 0.2 \text{ W m}^{-1} \text{ }^\circ\text{C}^{-1}$ ). In the latter case, the thermal behavior is dominated by the epoxy phase. The role of glass fibers, hence, appears to be significantly undermined by the polymeric matrix phase.

## 4 Conclusions

In this attempt, it has been established that the FE approach is reliable in predicting the behavior of GFRP composite under milling. In addition to its efficiency in correlating the temperature histories to the spindle speed, the proposed model makes it possible to characterize the HAZ as a function of input data. Referring to predictions obtained, the following conclusions can be drawn:

- Although ignorance of mechanical phenomenon which needs computationally expensive thermo-mechanical coupling to predict its behavior, a pure thermal analysis was found promising for predicting the HAZ during milling.
- It was revealed from predictions that as the milling progresses, the mechanical dissipation increases, which potentially raises the generated temperature gradually.
- FE analysis is a useful tool to quantify the temperature fields distributed within the GFRP structure. It, however, requires an experimental database to validate the numerical model. Since it is practically difficult to obtain the temperature histories over the entire specimen, interpretation of time-temperature curves is even more problematic.

## References

- Aadmi M, Karkri M, Ibos L, El Hammouti M (2014) Effective thermal conductivity of random two-phase composites. *J Reinf Plast Comp* 33:69–80
- Arola D, Sultan MB, Ramulu M (2002) Finite element modeling of edge trimming fiber reinforced plastics. *J Manuf Sci Eng-Trans ASME* 124:32–41
- Ben Soussia A, Mkaddem A, El Mansori M (2014) Rigorous treatment of dry cutting of FRP—interface consumption concept: a review. *Int J Mech Sci* 83:1–29
- Brinksmeier E, Fangmann S, Rentsch R (2011) Drilling of composites and resulting surface integrity. *CIRP Ann Manuf Technol* 60:57–60
- Grzesik W, Nieslony P (2004) Physics based modelling of interface temperatures in machining with multilayer coated tools at moderate cutting speeds. *Int J Mach Tool Manuf* 44:889–901
- Jeon J, Muliana A, La Saponara V (2014) Thermal stress and deformation analyses in fiber reinforced polymer composites undergoing heat conduction and mechanical loading. *Compos Struct* 111:31–44
- Johnson S (2014) Thermoelastic stress analysis for detecting and characterizing static damage initiation in composite lap shear joints. *Compos B* 56:740–748

- Kerboua B, Bensaid I, Addabedi E (2012) Analysis of interfacial thermal stresses for damaged structures: new theoretical model. *Compos Interfaces* 19:533–544
- Liu J, Chen G, Ji C, Qin X, Li H, Ren C (2014a) An investigation of workpiece temperature variation of helical milling for carbon fiber reinforced plastics (CFRP). *Int J Mach Tool Manuf* 86:89–103
- Liu J, Ren CZ, Qin XD, Li H (2014b) Prediction of heat transfer process in helical milling. *Int J Adv Manuf Technol* 72:693–705
- Mahesha C, Govindarajulub K, Balakrishna Murthya V (2015) Homogenization of partial debond effect on the effective thermal conductivities of FRP composite using finite element analysis. *Compos Interfaces* 22:51–65
- Mkaddem A, Demirci I, El Mansori M (2008) A micro–macro combined approach using FEM for modelling of machining of FRP composites: cutting forces analysis. *Compos Sci Technol* 68:3123–3127
- Mkaddem A, Ben Soussia A, El Mansori M (2013) Wear resistance of CVD and PVD multilayer coatings when dry cutting fiber reinforced polymers (FRP). *Wear* 302:946–954
- Pecata O, Rentsch R, Brinksmeier E (2012) Influence of milling process parameters on the surface integrity of CFRP. *Procedia CIRP* 1:466–470
- Spănu P, Iliescu M (2008) Mathematical model of temperature in milling glass fiber reinforced polymeric composites. *UPB Sci Bull (Ser B)* 70:63–72
- Summers PT, Lattimer BY, Case S, Feih S (2012) Sensitivity of thermo-structural model for composite laminates in fire. *Compos A* 43:783–792
- Tian N, Zhou A (2011) Sensitivity and uncertainty analyses for ignition of fiber-reinforced polymer panels. *Fire Mater* 1:1–20
- Wang H, Dinwiddie RB, Kenneth E, Wilkes KE (2003) Thermal conductivity measurements of fiberglass. Oak Ridge National Laboratory Report: ORNL/TM-2003/98, Owens Corning Inc
- Wiener O (1912) Die Theorie des Mischkörpers für das Feld der stationären Stromung. Erste Abhandlung die Mittelwertsätze für Kraft, Polarisation und Energie. *Abhandlungen der Mathematisch-Physischen Klasse der Königlich-Sächsischen Gesellschaft der Wissenschaften* 32:509–604
- Yashiro T, Ogawa T, Sasahara H (2013) Temperature measurement of cutting tool and machined surface layer in milling of CFRP. *Int J Mach Tool Manuf* 70:63–69
- Zain-ul-Abdein M, Nelias D, Jullien JF, Deloison D (2009) Prediction of laser beam welding-induced distortions and residual stresses by numerical simulation for aeronautic application. *J Mater Process Technol* 209:2907–2917

# A Comparative Assessment of In-Operation Modal Analysis and Frequency Domain Decomposition Algorithm Using Simulated Data

Maher Abdelghani, Morteza Ghalishooyan and Ahmad Shoostari

**Abstract** Recently a new In-Operation modal identification algorithm has been proposed by one of the authors (INOPMA). The algorithm is based on considering the correlation sequence of the outputs of the structure as an impulse response but with a certain phase shift. A numerical modal appropriation is then performed and it is shown that a mode is isolated at a certain characteristic frequency. The estimation of the modal parameters is then done in a standard way. We investigate in this paper the performance of INOPMA under realistic excitation and we compare it to the Frequency Domain Decomposition algorithm (FDD). The example is a 3DOF system under El-Centro seismic excitation. It is shown that both methods perform equally well.

**Keywords** In-operation modal identification · Modal appropriation · Modal analysis · Identification

## 1 Introduction

The algorithms estimating the dynamic parameters of structures just based on the output responses became popular as operational modal analysis (OMA) or output-only modal analysis or ambient vibration analysis or in-operation modal analysis. Primary studies about OMA were established in 1990s. Researchers, particularly civil engineering community, deeply focused on OMA techniques since

---

M. Abdelghani (✉)

Department of Mechanical Engineering, ISSAT-University of Sousse,  
Sousse, Tunisia  
e-mail: maher.abdelghani@gmail.com

M. Ghalishooyan · A. Shoostari

Department of Civil Engineering, Ferdowsi University, Mashhad, Iran  
e-mail: morteza.ghalishooyan@stu.um.ac.ir; mghalishooyan@yahoo.com

A. Shoostari

e-mail: ashoosht@um.ac.ir; Ahmadshoostari@yahoo.com

about 15 years ago. Because, mostly there is no need to artificially excite the structures which will be expensive in the case of large structures. On the other hand, applying this method doesn't interrupt the daily usage of the structures. Over the years, OMA has evolved as an autonomous discipline and have been attracting great research interest for many years. According to the domain of implementation, OMA methods can be categorized into time domain and frequency domain approaches.

For the past 20 years, different OMA procedures have been proposed by researcher. Natural excitation technique (NExT) is regarded as one of the earliest algorithms of OMA which presented in the 1990s (James et al. 1995). To identify the structural modal parameters when applying NExT, several basic system estimation time domain methods such as Least Square Complex Estimation (LSCE) (Brown et al. 1979), Ibrahim Time Domain (ITD) (Ibrahim and Mikulcik 1977), Polyreference Time Domain (PTD) (Vold and Rocklin 1982) and Eigensystem Realization Algorithm (ERA) (Juang and Pappa 1985) are utilized. Auto-Regressive Moving Average (ARMA) model was widely used for estimating the modal parameter of civil engineering structures excited by white noise (Ljung 1999). In spite of wide application of ARMA techniques in the past, high computational time and low capability of convergence decreased their popularity. In fact, stochastic subspace models were replaced ARMA models and now are regarded as robust methods in the case of OMA. Stochastic subspace identification (SSI) methods are classified as Covariance-Driven Stochastic Subspace Identification (Cov-SSI) and Data-Driven Stochastic Subspace Identification (DD-SSI) (Van Overschee and De Moor 1993).

Among the frequency domain algorithms, Basic frequency domain (BFD) or peak picking (PP) method is the first and most simple OMA method applied in modal identification of single degree of freedom structures. This technique is effective for the structures with low damping and well separated modes (Ewins 2000). Brincker et al. proposed one of the most popular OMA algorithms known as frequency domain decomposition (FDD) (Brincker et al. 2000). FDD method removes the shortcomings of the PP, but is still user friendliness. Later, Brincker et al. presented the enhanced frequency domain decomposition (EFDD) method to estimate not only modal frequencies (with higher accuracy in the comparison with FDD) and mode shapes, but also modal damping ratios (Brincker et al. 2001). Several other OMA methods also have been proposed in the literatures over the years. Least squares complex frequency (LSCF) algorithm is the implementation of the frequency-domain linear least squares estimator optimized for modal parameters estimation (Verboven 2002). Moreover, a poly-reference version of LSCF method was proposed to deal with the modal parameter estimation of closely spaced modes (Guillaume et al. 2003). More recently, system identification methods have been proposed based on the concepts of transmissibility (Devriendt and Guillaume 2007). When using transmissibility, unknown operational forces can be arbitrary (colored noise, swept sine, impact, etc.). Abdelghani and Inman proposed a numerical modal appropriation method for use with in-operation modal analysis (INOPMA) (Abdelghani and Inman 2013). The key idea about this approach is to realize that the correlation sequence of the system output is the sum of decaying sinusoids with a certain phase shift and therefore it may be considered as an impulse response. High capability of this approach has been

validated in the comparison with a subspace identification method (Abdelghani and Inman 2015). This paper aims to present a comparative assessment of INOPMA and FDD methods based on the simulated data of a 3 DoF structure subjected to the El-Centro earthquake base excitation.

## 2 The INOPMA Algorithm

The IN-Operation Modal Appropriation algorithm is based on considering the correlation sequence of the structure outputs under the hypothesis of proportional damping as a sum of decaying sinusoids and hence impulse response (Abdelghani and Inman 2015). The key idea is then to perform a numerical convolution of a set of harmonic forces with the correlation sequence and it is shown that the phase shift between the forces and the outputs is exactly zero at a specific frequency (Abdelghani and Inman 2015). The remaining steps are similar to those described in Balmès et al. (1996).

## 3 Frequency Domain Decomposition Algorithm

Frequency domain decomposition (FDD) is one of the most well-known OMA algorithms proposed by Brincker et al. (2000). FFD technique removes the shortcomings of Basic frequency domain (BFD) or peak picking (PP) method, but is still user friendliness. In fact, this method is an extension of the BFD approach concerning the modal parameters identification of closely spaced modes. In FDD algorithm, the output power spectral density (PSD) matrix is calculated and then the singular value decomposition (SVD) is used to estimate the modal parameters of the system. Since the input is proposed to be a white noise in OMA algorithms, the input power spectral density is constant and the input-output relation can be written as:

$$[G_{yy}(\omega)] \propto [H(\omega)][I][H(\omega)]^H \quad (1)$$

where  $[G_{yy}(\omega)]$  and  $[H(\omega)]$  are the output PSD matrix and the frequency response function (FRF) matrix, respectively. Superscript  $H$  denotes the Hermitian of a matrix. It is to be noted that, the concept of FDD method has already been utilized for modal parameter identification as the complex mode indicator function (CMIF) algorithm (Shih et al. 1989). In CMIF approach SVD is applied on the receptance FRF matrix of the system. While, for FFD method the PSD matrix of outputs is decomposed. At a specific frequency of  $\omega_k$  the SVD of  $[G_{yy}(\omega)]$  leads to:

$$[G_{yy}(\omega_k)] \propto [U][S][V]^H \quad (2)$$

In this equation, the matrices  $[U]$  and  $[V]$  are unitary matrices holding the singular vectors and  $[S]$  is the matrix of singular values arranged in descending orders. For the SPD matrix (which is a square Hermitian matrix) the singular vector matrices of  $[U]$  and  $[V]$  are theoretically the same. So, the SVD equation can be rewritten as:

$$[G_{yy}(\omega_k)] \propto [U][S][U]^H \quad (3)$$

Near a resonance, the singular vectors are applied as a suitable estimation of mode shapes. On the other hand, the modal frequency is obtained by the SDOF peak picking approach. At a specific frequency, the number of non-zero singular values illustrates the number of modes which are dominant in the system response. In the presence of several closely spaced modes, several singular values with significant amplitudes will appear. In this case, the corresponding mode shapes are derived based on the singular vectors of the picks of the mentioned singular values. Brincker et al. also presented the enhanced frequency domain decomposition (EFDD) method to estimate not only modal frequencies (with higher accuracy in the comparison with FDD) and mode shapes, but also modal damping ratios (Brincker et al. 2001). In this method, The PSD function at a pick of resonance is taken back to the time domain using the inverse discrete Fourier transform (IDFT). The resonance frequency is obtained by determining the zero crossing times and the damping by the logarithmic decrement of the corresponding normalized auto correlation function.

## 4 Simulated Example

In order to perform the comparative study, a 3-story 2D shear frame depicted in Fig. 1 was modeled as a 3 DoF system. This structural model was subjected to the ground acceleration of El-Centro earthquake. Story masses of  $m_1$ ,  $m_2$  and  $m_3$  are

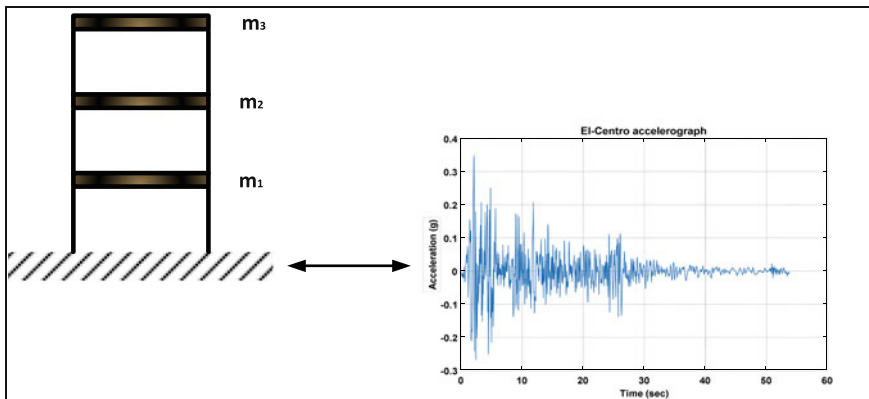


**Fig. 1** 3 DoF structure subjected to El-Centro earthquake as base excitation



**Table 1** Analysis results

Mode numbers	Exact values			FDD			INOPMA		
	Natural frequencies (Hz)	Damping ratios (%)	Mode shapes	Natural frequencies (Hz)	Damping ratios (%)	Mode shapes	Natural frequencies (Hz)	Damping ratios (%)	Mode shapes
First mode	2.11	2	0.36	2.15	1.95	0.36	2.16	1.92	0.35
			0.74			0.73			0.71
			1			1			1
Second mode	5.22	3	-0.82	5.13	2.03	-0.72	5.31	2.58	-0.73
			-0.62			-0.48			-0.57
			1			1			1
Third mode	7.49	4	2.65	7.28	2.14	2.08	7.32	3.76	2.31
			-2.32			-1.11			-2.08
			1			1			1

assumed to be 2, 2 and 1.5 kip s<sup>2</sup>/in respectively. First, second and third story stiffness are also regarded as 1800, 1400 and 1000 kips/in respectively. The damping mechanism of the structure is considered as proportional viscous damping. Damping ratio of the first and third modes are supposed to be  $\xi_1 = 2\%$  and  $\xi_3 = 4\%$  respectively. Therefore, proportional coefficients are calculated as the following.

$$[C] = \alpha[M] + \beta[K] \quad \alpha = 0.25138, \beta = 0.00159 \tag{4}$$

Damping ratio of the second mode is also derived as  $\xi_2 = 3\%$ . Linear dynamic time history analysis was performed on the structure and the time history response of each DoF has been calculated using fourth-order Runge-Kutta procedure.

Results of the comparison process are shown in Table 1. It should be mentioned that the damping ratios have been derived based on the logarithmic decrement of the corresponding normalized auto correlation function. As a consequence, suitable intervals should be chosen for correlation functions and calculating the linear regression. The mode shapes are also depicted in Fig. 2. Also, estimation error of FDD and INOPMA for mode shapes is assessed based on modal assurance criterion (MAC) which is illustrated in Fig. 3.

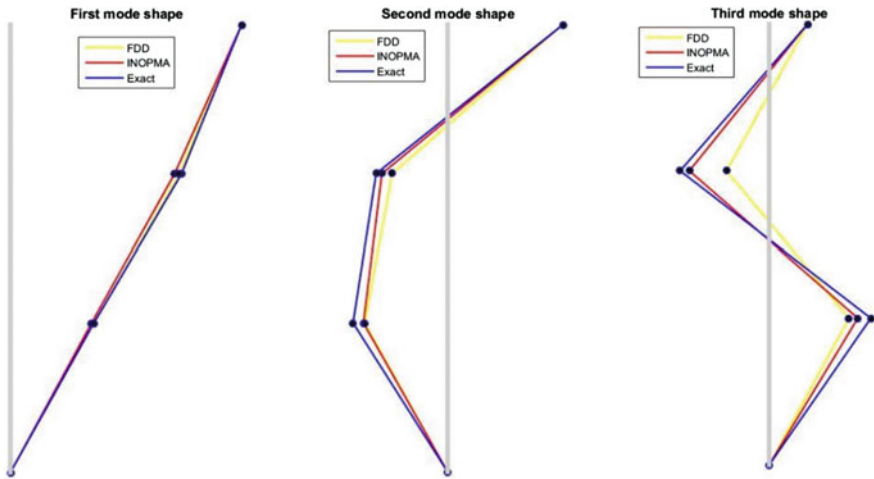


Fig. 2 Mode shapes diagram for FDD, INOPMA and exact values

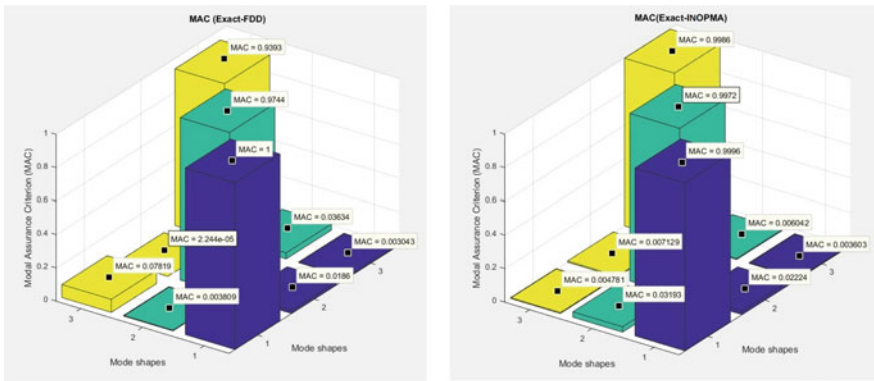


Fig. 3 MAC for mode shapes of FDD and exact (left), INOPMA and exact (right)

## 5 Conclusion

The performance of the INOPMA algorithm is investigated through its comparison with the FDD algorithm. A simulated 3DOF system under El-Centro seismic excitation is used for this study. Both algorithms perform equally well. Future work includes a statistical study for the evaluation of bias and variance of the estimated modal parameters.

## References

- Abdelghani M, Inman DJ (2013) Modal appropriation for use with in-operation modal analysis. In: Proceedings of the 5th international congress on design and modeling of mechanical systems, Djerba, Tunisia
- Abdelghani M, Inman DJ (2015) Modal appropriation for use with in-operation modal analysis. Shock Vib, ID 537030
- Balmès E, Chapelier C, Lubrina P, Fargette P (1996) An evaluation of modal testing results based on the force appropriation method. IMAC
- Brincker R, Zhang L, Andersen P (2000) Modal identification from ambient responses using frequency domain decomposition. In: Proceedings of the 18th IMAC, San Antonio, Texas
- Brincker R, Ventura C, Andersen P (2001) Damping estimation by frequency domain decomposition. In: Proceedings of the 19th IMAC, Orlando, Florida
- Brown DL, Allemang RJ, Zimmerman R, Mergey M (1979) Parameter estimation techniques for modal analysis. SAE Technical Paper, No. 790221, Warrendale, PA
- Devriendt C, Guillaume P (2007) The use of transmissibility measurements in output-only modal analysis. Mech Syst Signal Process 21:2689–2696
- Ewins DJ (2000) Modal testing, theory, practice, and application. Research Studies Pre, Baldock, Hertfordshire, England, Philadelphia, PA
- Guillaume P, Verboven P, Vanlanduit S, Van der Auweraer H, Peeters B (2003) A poly-reference implementation of the least-squares complex frequency-domain estimator. In: Proceedings of the 21st IMAC, Kissimmee, Florida
- Ibrahim SR, Mikulcik EC (1977) A method for the direct identification of vibration parameters from the free response. Shock Vib Bull 47:183–198
- James GH, Crane TG, Laufer J (1995) The natural excitation technique (NExT) for modal parameter extraction from operating structures. Int J Anal Exp Modal Anal 10:260–277
- Juang JN, Pappa RS (1985) An eigensystem realization algorithm for modal parameter identification and model reduction. J Guid Control Dyn 8:620–627
- Ljung L (1999) System identification: theory for the user. Prentice Hall, Upper Saddle River, New Jersey
- Shih CY, Tsuei YG, Allemang RJ, Brown DL (1989) Complex mode indicator function and its applications to spatial domain parameter estimation. In: Proceedings of the 7th IMAC, Las Vegas, Nevada
- Van Overschee P, De Moor B (1993) Subspace algorithms for the stochastic identification problem. Automatica 29:649–660
- Verboven P (2002) Frequency-domain system identification for modal analysis. Ph.D. thesis, Vrije Universiteit Brussels, Brussels
- Vold H, Rocklin T (1982) The numerical implementation of a multi-input modal estimation algorithm for mini-computers. In: Proceedings of the 1st IMAC, Orlando, Florida

# Experimental Investigation for Forced Vibration of Honeycomb Sandwich Beams

Souhir Zghal and Rachid Nasri

**Abstract** The present paper deals with vibration analysis of laminated sandwich beams made of Honeycomb cores. An experimental investigation of two sandwich beams made of Aluminum and Nomex cores is proposed. The vibration tests were performed for clamped-free boundary conditions using forced vibration method. A series of measurements varying excitation and response points are carried out. Experimental results have been presented leading to perform the vibration characteristics of Honeycomb sandwich beams in terms of natural frequencies, damping factors and vibration amplitudes.

**Keywords** Honeycomb · Sandwich · Beam · Forced vibration · Experimental investigation

## 1 Introduction

Sandwich materials (Berthelot 1992; Reddy 1997) have shown considerable potential in different engineering applications such as aerospace, automobile, nuclear, marine, biomedical and civil engineering. This is due to its high strength and high stiffness to weight ratio, good resistance to fatigue and corrosion phenomenon. In fact, there are attempts to replace components with classical materials (steel, concrete) by laminated materials especially sandwich materials made of Honeycomb cores. Honeycomb sandwich constructions offers, hence, the development of new materials with lightweight, high flexural stiffness and high vibration control especially with the increase of high performance industrial requirements.

---

S. Zghal (✉) · R. Nasri

Applied Mechanics and Engineering Laboratory, National School of Engineers of Tunis (ENIT), University of Tunis El Manar, BP37, 1002, Belvédère, Tunis, Tunisia  
e-mail: souhirzghal@yahoo.fr

R. Nasri

e-mail: rachid.nasri@enit.rnu.tn

Therefore, knowledge of dynamic behavior of these structures in terms of natural frequencies, damping factor and vibration amplitude is important especially when they incorporated Honeycomb cores.

Numerous studies for dynamic analysis of sandwich beams have been reported in the literature (Di Taranto 1965; Mead and Markus 1969; Mindlin and Goodman 1950; Cowper 1968; Banerjee 2001, 2004; Nilsson and Nilsson 2002; Bickford 1982; Heyliger and Reddy 1988; Marur and Kant 1996; Subramanian 2006; Damanpack and Khalili 2012; Carrera et al. 2013; Grygorowicz et al. 2015) but not much paper has reported with Honeycomb cores. In fact, Di Taranto (1965) and Mead and Markus (1969) are the earliest investigators who studied the forced vibration of sandwich beams using the classical (Euler Bernoulli) theory. Then, other researchers (Mindlin and Goodman 1950; Cowper 1968; Banerjee 2001, 2004; Nilsson and Nilsson 2002) have analyzed the vibration characteristics of sandwich beams using Timoshenko theory to take into account the effect of shear deformations. In recent years, many scientists have investigated vibration analysis of sandwich beams using High order theory. Some of these investigations can be given in the following references Bickford (1982), Heyliger and Reddy (1988), Marur and Kant (1996), Subramanian (2006), Damanpack and Khalili (2012), Carrera et al. (2013). However, all of these mentioned papers are focused in theory with analytical or numerical assessments especially that numerical implementation of these theories requires generally expensive computational costs. On other hand, this literature search shows that papers on sandwich beams with Honeycomb cores, and in particular experimental investigations on forced vibrations behavior of such structures are rather scarce.

In this paper, an experimental investigation for forced vibration of Honeycomb sandwich beams made of Aluminum and Nomex cores is proposed. This investigation is carried out in order to make a contribution towards the dynamic analysis of sandwich beams made of Honeycomb cores and to give an efficient reference which can be used to validate theoretical assessments.

## 2 Experimental Investigation

### 2.1 *Materials of Used Sandwich Beams*

The used Honeycomb (HC) sandwich panels are constituted by two elastic faces made of Aluminum and a Honeycomb core made of Aluminum alloy or aramid fibres (Nomex) materials which are folded and glued together forming a hexagonal cell structure (Fig. 1). The mechanical and geometrical characteristics of the used sandwich beams are shown in Table 1.

A static bending test taking into account the effect of shear deformations (the thickness of the specimen is relatively large) enable to determine the static stiffness  $EI_z$  and  $kGS$ . In these assessments, it is assuming that the study domain is linear



**Fig. 1** Honeycomb sandwich beams with **a** Nomex and **b** Aluminum alloy cores

**Table 1** Characteristics of the sandwich specimens: Al/Al (HC)/Al and Al/Nomex (HC)/Al

Elastic faces	Young modulus	$E_f = 70 \times 10^9 \text{ N/m}^2$
	Poisson ratio	$\nu_f = 0.3$
	Mass density	$\rho_f = 2700 \text{ kg/m}^3$
	Thickness Al (HC)	$e_{fAl} = 0.75 \text{ mm}$
	Thickness Nomex (HC)	$e_{fNm} = 0.5 \text{ mm}$
Homogeneous	Young modulus: Al (HC)	$E_{cAl} = 130 \times 10^6 \text{ N/m}^2$
	Young modulus: Nomex (HC)	$E_{cNm} = 2.5 \times 10^6 \text{ N/m}^2$
Honeycomb cores	Poisson ratio	$\nu_c = 0.33$
	Mass density: Al (HC)	$\rho_{cAl} = 573 \text{ kg/m}^3$
	Mass density: Nomex (HC)	$\rho_{cNm} = 221 \text{ kg/m}^3$
	Thickness Al (HC)	$e_{cAl} = 5 \text{ mm}$
	Thickness Nomex (HC)	$e_{cNm} = 8 \text{ mm}$
	Shear modulus: Al (HC)	$G_{cAl} = 5600 \times 10^6 \text{ N/m}^2$
	Shear modulus: Nomex (HC)	$G_{cNm} = 28 \times 10^6 \text{ N/m}^2$
Sandwich beam dimensions	Length	$L = 250 \text{ mm}$
	Width	$b = 53 \text{ mm}$

elastic with small displacements, the length of the beam is quite large compared to others dimensions (beams theory), the faces and the Honeycomb core materials are isotropic homogeneous. Furthermore, the continuity of displacements along the interfaces between the layers is considered. No slip or delamination between the layers. In fact, linear elastic domain is verified in the used load zone.

## 2.2 Experimental Descriptions

For the sake of brevity, the experimental setup is shown only for Nomex (HC) core sandwich beam which is the same methodology for Aluminum (HC) core but the

**Fig. 2** Equipment: impact hammer, sensor and spectrum analyzer



results will be shown for both investigations. The used Equipment is shown in Fig. 2. The measurement setup consists of an impact hammer, spectrum analyzer, an accelerometer for a glue montage and a force sensor. In fact, the sandwich beam, which is clamped-free, is suspended vertically to avoid the effect of static deflection. An impact hammer with rubber tip and incorporated sensor force was used to provide a harmonic excitation force. The used accelerometer is relied to the sandwich beam by glue beeswax (Fig. 3). The location of measurement points are chosen in order to describe adequately the dynamic response of the beam in the frequency band [0–200] Hz which is imposed by the bandwidth of an accelerometer for a glue montage. The beam dynamic responses were collected by a spectrum analyzer with two channels which gives the average of frequency response function (FRF) of several sandwich beams. The coherence function is checked at each test and it is close to the unity. Furthermore, the mass of the sensor is not neglected relative to the sandwich beam mass which its effect will be considered.

### 2.3 *Experimental Results*

This investigation presents a forced vibration method which consists of a series of measurement of the frequency responses functions (FRFs) of the studied sandwich beams by varying the location of the mass sensor along the length of the structure as shown in Fig. 4. The variation of excitation and response points is examined and

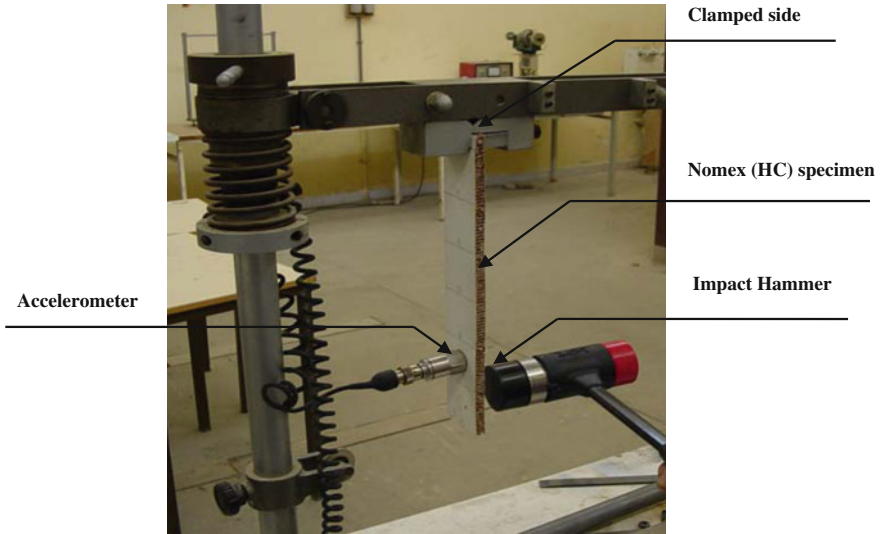


Fig. 3 Measurement setup: fixation and excitation of the sandwich beam

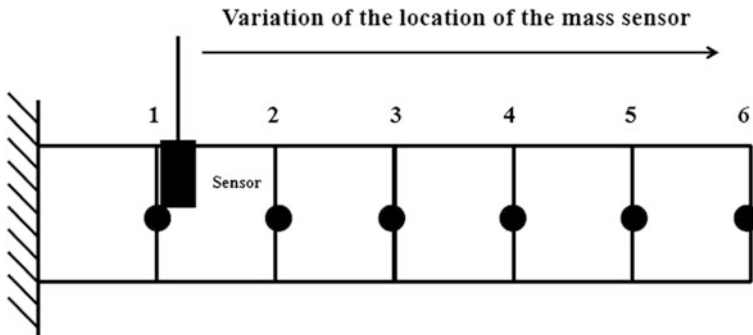


Fig. 4 Sketch of variation of the location of excitation and response points

the corresponding (FRFs) and phase responses are determined enabling hence to derive natural frequencies, damping factor and the amplitude of vibration of both Honeycomb (Al) and (Nomex) sandwich beams.

The frequency response function (FRF) of the sandwich beam is determined through the evaluation of the (acceleration/force) ratio by sweeping different excitation points (1 → 6) and various response points (1 → 6). Hence, this function is defined as follows:



$$H_{ij} = \frac{TF(\gamma_i)}{TF(F_j)} \tag{1}$$

where,

$TF(\gamma_i)$  is the FFT of the acceleration.

$TF(F_j)$  is the FFT of the excitation. With  $(i, j) = (1, \dots, 6)$

Then, the FRF amplitudes have been computed in decibels [dB] through the following expression:

$$Amplitude[dB] = 20 \log_{10}(H_{ij}) \tag{2}$$

Furthermore, the corresponding damping factor ( $\varepsilon$ ) is evaluated using the half power bandwidth method and it can be expressed as follows:

$$\varepsilon = \frac{1 \Delta f}{2 f_0} \tag{3}$$

where  $\Delta f$  represents the half power frequency bandwidth and  $f_0$  represents the natural frequency of the corresponding peak of the FRF response.

The modal characteristics of both Al and Nomex cores sandwich beams are identified from the frequency responses functions (FRFs). Hence, the identification results in terms of natural frequencies, damping factor and amplitude for various excitation and response points are shown respectively in Figs. 5, 6, 7, 8, 9 and 10 for both Al and Nomex (HC) sandwich beams.

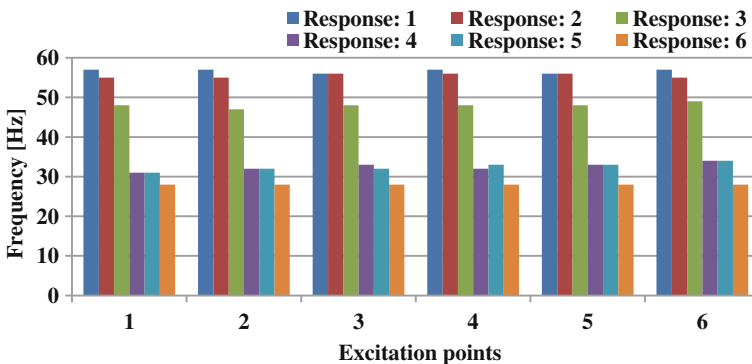


**Fig. 5** Effect of the variation of response point on natural frequencies for various excitation points (1 → 6) of the Al (HC) sandwich beam

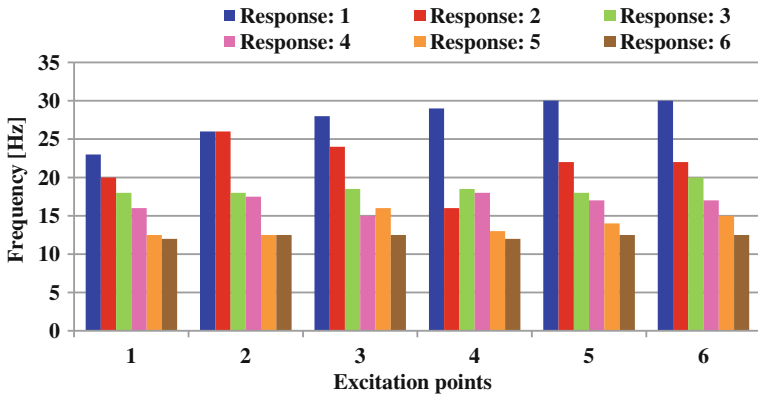


**Fig. 6** Effect of the variation of response point on natural frequencies for various excitation points (1 → 6) of the Nomex (HC) sandwich beam

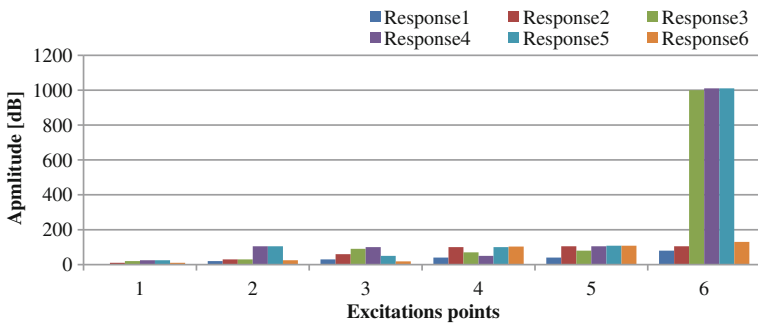


**Fig. 7** Effect of the variation of response point on amplitudes for various excitation points (1 → 6) of the Al (HC) sandwich beam

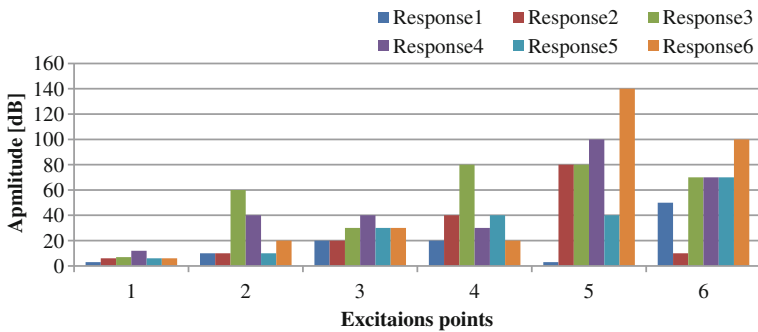


**Fig. 8** Effect of the variation of response point on amplitudes for various excitation points (1 → 6) of the Nomex (HC) sandwich beam

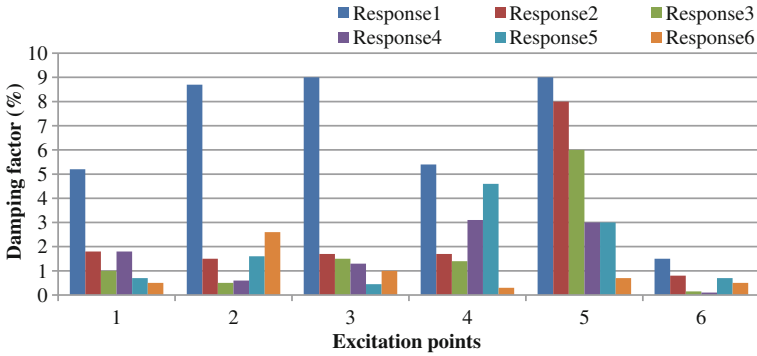


**Fig. 9** Effect of the variation of response point on damping factor in (%) for various excitation points (1 → 6) of the Al (HC) sandwich beam

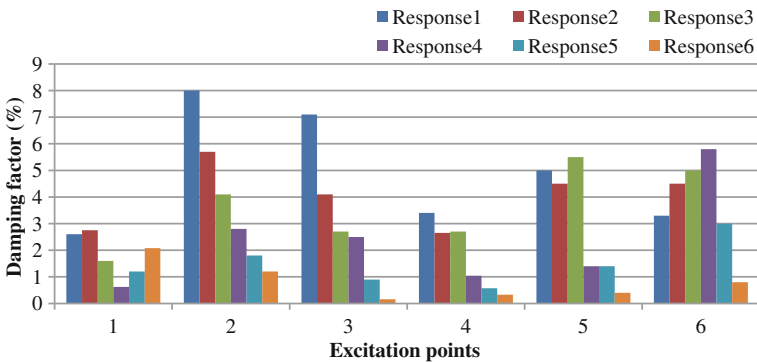


**Fig. 10** Effect of the variation of response point on damping factor in (%) for various excitation points (1 → 6) of the Nomex (HC) sandwich beam

### 3 Results and Discussion

In this section, the results of experimental investigation in terms of natural frequencies, damping factors and vibration amplitudes for the two studied sandwich beams are analyzed and discussed. In fact, Figs. 5 and 6 show the different natural frequencies of the Al and Nomex honeycomb sandwich beams obtained for various excitation points.

These frequencies correspond to the first mode of vibration derived from the plotted (FRFs) in the restricted frequency band [0–200] Hz which is imposed by the capacity of the accelerometer for glue montage. For the sake of brevity, only the (FRFs) plotted in point 1 (clamped edge) and exited in point 6 (free end) will be presented for each sandwich beam to illustrate the identification process of the vibration characteristics of these structures which is the same manner for the other points. As can be remarked from Figs. 5 and 6, the natural frequencies of the

sandwich beams decreases from the clamped edge (response in point 1) to the free edge which (response in the point 6) for each excitation point. In fact, this decrease indicates that the natural frequencies of the sandwich beams are affected by the choice of the response point due to the variation of the location of the mass sensor.

On other hand, from the same observation point, the amplitude of vibration varies in terms of excitation point as shown in Figs. 7 and 8.

For instance, the amplitude value of the sandwich beam made of Aluminum core in the observation point closer to the clamped edge (point 1) is equal to 3 dB while it reaches 80 dB in the point 6 of the free end. Moreover, this amplitude increases from 3 to 50 dB in the observation point 1 for the sandwich beam made of Nomex core. This increases in amplitude can be explained, hence, by the variation of the location of mass sensor which has a significantly effect in the free end of the (HC) sandwich beam.

Furthermore, the damping factor in (%) decreases from the clamped edge (response in point 1) to the free end (response in point 6) as illustrated in Figs. 9 and 10. This result can be explained by the dissipation of energy which its impact becomes less important in the free end. Hence, more the observation point of the response is closer to the clamped edge and the excitation point is closer to the free end, more the dynamic response of the sandwich beam is pronounced. This can be explained by three contributions: location of the mass sensor, Amplitude level and energy dissipation. In fact, for a response point chosen closer to the clamped edge, the location of the mass sensor has the lowest effect while the damping factor rise its maximum and for the excitation point chosen closer to the free end, the Amplitude of vibration has the biggest level.

For these reasons, one can choose excitation point in free end and response point in clamped edge to satisfy a good accuracy results for dynamic analysis of Honeycomb sandwich beams. The (FRFs) responses for this choice are illustrated for both sandwich beams respectively in Figs. 11 and 12.

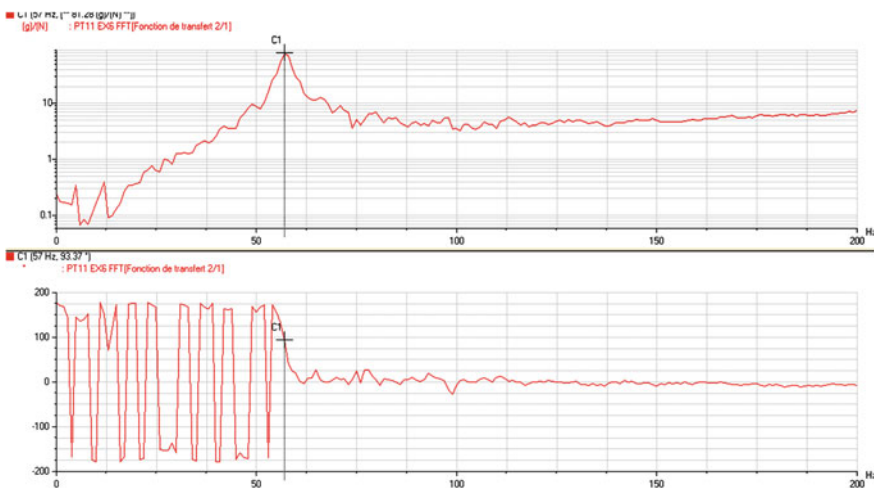


Fig. 11 FRF response of the Al (HC) sandwich beam plotted in point 1 and excited in point 6

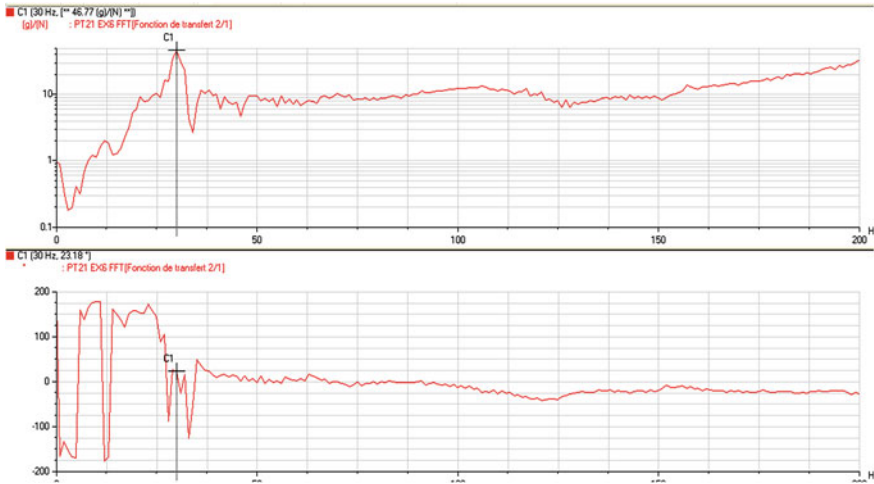


Fig. 12 FRF response of the Al (HC) sandwich beam plotted in point 1 and excited in point 6

For these reasons, one can choose excitation point in free end and response point in clamped edge to satisfy a good accuracy results for dynamic analysis of Honeycomb sandwich beams. The (FRFs) responses for this choice are illustrated for both sandwich beams respectively in Figs. 11 and 12.

## 4 Conclusions

In this paper, experimental investigation for forced vibration of two Honeycomb sandwich beams is presented. Vibration tests are carried out using various excitation and response points leading to perform natural frequencies, damping factors and vibration amplitudes. The variation of excitation and response points is examined by varying the location of the used mass sensor. This variation was shown that the dynamic behavior of such structures is very sensitive to the emplacement of the excitation and response point. In fact, more this point is adequately chosen, more the results are accurate.

On other hand, even this investigation is presented only for the first mode of vibration due to the limited capacity of the used accelerometer for a glue montage, the obtained results in terms of natural frequencies, damping factors and vibration amplitudes constitute an advantage to control the dynamic behavior of such sandwich structures.

## References

- Banerjee JR (2001) Frequency equation and mode shape formulae for composite Timoshenko beams. *Compos Struct* 51:381–388
- Banerjee JR (2004) Development of an exact dynamic stiffness matrix for free vibration analysis of a twisted Timoshenko beam. *J Sound Vib* 270:379–401
- Berthelot JM (1992) *Matériaux Composites: Comportement Mécanique et Analyse des Structures*, Paris, Masson
- Bickford WB (1982) A consistent high order beam theory. *Dev Theor Appl Mech* 11:137–142
- Carrera E, Filippi M, Zappino E (2013) Free vibration analysis of laminated beam by polynomial, trigonometric, exponential and zig-zag theories. *J Compos Mater*, 1–18. doi:[10.1177/0021998313497775](https://doi.org/10.1177/0021998313497775)
- Cowper GR (1968) On the accuracy of Timoshenko's beam theory. *Eng Mech Div* 94:1447–1453
- Damanpack AR, Khalili SRM (2012) High order free vibration analysis of sandwich beams with a flexible core using dynamic stiffness method. *Compos Struct* 94(5):1503–1514
- Di Taranto RA (1965) Theory of vibratory bending for elastic and viscoelastic layered finite length beams. *Appl Mech* 87:1–6
- Grygorowicz M, Magnucki K, Malinowski M (2015) Elastic buckling of a sandwich beam with variable mechanical properties of the core. *Thin-Walled Struct* 87:127–132
- Heyliger PR, Reddy JN (1988) A high order beam finite element for bending and vibration problems. *J Sound Vib* 126:309–326
- Marur SR, Kant T (1996) Free vibration analysis of fiber reinforced composite beams using high order theories and finite element modeling. *J Sound Vib* 194(3):337–351
- Mead DJ, Markus S (1969) The forced vibration of a three-layer damped sandwich beam with arbitrary boundary condition. *J Sound Vib* 10:63–75
- Mindlin RD, Goodman LE (1950) Beam vibration with time-dependent boundary conditions. *J Appl Mech* 72:376–379
- Nilsson E, Nilsson AC (2002) Prediction and Measurement of some dynamic properties of sandwich structures with honeycomb and foam cores. *J Sound Vib* 251(3):409–430
- Reddy JN (1997) *Mechanics of laminated composite plates: theory and analysis*, 2nd edn. Florida, New York
- Subramanian P (2006) Dynamic analysis of laminated composite beams using higher order theories and finite elements. *Compos Struct* 73:342–353

# Theoretical and Experimental Analysis of the Vibrational Behavior of a Polyester Composite Material

Idris Chenini, Charfeddine Mrad and Rachid Nasri

**Abstract** Polyester composite materials are being used increasingly in numerous and diversified activities, they are often subjected to harmful vibrations. The molding techniques of the polyester composite materials have been developing increasingly, among these techniques we name: contact molding and projection molding. This work aims to study the vibrational behavior of two polyester composite beams obtained using the two mentioned techniques. To this end, we proceed to an experimental study to determine the mechanical characteristics of the polyester composite beams, and we conduct a vibrational analysis. Besides, we proceed to a theoretical study using a polynomial field of displacement based on trigonometric series, and we apply the Hamilton's principle. The experimental results allow adjusting the analytical method used, and comparing the two molding techniques of polyester composite materials.

**Keywords** Polyester composite beams · Bending vibration · Molding techniques · Displacement fields · Natural frequencies

---

I. Chenini (✉)

ESIER, Route du Kef, km 5, 9070 Medjez Elbab, Beja, Tunisia

e-mail: chenini.idris@yahoo.fr

C. Mrad · R. Nasri

ENIT, Le Belvédère, BP 37, 1002 Tunis, Tunisia

e-mail: charfeddine.mrad@enit.rnu.tn

R. Nasri

e-mail: rachid.nasri@enit.rnu.tn

I. Chenini · C. Mrad · R. Nasri

Applied Mechanics and Engineering Research Laboratory (LMAI-ENIT-UTM-Tunisia),  
Tunis, Tunisia

## 1 Introduction

Orak (2000) studied the damping evolution of different composite specimens containing the same amount of polyester resin but with different amounts of fiber.

Thin and Quoc (2010) studied the bending vibration of laminated composite plates reinforced by polyester resin and glass fiber using the finite element method (FEM). The natural frequencies were determined experimentally and were compared to theoretical results for different boundary conditions.

Liu and Banerjee (2015a, b) combined the spline dynamic method (SDM) and the spectral method in order to analyze the vibration of orthotropic composite plates using the FEM and the frontier element method. An algorithm to solve the differential equations was proposed.

Liu and Banerjee (2015a, b) used an exact dynamic spectral rigidity method (S-DSM) to analyze the vibration of orthotropic composite plates and to demonstrate the validity of a proposed model at high and low frequencies, with different boundary conditions.

Guan et al. (2015) used the free vibration method to determine the dynamic elastic modulus of three different composite panels in real scale, and conducted bending tests on three specimens from the three panels. They found that the vibration analysis method can be used in composites fabrication and quality control.

Assae and Hasani (2015) studied the forced vibrations of composite thin cylindrical shells using the finite strip method (FSM). The results were validated using a formulation combining the classic shell bending theory with the Sonder-Koiter's displacement.

Della (2015) used the Euler-Bernoulli's theory to study the free vibration of delaminated composite beams subjected to compression loads. He proposed analytical solutions that can be generalized to study the flaring of delaminated composites.

Park and Lee (2015) studied the vibrational behavior of symmetric laminated composite plates with finite size and along the two directions. They proposed a spectral element model based on the splitting of original boundary conditions and the super spectral element method. The proposed model presents lesser calculation time relatively to the FEM. They ended by comparing their results to the published exact theories results.

Zhang et al. (2015a, b) used the Ritz's least square method (IMLS) to analyze the vibrational behavior of thick rectangular plates reinforced by carbon nanotubes, taking into account transversal shear and rotational inertia. The numerical results were validated by comparison and solutions convergence.

Zhang et al. (2015a, b) also studied the vibrational behavior of composite plates reinforced by carbon nanotubes, the plate displacement domains are determined using the Reddy's higher order shear deformation theory (HSDT). The motion equations are obtained using Hamilton's principle. The natural frequencies and the modal shapes were specified for plates of different thicknesses and simply supported at their ends.



Selim et al. (2015) analyzed the free vibration of composite plates reinforced by carbon nanotubes within a thermal environment, basing on Reddy's theory (HSDT) and using the Kp-Ritz's theory. The model numerical results were validated referring to published results.

Jafari-Talookolaei et al. (2016) analyzed the free vibration of composite curved beams taking into account transversal shear and rotational inertia, with applying the Hamilton's principle at different boundary conditions. The obtained natural frequencies and the modal shapes were validated by solutions convergence and comparison with published results.

Dey et al. (2016) presented a numerical simulation model for free vibration of composite plates which can describe high displacement ranges with few degrees of freedom, high precision is possible within low calculation time. The results were compared with published results.

Lei et al. (2016) used the Ritz's method (IMLS) to study the free vibrational behavior of thick rectangular composite plates, the formulation was conducted using the first order shear deformation theory (FSDT) at different boundary conditions and taking into account transversal shear and rotational inertia.

Wu et al. (2016) studied the nonlinear vibration of composite beams reinforced by carbon nanotubes using the Ritz's theory (IMLS). The obtained equations are solved by an iteration method. The results were compared to linear vibration results.

This work aims to study the vibrational behavior of two polyester composite beams obtained using two different techniques. An experimental study is conducted to determine the mechanical characteristics of the polyester composite beams, and their natural frequencies. In addition, an analytical study is conducted to determine the polyester composite beams natural frequencies. The experimental and theoretical results are compared, and the two molding techniques are evaluated.

## 2 Composites and Molding

The aeronautic, automobile, and naval industries are using increasingly polyester composite materials, composed of fiber layers impregnated with resin, in order to gain on mechanical resistance. The fiber layers stick together due to resin, the resin ensures adhesion but also protection from external aggressions. The resin ensures also the transmission of loads to fibers and improves their distribution across all directions. Other materials may be added to give to the composite material special properties related to: inflammability, weight, stability, conductivity, unmolding, price, color, etc.; called additives when they exceed 5 %.

Several fabrication techniques were developed, among these techniques we may cite: contact molding, projection molding, vacuum molding, resin injection (RTM), press molding, compound injection (BMC), impregnated fiber compression (SMC), thread flow molding, centrifugation molding, pultrusion molding, short fiber reinforced reactive resin injection (RRIM), long fiber reinforced reactive resin injection (SRIM). The most used techniques are: contact molding and projection molding.

## 2.1 Contact Molding

Contact molding (Lay-Up) consists on impregnating fibers with resin using a laminating tool within an open mold.

The mold is initially coated by an unmolding material and a gel-coat allowing a smoother surface to the composite material (Fig. 1).

## 2.2 Projection Molding

Projection molding (Spray-Up) consists on projecting short glass fibers and resin simultaneously within an open mold.

The mold is initially coated by an unmolding material. Impregnation is conducted later using a laminating tool (Fig. 2).

## 3 Experimental Study

Tensile and flexure tests are conducted on polyester composite beams obtained using the two different techniques: contact molding and projection molding. The same amounts of polyester resin and short fibers are used for both techniques to make the comparison possible. Particular measures are taken to avoid any accidental failure of the specimens.

The tensile tests allow studying the mechanical behavior of the polyester composite material, to identify the material characteristics to be used in the theoretical study (Table 1; Figs. 3, 4 and 5).

The polyester composite beams are then fixed on a vibratory table at one end, to study the vibrational behavior of the polyester composite material. The vibratory table is equipped with an excitation motor, a speed controller, and a frequency meter.

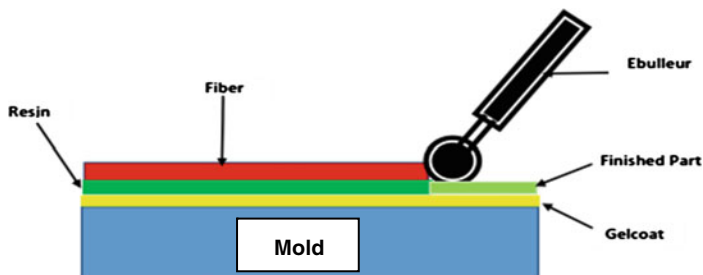


**Fig. 1** Contact molding technique

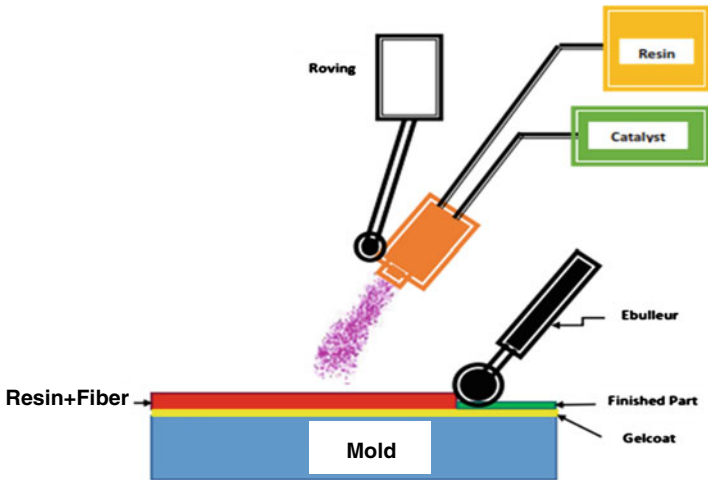


Fig. 2 Projection molding technique

Table 1 Specimens characteristics

Parameters	Contact molding	Projection molding
Density ( $\text{kg/m}^3$ )	1540	1655
Young's modulus (Pa)	$6.5 \times 10^9$	$7.6 \times 10^9$
Length (mm)	230	230
Width (mm)	20	20
Thickness (mm)	3.3	2.25
Poisson's coefficient	0.3	0.3



Fig. 3 Specimens shape

The motor frequency is increased gradually until reaching a resonance, the frequency is then noted. For the contact molding specimen, the first natural frequency is around 27 Hz, and the second natural frequency is around 150 Hz. For the projection molding specimen, the first natural frequency is around 14 Hz, and the second natural frequency is around 90 Hz (Figs. 6 and 7).

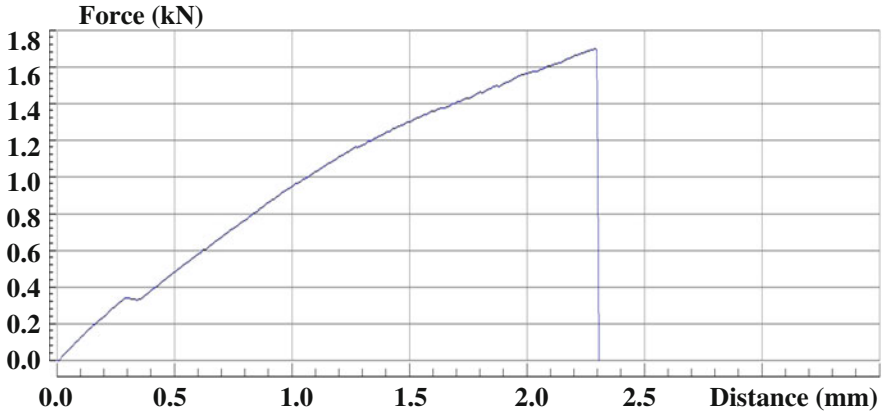


Fig. 4 Contact molding specimen tensile test

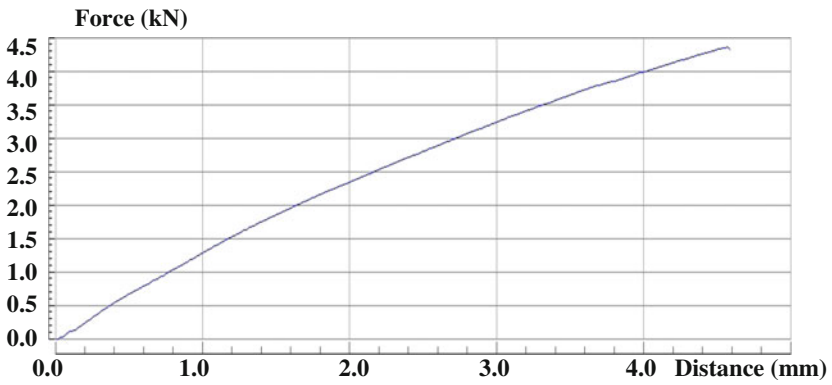


Fig. 5 Projection molding specimen tensile test

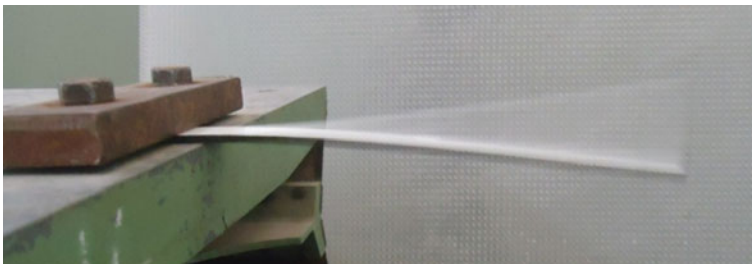


Fig. 6 Contact molding beam first modal shape

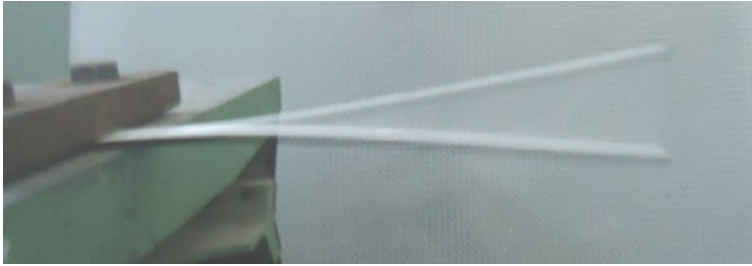


Fig. 7 Projection molding beam first modal shape

### 4 Theoretical Study

A study of the vibratory behavior of the polyester composite beams is conducted using an energetic approach. Indeed, the displacement fields, the strain fields, and the stress fields are presented, without considering shear and distortion, and the Hamilton’s principle is applied (Fig. 8).

The displacement field at a point  $M(x, z)$  is written as:

$$U (M) = \left\{ \begin{array}{l} u = u_0 - z \frac{\partial w_b}{\partial X} \\ w = w_b \end{array} \right\} \tag{1}$$

$u_0(x, t)$ : Translation displacement, X direction.

$w_b(x, t)$ : Bending displacement, XZ plane.

All variables are calculated referring to the medium plane.

The strain field, function of the displacements (1), is written as:

$$\varepsilon = \left\{ \begin{array}{l} \varepsilon_{xx} = \frac{\partial u}{\partial X} \\ \varepsilon_{zz} = \frac{\partial w}{\partial Z} \\ \varepsilon_{xz} = \frac{1}{2} \left( \frac{\partial u}{\partial Z} + \frac{\partial w}{\partial X} \right) \end{array} \right. \tag{2}$$

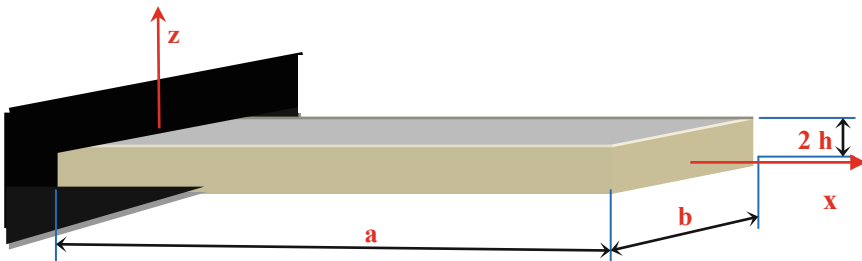


Fig. 8 Beams geometry

The strain field (2), may also be written as:

$$\varepsilon = \begin{cases} \varepsilon_{xx} = \frac{\partial u_0}{\partial X} - z \frac{\partial^2 w_b}{\partial X^2} \\ \varepsilon_{zz} = 0 \\ \varepsilon_{xz} = 0 \end{cases}$$

With  $\varepsilon_{xx} = \varepsilon^0 + z\varepsilon^1$ ; where  $\varepsilon^0 = \frac{\partial u_0}{\partial X}$  and  $\varepsilon^1 = \frac{\partial^2 w_b}{\partial X^2}$  (3)

The stress field, function of the strain field, is written as:

$$\begin{pmatrix} \sigma_{xx} \\ \sigma_{yy} \\ \sigma_{xy} \end{pmatrix} = \begin{bmatrix} \frac{E}{1-\nu^2} & \frac{\nu E}{1-\nu^2} & 0 \\ \frac{\nu E}{1-\nu^2} & \frac{E}{1-\nu^2} & 0 \\ 0 & 0 & G \end{bmatrix} \begin{pmatrix} \varepsilon_{xx} \\ \varepsilon_{yy} \\ \varepsilon_{xy} \end{pmatrix} \quad (4)$$

E Young’s modulus.

G Coulomb’s modulus.

$\nu$  Poisson’s Coefficient.

The Hamilton’s principle is written as:

$$\int_0^t \delta(T - U)dt = 0 \quad (5)$$

T is the kinetic energy:  $T = \frac{1}{2} \int_V \rho(\dot{u}^2 + \dot{w}^2)dV$ .

U is the potential energy:  $U = \frac{1}{2} \int_V (\sigma_{xx}\varepsilon_{xx} + \sigma_{zz}\varepsilon_{zz} + \sigma_{xz}\varepsilon_{xz})dV$ .

With  $\dot{u}$  and  $\dot{w}$  are the derivatees relatively to time of respectively u and w.

Using  $\varepsilon_{zz} = \varepsilon_{xz} = 0$ , the motion equation, using (3), (4), and (5), is written as:

$$\int_0^t \int_V \left[ \sigma_{xx} \left( \frac{\partial \delta u_0}{\partial X} - z \frac{\partial^2 \delta w_b}{\partial X^2} \right) - \rho \left\{ \left( \frac{\partial^2 u_0}{\partial t^2} - z \frac{\partial^3 w_b}{\partial X \partial t^2} \right) \delta u_0 + \left( \frac{\partial^2 w_b}{\partial t^2} - z \frac{\partial^3 u_0}{\partial X \partial t^2} + z^2 \frac{\partial^4 w_b}{\partial X^2 \partial t^2} \right) \delta w_b \right\} \right] dV dt = 0 \quad (6)$$

The forces, moments, and inertia moments are respectively defined as:

$$(N, M) = \int_{-h}^h \sigma_{xx}(1, z)dz \quad (I_0, I_1, I_2) = \int_{-h}^h \rho(1, z, z^2)dz. \quad (7)$$

**Table 2** First three natural frequencies

	$f_1$ (Hz)	$f_2$ (Hz)	$f_3$ (Hz)
Contact molding	23	165	347
Projection molding	15	104	285

Using Eqs. (6) and (7), and integrating part by part, the following system is obtained:

$$\begin{cases} \frac{\partial N}{\partial X} - I_0 \frac{\partial^2 u_0}{\partial t^2} + I_1 \frac{\partial^3 w_b}{\partial X \partial t^2} = 0 \\ -\frac{\partial^2 M}{\partial X^2} - I_0 \frac{\partial^2 w_b}{\partial t^2} + I_1 \frac{\partial^3 u_0}{\partial X \partial t^2} - I_2 \frac{\partial^4 w_b}{\partial X^2 \partial t^2} = 0 \end{cases} \tag{8}$$

The rigidity constants are defined as follows:

$$\begin{aligned} (A_{11}, A_{12}, A_{13}, A_{14}) &= \int_{-h}^h \frac{E}{1 - \nu^2} (1, z, z^3, z^5) dz \\ (B_{11}, B_{12}, B_{13}) &= \int_{-h}^h \frac{E}{1 - \nu^2} (z^2, z^4, z^6) dz. \end{aligned} \tag{9}$$

The system of Eqs. (8) becomes, using (9) and (10):

$$\begin{cases} A_{11} \frac{\partial^2 u_0}{\partial x^2} - A_{12} \frac{\partial^3 w_b}{\partial x^3} - I_0 \frac{\partial^2 u_0}{\partial t^2} + I_1 \frac{\partial^3 w_b}{\partial x \partial t^2} = 0 \\ -A_{12} \frac{\partial^3 u_0}{\partial x^3} + B_{11} \frac{\partial^4 w_b}{\partial x^4} - I_0 \frac{\partial^2 w_b}{\partial t^2} + I_1 \frac{\partial^3 u_0}{\partial x \partial t^2} - I_2 \frac{\partial^4 w_b}{\partial x^2 \partial t^2} = 0 \end{cases} \tag{10}$$

The system resolution gives the following frequencies, when:

$u_0(x, t)$ : Trigonometric series-polynomial, verifying the boundary conditions (Table 2).

$w_b(x, t)$ : Trigonometric series-polynomial, verifying the boundary conditions.

## 5 Comparison

The contact molding beam natural frequencies are neatly higher than the projection molding beam natural frequencies, the contact molding gives harder composite material. The projection molding gives thus softer composite material which is good not only for dynamic loads but also for static loads.

The experimental natural frequencies are slightly higher than the theoretical natural frequencies, the absolute error is around 10 %. This confirms the advanced theoretical development, and is probably due to the thickness irregularity of the specimens.

## 6 Conclusion

The molding techniques of the polyester composite materials have been developing increasingly, among these techniques we may name: contact molding and projection molding.

This work aimed to study the vibrational behavior of two polyester composite beams obtained using two different techniques: contact molding and projection molding. An experimental study was conducted to determine the mechanical characteristics of the polyester composite beams, and their natural frequencies. In addition, an analytical study was conducted to determine the polyester composite beams natural frequencies. The experimental and theoretical results were compared, and the two molding techniques were evaluated.

The experimental results are compatible with the theoretical results and the projection molding gives more tensile and flexure resistance to the composite material relatively to contact molding.

**Acknowledgments** The authors gratefully acknowledge the helpful comments of the reviewers, which have improved the presentation.

## References

- Assae H, Hasani H (2015) Forced vibration analysis of composite cylindrical shells using spline finite strip method. *Thin-Walled Struct* 97:207–214
- Della CN (2015) Free vibration analysis of composite beams with overlapping delaminations under axial compressive loading. *Compos Struct* 133:1168–1176
- Dey P, Haldar S, Sengupta D, Sheikh AH (2016) An efficient plate element for the vibration of composite plates. *Appl Math Modell* 40:5589–5604
- Guan C, Zhang H, Zhou L, Wang X (2015) Dynamic determination of modulus of elasticity of full-size wood composite panels using a vibration method. *Constr Build Mater* 100:201–206
- Jafari-Talookolaei RA, Abedi M, Hajianmaleki M (2016) Vibration characteristics of generally laminated composite curved beams with single through-the-width delamination. *Compos Struct* 138:172–183
- Lei ZX, Zhang LW, Liew KM (2016) Vibration of FG-CNT reinforced composite thick quadrilateral plates resting on Pasternak foundations. *Eng Anal Bound Elem* 64:1–11
- Liu X, Banerjee JR (2015a) An exact spectral-dynamic stiffness method for free flexural vibration analysis of orthotropic composite plate assemblies—Part I: theory. *Compos Struct* 132:1274–1287
- Liu X, Banerjee JR (2015b) An exact spectral-dynamic stiffness method for free flexural vibration analysis of orthotropic composite plate assemblies—Part II: applications. *Compos Struct* 132:1288–1302
- Orak S (2000) Investigation of vibration damping on polymer concrete with polyester resin. *Cem Concr Res* 30(2):171–174
- Park I, Lee U (2015) Spectral element modeling and analysis of the transverse vibration of a laminated composite plate. *Compos Struct* 134:905–917
- Selim BA, Zhang LW, Liew KM (2015) Vibration analysis of CNT reinforced functionally graded composite plates in a thermal environment based on Reddy's higher-order shear deformation theory. In: *Composite structures*



- Thinh TI, Quoc TH (2010) Finite element modeling and experimental study on bending and vibration of laminated stiffened glass fiber/polyester composite plates. *Comput Mater Sci* 49 (4):S383–S389
- Wu HL, Yang J, Kitipornchai S (2016) Nonlinear vibration of functionally graded carbon nanotube-reinforced composite beams with geometric imperfections. *Compos B Eng* 90:86–96
- Zhang LW, Cui WC, Liew KM (2015a) Vibration analysis of functionally graded carbon nanotube reinforced composite thick plates with elastically restrained edges. *Int J Mech Sci* 103:9–21
- Zhang LW, Song ZG, Liew KM (2015b) State-space Levy method for vibration analysis of FG-CNT composite plates subjected to in-plane loads based on higher-order shear deformation theory. *Compos Struct* 134:989–1003

# Robust Multi-objective Collaborative Optimization of Complex Structures

H. Chagraoui, M. Soula and M. Guedri

**Abstract** This paper presents a new approach aims to solve robust multidisciplinary design optimization MDO problem called Improved Multi-objective Robust Collaborative Optimization. This method combines the Multi-objective Robust Collaborative Optimization method, the Worst Possible Point constraint cuts and the Genetic algorithm NSGA-II type as an optimizer to solve the robust optimization problem of complex structure named Y-stiffened panel under interval uncertainty. The proposed approach hierarchically decomposes the optimization problem into a structure level considered as an upper level in the Y-stiffened panel and a second level considered as a lower level of the studied panel. A robust multi-objective optimization problem intended to optimize the eigenfrequency, the global mass and the displacement at a fixed point of the Y-stiffened panel at the first level and each structure's robust optimization problem allows optimizing its eigenfrequency and mass limited by their local constraint functions at the second one. To demonstrate our method, an engineering example of Y-stiffened panel is treated. A good performance of proposed method is proved by a comparison between obtained results and Non-Distributed Multi-objective Robust Optimization.

---

H. Chagraoui (✉) · M. Guedri

Research Unit in Structural Dynamics, Modeling and Engineering of Multi-physics Systems,  
Preparatory Engineering Institute of Nabeul (IPEIN), 8000 M<sup>r</sup>ezgua, Nabeul, Tunisia  
e-mail: hmdchagraoui@gmail.com

M. Guedri

e-mail: mohamed.guedri@isetn.rnu.tn

M. Soula

Laboratory of Applied Mechanics and Engineering, ENIT, High Institute of Sciences  
and Techniques of Tunis (ENSIT), Tunis University, Tunis, Tunisia  
e-mail: Soulamed2003@Yahoo.fr

M. Guedri

College of Technology at Makkah, Technical and Vocational Training Corporation,  
Makkah, Kingdom of Saudi Arabia

**Keywords** Multidisciplinary design optimization (MDO) · Improved multi objective robust collaborative optimization (IMORCO) · Non-distributed multi-objective robust optimization (NDMORO) · Interval uncertainty

## 1 Introduction

In multi-objective optimization problems of complex structures, generally speaking, there are design variables with uncontrollable variations due to noise or uncertainty. These variations might have significant effects on the performance of optimum solutions and can change their feasibility. The complex structures designed with a deterministic approach can deteriorate the performance of an optimum solution and may lead to complex structures failure. Therefore, in order to conceive complex structures optimally and with minimal sensitivity (robust) to uncertainty, we used the robustness criteria in the optimization framework.

Just as the non-distributed design optimization approach, MDO methods can be subject to uncertainty affecting the input parameters. In this context, the robustness measure is unavoidable in MDO framework. Recent work has led to the development of an approach with interval uncertainty in Multi-objective collaborative Optimization framework. For example, (Li and Azarm 2008) presented a Multi-objective collaborative Robust Optimization that uses an interdisciplinary uncertainty propagation method for decentralized MDO problems under interval uncertainty. Weiwei et al. (2013) developed a new Approximation Assisted Multi-objective collaborative Robust Optimization New AA-McRO under interval uncertainty for MDO.

In this study, the presented IMORCO method to find the robust solutions of complex structures with design parameter uncertainty within substructures and coupling variables. Our suggested IMORCO approach uses a sequential optimization technique where each level of optimization resolved in two steps: (i) a deterministic multi objective problem, and (ii) a robustness assessment. This approach uses a coordinator between the complex structures level optimizer and the complex substructures level optimizer whose function is to minimize the difference between the shared and the coupling variables transferred from different substructure in order to avoid conflict during the optimization. In addition, the coordinator helps the designer to choose the optimal value of design variables obtained from each substructure level optimizer. These values then sent to the structure level optimizer.

The organization of the remainder of this paper is as follows: The Non-Distributed Multi-objective Optimization (NDMO) problem presented in Sect. 2. In Sect. 3 a description of the suggested methodology is presented. Section 4 considers an engineering example of this new strategy. The paper concludes with a summary in Sect. 5.

## 2 Non-distributed Multi-objective Optimization (NDMO)

The multi-objective optimization problem in Eq. (1) relates the behavior of a structure with two substructures resolved following the NDMO approach.

$$\begin{aligned}
 & \min_{\mathbf{x}_{sh}, \mathbf{x}_2} f_1(\mathbf{x}_{sh}, \mathbf{p}_{sh}, \mathbf{x}_1, \mathbf{p}_2, \mathbf{y}_{21}) \\
 & \min_{\mathbf{x}_{sh}, \mathbf{x}_2} f_2(\mathbf{x}_{sh}, \mathbf{p}_{sh}, \mathbf{x}_2, \mathbf{p}_2, \mathbf{y}_{12}) \\
 & s.t \quad g_1(\mathbf{x}_{sh}, \mathbf{p}_{sh}, \mathbf{x}_1, \mathbf{p}_1, \mathbf{y}_{12}) \leq 0 \\
 & \quad \quad g_2(\mathbf{x}_{sh}, \mathbf{p}_{sh}, \mathbf{x}_2, \mathbf{p}_2, \mathbf{y}_{21}) \leq 0 \\
 & \text{with} \\
 & \mathbf{y}_{12} = Y_1(\mathbf{x}_{sh}, \mathbf{p}_{sh}, \mathbf{x}_1, \mathbf{p}_1, \mathbf{y}_{21}); \mathbf{y}_{21} = Y_2(\mathbf{x}_{sh}, \mathbf{p}_{sh}, \mathbf{x}_2, \mathbf{p}_2, \mathbf{y}_{12}) \\
 & \mathbf{X} \equiv [\mathbf{x}_{sh}, \mathbf{x}_1, \mathbf{x}_2]; \mathbf{P} \equiv [\mathbf{p}_{sh}, \mathbf{p}_1, \mathbf{p}_2]; \mathbf{X} \in [\mathbf{X}^{\min}, \mathbf{X}^{\max}]; \mathbf{P} \in [\mathbf{P}^{\min}, \mathbf{P}^{\max}]
 \end{aligned} \tag{1}$$

In Eq. (1) the write  $\mathbf{x}_{sh}$  and  $\mathbf{p}_{sh}$  represent a vector of shared variables and uncontrolled parameters between two substructures, respectively.  $\mathbf{p}_1$  and  $\mathbf{p}_2$  describe the substructure uncontrolled parameters, with the superscript ‘1’ and ‘2’ referring to substructure 1 and substructure 2, respectively.  $Y_1$  and  $Y_2$  represent the functions used to compute the substructure 1  $\mathbf{y}_{12}$  and substructure 2  $\mathbf{y}_{21}$  coupling variables, respectively. In this optimization problem, each substructure has its associated input design variables ( $\mathbf{x}_1, \mathbf{x}_2$ ), and substructure objectives functions ( $f_1, f_2$ ) and constraints ( $g_1, g_2$ ). The overall objective functions and constraints of the complex structure are represented by  $f_s$  and  $g_s$ . In order to assess the performance of each substructure individually, we use the proposed IMORCO approach for decomposing the NDMO problem of the complex structure in Eq. (1) into two levels of optimization.

## 3 Improved Multi-objective Robust Collaborative Optimization

The proposed IMORCO method combines the Improved Multi-objective Robust Collaborative Optimization MORO (Hu et al. 2009) and Improved Multi-objective Collaborative Optimization IMOCO method (Chagraoui et al. 2015). In IMORCO approach, the output variable from a substructure can be as input variable in another substructure; thus, allowing a variation range for an output variable, which creates an input uncertainty to another substructure. To overcome these shortcomings, we used the interdisciplinary propagation of uncertainty (Li and Azarm 2008) in this study in order to ensure the collaborative robustness in IMORCO framework. The details of the IMORCO approach for the complex structures and their substructures optimization problems are presented below.

In this framework, the IMORCO approach decomposes the complex structure’s optimization problem in Eq. (1) in two levels (structure and substructure). Here,

each optimization problem in structure and substructure level resolved in two steps as following:

**First step: structure's deterministic optimization:**

$$\begin{aligned}
 & \min_{\mathbf{X}_s} f_s(\mathbf{X}_s, \mathbf{P}_s, \mathbf{aux}_s, \mathbf{x}_1^*, \mathbf{x}_2^*) \\
 & s.t \\
 & g_s(\mathbf{x}_{sh}^s, \mathbf{P}_s + \Delta\mathbf{P}_s, \mathbf{aux}_s + \Delta\mathbf{aux}_s) \leq 0 \\
 & |f_s(\mathbf{x}_{sh}^s, \mathbf{P}_s + \Delta\mathbf{P}_s, \mathbf{aux}_s + \Delta\mathbf{aux}_s, \mathbf{x}_1^*, \mathbf{x}_2^*) - f_s(\mathbf{x}_{sh}^s, \mathbf{P}_s, \mathbf{aux}_s, \mathbf{x}_1^*, \mathbf{x}_2^*)| - \Delta f_s \leq 0 \quad (2a) \\
 & \mathbf{X}_s \equiv [\mathbf{x}_{sh}^s, \mathbf{aux}_s]; \mathbf{aux}_s \equiv [\mathbf{aux}_{me}^s, \mathbf{aux}_{21}^s]; \\
 & \mathbf{P}_s \equiv [\mathbf{p}_s, \mathbf{p}_{sh}^s]; \mathbf{X}_s \in [\mathbf{X}_s^{\min}, \mathbf{X}_s^{\max}] \\
 & \forall \Delta\mathbf{P}_s, \Delta\mathbf{aux}_s \in S_{sWPP}
 \end{aligned}$$

**Second step: structure's robustness assessment:**

$$\begin{aligned}
 & C_s \leq 0 \\
 & with \\
 & C_s = \max_{\Delta\mathbf{p}_s, \Delta\mathbf{aux}_s} \left[ \begin{array}{l} |f_s(\mathbf{X}_s, \mathbf{p}_s + \Delta\mathbf{p}_s, \mathbf{aux}_s + \Delta\mathbf{aux}_s, \mathbf{x}_1^*, \mathbf{x}_2^*) - f_s(\mathbf{X}_s, \mathbf{p}_s, \mathbf{aux}_s, \mathbf{x}_1^*, \mathbf{x}_2^*)| - \Delta f_s, \\ g_s(\mathbf{X}_s, \mathbf{p}_s + \Delta\mathbf{p}_s, \mathbf{aux}_s + \Delta\mathbf{aux}_s), \\ |y_{12}(\mathbf{X}_s, \mathbf{p}_s + \Delta\mathbf{p}_s, \mathbf{aux}_s + \Delta\mathbf{aux}_s, \mathbf{x}_1^*) - y_{12}(\mathbf{X}_s, \mathbf{p}_s, \mathbf{aux}_s, \mathbf{x}_1^*)| - \Delta\mathbf{aux}_s, \\ |y_{21}(\mathbf{X}_s, \mathbf{p}_s + \Delta\mathbf{p}_s, \mathbf{aux}_s + \Delta\mathbf{aux}_s, \mathbf{x}_2^*) - y_{21}(\mathbf{X}_s, \mathbf{p}_s, \mathbf{aux}_s, \mathbf{x}_2^*)| - \Delta\mathbf{aux}_s \end{array} \right] \\
 & \Delta\mathbf{p}_s \in [\Delta\mathbf{p}_s^{\min}, \Delta\mathbf{p}_s^{\max}], \Delta\mathbf{aux}_s \in [\Delta\mathbf{aux}_s^{\min}, \Delta\mathbf{aux}_s^{\max}], \Delta\mathbf{aux}_s \equiv [\Delta\mathbf{aux}_{me}^s, \Delta\mathbf{aux}_{em}^s]
 \end{aligned} \quad (2b)$$

In the first step, a deterministic multi-objective optimization problem, Eq. (2a), resolved to obtain a set of optimal solutions of the complex structure. In the second step, a robustness assessment problem in Eq. (2b), uses the Pareto optimal solutions obtained in Eq. (2a) in order to find the WPPs (Hu et al. 2009). This is done by optimization over the vector of uncontrolled design parameters  $\Delta\mathbf{P}_s$  and  $\Delta\mathbf{aux}_s$ .

The robustness of the optimal solution obtained from Eq. (2a) is checked through the constraint  $C_s \leq 0$  of Eq. (2b). The distinct optimal solutions  $(\Delta\mathbf{P}_s, \Delta\mathbf{aux}_s)$  are inserted in the set  $S_{sWPP}$  and then replaced in Eq. (2a). This creates “constraint cuts” (Hu et al. 2009) used to restrict the feasible domain. In fact, the constraint  $C_s$  can be used as a robustness indicator for optimal solutions.

We applied the same robustness assessment to both substructures in Eqs. (3a, b), and (4a, b). For both substructures, each multi-objective optimization problem is decomposed into two steps in order to assess the robustness.

**First step: substructure 1's deterministic optimization:**

$$\begin{aligned}
& \min_{X_1} \left( f_1(X_1, P_1) + \left\| 1 - \frac{x_{sh}^1}{x_{sh}^s} \right\|_2 + \left\| 1 - \frac{y_{12}}{aux_{12}^s} \right\|_2 + \left\| 1 - \frac{aux_{12}^1}{aux_{12}^s} \right\|_2 \right) \\
& s.t \\
& g_1(x_1, x_{sh}^1, P_1 + \Delta P_1, aux_{21}^1 + \Delta aux_{21}) \leq 0 \\
& |f_1(x_1, x_{sh}^1, P_1 + \Delta P_1, aux_{21}^1 + \Delta aux_{21}) - f_1(x_1, x_{sh}^1, P_1, aux_{21}^1)| - \Delta f_1 \leq 0 \\
& |y_{12}(x_1, x_{sh}^1, P_1 + \Delta P_1, aux_{21}^1 + \Delta aux_{21}) - y_{12}(x_1, x_{sh}^1, P_1, aux_{21}^1)| - \Delta y_{12} \leq 0 \\
& y_{12} = Y_1(X_1, P_1) \quad \forall \quad \Delta P_1, \Delta aux_{21} \in S_{1_{wpp}} \\
& X_1 \equiv [x_1, x_{sh}^1, aux_{21}^1]; \quad X_1 \in [X_1^{\min}, X_1^{\max}]; \quad P_1 \equiv [p_1, p_{sh}],
\end{aligned} \tag{3a}$$

**Second step: substructure 1's robustness assessment:**

$$\begin{aligned}
& C_1 \leq 0 \\
& with \\
& C_1 = \max_{\Delta P_1, \Delta aux_{21}} \left[ \begin{array}{l} |f_1(x_1, x_{sh}^1, P_1 + \Delta P_1, aux_{21}^1 + \Delta aux_{21}) - f_1(x_1, x_{sh}^1, P_1, aux_{21}^1)| - \Delta f_1, \\ |y_{12}(x_1, x_{sh}^1, P_1 + \Delta P_1, aux_{21}^1 + \Delta aux_{21}) - y_{12}(x_1, x_{sh}^1, P_1, aux_{21}^1)| - \Delta y_{12}, \\ g_1(x_1, x_{sh}^1, P_1 + \Delta P_1, aux_{21}^1 + \Delta aux_{21}) \end{array} \right] \\
& \Delta aux_{21} \in [\Delta aux_{21}^{\min}, \Delta aux_{21}^{\max}]; \quad \Delta P_1 \in [\Delta P_1^{\min}, \Delta P_1^{\max}]
\end{aligned} \tag{3b}$$

The Substructure 1's optimization problem is divided into two optimization steps. The first is indicated in Eq. (3a) which aims to search the optimal solutions set; while in the second, the robustness assessment problem in Eq. (3b) aims to assess the robustness for each optimal solution obtained in Eq. (3a).

**First step: substructure 2's deterministic optimization:**

$$\begin{aligned}
& \min_{X_2} \left( f_2(X_2, P_2) + \left\| 1 - \frac{x_{sh}^2}{x_{sh}^s} \right\|_2 + \left\| 1 - \frac{y_{21}}{aux_{21}^s} \right\|_2 + \left\| 1 - \frac{aux_{12}^2}{aux_{12}^s} \right\|_2 \right) \\
& s.t \\
& g_2(x_2, x_{sh}^2, P_2 + \Delta P_2, aux_{12}^2 + \Delta aux_{12}) \leq 0 \\
& |f_2(x_2, x_{sh}^2, P_2 + \Delta P_2, aux_{12}^2 + \Delta aux_{12}) - f_2(x_2, x_{sh}^2, P_2, aux_{12}^2)| - \Delta f_2 \leq 0 \\
& |y_{21}(x_2, x_{sh}^2, P_2 + \Delta P_2, aux_{12}^2 + \Delta aux_{12}) - y_{21}(x_2, x_{sh}^2, P_2, aux_{12}^2)| - \Delta y_{21} \leq 0 \\
& X_2 \equiv [x_2, x_{sh}^2, aux_{12}^2]; \quad P_2 \equiv [p_2, p_{sh}]; \quad X_2 \in [X_2^{\min}, X_2^{\max}], \\
& \quad \quad \quad \forall \quad \Delta P_2, \Delta aux_{12} \in S_{2_{wpp}}
\end{aligned} \tag{4a}$$

**Second step: substructure 2’s robustness assessment:**

$$C_2 \leq 0$$

with

$$C_2 = \max_{\Delta P_2, \Delta aux_{12}} \left[ \begin{array}{l} |f_2(x_2, x_{sh}^2, P_2 + \Delta P_2, aux_{12}^2 + \Delta aux_{12}) - f_2(x_2, x_{sh}^2, P_2, aux_{12}^2)| - \Delta f_2, \\ |y_{21}(x_2, x_{sh}^2, P_2 + \Delta P_2, aux_{12}^2 + \Delta aux_{12}) - y_{21}(x_2, x_{sh}^2, P_2, aux_{12}^2)| - \Delta y_{21}, \\ g_2(x_2, x_{sh}^2, P_2 + \Delta P_2, aux_{12}^2 + \Delta aux_{12}) \end{array} \right]$$

$$\Delta aux_{12} \in [\Delta aux_{12}^{\min}, \Delta aux_{12}^{\max}]; \Delta P_2 \in [\Delta P_2^{\min}, \Delta P_2^{\max}]$$

(4b)

Similarly, The Substructure 2’s optimization problem divided also in two optimization steps. The first step, Eq. (4a), optimal solutions related to the Substructure 2 are sought out; while in the second step, Eq. (4b), the robustness of each optimal solution obtained from Eq. (4a) is assessed.

**4 Engineering Problem: Y-Stiffened Panel**

To demonstrate our proposed approach, we treat a complex mechanical structure Y-stiffened panel type (Badran et al. 2009; Soares and Fricke 2011). As shown in Fig. 1a, this engineering problem contains three substructures (plate, Hat section and Tee section). In this study, a genetic algorithm NSGA-II type is coupled with finite element model (EF) in ANSYS® (couplage between ANSYS® and MATLAB®) in order to increase the efficiency of the Y-stiffened panel. The free vibrations of the Y-stiffened panel are studied. Figure 1b shows the mesh of the Y-stiffened panel using SHELL181 (4-Node finite strain shell element). The FE mesh consists of 1763 nodes and 1720 elements. The Young’s modulus for the used

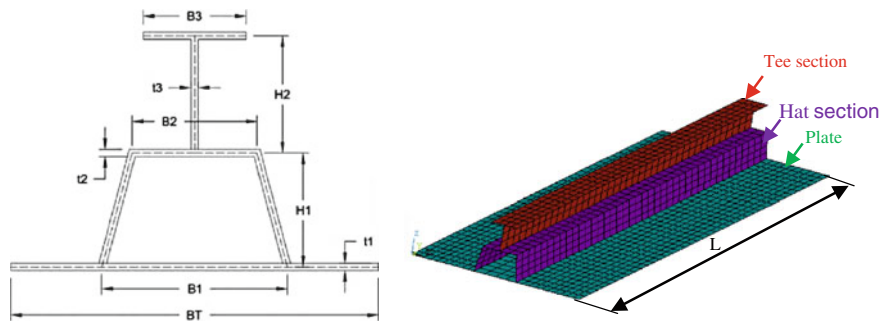


**Fig. 1 a** Cross-section geometry of Y-stiffener panel (Soares and Fricke 2011). **b** Finite element model (EF) of Y-stiffener panel

**Table 1** Geometrical properties of the studied Y-stiffened panel

Y-stiffened panel									
Plate			Hat section			Tee section			
L	BT	t1	B1	B2	H1	t2	H2	B3	t3
15,000	4000	25	1000	800	600	20	600	600	20

material is  $E = 210$  GPa, the poisson’s ration is  $\nu = 0.3$  and the density is equal to  $7850 \text{ kg/m}^3$  (Soares and Fricke 2011). Table 1 summarizes the geometrical properties (mm) of the Y-stiffened panel.

The robust multi-objective optimization problem of the Y-stiffened panel to solve following the NDMORO approach has three objective functions and twelve design variables: (i) maximize the eigenfrequency of the Y-stiffened panel  $f_r(x)$ , (ii) minimize the displacement at node 627  $Disp_{627}(x)$ , and (iii) minimize the Total mass  $Mass_{panel}(y)$ , as indicated in Eq. (5a). The interval uncertainty  $[\Delta t_1, \Delta t_2, \Delta t_3]$  of the design variables  $(t_1, t_2, t_3)$  is assumed to be within  $\pm 20\%$  from nominal values, while the acceptable objective variation range (AOVR) (Li et al. 2006) for the objectives functions  $(\Delta f_r, \Delta Disp_{627}, \Delta Mass)$  in the plate, Hat section and Tee section are  $\pm 20\%$  of their nominal values.

In the first step, a deterministic multi-objective optimization problem in Eq. (5a) aims to find and pass the Pareto optimal solutions to the robustness assessment problem in Eq. (5b). In the second step, (see Eq. 5b), the robustness of all optimal solutions obtained from Eq. (5a) are evaluated. The Worst Possible Points (WPPS) in Eq. (5a) are obtained by maximizing the objective function  $f_{panel}$  of Eq. (5b), which depends on the  $[\Delta t_1, \Delta t_2, \Delta t_3]$  while ensuring that the inequality constraint  $f_{panel} \leq 0$  is satisfied. The distinct optimal solutions  $[\Delta t_1, \Delta t_2, \Delta t_3]$  are inserted in set  $S_{panel\ WPP}$  and then introduced into Eq. (5a). The deterministic multi-objective optimization problem in Eq. (5a) uses the returned WPPs from the robustness assessment problem in order to create “constraint cuts”. This way, the feasible domain of the deterministic multi-objective optimization problem is iteratively restricted in order to identify robust optimal solutions according to Hu et al. (2009).

**First step: structure’s deterministic optimization:**

$$\begin{aligned}
 &\min(-f_r(X), Disp(X), Mass_{panel}(X)) \\
 &s.t \\
 &|f_r(X, \Delta t_1, \Delta t_2, \Delta t_3) - f_r(X)| - \Delta f_r \leq 0 \\
 &|Disp_{627}(X, \Delta t_1, \Delta t_2, \Delta t_3) - Disp_{627}(X)| - \Delta Disp_{627} \leq 0 \\
 &|Mass_{panel}(X, \Delta t_1, \Delta t_2, \Delta t_3) - Mass_{panel}(X)| - \Delta Mass_{panel} \leq 0 \\
 &X \in [L, B_T, t_1, H_1, B_2, t_2, H_2, B_3, t_3, E, \rho]; \quad \forall \quad \Delta t_1, \Delta t_2, \Delta t_3 \in S_{panel\ wpp}
 \end{aligned}
 \tag{5a}$$



### Second step: structure's robustness assessment:

$$\begin{aligned}
 & f_{panel} \leq 0 \\
 & \text{with} \\
 & f_{panel} = \max_{\Delta t_{1,2,3}} \left[ \begin{array}{l} |f_r(X, \Delta t_1, \Delta t_2, \Delta t_3) - f_r(X)| - \Delta f_r, \\ |Disp_{627}(X, \Delta t_1, \Delta t_2, \Delta t_3) - Disp_{627}(X)| - \Delta Disp_{627}, \\ |Mass_{panel}(X, \Delta t_1, \Delta t_2, \Delta t_3) - Mass_{panel}(X)| - \Delta Mass_{panel} \end{array} \right] \quad (5b) \\
 & \Delta t_{1,2,3} \in [-20\% t_{1,2,3} + 20\% t_{1,2,3}]
 \end{aligned}$$

Using our proposed IMORCO approach, the problem in Eqs. (5a and b) is decomposed in tow levels problems. The problem at the structure-level as shown in Eq. (6). The substructure level contains the following three substructures

- Plate in Eq. (7),
- Hat section in Eq. (8)
- and Tee section in Eq. (9).

Equation (6) represents the structure level robust optimization problem. Although each substructure has its own design variables, two shared variables between the optimization problems at the structure level and the substructure level. The shared variables are the Young's modulus ( $E$ ) and the density of the Y-stiffened panel ( $\rho$ ).

### Structure's deterministic optimization:

$$\begin{aligned}
 \min_{X_s} \left\{ \begin{array}{l} -f_r(\mathbf{X}_s, \mathbf{x}_p^*, \mathbf{x}_H^*, \mathbf{x}_T^*) \\ Disp_{627}(\mathbf{X}_s, \mathbf{x}_p^*, \mathbf{x}_H^*, \mathbf{x}_T^*) \\ Mass_{panel}(\rho, aux_{PHT}^s, \mathbf{x}_p^*, \mathbf{x}_H^*, \mathbf{x}_T^*) \end{array} \right. \quad (6) \\
 \mathbf{x}_{sh}^s \equiv [E_1, \rho]; \quad \mathbf{X}_s \equiv [\mathbf{x}_{sh}^s, aux_{PHT}^s]
 \end{aligned}$$

In the structure level robust optimization problem,  $X_s \equiv [x_{sh}, aux_{PHT}^s]$  includes the four shared design variables  $[E, \rho]$ ; and the auxiliary variable  $aux_{PHT}^s$  corresponds to the coupling variable  $y_{PHT}$ . The super script (\*) indicates that the variables are optimized at the substructure level.

The robust optimization problem of plate includes local design variable is ( $\mathbf{x}_p$ ), as indicated in Eq. (7), aims to maximize the local eigenfrequency ( $f_p$ ) and the mass ( $M_p$ ) limited by the local constraint ( $Disp_{pMax}$ ). Equally, The Hat section's robust optimization problem in Eq. (8) aims to maximize the local eigenfrequency ( $f_H$ ) and minimize the mass ( $M_H$ ) limited by the local constraint ( $Disp_{HMax}$ ) while respecting the design variable  $\mathbf{X}_H$ , which includes mechanical optimizer variables  $\mathbf{x}_H$ , shared variables  $\mathbf{x}_{sh}^H$  and auxiliary (target) variables  $aux_{PHT}^H$ .

**First step: Plate's deterministic optimization**

$$\begin{aligned} & \min_{X_P} (-f_P, M_P) \\ & \text{s.t. } Disp_P(X_P, \Delta t_1) \leq Disp_{PMax} \\ & |f_P(X_P, \Delta t_1) - f_P(X_P)| - \Delta f_P \leq 0 \\ & |M_P(X_P, \Delta t_1) - M_P(X_P)| - \Delta M_P \leq 0 \\ & \mathbf{x}_{sh}^P \equiv [E, \rho]; \mathbf{x}_P \equiv [B_T, t_1]; y_{PTH} = L \\ & X_P \equiv [\mathbf{x}_P, \mathbf{x}_{sh}^P, aux_{PHT}^P], \forall \Delta t_1 \in S_{Pwpp} \end{aligned}$$

**Second step: Plate's robustness assessment:**

$$\begin{aligned} & f_{Plate} \leq 0 \\ & \text{with} \\ & f_{Plate} = \max_{\Delta t_1} \left[ \begin{aligned} & Disp_P(X_P, \Delta t_1) - Disp_{PMax}, \\ & |f_P(X_P, \Delta t_1) - f_P(X_P)| - \Delta f_P, \\ & |M_P(X_P, \Delta t_1) - M_P(X_P)| - \Delta M_P \end{aligned} \right] \\ & \Delta t_1 \in [-20\% t_1, 20\% t_1] \end{aligned}$$

(7)

**First step: Hat section's deterministic optimization**

$$\begin{aligned} & \min_{X_H} (-f_H, M_H) \\ & \text{s.t. } Disp_H(X_H, \Delta t_2) \leq Disp_{HMax} \\ & |f_H(X_H, \Delta t_2) - f_H(X_H)| - \Delta f_H \leq 0 \\ & |M_H(X_H, \Delta t_2) - M_H(X_H)| - \Delta M_H \leq 0 \\ & \mathbf{x}_{sh}^H \equiv [E, \rho]; \mathbf{x}_H \equiv [H_1, B_2, t_2] \\ & X_H \equiv [\mathbf{x}_H, \mathbf{x}_{sh}^H, aux_{PHT}^H], \forall \Delta t_2 \in S_{Hwpp} \end{aligned}$$

**Second step: Hat section's robustness assessment:**

$$\begin{aligned} & f_{Hat} \leq 0 \\ & \text{with} \\ & f_{Hat} = \max_{\Delta t_2} \left[ \begin{aligned} & Disp_H(X_H, \Delta t_2) - Disp_{HMax}, \\ & |f_H(X_H, \Delta t_2) - f_H(X_H)| - \Delta f_H, \\ & |M_H(X_H, \Delta t_2) - M_H(X_H)| - \Delta M_H \end{aligned} \right] \\ & \Delta t_2 \in [-20\% t_2, 20\% t_2] \end{aligned}$$

(8)

The robust optimization problem of Tee section (see Eq. (9)) aims to increase the objective function ( $f_T$ ) and to reduce a minimum of the Tee section's mass ( $M_T$ ) and which is associated with a local constraint ( $Disp_{TMax}$ ).  $X_T$  represents a solution to this optimization problem, which includes Tee section optimizer's variables  $\mathbf{x}_T$ , shared variables  $\mathbf{x}_{sh}^T$  and auxiliary (target) variables  $aux_{PTH}^T$ .

**First step: Tee section's deterministic optimization:**

$$\begin{aligned} & \min_{X_T} (-f_T, M_T) \\ & \text{s.t. } Disp_T(X_T, \Delta t_3) \leq Disp_{TMax} \\ & |f_T(X_T, \Delta t_3) - f_T(X_T)| - \Delta f_T \leq 0 \\ & |M_T(X_T, \Delta t_3) - M_T(X_T)| - \Delta M_T \leq 0 \\ & \mathbf{x}_{sh}^T \equiv [E, \rho]; \mathbf{x}_T \equiv [H_2, B_3, t_3]; \\ & X_T \equiv [\mathbf{x}_T, \mathbf{x}_{sh}^T, aux_{PTH}^T], \forall \Delta t_3 \in S_{Twpp} \end{aligned}$$

**Second step : Tee section's robustness assessment:**

$$\begin{aligned} & f_{Tee} \leq 0 \\ & \text{with} \\ & f_{Tee} = \max_{\Delta t_3} \left[ \begin{aligned} & Disp_T(X_T, \Delta t_3) - Disp_{TMax}, \\ & |f_T(X_T, \Delta t_3) - f_T(X_T)| - \Delta f_T, \\ & |M_T(X_T, \Delta t_3) - M_T(X_T)| - \Delta M_T \end{aligned} \right] \\ & \Delta t_3 \in [-20\% t_3, 20\% t_3] \end{aligned}$$

(9)

After the optimization of coordination problem in Eq. (10) and the optimal solutions with the smallest value of the penalty function we chose the optimal variables ( $x_P^*, x_H^*, x_T^*$ ) at substructure level, which are then transferred towards the structure level (see Eq. 6).

$$\begin{aligned}
 \text{minimize } C(X) &= \left\| 1 - (x_{sh}^P/x_{sh}) \right\|_2 + \left\| 1 - (x_{sh}^H/x_{sh}) \right\|_2 + \left\| 1 - (x_{sh}^T/x_{sh}) \right\|_2 \\
 &+ \left\| 1 - (y_{PTH}/aux_{PTH}) \right\|_2 + \left\| 1 - (aux_{PTH}^H/aux_{PTH}) \right\|_2 \\
 &+ \left\| 1 - (aux_{PTH}^T/aux_{PTH}) \right\|_2 \\
 X &\equiv [x_{sh}, aux_{PTH}]; X^{\min} \leq X \leq X^{\max}
 \end{aligned}
 \tag{10}$$

The robust Pareto frontier of the optimization problem at upper level in Eq. (6) by NDMORO and IMORCO approach are plotted in the objective space as in Fig. 2. Figure 2 shows that the robust Pareto set obtained by the IMORCO approach closed to the robust Pareto frontier obtained by NDMORO approach. This is also confirmed by the Mahalanobis distance MD<sup>2</sup> (De Maesschalck et al. 2000) between NDMORO and IMORCO. As shown in Table 2 that the proposed approach reduces the CPU time to 60 %. Based on the results of this example, we can see that the robust solutions obtained by the proposed IMORCO are consistent with NDMORO.

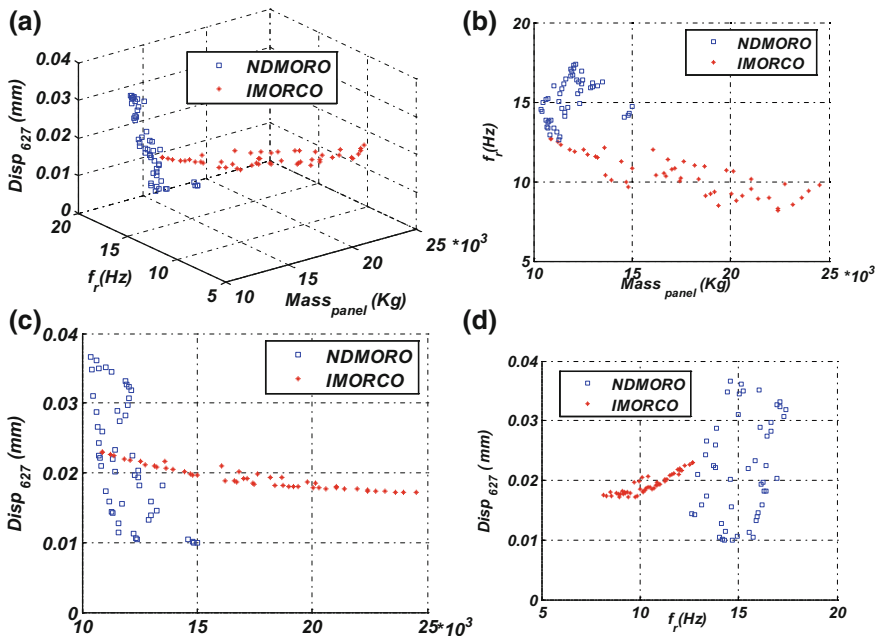


**Fig. 2** Robust Pareto optimal solutions for engineering example in the plane: **a**  $Mass_{panel}$  (kg),  $f_r$  (Hz) and  $Disp_{627}$  (mm); **b**  $Mass_{panel}$  (kg) and  $f_r$  (Hz); **c**  $Mass_{panel}$  (kg) and  $Disp_{627}$  (mm); **d**  $f_r$  (Hz) and  $Disp_{627}$  (mm)

**Table 2** Performance of the proposed IMORCO method versus NDMORO method

Approach	CPU (%)	Reduction (%)	DM <sup>2</sup>
NDMORO	100	59	14.957
IMORCO	41		

## 5 Conclusion

In this study, we developed a new two-level robust multi-objective optimization approach in CO framework to handle the complex structures with multiple objectives/constraints at the structure and substructure levels. The IMORCO approach achieves the same task taking into consideration interval uncertainty. In these two original approaches, we introduced a coordination problem between the upper and lower level, which permits to minimize the difference between the shared and the coupling variables transmitted from all substructures in order to avoid discrepancy during optimization.

We applied the original approach to an engineering example Y-stiffened panel type. The obtained results are compared with the NDMORO method. From the results presented in this example, we observed in this case that there is a good agreement between the robust Pareto frontier obtained by NDMORO and by proposed IMORCO. In addition, the robust Pareto set created by the proposed IMORCO approach converge to the robust Pareto frontier obtained by NDMORO.

Finally, it could be concluded that IMORCO approach provide solutions that are consistent robust solutions with the NDMORO method. These proposed two methods require less computational efforts that the NDMORO approach.

## References

- Badran SF, Nassef AO, Metwalli SM (2009) Y-stiffened panel multi-objective optimization using genetic algorithm. *Thin Wall Struct* 47:1331–1342. doi:[10.1016/j.tws.2009.03.011](https://doi.org/10.1016/j.tws.2009.03.011)
- Chagraoui H, Ghanmi S, Guedri M, Soula M, Bouhaddi N (2015) Multi-objective and multi-physics optimization of fully coupled complex structures. In: *Design and modeling of mechanical systems-II*. Springer, pp 29–39. doi:[10.1007/978-3-319-17527-0\\_4](https://doi.org/10.1007/978-3-319-17527-0_4)
- De Maesschalck R, Jouan-Rimbaud D, Massart DL (2000) The Mahalanobis distance. *Chemometr Intell Lab Syst* 50:1–18. doi:[10.1016/S0169-7439\(99\)00047-7](https://doi.org/10.1016/S0169-7439(99)00047-7)
- Hu W, Li M, Azarm S, Al Hashimi S, Almansoori A, Al-Qasas N (2009) Improving multi-objective robust optimization under interval uncertainty using worst possible point constraint cuts. *J Mech Des* 1193–1203. doi:[10.1115/DETC2009-87312](https://doi.org/10.1115/DETC2009-87312)
- Li M, Azarm S (2008) Multiobjective collaborative robust optimization with interval uncertainty and interdisciplinary uncertainty propagation. *J Mech Des* 130:719–729. doi:[10.1115/DETC2007-34818](https://doi.org/10.1115/DETC2007-34818)
- Li M, Azarm S, Boyars A (2006) A new deterministic approach using sensitivity region measures for multi-objective robust and feasibility robust design optimization. *J Mech Des* 128:874–883. doi:[10.1115/1.2202884](https://doi.org/10.1115/1.2202884)

Soares CG, Fricke W (2011) *Advances in marine structures*. CRC Press

Weiwei H, Azarm S, Al mansoori A (2013) New approximation assisted multi-objective collaborative robust optimization (new AA-McRO) under interval uncertainty. *Struct Multidiscip Optim* 47:19–35. doi:[10.1007/s00158-012-0816-2](https://doi.org/10.1007/s00158-012-0816-2)

# Investigations on the Validity of the Poisson Assumption in Reliability Based Optimization of TMD Parameters

E. Mrabet, M. Guedri, M. Soula, M. Ichchou and S. Ghanmi

**Abstract** The purpose of the present work is to investigate the validity of the Poisson assumption used in the failure analysis, which is in turn required for the reliability based optimization (RBO) of tuned mass dampers (TMD) parameters. The TMD is a widely used device aiming to mitigate induced vibrations into structures under stochastic loading. The performance of this device is deeply related to its parameters that should be carefully chosen and in this context the RBO strategy can be used. The RBO problem required failure analysis, usually, performed based on analytical approximations and among them we can find: the Poisson, the Vanmarcke and the modified Vanmarcke approximations. The failure analysis based on Poisson assumption is very simple and widely used for its lower computational cost compared with the other approximations. Nevertheless, it's also known that the Poisson approximation is inappropriate for narrowband process and/or for low threshold values, whereas, the other approximations could be used in such conditions. By studying a single degree of freedom system (SDOF), submitted to stochastic base acceleration, we investigate the relative error, in the optimum TMD parameters, induced by these approximations and we show that the Poisson

---

E. Mrabet (✉) · M. Guedri · S. Ghanmi  
Unité de Recherche en Dynamique des Structures, Modélisation et Ingénierie des Systèmes Multi-physiques, Preparatory Engineering Institute of Nabeul (IPEIN), 8000 M'ezgua, Nabeul, Tunisia  
e-mail: elyes.mrabet@yahoo.fr

M. Soula  
Laboratory of Applied Mechanics and Engineering, ENIT, Mechanical Engineering Department, École Nationale Supérieure des Ingénieurs de Tunis, University of Tunis, 5 Avenue Taha Hussein Montfleury, 1008 Tunis, Tunisia

M. Ichchou  
LTDS UMR5513 Ecole Centrale de Lyon, 36 Avenue Guy de Collongue, 69134 Ecully, France

M. Guedri  
College of Technology at Makkah, Technical and Vocational Training Corporation, Makkah, Kingdom of Saudi Arabia

assumption is relatively accurate and valid for high threshold level, even for narrowband excitations.

**Keywords** Reliability based optimization of TMD • Poisson assumption • Rice's formula • Vanmarcke approximation • Modified vanmarcke approximation

## 1 Introduction

The use of the TMD devices in engineering to mitigate vibrations in linear structures subject to stationary stochastic loading has taken wide interests in last years. The performance of such device strongly depends on its parameters that should, carefully, optimized and among the existing strategies one can find the RBO approach (Mrabet et al. 2015). For every value of the design parameters, the RBO loop can be performed using two steps (Lutes and Sarkani 2004): (1) dynamic analysis, performed to get stochastic responses; (2) failure analysis, performed to compute the failure probability related to a certain failure mode.

The computation of the failure probability, required in the RBO strategy, constitutes a time depending problem of reliability analysis and is usually performed using analytical approximations instead of simulation techniques that involve high computational costs. Among the existing approximations method we can find: the Poisson, the Vanmarcke and the modified Vanmarcke approximations.

The Poisson approximation provides very conservative estimates of the failure probabilities for low failure thresholds and narrowband processes. In such conditions, the Vanmarcke and the modified Vanmarcke approximations can be used taking into account the bandwidth of the considered process.

Nevertheless, the use of the Vanmarcke or the modified Vanmarcke approximations requires the computation of spectral moments that are more demanding for the computationally effort.

In the present work we investigate the accuracy of the proposed approximation techniques on the optimum TMD parameters and showed that the use of the Poisson approximation, considering high threshold level, provide good compromise between accuracy and computational effort even for narrowband excitation process. The numerical investigations are made using a generic SDOF system equipped by TMD and submitted to stationary stochastic loading. The considered failure probability is related to the outcrossing of the displacement of the primary structure across a given threshold during some interval time. The obtained results showed that the relative error between optimum TMD parameters, obtained using the proposed approximations, are very small and are asymptotically (for high threshold levels) equal to zeros, consequently the accuracy of the proposed approximations are similar.

## 2 Dynamic Analysis and Covariance Responses

Figure 1 shows an idealized mechanical model of a TMD attached to a primary structure. The TMD device is described by mass  $m_T$ , spring stiffness  $k_T$  and damping  $c_T$ . The SDOF primary structure is characterized by mass  $m_s$ , spring stiffness  $k_s$  and damping  $c_s$ .

The system is subjected to a base acceleration  $\ddot{y}_b$  due to seismic motion. Let  $\mathbf{y}(t) = (y_T, y_s)^T$  be the relative displacement vector of the TMD device and the primary structure, respectively, the governing equation (Carlo Marano et al. 2010) of the dynamic system can be expressed as follows:

$$\mathbf{M}\ddot{\mathbf{y}}(t) + \mathbf{C}\dot{\mathbf{y}}(t) + \mathbf{K}\mathbf{y}(t) = -\mathbf{M}\mathbf{r}\ddot{y}_b \tag{1}$$

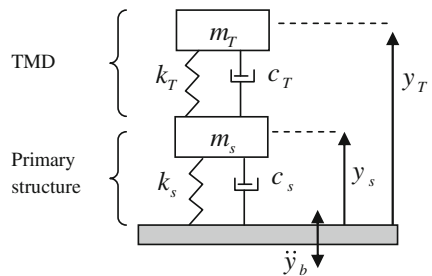
where the overdot represents the time derivative,  $\mathbf{M} = \begin{pmatrix} m_T & 0 \\ 0 & m_s \end{pmatrix}$ ,  $\mathbf{C} = \begin{pmatrix} c_T & -c_T \\ -c_T & c_T + c_s \end{pmatrix}$ ,  $\mathbf{K} = \begin{pmatrix} k_T & -k_T \\ -k_T & k_T + k_s \end{pmatrix}$  and  $\mathbf{r} = [1 \quad 1]^T$ .

The base acceleration  $\ddot{y}_b$  can be modeled by the Kanai-Tajimi stationary stochastic process (Marano et al. 2010). Then, the base acceleration satisfies the following equations:

$$\ddot{y}_f + 2\xi_f\omega_f\dot{y}_f + \omega_f^2y_f = -w(t) \text{ and } \ddot{y}_b = \ddot{y}_f + w(t) = -(2\xi_f\omega_f\dot{y}_f + \omega_f^2y_f) \tag{2}$$

where  $w(t)$  is a stationary zero mean white noise process applied at the bed rock. It represents the excitation of the dynamic system and it has intensity  $S_0$ .  $\xi_f$ ,  $\omega_f$  and  $y_f$  are the damping ratio, the natural frequency and the relative response (with respect to the ground) of the elastic filter (Mrabet et al. 2015). Considering the Kanai-Tajimi model, the global space state vector of the mechanical system is given by  $\mathbf{Z} = (y_T, y_s, y_f, \dot{y}_T, \dot{y}_s, \dot{y}_f)^T$  and the equation of motion can be written in the space state form (Carlo Marano et al. 2010) as  $\dot{\mathbf{Z}} = \mathbf{A}\mathbf{Z} + \mathbf{f}$  where  $\mathbf{f} = [0 \quad 0 \quad 0 \quad 0 \quad 0 \quad -w(t)]^T$  and

**Fig. 1** The primary structure with the TMD device





$$\mathbf{A} = \begin{pmatrix} 0 & 0 & 0 & 1 & 0 & 0 \\ 0 & 0 & 0 & 0 & 1 & 0 \\ 0 & 0 & 0 & 0 & 0 & 1 \\ -\omega_T^2 & \omega_T^2 & \omega_f^2 & -2\xi_T\omega_T & 2\xi_T\omega_T & 2\xi_f\omega_f \\ \mu\omega_T^2 & -(\mu\omega_T^2 + \omega_s^2) & \omega_f^2 & 2\mu\xi_T\omega_T & -2(\xi_s\omega_s + \mu\xi_T\omega_T) & 2\xi_f\omega_f \\ 0 & 0 & -\omega_f^2 & 0 & 0 & -2\xi_f\omega_f \end{pmatrix}$$

In the above expression,  $\mu = m_T/m_s$  is the mass ratio,  $\omega_T = \sqrt{k_T/m_T}$  and  $\xi_T = c_T/2\sqrt{k_Tm_T}$  are the natural frequency and the damping ratio, respectively, of the TMD device, whereas  $\omega_s = \sqrt{k_s/m_s}$  and  $\xi_s = c_s/2\sqrt{k_s m_s}$  are the natural frequency and the damping ratio, respectively, of the primary structure.

The stochastic response of the mechanical system is completely known by the space state covariance matrix  $\mathbf{R}$  which is the solution of the Lyapunov equation given, in stationary condition, as follows:

$$\mathbf{A}\mathbf{R} + \mathbf{R}\mathbf{A}^T + \mathbf{B} = \mathbf{0} \tag{3}$$

where  $\mathbf{B}$  has all zero elements, except the last one  $[\mathbf{B}]_{(6,6)} = 2\pi S_0$ . The root mean square displacement (rmsd) of the primary system can be obtained as  $\sigma_{y_s} = \sqrt{\mathbf{R}(2,2)}$ . The root mean square velocity (rmsv) is expressed as  $\sigma_{\dot{y}_s} = \sqrt{\mathbf{R}(5,5)}$ . Let  $\langle \cdot \rangle$  denotes the expectation, the acceleration covariance matrix is related to the covariance matrix  $\mathbf{R}$  and it is given by:

$$\mathbf{R}_{\ddot{\mathbf{y}}\ddot{\mathbf{y}}} = \langle \ddot{\mathbf{y}}\ddot{\mathbf{y}}^T \rangle = \begin{pmatrix} \sigma_{\dot{y}_T}^2 & \langle \dot{y}_T\dot{y}_s \rangle \\ \langle \dot{y}_s\dot{y}_T \rangle & \sigma_{\dot{y}_s}^2 \end{pmatrix} = (\mathbf{D}_1 \quad \mathbf{D}_2) \mathbf{R} (\mathbf{D}_1 \quad \mathbf{D}_2)^T, \text{ where}$$

$$\mathbf{D}_1 = \begin{pmatrix} -\omega_T^2 & \omega_T^2 & \omega_f^2 \\ \mu\omega_T & -(\mu\omega_T^2 + \omega_s^2) & \omega_f^2 \end{pmatrix} \text{ and}$$

$$\mathbf{D}_2 = \begin{pmatrix} -2\xi_T\omega_T & 2\xi_T\omega_T & 2\xi_f\omega_f \\ 2\mu\xi_T\omega_T & -2(\xi_s\omega_s + \mu\xi_T\omega_T) & 2\xi_f\omega_f \end{pmatrix}$$

Hence, the root mean square  $\sigma_{\ddot{y}_s}$  of the relative acceleration  $\ddot{y}_s$  can be immediately deduced and written as  $\sigma_{\ddot{y}_s} = \sqrt{\mathbf{R}_{\ddot{\mathbf{y}}\ddot{\mathbf{y}}}(2,2)}$ .

### 3 Optimization Strategy and Failure Analysis

In the present work the failure probability is related to the primary structure displacement  $y_s$ . The RBO strategy consists to find the optimum design parameters  $\mathbf{d} = (\omega_T, \xi_T)$  of the TMD device that minimizes the failure probability  $P_f$

characterized by the outcrossing, for the first time, of the absolute value of the displacement  $|y_s|$  (symmetric double-barrier problem) across a certain threshold value  $\beta$  during some interval time  $[0, T]$ .

The evaluation of  $P_f$  constitutes a time-variant first-passage failure probability that can be expressed, from at-rest initial conditions, as follows (Lutes and Sarkani 2004):

$$P_f(\beta, T) \approx 1 - \exp\left(-\int_0^T h(\beta, t) dt\right) \tag{4}$$

where  $h(\beta, t)$  is time-variant hazard function for the symmetric double-barrier problem.

The Poisson approximation assumes that the out crossings are independents then the number of these outcrossing events is Poisson distributed, consequently the hazard function is assumed to be equal to the mean outcrossing rate  $v_\beta(\beta, t)$  of the process  $y_s$ . The mean outcrossing rate can be obtained using the classical Rice’s formula, in stationary conditions, as follows:

$$v_\beta(\beta) = \int_0^\infty \dot{y}_s \cdot p_{Y_s \dot{Y}_s}(\beta, \dot{y}_s) d\dot{y}_s \tag{5}$$

where  $p_{Y_s \dot{Y}_s}$  is the joint probabilities functions of the considered processes and its time derivatives. Both processes  $y_s$  and  $\dot{y}_s$  are stationary zeros means Gaussian then the hazard function is expressed as follows:

$$h(\beta) = v_\beta = (\sigma_{\dot{y}_s} / \pi \sigma_{y_s}) \exp\left(-\beta^2 / 2\sigma_{y_s}^2\right) \tag{6}$$

The Poisson approximation is well suitable, only, for infinite threshold values and/or broadband processes (Lutes and Sarkani 2004). Indeed, it has been shown that its accuracy, for threshold levels, of practical significance (Vanmarcke 1975; Lutes and Sarkani 2004), critically depends on the bandwidth of the process. In this context, the Vanmarcke approximation takes into account the bandwidth parameters of the considered process and the hazard function is expressed as follows:

$$h(\beta) = v(\beta) \times \frac{1 - \exp(\sqrt{\pi/2} \times q \times \beta / \sigma_{y_s})}{1 - \exp(-0.5 \times \beta^2 / \sigma_{y_s}^2)} \tag{7}$$

where  $q$  is the Vanmarcke’s bandwidth parameter computed using the spectral moments of the power spectral density (PSD) function of the process  $y_s$ ; the bandwidth parameter is expressed as follows (Lutes and Sarkani 2004):

$$q = (1 - \lambda_1^2 / \lambda_0 \lambda_2)^{1/2} \quad (8)$$

where  $\lambda_i$  are the spectral moments,  $\lambda_i = \int_0^\infty \omega^i G_{y_s}(\omega) d\omega$  ( $n = 0, 1, 2, \dots$ ) and  $G_{y_s}(\omega)$  is the single-sided PSD of  $y_s$ . It can be noted that  $\lambda_0 = \sigma_{y_s}^2$ ,  $\lambda_2 = \sigma_{\dot{y}_s}^2$  and  $\lambda_4 = \sigma_{\ddot{y}_s}^2$ .

The modified Vanmarcke approximation heuristically accounts for superclumping effects (Vanmarcke 1975) by introducing an exponent equal to 1.2 for the bandwidth parameter and then, the hazard function is obtained as follows:

$$h(\beta) = v(\beta) \times \frac{1 - \exp(\sqrt{\pi/2} \times q^{1.2} \times \beta / \sigma_{y_s})}{1 - \exp(-0.5 \times \beta^2 / \sigma_{y_s}^2)} \quad (9)$$

Once the hazard functions, for the three approximations, are computed, the RBO problem can be formulated as follows:

$$\text{Find } \mathbf{d} = (\omega_T, \xi_T) \text{ to minimize } P_f(\mathbf{d}) = 1 - \exp\{-T \times h(\beta, \mathbf{d})\} \quad (10)$$

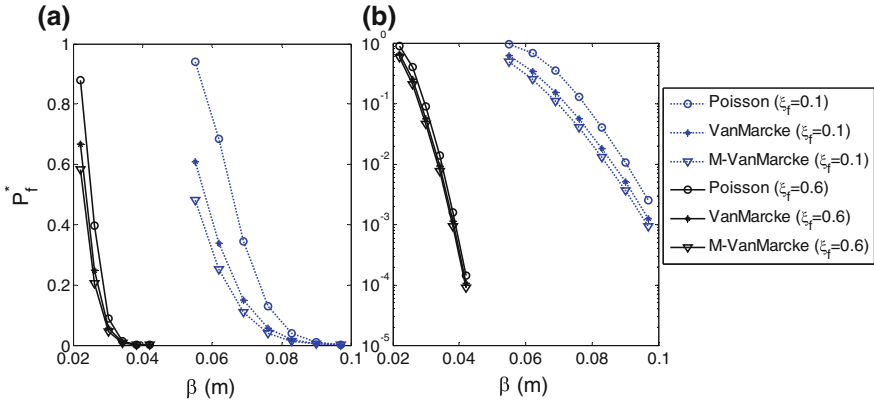
## 4 Numerical Study

The purpose of the numerical study is to evaluate the relative error obtained for the optimum TMD parameters when the proposed approximations are used. To this end, two cases are considered: (1) the studied system is submitted to broadband excitation ( $\xi_f = 0.6$ ) and (2) the studied system is submitted to narrowband excitation ( $\xi_f = 0.1$ ). The other structural parameters are assumed to be  $\omega_s = 8.4\pi$ ,  $\xi_s = 0.03$ ,  $\omega_f = 0.9 \times \omega_s$ ,  $S_0 = 0.03$ ,  $\mu = 2\%$  and  $T = 10$  s. For the optimization, the genetic algorithm routine available in Matlab is used.

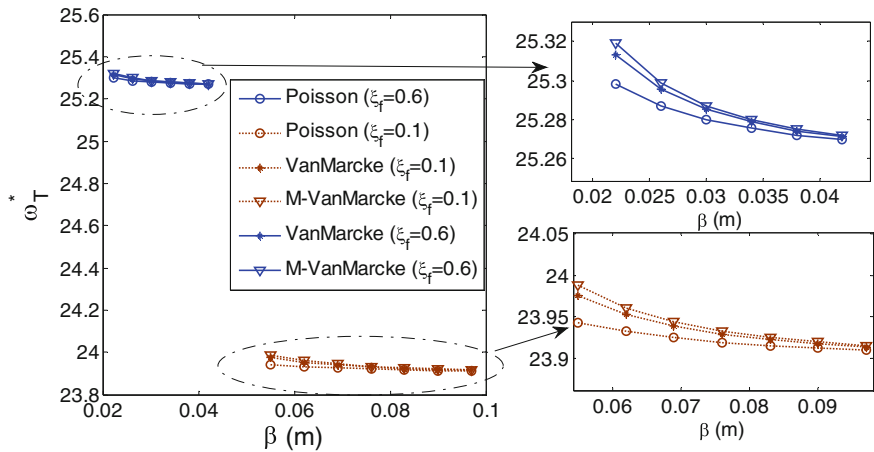
Figure 2 shows the evolutions of the optimized failure probabilities when varying the threshold values for the two cases, broadband and narrowband excitations.

Figure 2 demonstrate that the optimized failure probabilities strongly depend on the threshold values and on the frequency content of the excitation (i.e. value of  $\xi_f$ ). Also, it has been observed that, in one hand, the results obtained in the case of broadband excitation are very close especially for high threshold values and in the other hand, that the error is more significant for the narrowband case, especially for low threshold values. This fact is completely predictable because the Poisson assumption is less appropriate for narrowband processes where the assumption of independent outcrossing is seriously in error.

In Fig. 3 are shown the corresponding optimum TMD parameters obtained in the two cases of frequency content (broadband and narrowband excitations) and with



**Fig. 2** Optimized failure probabilities considering narrowband and broadband excitations; **a** linear scale, **b** semi-log scale



**Fig. 3** Optimum natural frequencies (narrowband and broadband excitations)

variation of threshold values. The inspection of this figure shows that the optimum natural frequencies of the TMD strongly depend on the nature of the excitation. Besides, they are roughly constant when varying the threshold values especially when the Poisson assumption is adopted, for the two cases (broadband and narrowband excitations).

The same remarks done for Fig. 4 can be observed for the optimum damping ratios in Fig. 4, except for low threshold values in the narrowband case.

For further investigations, the relative error between the optimum TMD parameters obtained using the proposed approximations, are presented in Figs. 5 and 6 (for the narrowband case) and in Figs. 7 and 8 (for the broadband case). The

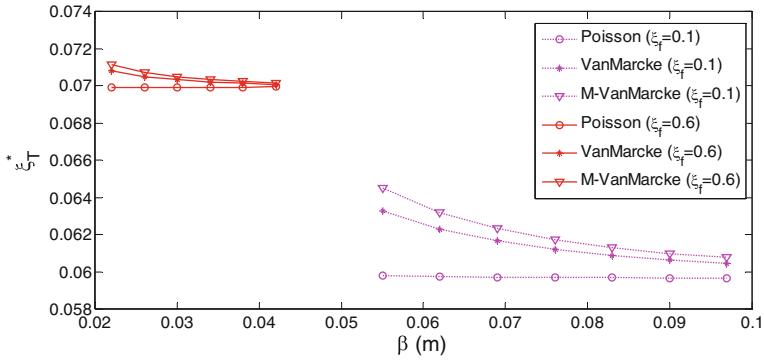


Fig. 4 Optimum damping ratio (narrowband and broadband excitations)

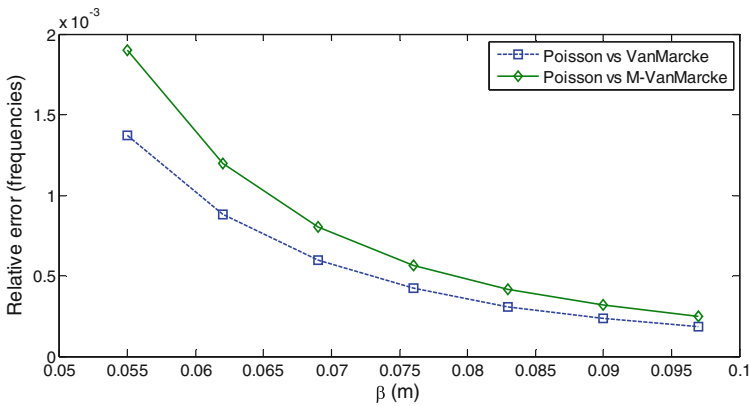


Fig. 5 Relative error between the optimum frequencies (narrowband excitation,  $\xi_f = 0.1$ )

observation of these figures shows that the relative error between the Poisson and the Vanmarcke approximations are always the smaller and tends to zero as the threshold value  $\beta$  increases.

Besides, even for the case of narrowband excitation (Fig. 5), the relative error (Poisson vs. Vanmarcke) for the optimum frequencies is less than 0.02 % while it's less than 1.4 % for the optimum damping ratios (Fig. 6). For the broadband excitation case, the relative error (Poisson vs. Vanmarcke) is found less than 0.07 % for the optimum frequencies and it is less than 0.2 % for the damping ratio.

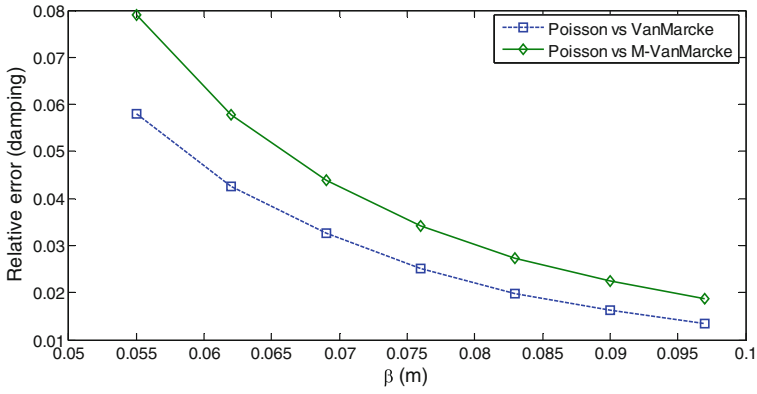


Fig. 6 Relative error between the optimum damping ratios (narrowband excitation,  $\xi_f = 0.1$ )

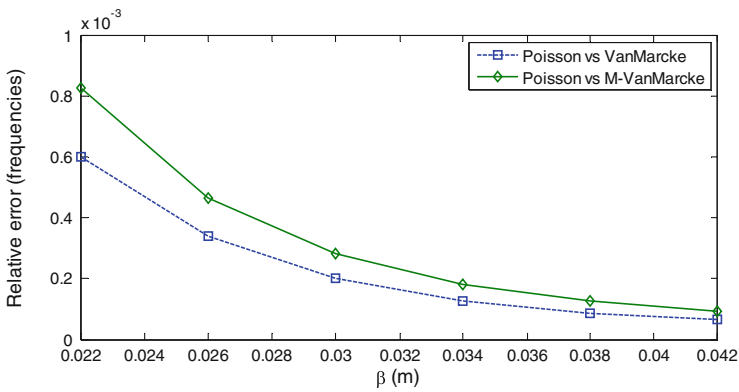


Fig. 7 Relative error between the optimum frequencies (broadband excitation  $\xi_f = 0.6$ )

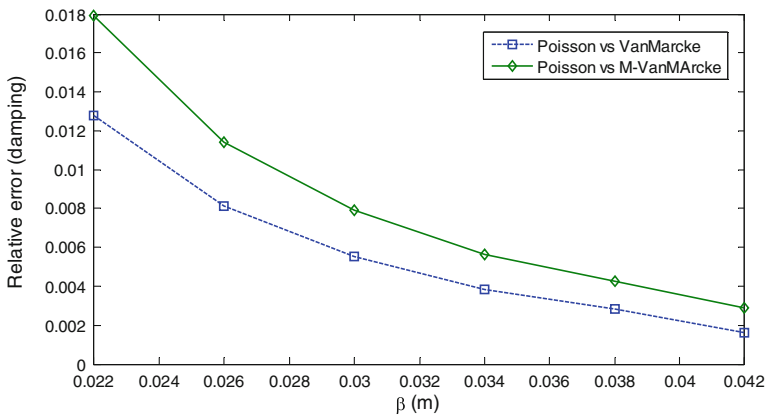


Fig. 8 Relative error between the damping ratios (broadband excitation,  $\xi_f = 0.6$ )

## 5 Concluding Remarks

In this paper a RBO problem of TMD parameters under stationary stochastic loading is considered and three approximations, for the failure analysis, are used. The first one is the Poisson approximation, which is the simpler, the other are the Vanmarcke and the modified Vanmarcke approximations.

In spite of the fact that the Poisson approximation is only suitable for high threshold values and/or for broadband processes, the obtained results showed that the Poisson approximation is valid and can be used, in the context of RBO problem, with very high threshold value even with narrowband excitation.

Indeed, it has been found that the relative error between the optimum TMD parameters based on the Poisson approximation and those based on Vanmarcke approximations, tends to zeros as the threshold value increases. This result is valid for both broadband and narrowband excitations.

After taking into account the nature of the excitation, the designer has only to choose a threshold value sufficiently high and the optimized TMD parameters based on Poisson approximation will be relatively accurate.

## References

- Carlo Marano G, Greco R, Chiaia B (2010) A comparison between different optimization criteria for tuned mass dampers design. *J Sound Vib* 329:4880–4890
- Lutes LD, Sarkani S (2004) *Random vibrations*. Elsevier
- Marano GC, Greco R, Sgobba S (2010) A comparison between different robust optimum design approaches: application to tuned mass dampers. *Probab Eng Mech* 25:108–118
- Mrabet E, Guedri M, Ichchou M et al (2015) New approaches in reliability based optimization of tuned mass damper in presence of uncertain bounded parameters. *J Sound Vib* 355:93–116
- Vanmarcke EH (1975) On the distribution of the first-passage time for normal stationary random processes. *J Appl Mech-T Asme* 42:215–220

# FE Modeling of Wear Mechanisms in UD-GFRP Composites Using Single-Indenter Scratch Test: A Micromechanical Approach

S. Mzali, F. Elwasli, A. Mkaddem and S. Mezlini

**Abstract** This paper addresses the sensitivity of the elementary wear mechanisms of UD-GFRP composite to the tribological parameters. A scanning electron microscope (SEM) was used to assess the wear mechanisms on the scratched UD-GFRP composite for different test conditions. A 3D FE micromechanical models was developed using ABAQUS/Explicit to simulate single indenter scratch test (SST). Both material behavior and damage of fibers and matrix are described using Johnson Cook behavior law. However, the fiber/matrix interface was modeled using the cohesive zone approach by the mean of the cohesive elements. The numerical results show a good agreement with the experimental wear mechanisms.

**Keywords** Scratch test · GFRP · Wear · Friction · Scratch map · FE

---

S. Mzali (✉) · F. Elwasli · S. Mezlini  
Laboratoire Génie Mécanique, École Nationale d'Ingénieurs de Monastir,  
Université de Monastir, Monastir, Tunisia  
e-mail: mzalislah@hotmail.com

F. Elwasli  
e-mail: elwaslifatma@gmail.com

S. Mezlini  
e-mail: salah.mezlini@gmail.com

A. Mkaddem  
Mechanical Engineering Department, Faculty of Engineering,  
University of Jeddah, PO. Box 80327, 21589 Jeddah, Saudi Arabia  
e-mail: amkaddem@uj.edu.sa

A. Mkaddem  
MSMP-EA7350 Arts et Métiers ParisTech, Rue Saint Dominique,  
BP. 508, 51006 Châlons-en-Champagne, France



## 1 Introduction

The mechanical characterization of surfaces is a major challenge today for the development of some industrial sectors such as aeronautics, astronautics, and transports. The mechanical characterization of surfaces requires a thorough knowledge of the scratch tests. Indeed, they identify locally surface mechanical properties, namely elasticity and visco-plasticity, and interface behavior such as friction, adhesion, and wear. Scratch test is widely used to characterize both heterogeneous (Mezlini et al. 2009; Gyawali et al. 2016) and homogeneous (Elleuch et al. 2006) materials tribological behavior.

Kim et al. (2012) studied the friction and the wear of polyamide 12 (PA12) reinforced with short glass fibers by using the block-on-ring tribotester. They studied the effect of the rate and the direction of the fibers on the tribological behavior. They demonstrated that the composite wear rate decreases with the increase of the fiber amount. A better wear resistance was detected with a composite containing 30 wt% of glass fiber. They also proved that the friction and the wear of the composite material were more dependent on the temperature and the fiber amount.

Using pin-on-disk configuration, Quintelier et al. (2006) studied the behavior of glass fiber reinforced polyester composites. They proved that regardless of the orientation of fibers, the initial breakage of the fibers is still in a cross section. In the case of a perpendicular orientation, the initial fracture of the fiber may be caused by bending introducing longitudinal strains. If the orientation is parallel to the direction of displacement, high stresses are the cause of the shearing forces. According the SEM observations they identified several typical composite wear mechanisms, namely, fiber breaking, fiber/matrix interface debonding, matrix fracture and fiber pull out.

The experiments are insufficient and incomplete to give a better understanding of the scratch materials behavior due to the complexities of the existing phenomena. Hence the numerical analysis can be used to support the experimental studies. Numerous studies of polymeric (Wredenberg and Larsson 2009) and metallic (Meneses-Amador et al. 2015) materials, based on a numerical approach, have been developed in recent years. However, the numerical simulation of composite materials remains very challenging and understudied.

Goda and Varadi (2002) have investigated the contact, the strain and the stress caused by scratching the surface of a unidirectional composite using a steel asperity. They proved that the finite element micromechanical model developed is more appropriate than the equivalent macro model generally used to model the wear mechanisms (Perillo et al. 2015). They examined the composite wear mechanisms and perceived the typical wear mechanisms using the micromechanical finite element models, namely the fibers cracking the shear rupture of the matrix and the fiber/matrix interface debonding.

The same micromechanical finite element model was used by Friedrich et al. (2002). They simulated the scratch of glass fiber reinforced polyester composite in

the parallel fibers orientation direction. The prevailing observed wear mechanisms are the thinning of the fiber, the fiber/matrix interface debonding and the wear of the matrix. However, the fibers thinning and cracking, the shearing of the matrix and the debonding of the fiber/matrix interface, for the anti-parallel fibers orientation, are the most prevailing wear mechanisms. They proved that the numerical analysis and the experiment results are in a good agreement.

The present paper aims at the development of a micromechanical FE model for the simulation of different wear mechanisms in UD-GFRP composite when it's scratching using a conical steel indenter. Particular attention is given to the effects of tribological parameters, namely, the normal load and the attack angle. The finite element micromechanical model proposed in this study was enough beneficial to give a good predict of the elementary wear mechanisms depending on the tribological parameters for SST.

## 2 Materials and Methods

### 2.1 Material

A unidirectional glass fiber reinforced polyester (UD-GFRP) composite material was used in this study. It is obtained by pultrusion as rectangular section bar. E glass long fiber with an average diameter of 23  $\mu\text{m}$  and a weight percentage of 21 % was chosen as reinforcement material. This UD-GFRP composite contain 14 % wt% clay filler (ASP400). Samples of  $50 \times 50 \times 6 \text{ mm}^3$  were already prepared and the scratches were realized on  $50 \times 50 \text{ mm}^2$  faces.

### 2.2 Scratch Test

Single indenter scratches were firstly performed using a scratch device as detailed elsewhere (Mzali et al. 2013). In this study, the scratch length and velocity are both fixed at 20 mm and 210 mm/min, respectively. However, the normal load are taken to range in 10–50 N by using dead weights and a range of attack angle from  $10^\circ$  to  $60^\circ$  was achieved. A single high speed steel conical indenter was firstly used. Throughout the study all tests were performed in dry environment at room temperature and repeated at least three times with the same conditions. The different damage mechanisms were inspected using Scanning Electronic Microscope (SEM). Using Coulomb's law the apparent friction coefficient ( $\mu_{\text{app}}$ ) was calculated as the ratio of the tangential force to the normal load.

### 2.3 Finite Element Micromechanical Modeling

The finite element micromechanical models were created and solved by the FE ABAQUS/Explicit code. In order to avoid convergence problems of solution the dynamic/explicit integration scheme was purposely chosen. In the implementation of composite material micromechanical models, several hypotheses regarding the constituents of the composite material, including the reinforcement, the matrix and the interface are chosen. In this model, hexagonal regular fiber arrangement was selected. The fiber weight percentage adopted is 21 %.

#### 2.3.1 Material Behavior

Both the fiber and the matrix were assimilated to homogenous isotropic elasto-plastic material. That's why, Johnson-Cook constitutive criteria (Johnson and Cook 1983) were used for modeling both fibers and matrix behavior and damage. Table 1 summarizes the fibers and the matrix properties and damage parameters considered in the proposed models. Based on Tenorio and Pelegri (2013) assumptions, the effects of strain rate and temperature are neglected, as well as damage parameters d2, d3, d4 and d5. The parameters of the Johnson-Cook law are determined by inverse approach (Kim et al. 2013; Langroudi 1999) via a routine developed using Matlab.

The homogenized composite is modeled using the equivalent homogeneous orthotropic material (EHOM) hypothesis. The homogenized composite properties parameters are determined by applying the homogenization approach developed by Chamis (1989).

$$E_1 = V^f E^f + V^m E^m \quad (1)$$

**Table 1** The fibers and the matrix properties and damage parameters

Material properties	Fiber (Kim et al. 2013)	Matrix (Langroudi 1999)
E (GPa)	54	7
$\nu$	0.21	0,4
$\rho$	2550	1200
<i>Johnson-Cook behavior parameters</i>		
A (MPa)	1340	49
B (MPa)	15,190	11
n	0.99	0.51
<i>Johnson-Cook damage parameters</i>		
d1	$10^{-7}$	$10^{-4}$
$G_f$ (J/m <sup>2</sup> )	500	100 (Vajari 2015)

**Table 2** The homogenized composite behavior properties

Mechanical properties	
$E_1$ (GPa)	22.98
$E_2$ (GPa)	14.21
$E_3$ (GPa)	14.21
$G_{12}$ (GPa)	5.18
$G_{13}$ (GPa)	5.18
$G_{23}$ (GPa)	5.18
$\nu_{12}$	0.33
$\nu_{13}$	0.33
$\nu_{23}$	0.37

**Table 3** The homogenized composite damage properties

Traction-separation law (QUADS)	
<i>Damage initiation</i>	
$t_n^0$ (MPa)	50
$t_s^0$ (MPa)	75
$t_t^0$ (MPa)	75
<i>Damage evolution</i>	
$G_n^C$ (J/m <sup>2</sup> )	10
$G_s^C$ (J/m <sup>2</sup> )	25
$G_t^C$ (J/m <sup>2</sup> )	25

$$E_2 = E_3 = \frac{E^m}{1 - \sqrt{V^f} \left(1 - \frac{E^m}{E^f}\right)} \tag{2}$$

$$\nu_{12} = \nu_{13} = V^f \nu^f + V^m \nu^m \tag{3}$$

$$G_{12} = G_{13} = G_{23} = \frac{G^m}{1 - \sqrt{V^f} \left(1 - \frac{G^m}{G^f}\right)} \tag{4}$$

$$\nu_{23} = \frac{E_2}{2G_{23}} - 1 \tag{5}$$

With  $E_i$ ,  $G_{ij}$  et  $\nu_{ij}$  are the Young’s modulus, the shear modulus and the Poisson’s ratios of the homogenized composite in i and j considered directions, respectively.  $E^f$  and  $E^m$  are the fibers and matrix Young’s modulus, respectively.  $\nu^f$  and  $\nu^m$  are the fibers and matrix Poisson’s ratios, respectively. And  $V^f$  and  $V^m$  are the fibers and the matrix volume fraction respectively (Table 2).

The concept of a cohesive zone model is generally used for the simulation of interfaces, adhesives and seals. The theory of cohesive method is modeled in ABAQUS through traction-separation law (Abaqus 6.12 2012). This model shows originally, an elastic-linear behavior followed by the initiation and evolution of damage. The fiber/matrix interface properties are listed in Table 3.

### 2.3.2 Mesh and Boundary Conditions

In order to simulate the SST using conical indenter, a 3D micromechanical model was developed. In this model, we simulate only the zone of interest of the sample in order to reduce the CPU time. The specimen is modeled as a rectangular parallelepiped of  $187 \times 200 \times 800 \mu\text{m}^3$  which is divided into two parts. The lower part represents the homogenized composite. However the top part represents the composite which is modeled by three components, namely, the matrix, the fibers, and the interfaces. Therefore, 20 fibers and 20 interfaces are used. Figure 1 presents boundary conditions and mesh constructions. A convergence test was conducted and we define for this model a mesh with 403,128 nodes and 316,215 elements in which the smallest element size is  $3.75 \times 10^{-6}$  m. A very fine mesh has been adopted close to the contact zone. In this model, the interactions indenter/fiber and indenter/matrix are defined by contact pairs' algorithm (surface to surface contact) with constant interfacial friction coefficient of 0.125. However, interactions at interfaces fiber/fiber and fiber/matrix are defined by a general contact algorithm. The two contacts are controlled by the Coulomb law.

The SST simulation can be divided into two steps. In the first one, the indenter moves vertically against the fixed sample until reaching the target penetration. Then, the scratching step begins and the indenter tangential sliding continues along the specified scratch length of  $160 \mu\text{m}$ . The bottom of the composite sample was constrained whereas symmetry conditions have been applied to its left and right sides.

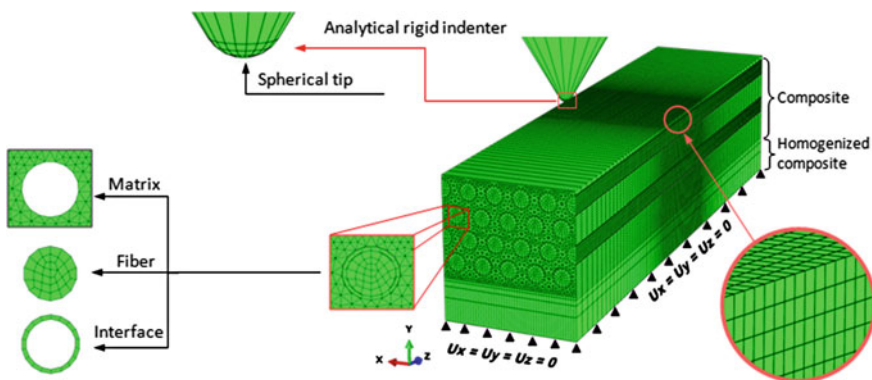


Fig. 1 Boundary conditions and mesh construction of SST model

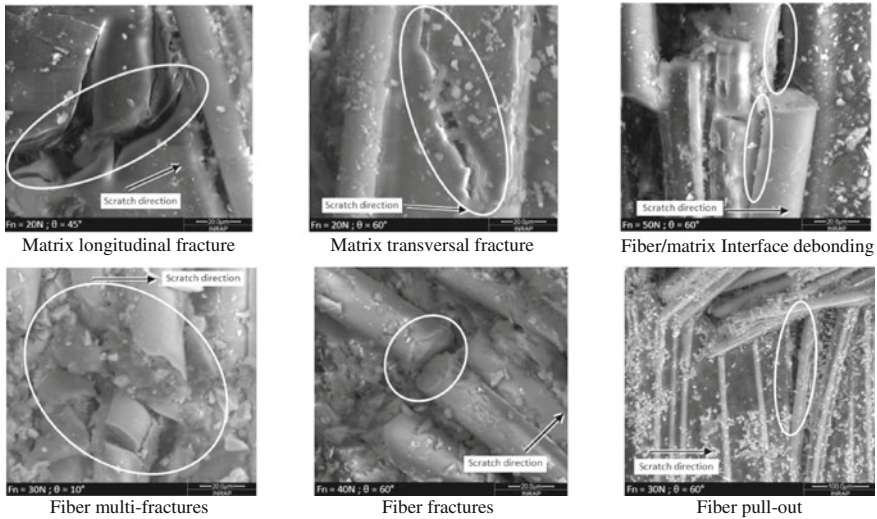


Fig. 2 Typical SST wear mechanisms

### 3 Results

#### 3.1 SST Wear Mechanisms

To highlight the different wear mechanisms, SEM observations were performed. In order to have a better understanding of the composite material behavior, microscopic analysis has been done. Figure 2 illustrates different damage mechanisms obtained by SST. Several wear mechanisms is observed, particularly, the fibers fracture, the fibers pull out, the matrix longitudinal and transverse fracture, the fiber/matrix interface debonding and the fibers multi-fractures. These different wear mechanisms can coexist in the same scratch. However the dominant damage mode differs depending on the tribological parameters.

#### 3.2 Results and Discussion

##### 3.2.1 Friction to Penetration and Attack Angle Sensitivity

In order to study the penetration effect, numerical simulations of the SST using an attack angles of 60° and different penetration depths varying from 5 to 100 μm are performed. The selection of these penetration depths was done so that we swept all possible configurations. Using the lower one (5 μm), the indenter doesn't reach the first fibers layer. With a penetration depth of 25 μm the indenter doesn't exceed the

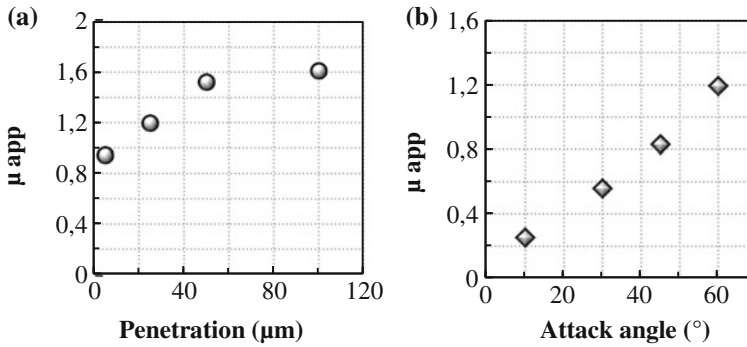


**Fig. 3** Predicted apparent friction coefficient versus **a** penetration ( $\theta = 60^\circ$ ), and **b** attack angle ( $p = 25 \mu\text{m}$ )

first fiber layer. Using a penetration depth of  $50 \mu\text{m}$  affects only the first fibers layer. However, when the indenter penetrates  $100 \mu\text{m}$  against the sample it affects several fibers layers. Figure 3a presents the evolution of the predicted apparent friction coefficient versus the penetration depth. It shows that the predicted apparent friction coefficient increases with the penetration depth with a more pronounced increase for a penetration less than  $50 \mu\text{m}$ . Actually, when the penetration depth passes from  $5$  to  $50 \mu\text{m}$ , it increases by about  $60\%$ , while between  $50$  and  $100 \mu\text{m}$  an increase of  $6\%$  only is observed.

To investigate the effect of the attack angle, numerical simulations of the SST using the same attack angles used in the experimental study ( $10^\circ$ ,  $30^\circ$ ,  $45^\circ$  and  $60^\circ$ ) are performed. The penetration depth ( $p$ ) is  $25 \mu\text{m}$ . The tip radius of  $10 \mu\text{m}$  is selected such that it promotes the effect of the conical part of the indenter. Figure 3b shows the evolution of the predicted apparent friction coefficient versus the attack angle. A linear increase with the attack angle is observed. Therefore the predicted apparent friction coefficient exhibits higher sensitivity to the indenter geometry and particularly to the attack angle. This result is already experimentally proven. Under these conditions, at low attack angles, the contact surface is larger, the indenter acts like a spherical pin and the material is not yet damaged. The indenter sliding induces a low resistance force. Consequently, the apparent friction coefficient is low of about  $0.25$ . However, for large attack angles, the contact surface is much lower. Furthermore, the penetration and the sliding of the indenter against the damaged material causes a greater resistance force giving rise to a high apparent friction coefficient.

The proposed model allows also the simulation of the material removal mechanisms for a fixed penetration depth of  $25 \mu\text{m}$ . Figure 4 illustrates the typical results versus the two extreme attack angles given by the proposed SST model. The numerical simulations allow drawing the following remarks.

For the low angle of attack of  $10^\circ$ , the material flow occurs, the matrix is plastically deformed with the appearance of some region of transverse fracture of the matrix just above superficial fibers layer. Similar results have been proved

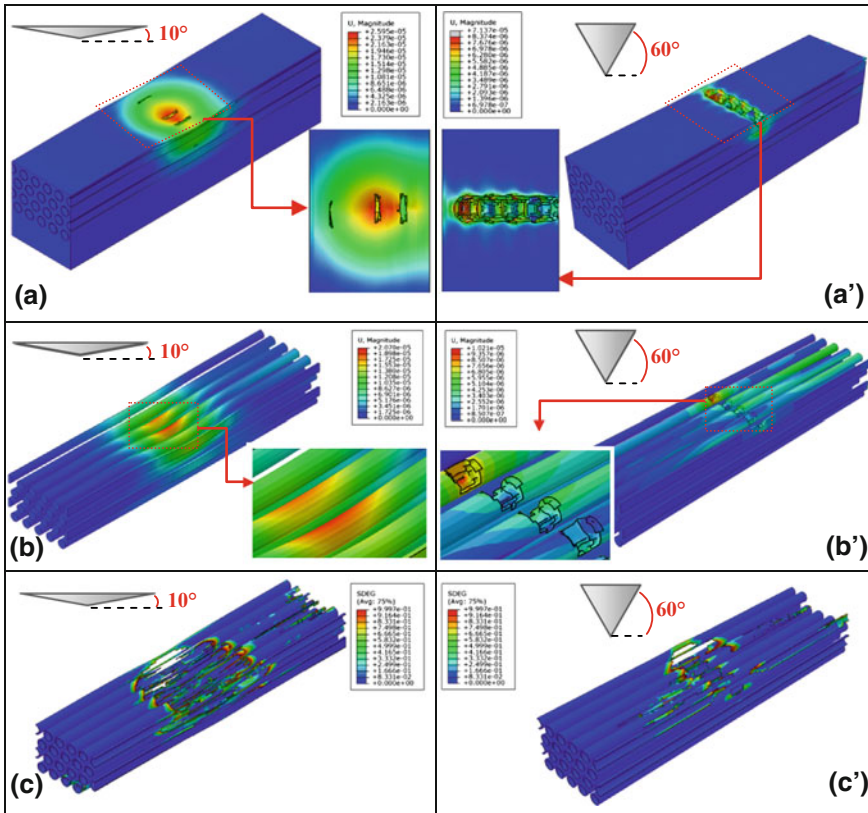


**Fig. 4** Material removal process obtained by the proposed SST model for the extreme attack angles ( $10^\circ$  and  $60^\circ$ ) of **a** the matrix, **b** the fibers, and **c** the fiber/matrix interface

experimentally (Fig. 4a). However, the fibers remain intact and no fracture occurs (Fig. 4b). The only dominant damage mechanism is the fiber/matrix interface debonding (Fig. 4c) which is spread over a wide area below the contact region between the indenter and the sample. This latter wear mechanism can't be seen experimentally.

However, for high attack angles, damage of the matrix (Fig. 4a'), fiber (Fig. 4b') and the fiber/matrix interface (Fig. 4c') is observed. The breaking of the matrix is localized essentially at the contact region with the indenter. The indenter reaches the first layer of fibers without exceeding the fiber diameter and material removal occurs. Under these conditions, the increase of the angle of attack causes the transition of the wear mechanisms from ploughing to the matrix break, the fiber damage and the interface debonding. Comparing to the SEM observation already done by Mzali et al. (2013), similar wear mechanisms was found experimentally under almost similar conditions.



## 4 Conclusion

In this paper, the investigation of elementary wear mechanisms in SST has been carried out. Both experimental and numerical approaches were used in order to understand the evolution of damage mechanisms. Particular attention is given to correlating the tribological parameters to the wear mechanisms. According the results the following conclusions can be hence drawn.

- $\mu_{app}$  obtained by the SST display a high dependency to the tribological parameters. Increasing the penetration depth increases  $\mu_{app}$ . A more pronounced sensitivity of  $\mu_{app}$  to the attack angle was demonstrated. As the attack angle increases as  $\mu_{app}$  increases and the wear mechanisms switch from ploughing to fibers fracture and fibers fracture and pull-out.
- An SST micromechanical 3D model was found very useful to predict the elementary wear mechanisms of the glass fiber reinforced polyester composite. The simulation results revealing the composite microscopic damage mechanisms are in good agreement with the experimental microscopic observations.

## References

- Abaqus 6.12 (2012) Analysis user's manual volume V: prescribed conditions, constraints & interactions. Abaqus Inc. [https://things.maths.cam.ac.uk/computing/software/abaqus\\_docs/docs/v6.12/pdf\\_books/ANALYSIS\\_5.pdf](https://things.maths.cam.ac.uk/computing/software/abaqus_docs/docs/v6.12/pdf_books/ANALYSIS_5.pdf)
- Chamis CC (1989) Mechanics of composite materials: past, present, and future. *J Compos Tech Res. ASTM* 1:3–14. doi:10.1520/CTR10143J
- Elleuch K, Mezlini S, Guermazi N, Kapsa Ph (2006) Abrasive wear of aluminum alloys rubbed against sand. *Wear* 261:1316–1321. doi:10.1016/j.wear.2006.03.016
- Friedrich K, Varadi K, Goda T, Giertzsch H (2002) Finite element analysis of a polymer composite subjected to a sliding steel asperity: part II: parallel and anti-parallel fibre orientations. *J Mater Sci* 37:3497–3507. doi:10.1023/A:1016571324836
- Goda T, Varadi K (2002) Finite element analysis of a polymer composite subjected to a sliding steel asperity: part I normal fibre orientation. *J Mater Sci* 37:1575–1583. doi:10.1023/A:1014937322276
- Gyawali G, Joshi B, Tripathi K, Lee SW (2016) Preparation of Ni–W–Si<sub>3</sub>N<sub>4</sub> composite coating sand evaluation of their scratch resistance properties. *Ceram Int* 2:3497–3503. doi:10.1016/j.ceramint.2015.10.153
- Johnson GR and Cook WH (1983) A constitutive model and data for metals subjected to large strains, high strain rate and high temperature. In: Proceedings of 7th international symposium on ballistics, <http://www.adhaesion.com/binary/A%20constitutive%20model%20and%20data%20for%20metals%20subjected%20to%20large%20strains,%20high%20strain%20rates%20and%20high%20temperatures.pdf>
- Kim T, Oshima K, Kawada H (2013) Impact tensile properties and strength development mechanism of glass for reinforcement fiber. *J Phys (Conf Ser)* 451:1–6. doi:10.1088/1742-6596/451/1/012006
- Kim SS, Shin MW, Jang H (2012) Tribological properties of short glass fiber reinforced polyamide 12 sliding on medium carbon steel. *Wear* 274–275:34–42. doi:10.1016/j.wear.2011.08.009

- Langroudi AE (1999) Etude de la déformation viscoélastique et plastique du PET amorphe et semi-cristallin autour de la transition vitreuse, PhD Thesis, National Institute of Applied Sciences Lyon. <http://theses.insa-lyon.fr/publication/1999ISAL0053/these.pdf>
- Meneses-Amador A, Jiménez-Tinoco LF et al (2015) Numerical evaluation of scratch tests on boride layers. *Surf. Coat. Tech.* 284:182–191. doi:10.1016/j.surfcoat.2015.06.088
- Mezlini S, Ben Tkaya M, El Mansori M, Zahouani H, Kapsa Ph (2009) Correlation between tribological parameters and wear mechanisms of homogeneous and heterogeneous material. *Tribol Lett* 33:153–159. doi:10.1007/s11249-008-9403-5
- Mzali S, Mezlini S, Zidi M (2013) Effect of tribological parameters on scratch behavior of a unidirectional E-glass fiber reinforced polyester composite. *Tribol Surf Mater Interfaces* 4:175–182. doi:10.1179/1751584X13Y.0000000048
- Perillo G, Grytten F, Sørbo S, Delhaye V (2015) Numerical/experimental impact events on filament wound composite pressure vessel. *Composites-Part B* 69:406–417. doi:10.1016/j.compositesb.2014.10.030
- Quintelier J, De Baets P, Samyn P, Van Hemelrijck D (2006) On the SEM features of glass–polyester composite system subjected to dry sliding wear. *Wear* 261:703–714. doi:10.1016/j.wear.2006.01.006
- Tenorio M, Pelegri AA (2013) Interfacial debonding of glass single fiber composites using the Johnson-Cook failure model. In: ASME 2013 international mechanical engineering congress and exposition ASME, pp 16–23. doi:10.1115/IMECE2013-66873
- Vajari DA (2015) A micromechanical study of porous composites under longitudinal shear and transverse normal loading. *Compos Struct* 125:266–276. doi:10.1016/j.compstruct.2015.02.026
- Wredenberg F, Larsson PL (2009) Scratch testing of metals and polymers: experiments and numerics. *Wear* 266:76–83. doi:10.1016/j.wear.2008.05.014

# Dynamic Analysis of the Perforation of Aluminum Alloy at Low Velocity Impact

S. Koubaa, J. Mars, M. Wali and F. Dammak

**Abstract** A finite element implementation of an anisotropic plasticity model for aluminum AA5754-O in impact simulations was performed, particularly for the case of perforation on low velocity (up to about 25 m/s). The elasto-viscoplastic model includes isotropic elasticity, anisotropic yielding, associated plastic flow and mixed non-linear isotropic/kinematic hardening. Coupling between elasto-viscoplastic model and isotropic ductile damage is investigated. Strain rate is integrated in numerical modeling. The material model is implemented into a user-defined material (VUMAT) subroutine for the commercial finite element code ABAQUS/Explicit to predict the numerical response of circular aluminum plate subjected to low velocity impact. Results include the effect of anisotropy on the material behavior. It is shown that anisotropy plays a significant role in penetration of the present plate material.

**Keywords** Dynamic analysis · Impact velocity · Perforation · Aluminum · Damage · Strain rate · Anisotropy

---

S. Koubaa (✉) · J. Mars · M. Wali · F. Dammak  
Mechanical Modeling and Manufacturing Laboratory (LA2MP), National Engineering  
School of Sfax, University of Sfax, B.P W3038, Sfax, Tunisia  
e-mail: koubaasana@yahoo.fr

J. Mars  
e-mail: jamelmars@yahoo.fr

M. Wali  
e-mail: mondherwali@yahoo.fr

F. Dammak  
e-mail: fakhreddine.dammak@enis.rnu.tn

## 1 Introduction

Nowadays, structural impact engineering is a common field in sectors as nuclear, chemical, transport, offshore, naval, aerospace, defense and process industries. The study of the response of structures subjected to intense dynamic loads, which produce large inelastic deformation, and failure has become increasingly important in structural design and safety calculation. The literature on impact loading includes a variety of materials, thicknesses and projectile geometries, as well as velocity ranges from low (Fagerholt et al. 2010; Mohotti et al. 2014; Grytten et al. 2009) to intense impact (Mohotti et al. 2013).

It is well known that the energy absorption capacity per unit density of aluminum is high when compared to conventional steel. Therefore, accurate constitutive models for aluminum alloys have been of significant interest.

A particular case of structural impact by missiles or projectiles is perforation of metal plating. Many articles were written on the perforation of aluminum plates for various ranges of velocities, (Marvin et al. 1978, Wilkins 1978; Corran et al. 1983, Iqbal et al. 2006). In the past, more attention was given to experimentally investigate the impact behavior of target and projectile (Børvik et al. 2004) and to construct approximate analytical models (Børvik et al. 2009). For instance, Jones and Paik (2012) focused on the low-velocity (up to about 20 m/s) and moderate-velocity (20–300 m/s, approximately) perforation of steel plates struck by projectiles having cylindrical bodies and various shaped impact faces. Nevertheless, few reported studies exist in which experimental results are directly compared with those found from finite element simulation. In numerical studies, the Johnson Cook phenomenological behavior law of the plate's material was considered (Antoinat et al. 2015; Iqbal et al. 2010; Rodriguez-Martinez et al. 2012; Dean et al. 2009; Abdulhamid et al. 2013; Børvik et al. 2009). Nevertheless, the anisotropy is an important aspect that should be taken into account when modeling inelastic materials impact behavior. Few studies were interested in anisotropy (Grytten et al. 2009; Barlat et al. 2005). A recent article (Mars et al. 2015) has discussed the influence of anisotropy on low velocity impact on aluminum plates.

This article is concerned primarily with finite element simulation of the perforation of aluminum alloy plates struck by projectiles travelling at low-initial impact velocities (say up to about 25 m/s). For this, a two-equation integration algorithm of a generalized quadratic yield criterion of Hill based on the mixed non-linear isotropic/kinematic hardening models of Chaboche is developed for computing elasto-viscoplastic stress during impact. The strain rate effect is integrated. The isotropic damage model is considered. The numerical simulation of the perforation problem is carried out using the commercial software ABAQUS/Explicit. The material constitutive law is implemented in a user-subroutine VUMAT. The effect of anisotropy on low velocity impact of aluminum plates is investigated so that a comparison is made between simulation results of the developed model and that derived from Johnson-Cook behavior.

## 2 Numerical Simulation

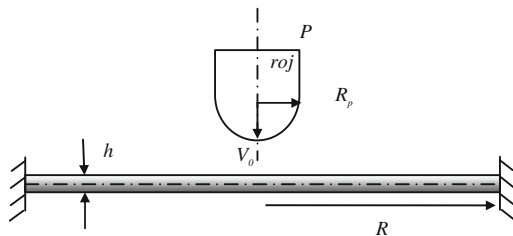
In this section, numerical simulations are conducted on the perforation of aluminum alloy plates struck by rigid hemispherical-nosed projectiles, using dynamic finite element code ABAQUS/Explicit. The target was modeled using the elasto-viscoplastic constitutive relation, which was implemented as a user-defined material model by means of a subroutine (VUMAT).

### 2.1 Finite Element Model

A clamped circular plate impacted at its center by a cylindrical impactor with hemispherical nose is considered. The proposed finite element models of projectiles are shown in Fig. 1. The projectile has the diameter of 6.35 mm and the circular shape of target aluminum plate has the radius of 60 and 0.5 mm thickness. The initial velocity of impactor is  $V_0$ . The deformation of the striker during impact is neglected and so it can be modeled as an analytical rigid surface with an associated mass reference point.

A 3D finite element model for the simulation of the penetration process was developed ABAQUS/VUMAT. The modeling is carried out by taking into account the geometric symmetry of the circular plate. Indeed, in three dimensional analyses, only the  $\frac{1}{4}$  of plate is taken into account in the impact analysis. The plate is meshed using 40000 C3D8R elements (8\_node linear brick, reduced integration with hourglass control). Mesh pattern of the area surrounding the contact region is depicted in Fig. 2 (0.4 mm in radius direction and 5 elements in thickness). Obviously, accurate results required fine mesh beneath the contact area and all the meshes contained three regions: a finely zoned region which had noticeable effect on computational accuracy, a coarsely zoned region which did not have noticeable effect on computational accuracy, and a transitional region between the two regions above. The element size in transitional region and coarsely zoned region was increased from the central part to the outer part of the target.

**Fig. 1** Cylindrical projectile impacted circular plate



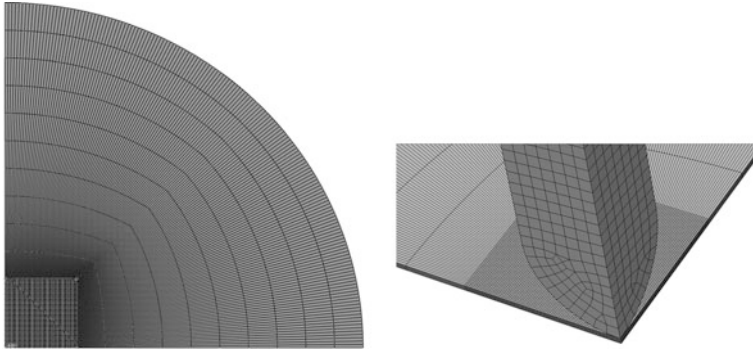


**Fig. 2** Three-dimensional problem: rigid impactor

A hard contact law is used for modeling the contact. To define contact interactions, the default finite-sliding formulation (surface to surface contact) is used. In order to define the boundary conditions for the impactor, the movement of the impactor is restrained in all directions except translation along normal vector of the plate. The validation of contact model was assessed in Mars et al. (2015).

## 2.2 Constitutive Relations

According to the damage model of Lemaitre and Chaboche (1990), the Helmholtz free energy is taken as the thermodynamic potential or state potential and is defined as

$$\begin{aligned} \psi(\varepsilon^e, \alpha_k, r, d) &= \psi^e(\varepsilon^e, d) + \psi^p(\alpha_k, r) \\ &= \frac{1}{2}(1-d)\varepsilon^e : \mathbf{D} : \varepsilon^e + \psi_{iso}(r) + \frac{1}{2} \sum_{k=1}^M a_k \alpha_k : \alpha_k \end{aligned} \quad (1)$$

where  $\alpha_k$  and  $r$  are internal variables corresponding to kinematics and isotropic hardening respectively and  $d$  is the damage variable.

The Chaboche model is based on the assumption of the strain additivity

$$\varepsilon = \varepsilon^e + \varepsilon^p \quad (2)$$

The thermodynamic forces associated with the internal variables can be determined as

$$\boldsymbol{\sigma} = \frac{\partial \psi}{\partial \boldsymbol{\varepsilon}^e} = (1 - d)\mathbf{D} : \boldsymbol{\varepsilon}^e \tag{3}$$

$$\mathbf{X}_k = \frac{\partial \psi}{\partial \boldsymbol{\alpha}_k} = a_k \boldsymbol{\alpha}_k \tag{4}$$

$$R = \frac{\partial \psi}{\partial r} \tag{5}$$

$$Y = -\frac{\partial \psi}{\partial d} = \frac{1}{2} \boldsymbol{\varepsilon}^e : \mathbf{D} : \boldsymbol{\varepsilon}^e \tag{6}$$

where  $\boldsymbol{\sigma}$  is the stress tensor,  $\mathbf{D}$  is the general elastic operator,  $\psi_{iso}(r)$  represents the potential associated with isotropic hardening,  $R$  is the thermodynamic force associated with isotropic hardening, which is an arbitrary scalar function of the isotropic internal variable,  $r$ ,  $\mathbf{X}$  represents the so-called back-stress tensor and  $Y$  is the thermodynamic force associated with damage.

The evolution equations for all the internal variables are derived from complementary dissipation potential, as

$$\dot{\boldsymbol{\varepsilon}}^p = \dot{\gamma} \frac{\partial F}{\partial \boldsymbol{\sigma}} = \frac{\dot{\gamma} \sqrt{3/2}}{(1 - d)^\delta} \mathbf{n}, \mathbf{n} = \frac{1}{\varphi} \mathbf{P} \boldsymbol{\xi}, \boldsymbol{\xi} = \boldsymbol{\sigma} - \mathbf{X} \tag{7}$$

$$\dot{\boldsymbol{\alpha}}_k = -\dot{\gamma} \frac{\partial F}{\partial \mathbf{X}} = \dot{\boldsymbol{\varepsilon}}^p - \dot{\gamma} \frac{b_k}{a_k} \mathbf{X}_k \tag{8}$$

$$\dot{r} = -\dot{\gamma} \frac{\partial F}{\partial R} = \dot{\gamma} \tag{9}$$

$$\dot{d} = \dot{\gamma} \frac{\partial F}{\partial Y} = \dot{\gamma} \bar{Y}, \bar{Y} = \frac{1}{(1 - d)^\beta} \left( \frac{1 - d}{1 - \bar{h}d} \right)^{2s} \left\langle \frac{Y - Y_0}{S} \right\rangle^s, \begin{cases} \bar{h} = 1 & \text{if } \eta \geq 0 \\ \bar{h} = h & \text{if } \eta < 0 \end{cases} \tag{10}$$

where  $\dot{\gamma}$  is the plastic multiplier,  $\varphi = \|\boldsymbol{\xi}\|_p = \sqrt{\boldsymbol{\xi}^t \mathbf{P} \boldsymbol{\xi}}$  is a generalized quadratic yield function,  $\mathbf{P}$  is a fourth order tensor,  $\beta, s, S, Y_0$  and  $h \in [0, 1]$  are material parameters and  $\eta$  is the stress triaxiality. The notation  $\langle x \rangle$  indicates the positive value of  $x$  i.e.  $\langle x \rangle = x$  if  $x > 0$  and  $\langle x \rangle = 0$  if  $x \leq 0$ .

In three-dimensional cases, it is given by

$$\mathbf{P} = \frac{2}{3} \begin{bmatrix} H + G & -H & -G & 0 & 0 & 0 \\ & H + F & -F & 0 & 0 & 0 \\ & & F + G & 0 & 0 & 0 \\ & & & 2N & 0 & 0 \\ & \text{Sym} & & & 2M & 0 \\ & & & & & 2L \end{bmatrix} \tag{11}$$

where  $F$ ,  $G$ ,  $H$ ,  $N$ ,  $M$  and  $L$  are material constants obtained by tests of the material in different orientations. The  $J_2$  plasticity yield criterion is recovered using

$$F = G = H = 0.5, N = M = L = 1.5 \quad (12)$$

Finally, by using the fully implicit backward Euler integration procedure, the coupled elastoplastic-damage model is reduced to two scalar equations as

$$\begin{cases} f_1(\Delta\gamma, d) = \frac{\sqrt{3/2}\varphi}{(1-d)^{\delta}} - \sigma_p = 0 \\ f_2(\Delta\gamma, d) = d - d_n - \Delta\gamma\bar{Y} = 0 \end{cases} \quad (13)$$

The unknowns of this system of equations are the plastic multiplier  $\Delta\gamma$  and the damage variable  $d$ . The system of equations, Eq. (13), is solved with the Newton-Raphson method. More details can be found in Wali et al. (2015a, b).

### 2.3 Extension to Viscoplasticity

Structural impact involves events such as plastic flow at high strain rates, possible local increase of temperature, and material fracture. In this paper, the loading/unloading condition, Eq. (13), for rate dependent plasticity is rewritten in terms of the function  $g(\cdot)$  as

$$f_1 = g\left(\frac{\Delta\gamma}{\Delta t}\right) \quad \text{for } f_1 > 0 \Leftrightarrow \Delta\gamma > 0 \quad (14)$$

Combining Eq. (13) with the consistency condition Eq. (14) gives the modified system as

$$\begin{cases} h_1(\Delta\gamma, d) = \frac{\sqrt{3/2}\varphi}{(1-d)^{\delta}} - \left[\sigma_p + g\left(\frac{\Delta\gamma}{\Delta t}\right)\right] = 0 \\ h_2(\Delta\gamma, d) = d - d_n - \Delta\gamma\bar{Y} = 0 \end{cases} \quad (15)$$

Instead, simple models, to introduce the rate dependent plasticity, consisting of rather few parameters seem to be more popular. One of the most frequently used in impact problems is the Johnson-Cook model. In this case, the function  $g$  is written as

$$g\left(\frac{\Delta\gamma}{\Delta t}\right) = C\sigma_p \text{Log}\left(\frac{\Delta\gamma}{\Delta t}\right) \quad (16)$$



According to Smerd et al. (2005), the estimated C-value of AA5754-O is equal to 0.004556.

### 3 Simulation Results

Numerical simulations were carried out to study the response of Aluminum AA5754-O target subjected to low velocity impact of hemispherical nosed projectiles. The effect of anisotropy is studied by comparing the two elasto-plastic models:  $J_2$  and Hill yield criteria with isotropic and mixed non-linear isotropic/kinematic hardening models, IH and NKH, respectively. The mechanical properties of both Aluminum plate are gathered in Table 1. Hardening parameters of the aluminum AA5754-O material are presented in Table 2. The initial impact velocity was 25 m/s.

Figure 3 depicts the failure of aluminum plate at different stages. The beginning of the petalling process during perforation is always associated with fracture initiation and the outward move of petals as perforation continues. At the time step 0.56 ms, when using  $J_2$ -IH, dishing formation occurs and the following motion of projectiles leads to the crack propagation of the impacted surface. At the same time, for the case of Hill-NKH, the projectile body is already passed through the perforated surface and the petal formation generated around it as shown in Fig. 3. It is clear that the final form of the petal bending is different for the two models. Hence, anisotropy seems to have an effect on material behavior on low impact velocity. The resulting force versus time curves are compared when considering the Von Mises yield criterion with IH and the anisotropic Hill criterion with NKH. Figure 5 shows an important difference between the isotropic and anisotropic models as the force level is affected. This is in a good agreement with results in Figs. 3 and 5, as perforation appears more rapidly in the second case (Fig. 4).

**Table 1** Mechanical properties of the aluminum AA5754-O material

Elastic Prop.		Hill'48 coefficients				Damage data		
E (GPa)	$\nu$	F	G	H	N	s	S	$\delta$
70	0.33	0.748	0.572	0.403	1.467	1.0	1.25	1

**Table 2** Hardening parameters of the aluminum AA5754-O material

Parameter	IH	NKH
$\sigma_y$ (MPa)	95	95
$Q$ (MPa)	159	92.6
$\beta$	9	11
$a$ (MPa)	–	1291
$b_1$	–	35.8

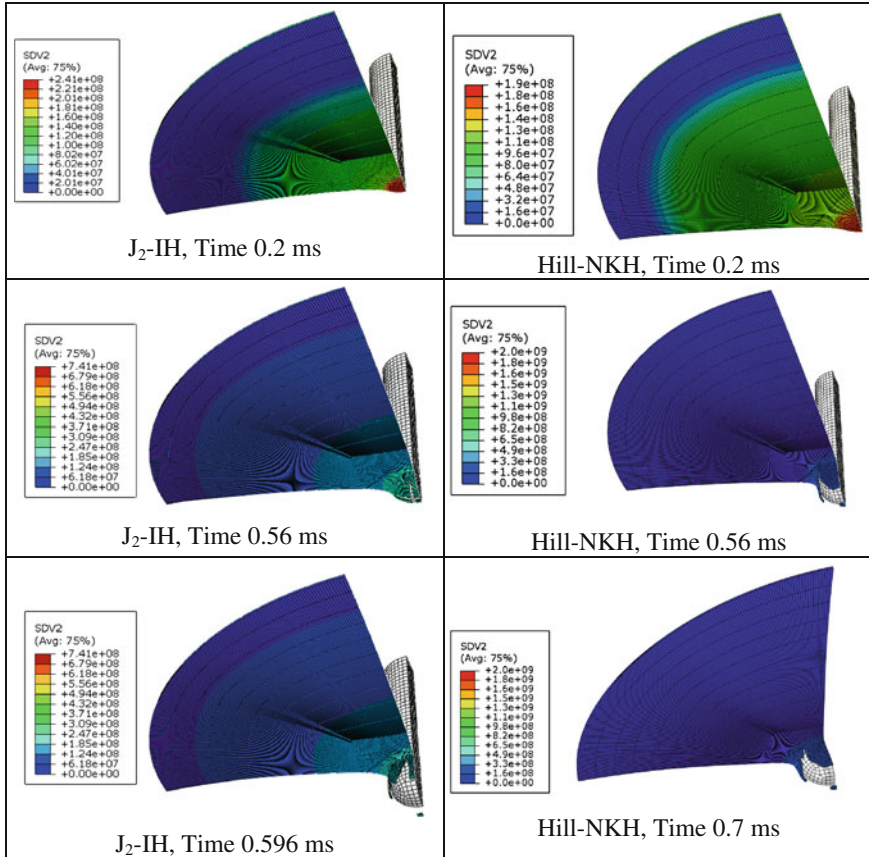
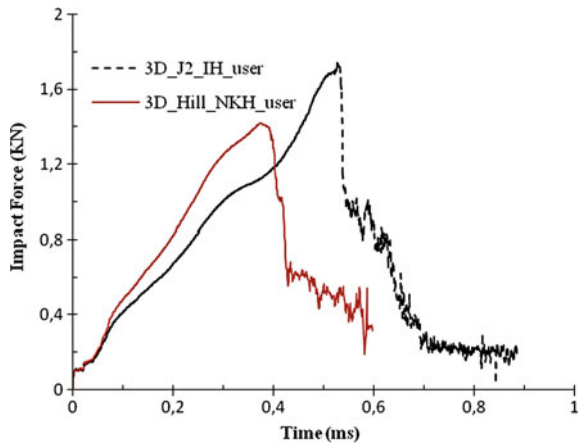
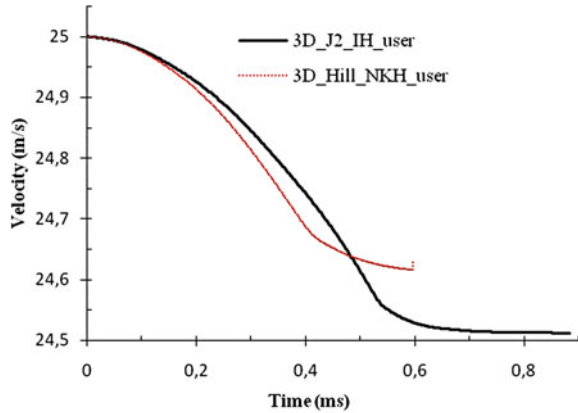


Fig. 3 Plate’s failure at different stages: pre and post perforation at velocity,  $V = 25$  m/s

Fig. 4 Forces versus time curves from simulation 4 ( $V_0 = 25$  m/s,  $h = 0.5$  mm,  $R = 70$  mm,  $R_p = 6.35$  mm)



**Fig. 5** Evolution of the projectile velocity during the impact



## 4 Conclusion

A numerical investigation has been carried out to analyze in details the perforation process of target aluminum plate when subjected to normal impact by hemispherical shape of projectile on low velocity. Numerical simulations have been performed using ABAQUS/Explicit finite element code. An elasto-viscoplastic model is implemented into a user-defined material (VUMAT) subroutine, taking into account the strain rate effect. Comparison between  $J_2$  and Hill yield criteria with isotropic and mixed non-linear isotropic/kinematic hardening models was conducted. According to results shown, the impact region of circular target is significantly influenced by anisotropy.

## References

- Abdulhamid H, Kolopp A, Bouvet C, Rivallant S (2013) Experimental and numerical study of AA5086-H111 aluminum plates subjected to impact. *Int J Impact Eng* 51:1–12
- Antoinat L, Kubler R, Barou JL, Viot P, Barrallier L (2015) Perforation of aluminium alloy thin plates. *Int J Impact Eng* 75:255–267
- Barlat F, Aretz H, Yoon JW, Karabin ME, Brem JC, Dick RE (2005) Linear transformation-based anisotropic yield functions. *Int J Plast* 21:1009–1039
- Børvik T, Clausen AH, Hopperstad OS, Langseth M (2004) Perforation of AA5083-H116 aluminium plates with conical-nose steel projectiles: experimental study. *Int J Impact Eng* 30:367–384
- Børvik T, Forrestal MJ, Hopperstad OS, Warren TL, Langseth M (2009) Perforation of AA5083-H116 aluminium plates with conical-nose steel projectiles—calculations. *Int J Impact Eng* 36:426–437
- Corran RSJ, Shadbolt PJ, Ruiz C (1983) Impact loading of plates—an experimental investigation. *Int J Impact Eng* 1:13–22

- Dean J, Dunleavy CS, Brown PM, Clyne TW (2009) Energy absorption during projectile perforation of thin steel plates and the kinetic energy of ejected fragments. *Int J Impact Eng* 36:1250–1258
- Fagerholt E, Grytten F, Gihleengen BE, Langseth M, Børvik T (2010) Continuous out-of-plane deformation measurements of AA5083-H116 plates subjected to low-velocity impact loading. *Int J Mech Sci* 52:689–705
- Grytten F, Børvik T, Hopperstad OS, Langseth M (2009) Low velocity perforation of AA5083-H116 aluminium plates. *Int J Impact Eng* 36:597–610
- Iqbal MA, Gupta NK, Sekhon GS (2006) Behaviour of thin aluminium plates subjected to impact by ogive-nosed projectiles. *Defence Sci J* 56:841–852
- Iqbal MA, Chakrabarti A, Beniwal S, Gupta NK (2010) 3D numerical simulations of sharp nosed projectile impact on ductile targets. *Int J Impact Eng* 37(1):85–195
- Jones N, Paik JK (2012) Impact perforation of aluminium alloy plates. *Int J Impact Eng* 48:46–53
- Lemaitre J, Chaboche JL (1990) *Mechanics of solid materials*. Cambridge Univ. Press
- Mars J, Wali M, Jarraya A, Dammak F, Dhiab A (2015) Finite element implementation of an orthotropic plasticity model for sheet metal in low velocity impact simulations. *Thin-Walled Struct* 89:93–100
- Mohotti D, Ngo T, Mendis P, Raman SN (2013) Polyurea coated composite aluminium plates subjected to high velocity projectile impact. *Int J Mater Des* 52:1–16
- Mohotti D, Ngo T, Raman SN, Ali M, Priyan M (2014) Plastic deformation of polyurea coated composite aluminium plates subjected to low velocity impact. *Int J Mater Des* 56:696–713
- Rodriguez-Martinez JA, Rusinek A, Pesci R, Zaera R (2012) Analysis of the strain induced martensitic transformation in austenitic steel subjected to dynamic perforation. *EDP Sci* 26. doi:[10.1051/epjconf/20122604036](https://doi.org/10.1051/epjconf/20122604036)
- Smerd R, Winkler S, Salisbury C, Worswick M, Lloyd D, Finn M (2005) High strain rate tensile testing of automotive aluminum alloy sheet. *Int J Impact Eng* 32:541–560
- Wali M, Chouchene H, Ben Said L, Dammak F (2015a) One-equation integration algorithm of a generalized quadratic yield function with Chaboche non-linear isotropic/kinematic hardening. *Int J Mech Sci* 92:223–232
- Wali M, Autay R, Mars J, Dammak F (2015b) A simple integration algorithm for a non-associated anisotropic plasticity model for sheet metal forming. *Int J Numer Meth Eng*. doi:[10.1002/nme.5158](https://doi.org/10.1002/nme.5158)
- Wilkins ML (1978) Mechanics of penetration and perforation. *Int J Eng Sci* 16:793–807

# Non-linear Dynamics Analysis of Multilayer Composite Shells with Enhanced Solid-Shell Elements

A. Hajlaoui, E. Triki, A. Frikha and F. Dammak

**Abstract** This paper presents the non linear dynamic response of multilayer composites with an enhanced solid-shell element. The transverse shear and transverse normal locking are treated using the Assumed Natural Strain formulation (ANS). For the enhanced part, one, three and five parameters are examined. Comparisons of numerical results with those extracted from literature show the good performance of the developed formulation in the isotropic case. The three enhancement choices give the same results in the multilayer composite case.

**Keywords** Nonlinear dynamic · Solid-shell elements · Multilayer composites

## 1 Introduction

Shell structures are widely used in aircraft and space systems due to their advantages of high stiffness and strength-to-weight ratios. Many shell elements which include 3D constitutive relations have been developed. Displacement-based solid elements are known to have poor performance in bending-dominated problems, such as in thin shells. To obtain the same performance as that of stress-resultant shell formulations with plane stress assumption, the class of volumetric shell or so-called solid-shell elements is a suitable alternative to pure volumetric element formulations.

---

A. Hajlaoui · E. Triki · A. Frikha · F. Dammak (✉)  
Mechanical Modélisation and Manufacturing Laboratory (LA2MP), National Engineering School of Sfax, University of Sfax, B.P W3038, Sfax, Tunisia  
e-mail: fakhreddine.dammak@enis.rnu.tn

A. Hajlaoui  
e-mail: abdhajlaoui@gmail.com

E. Triki  
e-mail: emna\_triiki@yahoo.fr

A. Frikha  
e-mail: frikhaahmed@yahoo.fr

To improve the bending behavior of low-order elements, the enhanced assumed strain, EAS, method was proposed by Simo and Rifai (1990). Klinkel et al. (1999), developed a solid-shell element with the ANS method for transverse strains and five parameters. Vu-Quoc and Tan (2003) proposed an EAS solid shell element with 7 parameters that pass the membrane and bending plate patch tests but does not completely eliminate volumetric locking (Hajlaoui et al. 2012). Betsch and Stein (1995) proposed a new interpolation function for thickness strains  $E_{33}$  for shell element and extended to solid-shell element by Klinkel et al. (1999). In the present eight-node solid-shell element, we use the EAS method. Three types of parameters have been analyzed: one, three and five parameters. For the transverse shear locking, the ANS formulation of Bathe and Dvorkin (1985) is used.

## 2 Basic Concept of the Non-linear Static Solid-Shell Element

The fixed spatial coordinate system is defined by a triad ( $\mathbf{E}_i$ ),  $i = 1, 2, 3$ . Associated variables with the undeformed state will be denoted by upper-case letters and by a lower-case letters when referred to the deformed configuration. Parameterizations of the shell material points are carried out in terms of curvilinear coordinates  $\xi = (\xi_1, \xi_2, \xi_3) = (\xi, \eta, \zeta)$ . The position vectors of the initial and the current configuration are denoted by  $\mathbf{X}$  and  $\mathbf{x}$ , respectively. The covariant base vectors in the initial and deformed configuration are given by

$$\mathbf{G}_k = \frac{\partial \mathbf{X}}{\partial \xi^k}, \quad \mathbf{g}_k = \frac{\partial \mathbf{x}}{\partial \xi^k}, \quad k = 1, 2, 3 \quad (1)$$

The covariant metric tensor  $\mathbf{G}$  at a material point  $\xi$ , in the initial and deformed configuration are defined by

$$\mathbf{G} = [\mathbf{G}_i \cdot \mathbf{G}_j], \quad \mathbf{g} = [\mathbf{g}_i \cdot \mathbf{g}_j], \quad i, j = 1, 2, 3 \quad (2)$$

This leads to the following Green-Lagrangean strain tensor

$$\mathbf{E} = \frac{1}{2}(\mathbf{g} - \mathbf{G}), \quad E_{ij} = \frac{1}{2}(g_{ij} - G_{ij}) \quad (3)$$

### 2.1 The Weak Form

The EAS method is based on the following assumption

$$\mathbf{E} = \mathbf{E}^c + \tilde{\mathbf{E}} \tag{4}$$

where  $\mathbf{E}^c$  and  $\tilde{\mathbf{E}}$  are respectively the compatible part and the enhanced part of the Green-Lagrange strain tensor. The variational framework of the EAS method, which is based on the three-field variational functional, in Lagrangean formulation, is written as

$$\Pi(\mathbf{u}, \tilde{\mathbf{E}}, \tilde{\mathbf{S}}) = \int_V [\psi(\mathbf{E}) - \tilde{\mathbf{S}} : \tilde{\mathbf{E}} - \mathbf{u} \cdot \mathbf{F}_V] dV - \int_{\partial V_f} \mathbf{u} \cdot \mathbf{F}_S dA = 0 \tag{5}$$

where  $\psi$  is the strain energy function and  $\mathbf{u}$ ,  $\tilde{\mathbf{E}}$  and  $\tilde{\mathbf{S}}$  are the independent tensorial quantities which are: displacement, enhanced assumed Lagrange strain and assumed second Piola-Kirchhoff stress fields respectively. Vectors,  $\mathbf{F}_V$  and  $\mathbf{F}_S$ , in Eq. (5), are the prescribed body force and surface traction respectively. When invoking the classical orthogonality condition,  $\int_V \tilde{\mathbf{S}} : \tilde{\mathbf{E}} dV = 0$ , the number of independent variables in the original functional is reduce to two  $(\mathbf{u}, \tilde{\mathbf{E}})$ . The weak form of this modified functional may be obtained as

$$W = \int_V [\delta \mathbf{E} : \mathbf{S} - \delta \mathbf{u} \cdot \mathbf{F}_V] dV - \int_{\partial V_f} \delta \mathbf{u} \cdot \mathbf{F}_S dA = 0 \tag{6}$$

where  $\mathbf{S}$  is the Piola-Kirchhoff stress tensor given by  $\mathbf{S} = \partial \psi / \partial \mathbf{E}$ .

### 2.2 Compatible Strains

To treat the transverse shear locking and transverse normal locking problems, the ANS is used. For the transverse shear strains,  $E_{13}^c$  and  $E_{23}^c$ , the ANS method proposed by Bathe and Dvorkin (1985) is used. However, for the thickness strains,  $E_{33}^c$ , we adopt the proposed ANS method used in Betsch and Stein (1995), Bischoff and Ramm (1997), Klinkel et al. (1999) and Hajlaoui et al. (2015, 2016). Then the compatible part of the Green-Lagrange strain tensor becomes as follows:

$$\mathbf{E}^c = \mathbf{T}^{-T} \begin{bmatrix} \frac{1}{2}(g_{11} - G_{11}) \\ \frac{1}{2}(g_{22} - G_{22}) \\ \sum_{A=1}^4 \frac{1}{4}(1 + \xi_A \zeta)(1 + \eta_A \eta) \frac{1}{2}(g_{33}^A - G_{33}^A) \\ (g_{12} - G_{12}) \\ \frac{1}{2} \left[ (1 - \eta)(g_{13}^B - G_{13}^B) + (1 + \eta)(g_{13}^D - G_{13}^D) \right] \\ \frac{1}{2} \left[ (1 - \zeta)(g_{23}^A - G_{23}^A) + (1 + \zeta)(g_{23}^C - G_{23}^C) \right] \end{bmatrix} \tag{7}$$

where the matrix  $\mathbf{T}$  is the transformation of the strain tensor from parametric coordinates to the local Cartesian coordinates given in Hajlaoui et al. (2015, 2016). For the finite element approximation, which is based on the hexahedral eight nodes element, the position vectors, within each element domain, in reference and current configurations are respectively given by

$$\mathbf{X} = \mathbf{N}\mathbf{X}_n, \quad \mathbf{x} = \mathbf{N}\mathbf{x}_n \quad (8)$$

where  $\mathbf{N}$  is the tri-linear shape functions matrix,  $\mathbf{x}_n$  and  $\mathbf{X}_n$  are nodal coordinates. The displacement field, with the corresponding variation and increment, is interpolated in a same manner as follows

$$\mathbf{u} = \mathbf{N}\mathbf{U}_n, \quad \delta\mathbf{u} = \mathbf{N}\delta\mathbf{U}_n, \quad \Delta\mathbf{u} = \mathbf{N}\Delta\mathbf{U}_n \quad (9)$$

where  $\mathbf{U}_n = [u_1, v_1, w_1, \dots, u_8, v_8, w_8]^T$  is the vector of nodal displacements at the element level. Using Eq. (7) and approximations (8) and (9), the virtual and incremental compatible Green Lagrange strain tensor are then given by

$$\delta\mathbf{E}^c = \mathbf{B} \delta\mathbf{U}_n, \quad \Delta\mathbf{E}^c = \mathbf{B} \Delta\mathbf{U}_n \quad (10)$$

where  $\mathbf{B}$  is the strain interpolation matrix, relative to a node ( $I$ ) and denoted  $\mathbf{B}_I$  is given by:

$$\mathbf{B}_I = \mathbf{T}^{-T} \begin{bmatrix} \mathbf{g}_1^T \mathbf{N}_{I,1} \\ \mathbf{g}_2^T \mathbf{N}_{I,2} \\ \sum_{A=1}^4 \frac{1}{4} (1 + \zeta_A \xi) (1 + \eta_A \eta) \mathbf{g}_3^T \mathbf{N}_{I,3} \\ \mathbf{g}_2^T \mathbf{N}_{I,1} + \mathbf{g}_1^T \mathbf{N}_{I,2} \\ \frac{1}{2} \left[ (1 - \eta) \left( \mathbf{g}_3^{B^T} \mathbf{N}_{I,1}^B + \mathbf{g}_1^{B^T} \mathbf{N}_{I,3}^B \right) + (1 + \eta) \left( \mathbf{g}_3^{D^T} \mathbf{N}_{I,1}^D + \mathbf{g}_1^{D^T} \mathbf{N}_{I,3}^D \right) \right] \\ \frac{1}{2} \left[ (1 - \zeta) \left( \mathbf{g}_3^{A^T} \mathbf{N}_{I,2}^A + \mathbf{g}_2^{A^T} \mathbf{N}_{I,3}^A \right) + (1 + \zeta) \left( \mathbf{g}_3^{C^T} \mathbf{N}_{I,2}^C + \mathbf{g}_2^{C^T} \mathbf{N}_{I,3}^C \right) \right] \end{bmatrix} \quad (11)$$

### 2.3 Enhanced Green Lagrange Strains

The enhanced Green-Lagrange strain part is related to the vector of the internal strain parameters  $\boldsymbol{\alpha}$  as:

$$\tilde{\mathbf{E}} = \tilde{\mathbf{M}}\boldsymbol{\alpha}, \quad \delta\tilde{\mathbf{E}} = \tilde{\mathbf{M}}\delta\boldsymbol{\alpha}, \quad \Delta\tilde{\mathbf{E}} = \tilde{\mathbf{M}}\Delta\boldsymbol{\alpha} \quad (12)$$

where  $\tilde{\mathbf{E}}$ ,  $\delta\tilde{\mathbf{E}}$  and  $\Delta\tilde{\mathbf{E}}$  are total, virtual and incremental enhanced Green Lagrange strain tensor respectively. The crucial assumption of the EAS method is the enforcement of the orthogonality conditions for the assumed stress field  $\tilde{\mathbf{S}}$  and the



enhanced strain  $\tilde{\mathbf{E}}$ . This orthogonality conditions impose the following choice for the interpolation function matrix  $\tilde{\mathbf{M}}$  to be expressed as follows

$$\tilde{\mathbf{M}} = \frac{\det \mathbf{J}_0}{\det \mathbf{J}} \mathbf{T}_0^{-T} \mathbf{M}_{\xi\eta\zeta}, \int_{-1}^1 \int_{-1}^1 \int_{-1}^1 \mathbf{M}_{\xi\eta\zeta} d\xi d\eta d\zeta = 0 \tag{13}$$

where the subscript ‘0’ means evaluation at the center of the element in the natural coordinates,  $\mathbf{J} = [\mathbf{G}_1, \mathbf{G}_2, \mathbf{G}_3]$  is the Jacobian matrix. The interpolation matrix  $\mathbf{M}_{\xi\eta\zeta}$ , in Eq. (15), is expression in term of the parametric coordinates ( $\xi, \eta, \zeta$ ). Three choices of matrix  $\mathbf{M}_{\xi\eta\zeta}$  will be considered: one, three and five parameters (C3D8S1, C3D8S3, C3D8S5).

$$\mathbf{M}_{\xi\eta\zeta}^1 = \begin{bmatrix} 0 \\ 0 \\ \zeta \\ 0 \\ 0 \\ 0 \\ 0 \\ 0 \end{bmatrix}, \quad \mathbf{M}_{\xi\eta\zeta}^3 = \begin{bmatrix} 0 & 0 & 0 \\ 0 & 0 & 0 \\ \zeta & \xi\zeta & \eta\zeta \\ 0 & 0 & 0 \\ 0 & 0 & 0 \\ 0 & 0 & 0 \\ 0 & 0 & 0 \end{bmatrix}, \quad \mathbf{M}_{\xi\eta\zeta}^5 = \begin{bmatrix} \zeta & 0 & 0 & 0 & 0 \\ 0 & \eta & 0 & 0 & 0 \\ 0 & 0 & \zeta & 0 & 0 \\ 0 & 0 & 0 & \xi & \eta \\ 0 & 0 & 0 & 0 & 0 \\ 0 & 0 & 0 & 0 & 0 \end{bmatrix} \tag{14}$$

### 2.4 Linearisation

With the finite element approximation, Eqs. (10) and (12), at hand, the continuum weak form, Eq. (6), became in a discrete form as

$$W = \delta \mathbf{U}_n^T \cdot (\mathbf{f}_{int} - \mathbf{f}_{ext}) + \delta \boldsymbol{\alpha}^T \cdot \mathbf{h} \tag{15}$$

where,  $\mathbf{f}_{int}$ ,  $\mathbf{f}_{ext}$  and  $\mathbf{h}$ , are given by the following expressions

$$\mathbf{f}_{int} = \int_V \mathbf{B}^T \mathbf{S} dV, \quad \mathbf{f}_{ext} = \int_V \mathbf{N}^T \mathbf{F}_V dV + \int_{\partial V_f} \mathbf{N}^T \mathbf{F}_S dA, \quad \mathbf{h} = \int_V \tilde{\mathbf{M}}^T \mathbf{S} dV \tag{16}$$

Equation (16) is a nonlinear equation that will be solved iteratively by the Newton-Raphson method which needs linearization. Linearization of Eq. (15) is given by

$$[\delta \mathbf{U}_n^T \quad \delta \boldsymbol{\alpha}^T] \left( \begin{bmatrix} \mathbf{K} & \mathbf{L}^T \\ \mathbf{L} & \mathbf{H} \end{bmatrix} \begin{Bmatrix} \Delta \mathbf{U}_n \\ \Delta \boldsymbol{\alpha} \end{Bmatrix} + \begin{bmatrix} \mathbf{f}_{int} - \mathbf{f}_{ext} \\ \mathbf{h} \end{bmatrix} \right) = 0 \tag{17}$$

where  $\mathbf{L}$ ,  $\mathbf{H}$  and  $\mathbf{K}$  are given by

$$\mathbf{L} = \int_V \tilde{\mathbf{M}}^T \mathbb{C} \mathbf{B} dV, \mathbf{H} = \int_V \tilde{\mathbf{M}}^T \mathbb{C} \tilde{\mathbf{M}} dV, \mathbf{K} = \mathbf{K}_D + \mathbf{K}_G \quad (18)$$

with  $\mathbb{C} = \frac{\partial^2 \psi}{\partial \mathbf{E} \partial \mathbf{E}}$  is the  $6 \times 6$  three dimensional material tangent moduli, and  $\mathbf{K}_D$  is given by

$$\mathbf{K}_D = \int_V \mathbf{B}^T \mathbb{C} \mathbf{B} dV \quad (19)$$

where  $\mathbf{B}$  matrix is given by Eq. (11) and  $\mathbf{K}_G$  is the geometric stiffness matrix. Relative to a couple of nodes  $(I, J)$ , it is given by

$$\mathbf{K}_G^{IJ} = \int_V \text{diag}[G_{IJ} \quad G_{IJ} \quad G_{IJ}] dV \quad (20)$$

$$G_{IJ} = \mathbf{S}^T \mathbf{T}^{-T} \begin{bmatrix} \mathbf{N}_{I,1} \mathbf{N}_{J,1} \\ \mathbf{N}_{I,2} \mathbf{N}_{J,2} \\ \sum_{L=1}^4 \frac{1}{4} (1 + \xi_L \xi) (1 + \eta_L \eta) \mathbf{N}_{I,3}^L \mathbf{N}_{J,3}^L \\ \mathbf{N}_{I,1} \mathbf{N}_{J,2} + \mathbf{N}_{I,2} \mathbf{N}_{J,1} \\ \frac{1}{2} \left[ (1 - \eta) \left( \mathbf{N}_{I,1}^B \mathbf{N}_{J,3}^B + \mathbf{N}_{I,3}^B \mathbf{N}_{J,1}^B \right) + (1 + \eta) \left( \mathbf{N}_{I,1}^D \mathbf{N}_{J,3}^D + \mathbf{N}_{I,3}^D \mathbf{N}_{J,1}^D \right) \right] \\ \frac{1}{2} \left[ (1 - \xi) \left( \mathbf{N}_{I,2}^A \mathbf{N}_{J,3}^A + \mathbf{N}_{I,3}^A \mathbf{N}_{J,2}^A \right) + (1 + \xi) \left( \mathbf{N}_{I,2}^C \mathbf{N}_{J,3}^C + \mathbf{N}_{I,3}^C \mathbf{N}_{J,2}^C \right) \right] \end{bmatrix} \quad (21)$$

The strain parameters  $\Delta \boldsymbol{\alpha}$  must be eliminated from Eq. (17) at the element level, which leads to following element tangent operator  $\mathbf{K}_T$  and residual vector  $\mathbf{R}$

$$\mathbf{K}_T = (\mathbf{K}_D - \mathbf{L}^T \mathbf{H}^{-1} \mathbf{L}) + \mathbf{K}_G, \mathbf{R} = \mathbf{f}_{ext} - \mathbf{f}_{int} + \mathbf{L}^T \mathbf{H}^{-1} \mathbf{h} \quad (22)$$

### 3 Transient Analysis of the Non-linear Formulation

In order to extend the variational formulation, Eq. (15), to accommodate transient analysis, the body force is replaced by  $\mathbf{F}_V \leftarrow \mathbf{F}_V - \rho \ddot{\mathbf{u}}$ . Then, with this replacement the variational equation became

$$W = \delta \mathbf{U}_n^T (\mathbf{f}_{int} + \mathbf{f}_{iner} - \mathbf{f}_{ext}) + \delta \boldsymbol{\alpha}^T \cdot \mathbf{h}, \mathbf{f}_{iner}^e = \int_V \mathbf{N}^T \rho \ddot{\mathbf{u}} dV \quad (23)$$

The acceleration in Eq. (23) is computed from the isoparametric interpolation as in Eq. (9). Thus the inertia term and residual vector may be written as

$$\mathbf{f}_{iner} = \mathbf{M}\ddot{\mathbf{u}}_n, \mathbf{R} = \mathbf{f}_{ext} - \mathbf{f}_{int} + \mathbf{L}^T \mathbf{H}^{-1} \mathbf{h} - \mathbf{M}\ddot{\mathbf{u}}_n \quad (24)$$

### 3.1 Newmark Algorithm

The Newmark method is a one step method which is used to advance the solution from time  $t_n$  to  $t_{n+1}$ . Firstly, given the initial displacement and velocity vectors, the initial acceleration is determined by solving Eq. (24). The Newmark formula to process the solution is given by

$$\mathbf{K}_T^* \Delta \mathbf{U}_{n+1}^{i+1} = \mathbf{R}_{n+1}^i, \quad \mathbf{K}_T^* = \mathbf{K}_T + \frac{\gamma}{\beta \Delta t} \mathbf{C}_T + \frac{1}{\beta \Delta t^2} \mathbf{M} \quad (25)$$

With the updating formulas

$$\begin{aligned} \mathbf{U}_{n+1}^{i+1} &= \mathbf{U}_{n+1}^i + \Delta \mathbf{U}_{n+1}^{i+1}, & \dot{\mathbf{U}}_{n+1}^{i+1} &= \dot{\mathbf{U}}_{n+1}^i + \frac{\gamma}{\beta \Delta t} \Delta \mathbf{U}_{n+1}^{i+1}, \\ \ddot{\mathbf{U}}_{n+1}^{i+1} &= \ddot{\mathbf{U}}_{n+1}^i + \frac{1}{\beta \Delta t^2} \Delta \mathbf{U}_{n+1}^{i+1} \end{aligned} \quad (26)$$

where the vectors  $\mathbf{U}_{n+1}^{i+1}$ ,  $\dot{\mathbf{U}}_{n+1}^{i+1}$ , and  $\ddot{\mathbf{U}}_{n+1}^{i+1}$  are displacement, velocity and acceleration given in the initial state by

$$\begin{aligned} \mathbf{U}_{n+1}^0 &= \mathbf{U}_n, & \dot{\mathbf{U}}_{n+1}^0 &= \left(1 - \frac{\gamma}{\beta}\right) \dot{\mathbf{U}}_n + \Delta t \left(1 - \frac{\gamma}{2\beta}\right) \ddot{\mathbf{U}}_n, \\ \ddot{\mathbf{U}}_{n+1}^0 &= -\frac{1}{2\beta} \dot{\mathbf{U}}_n + \left(1 - \frac{1}{2\beta}\right) \ddot{\mathbf{U}}_n \end{aligned} \quad (27)$$

The Newmark parameters  $\beta$  and  $\gamma$  are chosen as  $\beta = 1/3$ ,  $\gamma = 0.5$ .

## 4 Numerical Examples

In this section we present numerical simulations in order to illustrate the good performance of the proposed formulation. Firstly, the dynamic behavior of a clamped isotropic spherical shell under a concentrated apex load,  $F = 100$ , is presented. This test is proposed in Duarte Filho and Awruch (2004). Material and geometric properties for this test are  $E = 10^7$ ,  $\nu = 0.3$ ,  $\rho = 0.000245$ ,  $\theta = 10.9^\circ$ ,  $R = 4.76$ , and  $h = 0.01576$ . Loading and finite element mesh are shown in Fig. 1.

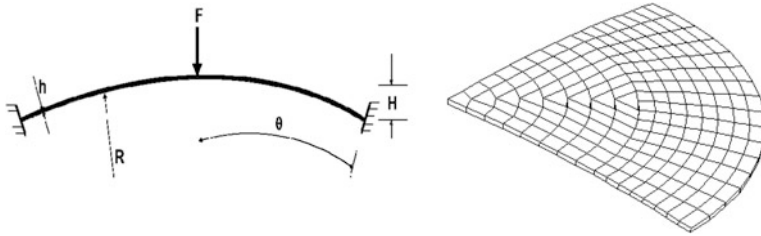


Fig. 1 Shallow spherical cap: geometry and finite element mesh

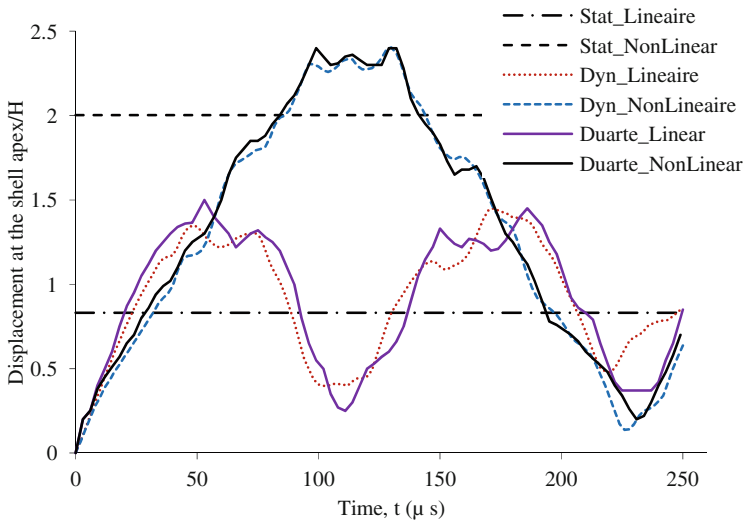
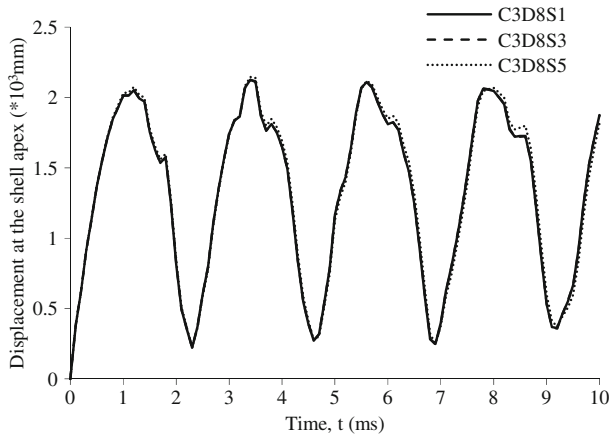


Fig. 2 Dynamic response of the isotropic shallow spherical cap

The time increment is  $\Delta t = 0.2 \mu s$  and the finite element mesh with 192 elements is used. The nonlinear dynamic response, represented by the vertical displacement at the mid-span, is shown in Fig. 2.

In the same figure, results obtained from a nonlinear and linear static analyses, as well as the linear dynamic analysis are also presented. These results are compared with the results of presented in the work of Duarte Filho and Awruch (2004). The proposed formulation presents very close results to Duarte Filho and Awruch (2004) results.

In a second simulation, the same spherical shell is analyzed with two layers  $[0^\circ/90^\circ]$  subjected to a concentrated apex load of  $F = 0.8 \text{ N}$ . Geometric and materials properties are  $E_1 = 138 \text{ GPa}$ ,  $E_2 = E_3 = 8.9 \text{ GPa}$ ,  $G_{12} = G_{13} = G_{23} = 4 \text{ GPa}$ ,  $\nu_{12} = \nu_{13} = \nu_{23} = 0.25$ ,  $\rho = 1824 \text{ kg/m}^3$ ,  $R = 4 \text{ m}$  and  $h = 0.02 \text{ m}$ . The time increment is  $\Delta t = 10^{-4} \text{ s}$  and the time period is 10 ms. The central deflection



**Fig. 3** Dynamic response of the non-symmetric orthotropic shallow spherical cap

is plotted with time in is shown in Fig. 3 for the three parameters choice Eq. (14) which give the same results.

## 5 Conclusion

In this paper, a solid-shell finite element with enhanced assumed strain is developed to study the non linear dynamics of multilayer composites. The transverse shear and transverse normal locking are treated using the Assumed Natural Strain formulation (ANS). The proposed formulation and those from literature are in good agreement in the isotropic case. The three choices of the number of enhancement parameters give the same results in the case of non-symmetric orthotropic laminates composites.

## References

- Bathe KJ, Dvorkin E (1985) A four-node plate bending element based on Mindlin/Reissner plate theory and a mixed interpolation. *Int J Numer Meth Eng* 21:367–383
- Betsch P, Stein E (1995) An assumed strain approach avoiding artificial thickness straining for a nonlinear 4-node shell element. *Commun Numer Methods Eng* 11:899–909
- Bischoff M, Ramm E (1997) Shear deformable shell elements for large strains and rotations. *Commun Numer Methods Eng* 40:4427–4449
- Duarte Filho LA, Awruch AM (2004) Geometrically nonlinear static and dynamic analysis of shells and plates using the eight-node hexahedral element with one-point quadrature. *Finite Elem Anal Des* 40(11):1297–1315

- Hajlaoui A, Jarraya A, Kallel-Kamoun I, Dammak F (2012) Buckling analysis of a laminated composite plate with delaminations using the enhanced assumed strain solid shell element. *J Mech Sci Tech* 26(10):3213–3221
- Hajlaoui AM, Wali M, Ben Jdidia M, Dammak F (2016) An improved enhanced solid shell element for static and buckling analysis of shell structures. *Mech Ind.* 17(5) p. 510
- Hajlaoui A, Jarraya A, El Bikri K, Dammak F (2015) Buckling analysis of functionally graded materials structures with enhanced solid-shell elements and transverse shear correction. *Compos Struct* 132:87–97
- Klinkel S, Gruttmann F, Wagner W (1999) A continuum based three-dimensional shell element for laminated structures. *Comput Struct* 71:43–62
- Simo J, Rifai M (1990) A class of mixed assumed strain methods and the method of incompatible modes. *Int J Numer Methods Eng* 29(8):1595–1638
- Vu-Quoc L, Tan XG (2003) Optimal solid shells for non-linear analyses of multilayer composites. II. Dynamics. *Comput Methods Appl Mech Eng* 192:1017–1059

# An Effective Method for the Identification of Support Features in Multi-supported Systems

A. Baklouti, J. Antunes, V. Debut, T. Fakhkakh  
and Mohamed Haddar

**Abstract** The mechanical properties of supports in a mechanical system strongly affect its dynamic behavior under real operating conditions. This work presents a new method for identifying the dynamical characteristics of local supports which has been developed along the lines of the work by Özgüven (Mech Syst Signal Process 4:53–63, 1990) and Debut et al. (Proceeding of the 19th international congress on sound and vibration, Vilnius, Lithuania, 2012), which combines measured frequency transfer functions and techniques from structural modifications. As typical for inverse problem, the noise in the frequency transfer functions lead to faulty identifications, so that regularization techniques have been implemented to mitigate noise amplification in the inverse problem. The proposed approach has been then numerically tested on a multi-supported structure, which can be seen as an idealized electricity generator rotor shaft. The results are satisfactory for noise-free data as well as under realistic noise levels.

**Keywords** Identification of support parameters · Regularization of inverse problem · Multi-supported structure · Structural modification

---

A. Baklouti (✉) · J. Antunes · V. Debut  
Centro de Ciências e Tecnologias Nucleares, Instituto Superior Técnico,  
Universidade de Lisboa, Estrada Nacional 10, km 139.7,  
2695-066 Bobadela LRS, Portugal  
e-mail: Ahmadbaklouti90@gmail.com

J. Antunes  
e-mail: jantunes@ctn.tecnico.ulisboa.pt

V. Debut  
e-mail: vincentdebut@ctn.tecnico.ulisboa.pt

A. Baklouti · T. Fakhkakh · M. Haddar  
Laboratory of Mechanics Modeling and Production,  
National School of Engineering of Sfax, University of Sfax, Sfax, Tunisia  
e-mail: tahar.fakhfakh@enis.rnu.tn

M. Haddar  
e-mail: Mohamed.Haddar@enis.rnu.tn

## 1 Introduction

In most industries using rotating machines, the application of large power combined with high speed while ensuring a continuous and reliable operation is becoming increasingly important. However, such components are prone to dynamical unbalance and instability problems which can affect rotors, as a result of the unbalanced forces related to rotor bending and also due to the dynamic behavior of the lubrication seals between the rotor and the structure. For many years, the causes of rotor instabilities were the subject of countless investigations. Ramsden (1968) was the first to conclude that designers must have accurate information about the stiffness and damping coefficients of bearings incorporated in the structure. In the late 70s, Dawson and Taylor (1980) conducted a survey on the impact of bearings on the dynamic behavior of rotors and reached the following conclusion: experiments in rotor-dynamics must be carried out to study the influence of the dynamic parameters of bearings and of the structure on the rotor responses. For that purpose, characterizing the dynamic behavior of the bearings is paramount. A suitable and economic procedure was proposed by Nordmann and Scholhom (1980) to identify the stiffness and damping parameters of a plain bearing. Ten years later, Chan and White (1991) used the impact method to identify the dynamic parameters of a bearing in a rotor mounted on two symmetrical bearings by adjusting the curves of the frequency responses. Since in most applications based on the rotors mounted on bearings, bearings are not symmetrical, the applications of the assumptions on which this method is based are limited. Later, Wang and Liou (1991) proposed the method of structural parameters identification of the joints. A method that has been extended by Arumugam et al. (1994) to identify linearized parameters of an oil film, using experimental frequency response functions (FRFs) and theoretical FRFs obtained from Finite Element modeling. Qiu and Tieu (1997) presented an algorithm to identify the dynamic parameters of a bearing from its impulse response. Tiwari et al. (2004) conducted a survey on the experimental identification of dynamic parameters of bearings and seals respectively. The method proposed in this paper, based on the formulation of structural modifications developed by Özgüven (1990) and Debut et al. (2012), identifies the characteristics of the support parameters of each rotor bearing, i.e. mass, stiffness and damping, from the modal parameters of the unconstrained rotor and from a matrix that represents the transfer functions connecting the dynamics of all measurement locations of the support-constrained rotor. One key point of the method is the relationships between the transfer functions of the unconstrained and constrained systems proposed by Özgüven (1990). The constrained system is represented in terms of the transfer functions measured at the supports location, while the unconstrained system is represented by a Finite Element model. In the presence of noise in the measured FRFs or when the mode shape value approach zero, the problem becomes ill-posed. To overcome these difficulties, the proposed formulation allows to better regulate the inverse problem through classical filtering techniques, namely by matrix singular values decomposition (SVD) and Tikhonov regularization. These are two convenient aspects of the developed



approach, which allow to address the inverse problem not by iterative optimization as it is pretty standard, but through linear inverse formulations. In addition, this method does not imply the experimental identification of the constrained modes of the system, which can be delicate in practice, because it is rooted instead on transfer function measurements only. As a first step in the development of the technique, the paper presents some preliminary identification results obtained from realistic simulated data for a model of an electricity generator shaft, under non-rotating conditions, which illustrates the satisfactory behavior of the approach.

## 2 Theoretical Model

The structure consists of a rotor with multiple spans, supported by ball bearings, connected to a fixed structure as shown in Fig. 1. Assuming the unconstrained structure, i.e. without accounting for the actual boundary conditions on the supports, the frequency transfer function between the *i*th and *j*th points matrices of the structure  $\mathbf{H}_{U_{ij}}(\omega)$ , can be calculated from the assembled matrices of the Finite Elements model as,

$$\mathbf{H}_U(\omega) = [-\omega^2\mathbf{M} + i\omega\mathbf{C} + \mathbf{K}]^{-1} \tag{1}$$

where  $\mathbf{M}$ ,  $\mathbf{C}$  and  $\mathbf{K}$  are the mass, the damping and the stiffness matrices, respectively.

The frequency transfer function matrix  $\mathbf{H}_C(\omega)$  of the constrained system can be written as follows:

$$\begin{aligned} \mathbf{H}_C(\omega) &= [-\omega^2\mathbf{M} + i\omega\mathbf{C} + \mathbf{K} - \omega^2\mathbf{M}_C + i\omega\mathbf{C}_C + \mathbf{K}_C]^{-1} \\ &= [\mathbf{H}_U(\omega)^{-1} - \omega^2\mathbf{M}_C + i\omega\mathbf{C}_C + \mathbf{K}_C]^{-1} \end{aligned} \tag{2}$$

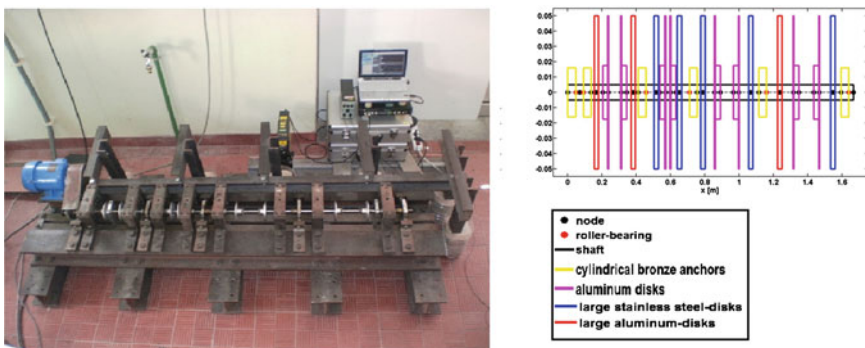


**Fig. 1** *Left* Picture of the rotor test rig at LDA of IST/CTN. *Right* Detail of the components of the rotor model

where, the matrix  $\mathbf{M}_C$ ,  $\mathbf{K}_C$  and  $\mathbf{C}_c$  contain the supports parameters. An interesting manner to estimate the matrix of constrained transfer functions  $\mathbf{H}_C(\omega)$  directly from the unconstrained matrix  $\mathbf{H}_U(\omega)$  was proposed by Özgüven (1990). From (1) and (2),  $\mathbf{H}_U(\omega)$  can be expressed as:

$$\mathbf{H}_U(\omega) = [\mathbf{I} - \mathbf{H}_C(\omega)[- \omega^2 \mathbf{M}_C + i\omega \mathbf{C}_C + \mathbf{K}_C]]^{-1} \mathbf{H}_C(\omega) \quad (3)$$

To obtain a convenient form for the identification of the support's parameters, we can multiply the left-hand side vector and the right-hand side vector by an external excitation. The resulting equations are obtained as:

$$\varphi_{U_m} = \mathbf{H}_C(\omega_{U_m}) [- \omega_{U_m}^2 \mathbf{M}_C + i\omega_{U_m} \mathbf{C}_C + \mathbf{K}_C] \varphi_{U_m} \quad (4)$$

where  $\omega_{U_m}$  and  $\varphi_U$  represent the modal frequencies and corresponding mode shapes of the unconstrained system.

Assuming that the constraints matrices of the supports are diagonal, Eq. (4) can be written as Özgüven (1990):

$$\varphi_{U_m} = \mathbf{H}_C(\omega_{U_m}) \phi_{U_m} \left( -\omega_{U_m}^2 \mathbf{m}_C + i\omega_{U_m} \mathbf{c}_C + \mathbf{k}_C \right) \quad (5)$$

where  $\phi_{U_m}$  is a diagonal matrix built from the terms of vector  $\varphi_{U_m}$  while  $\mathbf{m}_C$ ,  $\mathbf{c}_C$  and  $\mathbf{k}_C$  are vectors containing the terms of the diagonal constraints matrices  $\mathbf{M}_C$ ,  $\mathbf{C}_C$  and  $\mathbf{K}_C$ , or conversely:

$$-\omega_{U_m}^2 \mathbf{m}_C + i\omega_{U_m} \mathbf{c}_C + \mathbf{k}_C = [\mathbf{H}_C(\omega_{U_m}) \phi_{U_m}]^{-1} \varphi_{U_m} \quad (6)$$

Concerning the real part of this complex equation, we can write (6) for two unconstrained modes  $m$  and  $n$ :

$$-\omega_{U_m}^2 \mathbf{m}_C + \mathbf{k}_C = \text{Re} \left( [\mathbf{H}_C(\omega_{U_m}) \phi_{U_m}]^{-1} \varphi_{U_m} \right) \quad (7)$$

$$-\omega_{U_n}^2 \mathbf{m}_C + \mathbf{k}_C = \text{Re} \left( [\mathbf{H}_C(\omega_{U_n}) \phi_{U_n}]^{-1} \varphi_{U_n} \right) \quad (8)$$

In a compact matrix form, Eqs. (7) and (8) become:

$$\begin{Bmatrix} \mathbf{m}_C \\ \mathbf{k}_C \end{Bmatrix} = \begin{bmatrix} -\omega_{U_m}^2 \mathbf{I} & \mathbf{I} \\ -\omega_{U_n}^2 \mathbf{I} & \mathbf{I} \end{bmatrix}^{-1} \begin{Bmatrix} \text{Re} \left( [\mathbf{H}_C(\omega_{U_m}) \phi_{U_m}]^{-1} \varphi_{U_m} \right) \\ \text{Re} \left( [\mathbf{H}_C(\omega_{U_n}) \phi_{U_n}]^{-1} \varphi_{U_n} \right) \end{Bmatrix} \quad (9)$$

Concerning the dissipation terms on the supports, we have directly from the imaginary part of (6):

$$\mathbf{c}_C = \frac{1}{\omega_{U_m}} \text{Im} \left( [\mathbf{H}_C(\omega_{U_m}) \phi_{U_m}]^{-1} \varphi_{U_m} \right) \quad (10)$$

The identification accuracy can be improved by taking a set of  $N$  unconstrained modes, which leads to the following oversized system of equations:

$$\begin{Bmatrix} \mathbf{m}_C \\ \mathbf{k}_C \end{Bmatrix} = \begin{bmatrix} -\omega_{U_1}^2 \mathbf{I} & \mathbf{I} \\ \vdots & \vdots \\ -\omega_{U_N}^2 \mathbf{I} & \mathbf{I} \end{bmatrix} + \begin{Bmatrix} \text{Re} \left( [\mathbf{H}_C(\omega_{U_1}) \phi_{U_1}]^{-1} \varphi_{U_1} \right) \\ \vdots \\ \text{Re} \left( [\mathbf{H}_C(\omega_{U_N}) \phi_{U_N}]^{-1} \varphi_{U_N} \right) \end{Bmatrix} \quad (11)$$

and,

$$\mathbf{c}_C = \begin{bmatrix} \omega_{U_1} \mathbf{I} \\ \vdots \\ \omega_{U_N} \mathbf{I} \end{bmatrix} + \begin{Bmatrix} \text{Im} \left( [\mathbf{H}_C(\omega_{U_1}) \phi_{U_1}]^{-1} \varphi_{U_1} \right) \\ \vdots \\ \text{Im} \left( [\mathbf{H}_C(\omega_{U_N}) \phi_{U_N}]^{-1} \varphi_{U_N} \right) \end{Bmatrix} \quad (12)$$

For identical supports, Eqs. (11) and (12) become:

$$\begin{Bmatrix} m_C \\ k_C \end{Bmatrix} = \begin{bmatrix} -\omega_{U_1}^2 & 1 \\ \vdots & \vdots \\ -\omega_{U_N}^2 & 1 \end{bmatrix} + \begin{Bmatrix} \text{Re} \left( [\mathbf{H}_C(\omega_{U_1}) \phi_{U_1}]^{-1} \varphi_{U_1} \right) \\ \vdots \\ \text{Re} \left( [\mathbf{H}_C(\omega_{U_N}) \phi_{U_N}]^{-1} \varphi_{U_N} \right) \end{Bmatrix} \quad (13)$$

and

$$c_C = \begin{bmatrix} \omega_{U_1} \\ \vdots \\ \omega_{U_N} \end{bmatrix} + \begin{Bmatrix} \text{Im} \left( [\mathbf{H}_C(\omega_{U_1}) \phi_{U_1}]^{-1} \varphi_{U_1} \right) \\ \vdots \\ \text{Im} \left( [\mathbf{H}_C(\omega_{U_N}) \phi_{U_N}]^{-1} \varphi_{U_N} \right) \end{Bmatrix} \quad (14)$$

### 3 Regularization Procedures

In practice, the presence of noise in the measured transfer functions or for modes presenting a node of the mode shapes near a measurement location can lead to an ill-posed problem. Therefore it is necessary to consider, as possible as it can be, their existence to overcome this problem. The orders of magnitude of the terms  $\mathbf{m}_C$  and  $\mathbf{k}_C$  are very different. The conditioning of the formulation is improved by rescaling the formulation. Then, we can rewrite (11) as:

$$\begin{Bmatrix} \tilde{\mathbf{m}}_{\mathbf{C}} \\ \mathbf{k}_{\mathbf{C}} \end{Bmatrix} = \begin{bmatrix} \mathbf{I} & \mathbf{I} \\ \vdots & \vdots \\ -\frac{\omega_{U_N}^2}{\omega_{U_1}^2} \mathbf{I} & \mathbf{I} \end{bmatrix}^+ \begin{Bmatrix} \text{Re} \left( [\mathbf{H}_{\mathbf{C}}(\omega_{U_1}) \Phi_{U_1}]^{-1} \Phi_{U_1} \right) \\ \vdots \\ \text{Re} \left( [\mathbf{H}_{\mathbf{C}}(\omega_{U_N}) \Phi_{U_N}]^{-1} \Phi_{U_N} \right) \end{Bmatrix} \quad (15)$$

and the desired solution will be:

$$\begin{Bmatrix} \mathbf{m}_{\mathbf{C}} \\ \mathbf{k}_{\mathbf{C}} \end{Bmatrix} = \begin{Bmatrix} \frac{1}{\omega_{U_1}^2} \tilde{\mathbf{m}}_{\mathbf{C}} \\ \mathbf{k}_{\mathbf{C}} \end{Bmatrix} \quad (16)$$

Furthermore, the complex vector in the second member (15) and (16) can be written:

$$\begin{Bmatrix} [\mathbf{H}_{\mathbf{C}}(\omega_{U_1}) \Phi_{U_1}]^{-1} \Phi_{U_1} \\ \vdots \\ [\mathbf{H}_{\mathbf{C}}(\omega_{U_N}) \Phi_{U_N}]^{-1} \Phi_{U_N} \end{Bmatrix} = \begin{bmatrix} \Phi_{U_1} & \cdots & 0 \\ \vdots & \ddots & \vdots \\ 0 & \cdots & \Phi_{U_N} \end{bmatrix}^{-1} \begin{bmatrix} \mathbf{H}_{\mathbf{C}}(\omega_{U_1}) & \cdots & 0 \\ \vdots & \ddots & \vdots \\ 0 & \cdots & \mathbf{H}_{\mathbf{C}}(\omega_{U_N}) \end{bmatrix}^{-1} \begin{Bmatrix} \Phi_{U_1} \\ \vdots \\ \Phi_{U_N} \end{Bmatrix} \quad (17)$$

This formulation allows a much better regularization for the inverse problem by using either SVD or Tikhonov filtering, in order to mitigate the presence of noise or near-zero modal values in the matrix of mode shapes.

### 3.1 SVD Regularization

A regularization technique which appears very elegant and effective, among the various methods that have been used to overcome the ill-condition problem, is to filter by SVD decomposition of both the constrained system transfer function  $\mathbf{H}_{\mathbf{C}}(\omega_U)$  and mode shapes matrices. It is possible to quantify the singularity of a given matrix through the so-called condition number which is the ratio between the highest and the lowest singular values of the SVD decomposition

$$\mathbf{\Gamma} = \mathbf{U} \mathbf{\Sigma} \mathbf{V}^T \quad (18)$$

where  $\mathbf{\Gamma}$  refers to the constrained system frequency transfer function matrix or the unconstrained system mode shapes matrix,  $\mathbf{\Sigma} = \text{diag}(\sigma_1, \dots, \sigma_N)$  with  $\sigma_1 \geq \sigma_2 \geq \dots \geq \sigma_N \geq 0$  and  $\mathbf{U}$ ,  $\mathbf{V}$  are orthogonal matrices. Then, using the inverse of the condition number  $c = \sigma_{\min}/\sigma_{\max}$ , matrix  $\mathbf{\Gamma}$  is perfectly conditioned when  $c = 1$  and ill-conditioned as  $c$  decreases. The inverse transformation can be computed from the SVD terms as:

$$\mathbf{\Gamma}^{-1} = \mathbf{V}\mathbf{\Sigma}^{-1}\mathbf{U}^T \tag{19}$$

therefore:  $\mathbf{\Sigma}^{-1} = \text{diag}(1/\sigma_1, \dots, 1/\sigma_N)$ .

A way to solve the problem is to use a pseudo-inverse of the matrix  $\mathbf{\Gamma}$  so that:

$$\mathbf{\Sigma}_{reg}^{-1} = \begin{cases} 1/\sigma_i & \text{if } \sigma_i/\sigma_{\max} \geq \varepsilon \\ 0 & \text{if } \sigma_i/\sigma_{\max} \leq \varepsilon \end{cases} \tag{20}$$

where  $\varepsilon$  is called the truncation (filtering) boundary and,

$$\mathbf{\Gamma}_{reg} = \mathbf{V}\mathbf{\Sigma}_{reg}^{-1}\mathbf{U}^T \tag{21}$$

The result obtained by the proposed regularization technique seems effective, as later illustrated in the numerical computations. More details about the regularization method can be found in Debut V et al. (2010).

### 3.2 Tikhonov Regularization

Another technique commonly used to overcome the problem of ill-conditioning is to filter the inverse formulation through Tikhonov regularization. This technique is based on the introduction of a regularization parameter  $\varepsilon$  which acts as a lower boundary on the large band-matrix of the constrained system transfer function, beyond which filtering of the inverse problem is enabled. So (17) will be written:

$$\begin{aligned} \begin{Bmatrix} \widehat{\mathbf{m}}_{\mathbf{C}} \\ \mathbf{k}_{\mathbf{C}} \\ \mathbf{C}_{\mathbf{C}} \end{Bmatrix} &= \begin{bmatrix} \mathbf{I} & \mathbf{I} & j\mathbf{I} \\ \vdots & \vdots & \vdots \\ -\frac{\omega_{U_N}^2}{\omega_{U_1}^2}\mathbf{I} & \mathbf{I} & j\mathbf{I} \end{bmatrix}^+ \begin{bmatrix} \Phi_{U_1} & \dots & 0 \\ \vdots & \ddots & \vdots \\ 0 & \dots & \Phi_{U_N} \end{bmatrix}^{-1} \\ &= \begin{bmatrix} \mathbf{H}_{\mathbf{C}}(\omega_{U_1}) & \dots & 0 \\ \vdots & \ddots & \vdots \\ 0 & \dots & \mathbf{H}_{\mathbf{C}}(\omega_{U_N}) \end{bmatrix} - \varepsilon \begin{bmatrix} \mathbf{I} & \dots & 0 \\ \vdots & \ddots & \vdots \\ 0 & \dots & \mathbf{I} \end{bmatrix}^{-1} \begin{Bmatrix} \Phi_{U_1} \\ \vdots \\ \Phi_{U_N} \end{Bmatrix} \end{aligned} \tag{22}$$

If  $\varepsilon$  is too small, then regularization is negligible and excessively amplified noise is obtained as a result. On the other hand, if  $\varepsilon$  is too large, then regularization will “drown” the problem physics leading to a large error in the excessively smooth identified result. So an issue arises on the choice of an optimal value for the filtering parameter. These arguments present the motivation for using the classical L-curve diagram, where the norm of the regularized solution  $\|S(\varepsilon)\|$  is plotted as a function of the residual norm  $\|R(\varepsilon)\|$  where:  $S(\varepsilon) = \left\{ \mathbf{m}_{\mathbf{C}}(\varepsilon)^T \quad \mathbf{k}_{\mathbf{C}}(\varepsilon)^T \quad \mathbf{c}_{\mathbf{C}}(\varepsilon)^T \right\}^T$

and

$$R(\varepsilon) = \left\{ \begin{array}{l} \left[ \begin{array}{ccc} \mathbf{H}_C(\omega_{U_1}) & \cdots & 0 \\ \vdots & \ddots & \vdots \\ 0 & \cdots & \mathbf{H}_C(\omega_{U_N}) \end{array} \right] \left[ \begin{array}{ccc} \phi_{U_1} & \cdots & 0 \\ \vdots & \ddots & \vdots \\ 0 & \cdots & \phi_{U_N} \end{array} \right] \\ \left[ \begin{array}{ccc} \mathbf{I} & \mathbf{I} & j\mathbf{I} \\ \vdots & \vdots & \vdots \\ -\frac{\omega_{U_N}^2}{\omega_{U_1}^2}\mathbf{I} & \mathbf{I} & j\mathbf{I} \end{array} \right] \left\{ \begin{array}{l} \mathbf{m}_c(\varepsilon) \\ \mathbf{k}_c(\varepsilon) \\ \mathbf{c}_c(\varepsilon) \end{array} \right\} - \left\{ \begin{array}{l} \phi_{U_1} \\ \vdots \\ \phi_{U_N} \end{array} \right\} \end{array} \right. \quad (23)$$

More details about the regularization method can be found in Delaune et al. (2010).

## 4 Numerical Applications

### 4.1 System Description

The model shown in Fig. 1 presents the essence of the complexities that can be found in the shaft-lines of turbo electricity generators. The rotor is composed of a stainless steel shaft supported by six roller-bearings mounted on the shaft through cylindrical bronze-anchors, eight thin aluminum-disks maintained by cylindrical aluminum-anchors, five large stainless steel-disks and three large aluminum-disks which have identical dimensions. Numerical data of the rotor are shown in Table 1. Figure 1 illustrates in detail the distribution of the components of the rotor. The model is essentially composed of four spans of various lengths; each one contains two balance discs and two large discs.

**Table 1** Numerical data of the rotor

Length of the shaft	1.668 m	External diameter of aluminum-disks	0.1 m
Diameter of the shaft	0.01 m	Inner diameter of aluminum-disks	0.01 m
Shaft Young's modulus	210 Gpa	Thickness of aluminum-disks	0.025 m
Shaft density	8020 kg/m <sup>3</sup>	Aluminum-disks density	2700 kg
External diameter of stainless steel-disks	0.1 m	External diameter of aluminum-disks	0.1 m
Inner diameter of stainless steel-disks	0.01 m	Inner diameter of aluminum-disks	0.01 m
Thickness of stainless steel-disks	0.025 m	Thickness of aluminum-disks	0.005 m
Stainless steel-disks density	8020 kg	Aluminum-disks density	2700 kg
Length of bronze-anchors	0.045 m	Length of alum-anchors	0.032 m
External diameter of bronze-anchors	0.032 m	External diameter of alum-anchors	0.035 m
Inner diameter of bronze-anchors	0.01 m	Inner diameter of alum-anchors	0.01 m
Bronze-anchors Young's modulus	130 GPa	Young's modulus alum-anchors	130 GPa
Bronze-anchors density	8400 kg	Alum-anchors density	5550 kg

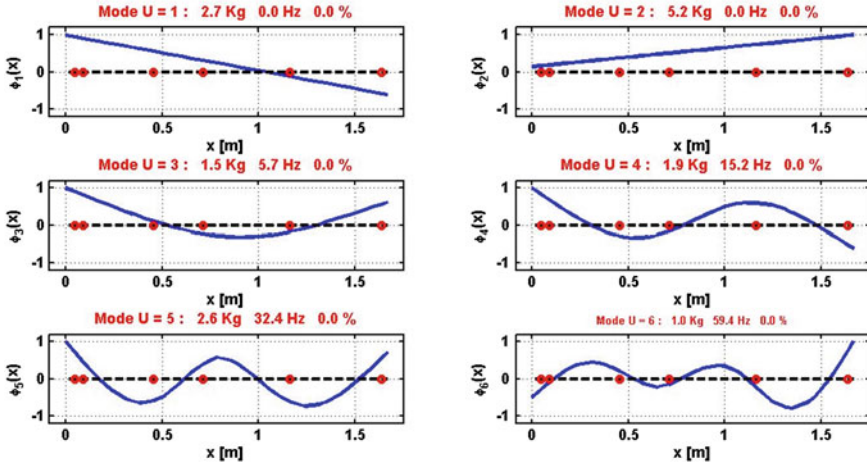


Fig. 2 First six mode shapes of the unconstrained system

### 4.2 Simulation Results

For numerical simulations, the structure was meshed into 37 linear elements based on its geometry. Note that we do not need to build the matrix  $\mathbf{H}_u(\omega)$  but just to know the modal frequencies  $\omega_U$  and their corresponding mode shapes  $\phi_U$ . So it can be calculated by solving an eigenvalue problem from the assembled matrices of the structure by Finite Elements modal analysis. Furthermore, we built numerically the frequency constrained transfer functions matrix  $\mathbf{H}_c(\omega)$  connecting the dynamics of all points of constrained rotor, which simulates measurements. For more realistic simulations, we add a random noise with Gaussian distribution  $\mathbf{H}_{noise}(\omega)$  to the constrained transfer functions matrix  $\mathbf{H}_c(\omega)$  as follows:

$$\mathbf{H}_{c_{noise}}(\omega) = \mathbf{H}_c(\omega) + \mathbf{H}_{noise}(\omega)$$

The first six computed mode shapes of the unconstrained system are displayed in Fig. 2.

### 4.3 Identification Results

An amount of 10 % of noise was injected in the simulated transfer functions. On the other hand, 5 % of modeling error was added to the Young’s modulus and the density of components structure. Figure 3a, b shows the identification results for the various support parameters.

It can be noticed that the noise in the transfer function has an important negative impact on the quality of our identification results, mainly for the support mass.

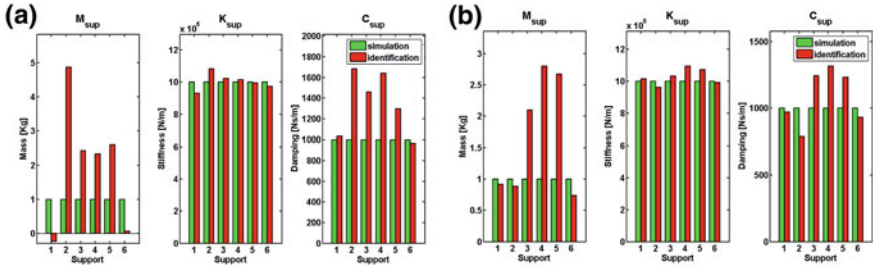


Fig. 3 a 10 % noise in the transfer function, b 5 % error in the model

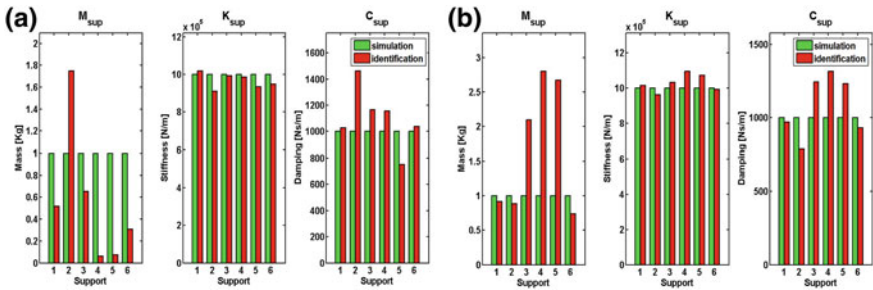


Fig. 4 a 10 % noise in transfer function, SVD regularization, b 10 % noise in transfer function, Tikhonov regularization

However, the introduction of the modeling error doesn't have a strong effect on the results. To overcome the problems related to the noise contribution, we implemented the SVD and Tikhonov regularization techniques, as previously described. The results are illustrated in Fig. 4.

Both SVD regularization and Tikhonov regularization allow better results for the identification procedure, however the mass parameters still present significant errors. It should be noted that, if the orders of magnitude of the support parameters are too different from each other, the smallest ones may have larger percentage of error due to the characteristics of least squares method.

In order to improve the identification results, another method is developed to identify the damping and mass coefficients separately, if they are too small in comparison with the stiffness coefficients. In order to solve the equation system (2), the support stiffness matrix  $\mathbf{k}_c$  is added to both sides of the equation, then a procedure similar to the derivation of Eq. (9) is used to identify the support damping and mass coefficients. The results obtained, shown in Fig. 5a, are clearly improved. When considering identical supports, the identification results using this method are presented in Fig. 5b.

This method shows satisfactory results, in particular for Fig. 5b which assumes identical supports. Using the various regularization strategies previously described, it can be said that the overall identification procedure is robust to noise pollution.



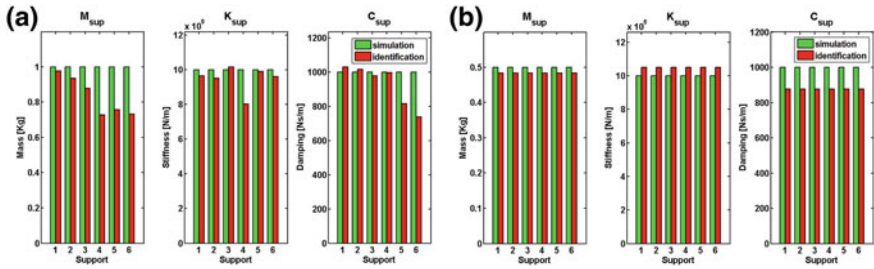


**Fig. 5** Identification with 10 % of noise in transfer function, **a** without considering identical supports, **b** considering identical supports

## 5 Conclusions

The dynamic behavior of a mechanical system is strongly affected by the properties of its supporting devices. In this work, a method for the identification of the supports properties which directly uses the measured frequency transfer functions of the constrained system and the modes of the unconstrained system was developed. There are several different methods using the transfer functions, directly or indirectly, to identify the structural parameters. However, most of those methods suffer from the problem of noise. Therefore, to overcome such difficulty, it is necessary to mitigate its influence. A new formulation was introduced to overcome the noise problem. This formulation benefits from SVD or Tikhonov regularization for mitigating the ill-conditioning of the inverse problem. The accuracy and feasibility of the proposed method were verified and demonstrated through realistic numerical simulations.

**Acknowledgments** This work was supported by the Portuguese FCT through the bilateral agreement Portugal/Tunisia 2013–2014.

## References

Arumugam P, Swarnamani S, Prabhu BS (1994) Experimental identification of linearized oil film coefficients of cylindrical and tilting pad bearings. In ASME 1994 international gas turbine and aeroengine congress and exposition. American Society of Mechanical Engineers, pp V005T14A012–V005T14A012

Chan SH, White MF (1991) Experimental determination of dynamic characteristics of a full size gas turbine tilting-pad journal bearing by an impact test method. In Modal analysis, modeling, diagnostics, and control: analytical and experimental, DE, vol 38, pp 291–298

Debut V, Delaune X, Antunes J (2010) Identification of the nonlinear excitation force acting on a bow string using the dynamical responses at remote locations. Int J Mech Sci 52(1419):1436

Debut V, Carvalho M, Antunes J (2012) Recovering the unconstrained modes of axisymmetric structures from measurements under constrained condition. In: Proceeding of the 19th international congress on sound and vibration, Vilnius, Lithuania

- Delaune X, Antunes J, Debut V, Piteau P, Borsoi L (2010) Modal techniques for the remote identification of nonlinear reaction at gap-supported tubes under turbulent excitation. *J Pressure Vessel Technol* 132:031801-3
- Dowson D, Taylor CM (1980) The state of knowledge in the field of bearing-influenced rotor dynamics. *Tribol Int* 13(5):196–198
- Nordmann R, Scholhom K (1980) Identification of stiffness and damping coefficient of journal bearing by impact method. In: *Proceedings of international conference on vibration in rotating machinery*, Institute of Mechanical Engineering, vol C285/80, pp 231–238
- Özgülven HN (1990) Structural modifications using frequency response functions. *Mech Syst Signal Process* 4:53–63
- Qiu ZL, Tieu AK (1997) Identification of sixteen force coefficients of two journal bearings from impulse responses. *Wear* 212(2):206–212
- Ramsden P (1968) Review of published data and their application to the design of large bearings for steam turbines. In: *Proceedings of conference in lubrication and wear: fundamentals and application to design*, IMechE, vol 182, Part 3A, pp 75–81
- Tiwari R, Lees AW, Friswell MI (2004) Identification of dynamic bearing parameters: a review. *Shock Vib Digest* 36(2):99–124
- Wang JH, Liou CM (1991) Experimental identification of mechanical joint parameters. *J Vib Acoust* 113(1):28–36

# Dynamic Analysis of a Wedge Disc Brake According to the Variations of Friction Coefficient

**K.R.M. Mahmoud**

**Abstract** Noise and vibrations associated with the braking process are mainly affected by the coefficient of friction. The aim of this work is to study the effect of principal parameters i.e. normal force, sliding speed and wedge inclination angle on the dynamic linear analysis of wedge disc brake and their comparisons with conventional disc brake system. The coefficient of friction is measured and expressed as a function of sliding speed and normal force for the two types of disc brakes. The results illustrate that there are noticeable differences in wedge disc brake resonance frequency and shoe factor step response with variations of coefficient of friction and wedge inclination angle. However, the coefficient of friction has a slight effect on the dynamic characteristics in the case of conventional disc brake. It was noted that the sliding speed has a considerable effect on wedge disc brake dynamics. It was concluded that the normal force has little effect on disc brake dynamic characteristics for both brakes.

**Keywords** Wedge disc brake · Stability · Friction · Dynamic characteristics

## 1 Introduction

Many of the brake mechanisms are proposed which are far from being promising enough to offer fully optimized performance. Experimental approaches using brake dynamometers have been widely used to investigate the brake performance and to study the influence of different design parameters at various operating conditions mainly to understand the characteristics of the brake system during braking event and to verify solutions of simulation models (Mahmoud and Mourad 2014; Blau and McLaughlin 2003).

---

K.R.M. Mahmoud (✉)

Automotive Department, Faculty of Engineering, Minia University, 61111 Minia, Egypt  
e-mail: drkm2005@gmail.com

K.R.M. Mahmoud

Mechanical Department, Faculty of Engineering, University of Jeddah, Jeddah, Kingdom of Saudi Arabia

In several research efforts, it was concerned to investigate mainly the friction process. Where, the braking process is originally a conversion of kinetic energy into heat through friction. Many studies showed that the coefficient of friction is affected by several conditions such as the surface finishing, material properties, temperature, sliding speed, and normal force. This leads to the observation that the friction coefficient varies with the brake time (Mitschke et al. 1995; Mahmoud 2005). Serverin and Dörsch (2001) have presented the variation of the shoe factor with the coefficient of friction variations. There were many efforts to determine accurately the coefficient of friction and its variation depending on the normal force, sliding speed and contact temperature. This leads to the observation that the coefficient of friction is varied with the brake time. There is a relationship between the sliding speed and the coefficient of friction especially under extreme loads. Many studies such as Blue (1995) concluded that the sliding friction greatly increases with the decrease of the sliding velocity. Also, it is observed that the coefficient of friction decreased with the increase of the sliding speed (Eriksson et al. 1999). Blau (1995) also researched to form the relation between the sliding speed and the coefficient of friction under extreme loads. The results indicate that the coefficient of friction decreases with the increase of the sliding velocity. Eriksson et al. (2002) have experimentally investigated the relation between the coefficient of friction and the sliding speed. They used five different types of brakes, and each brake had a trend that differed from the others, however, the coefficient of friction decreased with the sliding speed in all the brakes that were investigated in their study.

The brake shoe factor  $C^*$  is known as the ratio between friction (brake) force on the shoe to the applied force at the tip of the shoe. Whereas, the brake force between the rotor and the pad is as a result of the friction process (Mahmoud 2005). The shoe factor  $C^*$  depends mainly on the value of the coefficient of friction. The self-amplified brakes are characterized by high brake shoe factor but at the same time they have high sensitivity to the friction coefficient variations. From the other side, conventional disc brake has low brake shoe factor and it is less sensitive to the change of friction coefficient (Mitschke et al. 1995).

Wedge disc brake is introduced in different shapes by many investigators such as Dietrich et al. (2001) who invented it first, and Hartmann et al. (2003). In any case, all the innovations that are introduced depend mainly on the providence of the disc brake with an electromechanical system as well as to apply the self-amplification in the disc brake.

Many design forms of wedge disc brake were introduced to increase the brake effectiveness by changing the configuration of the brake. For example, a wedge disc brake which is provided by a wedge to increase the brake force. In the last few years' wedge-actuated disc brakes were presented but until now they are still in the research stage. These designs are still at an early development stage and requires further research before its full potential can be deployed (Mahmoud 2005; Ghazaly et al. 2014).

It is important to investigate the dynamic characteristic of vehicle brake. For example, Ćirović and Aleksendrić (2011) have presented a study aimed to investigate the disc brake using finite element analysis. Their results indicate that disc brake topography has a significant effect on dynamic characteristics as well as squeal generation.

In the present work, a set of experimental tests are conducted to study the effect of sliding speed and normal force on the friction coefficient of wedge and conventional disc brakes. The coefficient of friction is measured and expressed as a function of sliding speed and normal force for the two types of disc brakes. Then Matlab Simulink models are created to study the dynamic characteristics of wedge and conventional disc brakes with the variations of wedge inclination angle, coefficient of friction, sliding speed and normal force.

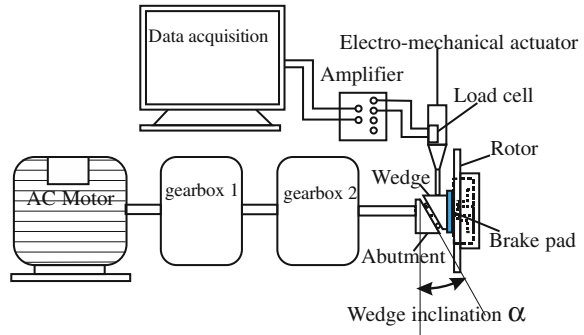
## 2 Experimental Setup

The brake dynamometer test rig, shown in Fig. 1 is designed to extend the brake system with necessary mechanical power, rotation speed and applied force to calculate the coefficient of friction between disc and pads as well as to evaluate the brake performance. Full details of the design are outlined in our previous work (Mahmoud and Mourad 2014). The test rig is divided into driving unit, braking unit and measurement facilities. The rotational speed is measured using a tachometer. An electromechanical actuator is used to generate the required applied force. The braking force as required output is obtained by load cell. The wedge inclination angle is maintained at  $30^\circ$ . Four-channel data acquisition system is used to collect the signal data. Figure 2 shows the test rig with its different units. The driving unit consists of an AC motor of 18.56 kW and 1500 rpm, that rotates the driving shaft at different rotating speeds. The braking unit comprises the new wedge disc brake assembly, as shown in Fig. 2. The instruments for measurement include rotational speed (tachometer), applied pressure (a pressure gauge) and tangential force (load cell) (Mostafa et al. 2013a, b).

**Fig. 1** Photo of brake dynamometer test setup and measurement instrumentation



**Fig. 2** Brake dynamometer test setup and measurement instrumentation



### 3 Wedge Disc Brake Modelling

Two Matlab Simulink models for conventional and wedge disc brakes are designed according to the following mathematical equations. All parameters used in these models such as brake pad mass, brake pad stiffness etc., have the same values for both conventional and wedge disc brakes. Figure 3 show the mathematical models for conventional and wedge disc brakes. Table 1 shows the operating parameters used in the conventional and wedge disc brake models.

First, conventional disc brake, the equations of motion can be expressed as follow:

$$m_a \ddot{x}_a + c_a (\dot{x}_a - \dot{x}_p) + k_a (x_a - x_p) = F_{app} \tag{1}$$

$$m_p \ddot{x}_p - c_a (\dot{x}_a - \dot{x}_p) - k_a (x_a - x_p) + c_p \dot{x}_p + k_p x_p = 0 \tag{2}$$

$$c_p \dot{x}_p + k_p x_p = F_N \tag{3}$$

Second, wedge disc brake, the equations of motion can be expressed as follow:

$$m_a \ddot{x}_1 + c_a (\dot{x}_1 - \dot{x}_2) + k_a (x_1 - x_2) = F_{app} \tag{4}$$

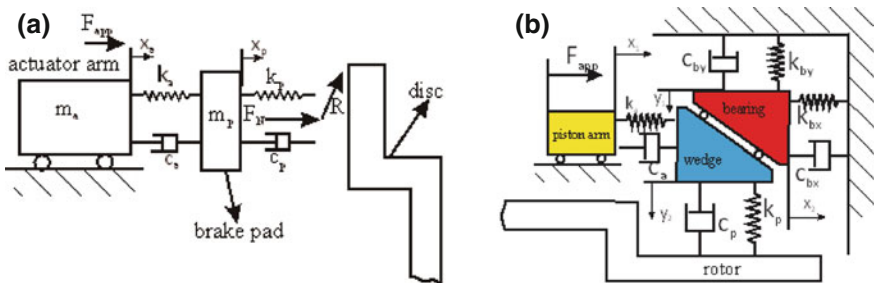


**Fig. 3** Disc brake mathematical models (a conventional, b wedge)

**Table 1** Conventional and wedge disc brakes parameters

Parameters	Symbol	Value
Piston arm mass (kg)	$m_a$	0.033
Piston arm stiffness (N/m)	$k_a$	$10^7$
Piston arm damping coeff. (Ns/m)	$c_a$	116
Brake pad mass (kg)	$m_p$	0.2
(Wedge and brake pad) mass (kg)	$m_w$	0.2
Brake pad damping coeff. (Ns/m)	$c_p$	89
Brake pad stiffness (N/m)	$k_p$	$10^6$
Bearing mass (kg)	$m_b$	0.2
Bearing damping coeff. (Ns/m)	$c_{bx}$ and $c_{by}$	282
Bearing stiffness (N/m)	$k_{bx}$ and $k_{by}$	$10^7$

$$m_b \ddot{x}_2 - c_a(\dot{x}_1 - \dot{x}_2) - k_a(x_1 - x_2) + c_{bx}\dot{x}_2 + k_{bx}x_2 = 0 \tag{5}$$

$$m_b \ddot{y}_1 + c_{by}(\dot{y}_1 - \dot{y}_2) + k_{by}(y_1 - y_2) = 0 \tag{6}$$

$$m_w \ddot{y}_2 - c_{by}(\dot{y}_1 - \dot{y}_2) - k_{by}(y_1 - y_2) + c_p \dot{y}_2 + k_p y_2 = 0 \tag{7}$$

$$c_p \dot{y}_2 + k_p y_2 = F_N \tag{8}$$

The coefficient of friction can be formed as:

$$\tan \alpha = \frac{y_2 - y_1}{x_2 - x_1} \tag{9}$$

$$\mu = \frac{R}{F_N} \tag{10}$$

Table 1 illustrates the models parameters.

## 4 Results and Discussions

The effect of normal force on the coefficient of friction for wedge and conventional disc brake at 1 m/s sliding speed is shown in Fig. 4. From this Figure it can be noticed that the higher the normal force, the slightly lower is the coefficient of friction for both brake types. These results are in agreement with Blau and McLaughlin (2003) who have also established that with low contact pressure, the chemistry of the contact areas plays key role in the variations of the coefficient of friction. With high normal force, many factors can be affected by many parameters such as surface softening by friction heating, increased blowing in the softer materials, and enhanced heat transfer and oxide film formation. The experimental results could be expressed with an acceptable error as follow:

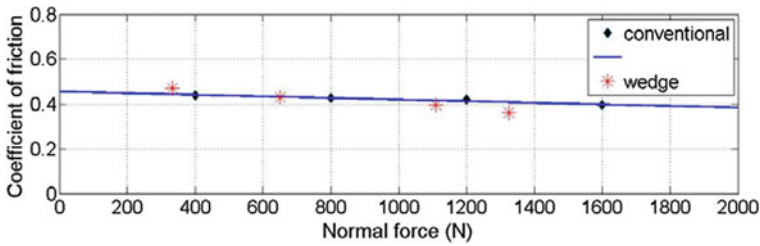


Fig. 4 Coefficient of friction variations with normal force

$$\mu = \mu_o - 0.00033F_N \tag{11}$$

where  $\mu$  is the coefficient of friction,  $\mu_o$  is the static friction coefficient and  $F_N$  is normal force in N.

Figure 5 illustrates the effect of sliding speed on the coefficient of friction for wedge and conventional disc brakes. It can be noticed that with the increase in sliding speed there is a decrease in the coefficient of friction for both types. These results are in agreement with many researchers such as Mahmoud (2005) and Blue (1995). With high sliding speed, friction is affected by many parameters such as surface softening by friction heating, increased plowing in the softer materials, enhanced transfer and oxide film formation. It is difficult to identify which parameter plays the main role on the coefficient of friction variations. The experimental results could be expressed with an acceptable error as follow:

$$\mu = \mu_o - 0.1v + 0.009v^2 \tag{12}$$

where  $\mu$  is the coefficient of friction,  $\mu_o$  is the static friction coefficient and  $v$  is sliding speed in m/s.

Figure 6a, b show the brake shoe factor  $C^*$  of wedge disc brake as time and frequency response with different inclination angles. It is obvious that as the wedge

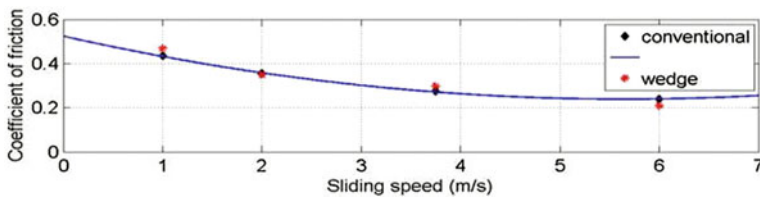
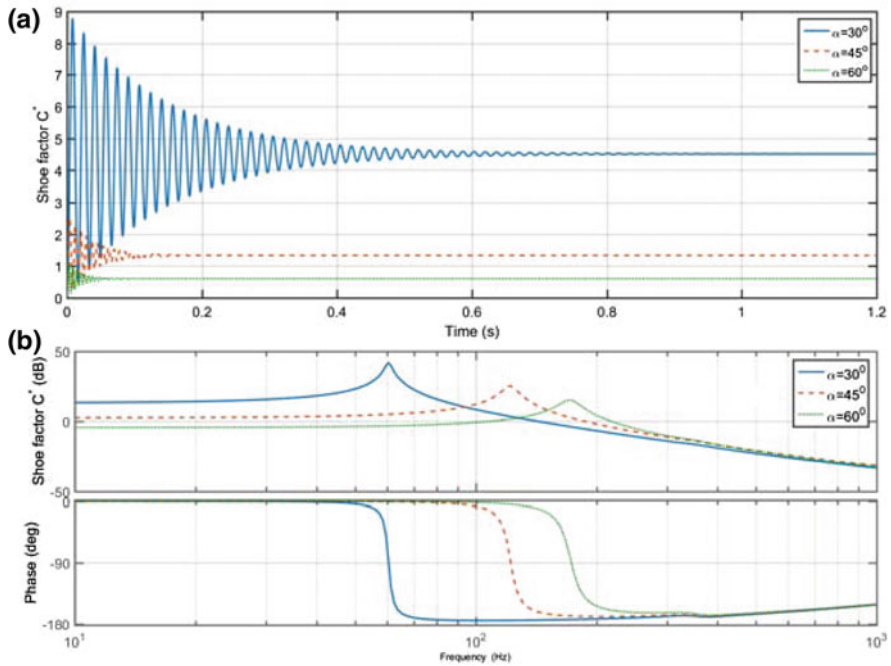


Fig. 5 Coefficient of friction variations with sliding speed





**Fig. 6** Linear analysis of wedge disc brake shoe factor with wedge inclination angle variations (**a** step response, **b** frequency response)

inclination angle  $\alpha$  decreases the brake shoe factor increases. The increase in brake shoe factor is associated with a delay in response time of as high as about 0.8 s at an inclination angle of  $30^\circ$ . On the other hand, the resonance frequency is strongly affected by wedge inclination angle, not to mention the significant decrease in frequency. Not only has the change in the inclination angle from  $30^\circ$  to  $60^\circ$  led to a decrease in the resonance frequency from about 105 to 80 Hz, it was also noted that the resonance frequency values are low which means it is more vulnerable to vibrations and noise. The findings could be attributed to the fact that the wedge disc brake has four degrees of freedom as compared to two in the case of conventional disc brake, which causes the delayed response of the system. And as a result the resonance frequency decreases. Also, the high sensitivity of wedge disc brake to the inclination angle and coefficient of friction leads to extreme vulnerability in the dynamic characteristics of wedge disc brake as concluded by Mahmoud and Mourad (2014) and Gombert et al. (2004).

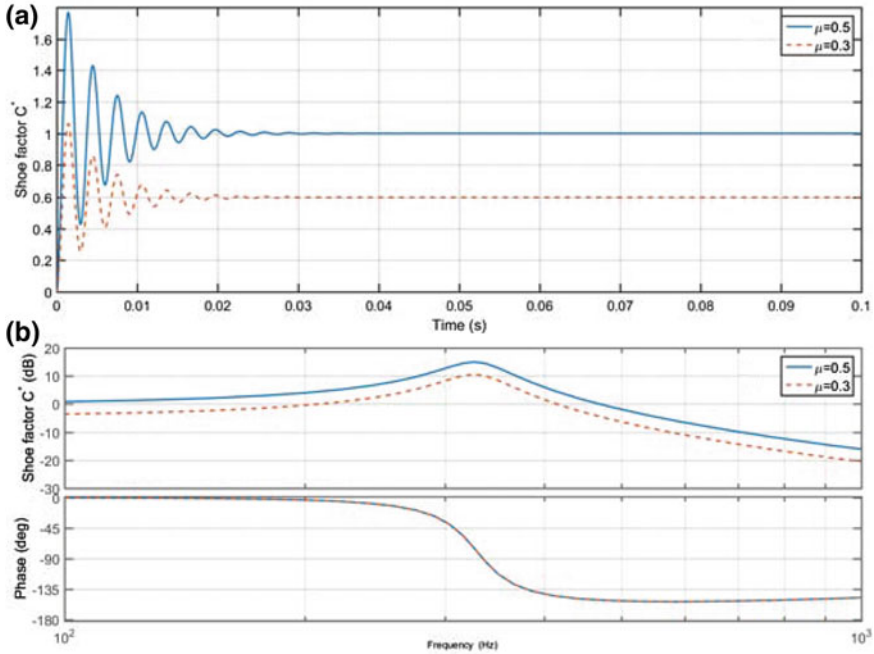


**Fig. 7** Linear analysis of conventional disc brake shoe factor with coefficient of friction variations (**a** step response, **b** frequency response)

The effect of the coefficient of friction on the conventional disc brake shoe factor as step and frequency responses is shown in Fig. 7a, b respectively. From these figures it can be seen that the brake shoe factor value was affected by the coefficient of friction such that the higher the coefficient of friction, the higher the brake shoe factor. However, there is no any change on step or frequency responses with the change in friction coefficient.

The effect of the coefficient of friction on shoe factor of wedge disc brake as step and frequency responses is illustrated in Fig. 8a, b respectively. It can be noticed that the increase of friction coefficient from 0.3 to 0.5 leads to significant increase in the brake shoe factor value. However, the higher the coefficient of friction the more delay in step response and the lower the resonance frequency. Increase in friction coefficient from 0.3 to 0.5 is accompanied with a reduction of the resonance frequency from about 83 to 40 Hz and an increase of transient time from about 0.2 to 1.2 s. By comparing these results with conventional disc brake, the transient time of conventional disc brake is much less than the wedge one for the same friction coefficient value. Therefore, the resonance frequency of conventional disc brake is much more than the wedge disk brake system.

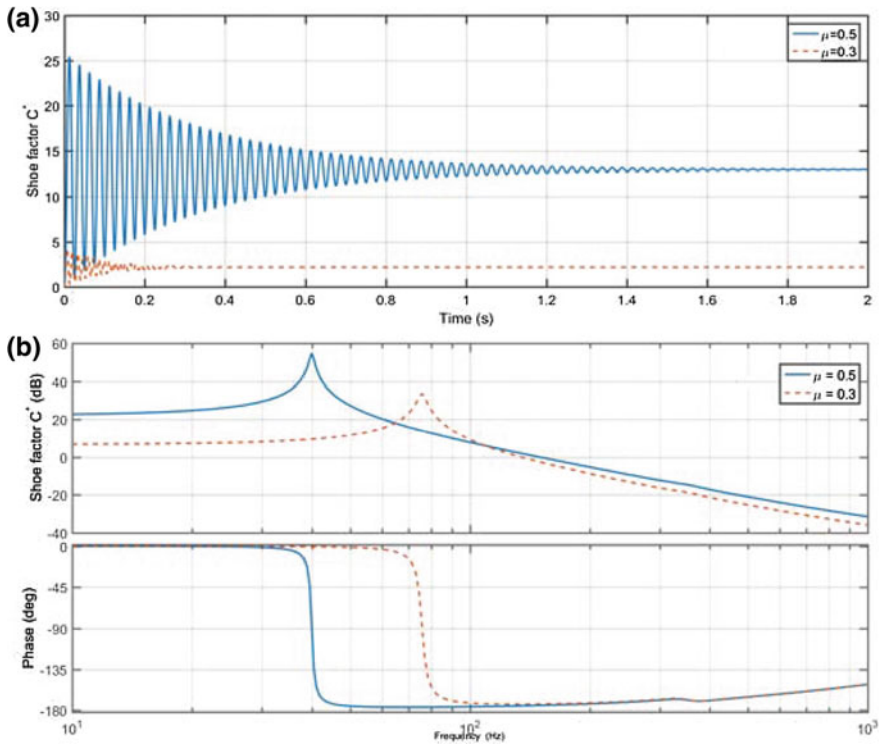


**Fig. 8** Linear analysis of wedge disc brake shoe factor with coefficient of friction variations (a step response, b frequency response)

The effect of sliding speed on conventional and wedge disc brake shoe factors are shown in Figs. 9 and 10 respectively. From these figures it can be seen that the higher the sliding speed the lower the brake shoe factor for both brake types. But still, the conventional disc brake is less sensitive than wedge disc brake to sliding speed variations. The response time and resonance frequency of conventional disc brake aren't being affected to the variations of sliding speed. While, the response time as well as resonance frequency are greatly influenced by the change in sliding speed. In other words, the resonance frequency remains the same for conventional disc brake and increases markedly with the increase in sliding speed. The resonance frequency of wedge disc brake increases from about 65 to 84 Hz when the sliding speed is increased from 1 to 5 m/s. But, the resonance frequency of conventional disc brake remains constant at about 220 Hz with the same sliding speed variations. This means that not only the resonance frequency of wedge disc brake is affected by

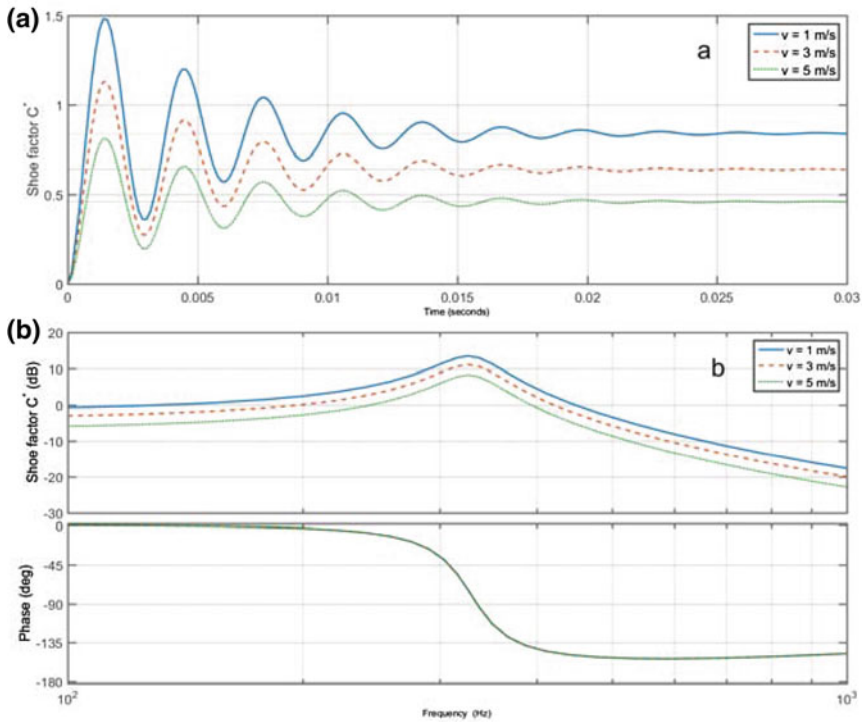


**Fig. 9** Linear analysis of conventional disc brake shoe factor with sliding speed variations (**a** step response, **b** frequency response)

sliding speed variations but also it was lower than the case of conventional disc brake. These findings are in agreement with the results of Blau (1995) and Mahmoud (2005) for brake pads materials. The friction at the start is low and remains at its initial value for some time and the factor mainly responsible for this low friction phenomenon is the presence of a layer of foreign material between brake pad and disc.

The effect of normal force on the step and frequency responses for conventional and wedge disc brakes is shown in Figs. 11 and 12 respectively. Noting these figures, it can be concluded that there is no big difference between the effect of sliding speed and normal force except that the normal force is less effective on brake shoe factor  $C^*$ . Change of normal force has no effect on the step or the frequency responses of conventional disc brake. However, in the case of wedge disc

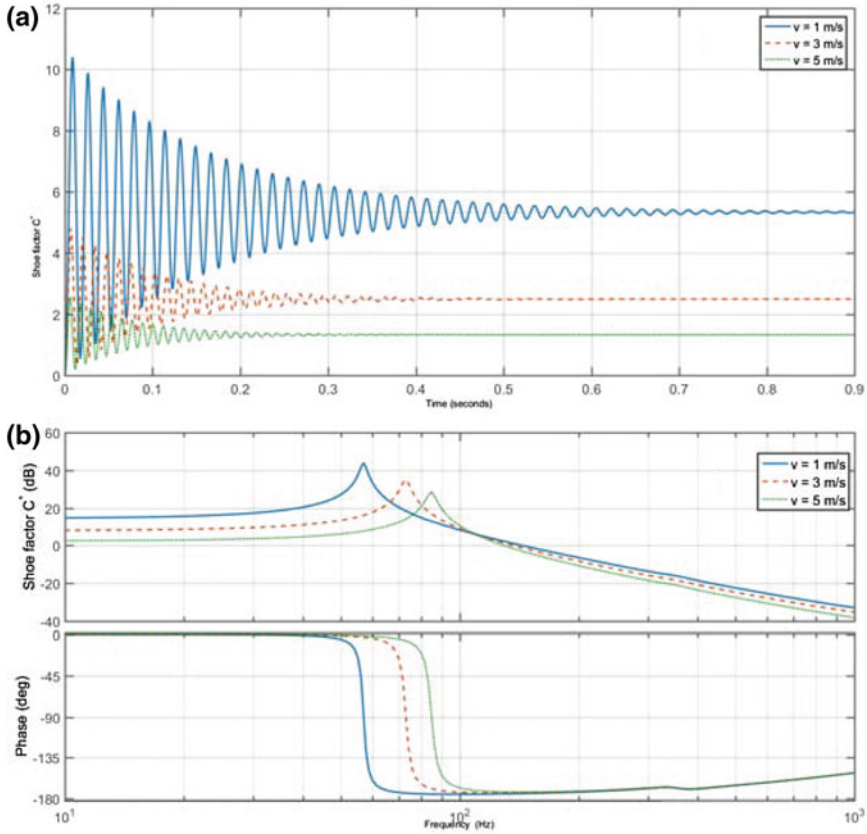


**Fig. 10** Linear analysis of wedge disc brake shoe factor with sliding speed variations (**a** step response, **b** frequency response)

brake, it appears that there is a noticeable but small effect of normal force on step and frequency responses. By increasing the normal force from 400 to 2000 N, the response time decreased from about 0.9 to 0.7 s and the resonance frequency increased from about 55 to 63 Hz. These results are in agreement with the results of Chowdhury et al. (2011). This may be attributed to the fact that the strength of these materials is greater at higher shear strain rates which results in a lower real area of contact and a lower coefficient of friction in dry contact conditions.

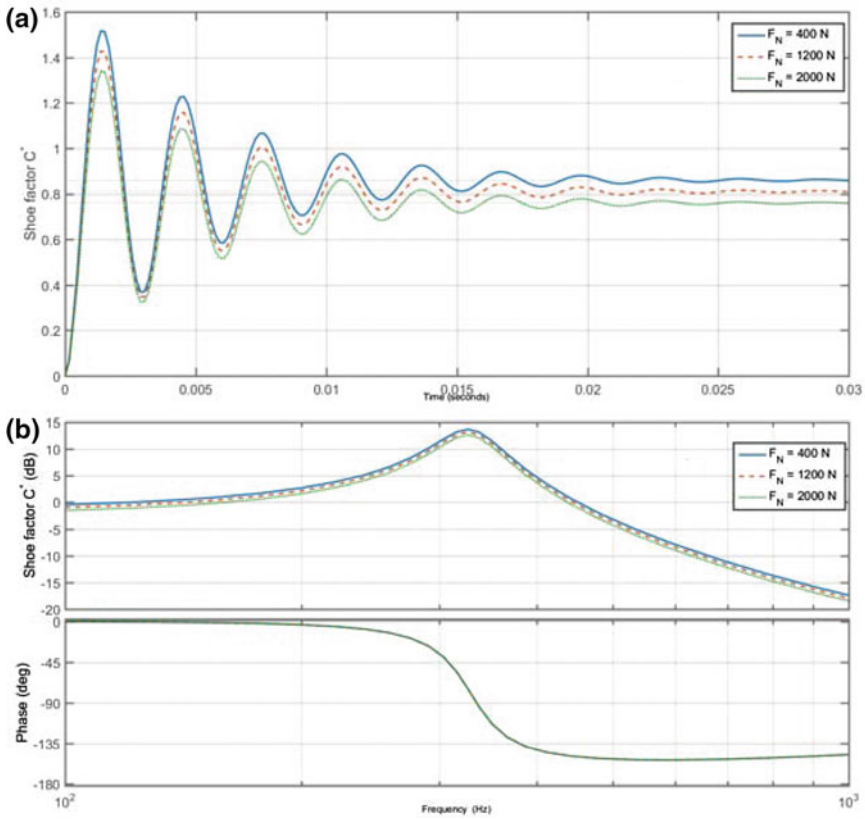
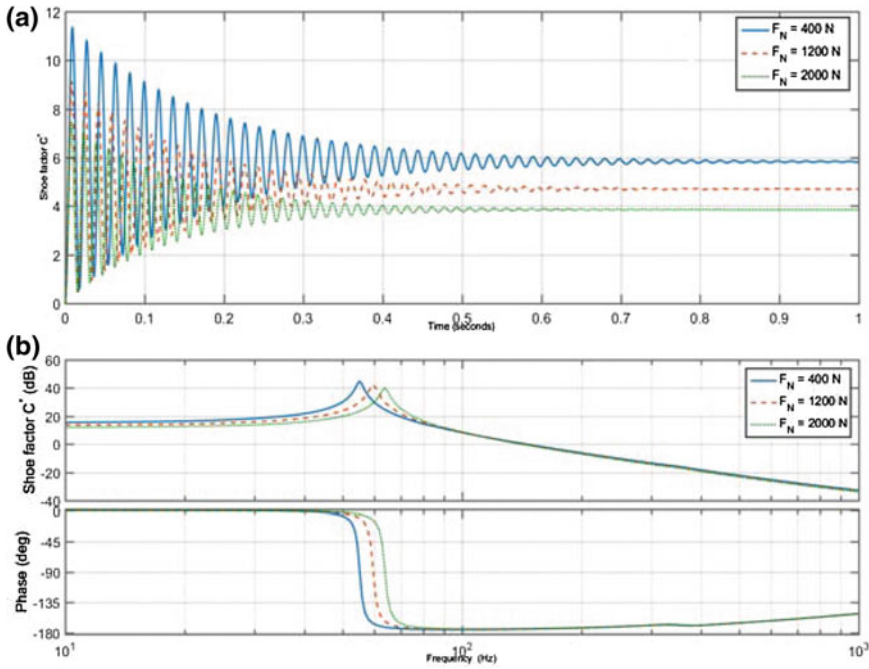


Fig. 11 Linear analysis of conventional disc brake shoe factor with normal force variations (a step response, b frequency response)

## 5 Conclusion

Series of experimental test were carried out to investigate the effect of sliding speed and normal force on the coefficient of friction between brake pad and disc. Coefficient of friction has a considerable effect on disc brakes dynamics; however, this effect was more noticeable with wedge disc brake mechanism as compared to the conventional disc brake system. Wedge disc brake shoe factor response is very late as compared to the conventional disc brake and the delay increases with the increase of the coefficient of friction as well as the decrease of wedge inclination



**Fig. 12** Linear analysis of wedge disc brake shoe factor with normal force variations (**a** step response, **b** frequency response)

angle. On the other hand, the wedge disc brake pad resonance frequency strongly decreases compared to that of conventional disc brake pad that has the same properties. This decrease is magnified as the coefficient of friction increases or the wedge inclination angle decreases. The normal force has relatively little effect on wedge disc brake dynamics and has a negligible effect on classical disc brake dynamics. The sliding speed has a considerable effect on disc brake dynamics; however, it affects more in the case of wedge disc brake.

## References

Blau PJ (1995) Friction science and technology. Dekker Mechanical Engineering. CRC Press, Boca Raton. ISBN 0824795768, 9780824795764

Blau PJ, McLaughlin JC (2003) Effects of water films and sliding speed on the frictional behavior of truck disc brake materials. *Tribol Int* 36:709–715

Chowdhury MA, Khalil MK, Nuruzzaman DM, Rahaman ML (2011) The effect of sliding speed and normal load on friction and wear property of aluminum. *Int J Mech Mechatron Eng IJMME-IJENS* 11(01)

Ćirović V, Aleksendrić D (2011) Dynamic modelling of disc brake contact phenomena. *FME Trans* 39(4):177–184

- Dietrich J, Gombert B, Grebenstein M (2001) Elektromechanische Bremse mit Selbstverstärkung. Patent DE 198 19 564 C2
- Eriksson M, Bergman F, Jacobson S (1999) Surface characterisation of brake pads after running under silent and squealing conditions. *Wear* 232:163–167
- Eriksson M, Bergman F, Jacobson S (2002) On the nature of tribological contact in automotive brakes. *Wear* 252:26–36
- Ghazaly NM, Makrahy MM, Gawwad KAAE, Mahmoud KR, Tawwab AMAE (2014) Experimental evaluation of an empirical model for wedge disc brake using Box-Behnken design. *Int J Veh Syst Struct* 6(3):58–63. doi:[10.4273/ijvss.6.3.03](https://doi.org/10.4273/ijvss.6.3.03)
- Gombert B, Hartmann H, Roberts R, Schautt M (2004) A Progress Report on the Mechatronic Wedge Brake (eBrake). eStop Publications reports
- Hartmann H, Schautt M, Pascucci A, Gombert B (2003) eBrake – The Mechatronic Brake. SAE Technical Paper 2003-01-2582
- Mahmoud KRM (2005) Theoretical and experimental investigations on a new adaptive duo servo drum brake with high and constant brake shoe factor. University of Paderborn
- Mahmoud KRM, Mourad M (2014) Parameters affecting wedge disc brake performance. *Int J Veh Perform* 1(3/4):254–263
- Mitschke M, Sellschopp J, Braun H (1995) Regelung der Bremsen an Kraftfahrzeugen im unterkritischen. Bereich VDI-Verlag GmbH. Düsseldorf
- Mostafa MM, Nouby MG, Gawwad KAAE, Mahmoud KR, Tawwab AMAE (2013a) A preliminary experimental investigation of a new wedge disc brake. *Int J Eng Res Appl* 3 (6):735–744
- Mostafa MM, Gawwad KA, Mahmoud KR, Tawwab AMAE (2013b) Optimization of operation parameters on a novel wedge disc brake by Taguchi method. *Am J Veh Des* 1(2):21–24
- Serverin D, Dörsch S (2001) Friction mechanism in industrial brakes. *Wear* 249:771–779



# Index

## A

Acoustic scattered fields, 43  
Affi, Z., 89  
Assumed natural strain formulation (ANS),  
291, 299

## B

Beam, 224–226, 230–232

## C

Centrifugal pump, 195, 198  
Characteristic curve, 198  
Chatter, 77  
Comfort, 89, 90, 96–99  
Composite, 115, 123  
Continuous wavelet, 101, 109

## D

2DNMF, 136–138, 141–143  
Damage  
besides mechanical, 206  
evolution in circumferential milling, 206  
Damping, 66, 68–72, 74, 115, 116, 123  
Diesel engine, 135, 137  
Distribution, 137, 140  
Distribution fault, 135, 137, 142, 143  
Distribution fault classes, 141  
Distribution of modal kinetic energies, 159  
Distribution of modal kinetic energies and  
modal strain energies, 154, 162  
Dynamic characteristics, 313, 315, 319

## E

Elastic coupling, 153, 155, 162  
Ensemble empirical mode decomposition  
(EEMD), 15–17, 19, 21  
Error position, 166  
Experimental investigation, 223, 224, 230, 232

## F

Faults detection, 15, 102  
FE, 269, 271, 272  
analysis, 213  
approach, 213  
finite element model, 207  
Finite element method, 116, 121–123  
Forced vibration, 224, 226, 232  
Friction, 269–271, 274–276, 313–315,  
317–325

## G

Gas turbine, 101–105, 112  
Gear, 13, 154  
Gearbox, 154  
Generation of residues, 102  
GFRP, 269, 271  
behavior of composite, 213  
cylindrical milling, 206  
material, 207  
plate dimensions, 207  
structure, 213  
Graa, 89

## H

Heat source  
a moveable cylindrical, 208  
motion played, 210  
vicinity, 207  
volumetric, 205  
Honeycomb, 223, 224, 227  
Honeycomb-core sandwich, 69  
Houidi, 89

## I

Identification, 66, 67, 301, 302, 309  
Improved multi objective robust collaborative  
optimization (IMORCO), 248, 254, 256,  
257

Independent component analysis (ICA),  
125–127, 129, 132

Inhomogeneous wave correlation (IWC), 66,  
68, 70, 72

Interpolation method, 35, 36, 38, 41

Interval uncertainty, 248, 253, 257

Inverse problem, 301

ISO 2631, 90, 99

**L**

Lateral dynamic vibration, 91

Load sharing, 166, 169, 171

**M**

Meshing phase, 166, 171

Milling, 85

- behavior of GFRP composite, 213
- circumferential, 206
- cylindrical, 206
- helical, 207
- operation, 207
- predicting the HAZ during, 213

Modal appropriation, 215–217

Modal dominant kinetic and strain energies  
distributions, 162

Modal strain energy, 160

Modified Vanmarcke approximation, 260, 264

Monitoring system, 102

Multibody dynamic, 91

Multidisciplinary design optimization (MDO),  
248

Music type method, 43

**N**

Najlaoui, 89

Natural frequencies, 154, 158, 162

Near-field operator, 44, 47, 49

Neural networks system, 102, 106, 108

Non-distributed multi-objective robust  
optimization (NDMORO), 253, 256,  
257

Non-negative matrix factorization, 135

**O**

Operational modal analysis (OMA), 125, 126,  
132

**P**

Phase meshes gear, 168

PID controller, 90, 96, 97

Piezoelectric patches, 23–25, 27, 28, 30, 32

Piping vibration, 195

Planetary gear, 165

Planetary gear load sharing, 166

Planets load sharing, 172

Planets position errors, 172

Poisson, The, 260

Poisson approximation, 263

Position errors of planets, 170

**Q**

Quarter car vehicle model, 125, 126, 128–132

Quasi-back-scattering configuration, 43–46

**R**

Rail vehicle, 89, 90, 96, 98

RBO strategy, 260

Regularization, 301, 305–307

Reliability based optimization, 259

Resonance, 195, 196, 200–203

Rice's formula, 263

Romdhane, 89

Rotating machine, 13, 15

Run up, 168, 172

**S**

Sampling method, 43

Sandwich, 223–226, 231, 232

Scratch map, 269

Scratch test, 269–271

Shunt, 23–25, 31, 32

Sound radiation, 35–39

Stability lobes, 77, 84

S-transform (ST), 135–137, 143

Structural modifications, 301

**T**

Temperature

- ambient, 208
- capturing, 206
- comparative analysis, 210
- computation of a transient, 207
- current, 208
- cutting, 206
- function, 210
- Heat Affected Zone, 210, 212
- histories' predictions, 210
- matrix vitrifying, 206
- order to simulate, 207
- peak, 205, 210
- ranges, 207
- sensitive evolution of peak, 210
- thermal conductivity governs, 209
- thermal conductivity values, 210
- tool-plate, 211
- typical, 210
- value and more disparity, 210
- variance, 206

Topology optimization, [24](#), [27](#), [30](#)  
Turning, [77](#)  
Two dimensional non-negative matrix  
factorization, [136](#)

**V**

Vanmarcke, The, [260](#)  
Vanmarcke approximation, [263](#)  
Varing condition, [102](#)

Vibration, [13–16](#), [115](#), [116](#), [123](#)  
Vibration modeling, [106](#)  
Vibration reduction, [23](#)  
Viscoelastic material, [123](#)

**W**

Wavenumber space, [66](#)  
Wear, [269–271](#), [275](#), [277](#), [278](#)  
Wedge disc brake, [313–316](#), [318–325](#)